ANALYSIS OF TRIMMING DIE DURABILITY AND SHEARED EDGE FORMABILITY OF ULTRA-HIGH STRENGTH STEELS

by

SAEID NASHERALAHKAMI

A dissertation submitted in partial fulfillment of the
requirements for the degree of

DOCTOR OF PHILOSOPHY IN MECHANICAL ENGINEERING

2025

Oakland University
Rochester, Michigan

Doctoral Advisory Committee:

Sergey Golovashchenko, Ph.D., Chair
Gary Barber, Ph.D.
Vijitashwa Pandey, Ph.D.
John Bonnen, Ph.D.

To my beloved parents, whose love and guidance have shaped who I am.

To my loving wife, Nahid, whose unwavering support, encouragement, and patience made this journey possible.

To my wonderful children, Lillian and Aaron, who have filled my life with joy, laughter, and perspective throughout this endeavor.

ACKNOWLEDGMENTS

I want to sincerely thank my supervisor, Professor Sergey Golovashchenko, for his valuable guidance, insightful suggestions, and encouragement throughout my doctoral journey. His expertise, patience, and steadfast support have been essential in shaping this work and helping me grow as a researcher.

I am also deeply thankful to my committee members – Dr. John Bonnen, Professor Gary Barber, and Professor Vijitashwa Pandey – for their time, constructive feedback, and valuable suggestions, which have significantly improved this dissertation. In particular, I would like to thank Dr. Bonnen for his insightful comments and generous help with the fatigue analysis portion of this work, which greatly enhanced the quality of this study. I am additionally thankful to Dr. Al Conle for reviewing the fatigue analysis and offering thoughtful comments that helped refine this section.

I gratefully acknowledge the financial support from Ford Motor Company and the Pacific Northwest National Laboratory (PNNL), which made this research possible.

Finally, I would like to thank my colleagues, friends, and family for their support and understanding, which have greatly helped me navigate the challenges of this endeavor.

Saeid Nasheralahkami

ABSTRACT

ANALYSIS OF TRIMMING DIE DURABILITY AND SHEARED EDGE FORMABILITY OF ULTRA-HIGH STRENGTH STEELS

By

Saeid Nasheralahkami

Adviser: Sergey Golovashchenko, Ph.D.

The increasing demand for lightweight, safe, and fuel-efficient vehicles has led to greater use of advanced high-strength steels (AHSS), especially dual-phase steels like DP980, in automotive structures. However, these materials are often sensitive to trimmed edge cracking if stretching along the sheared edge occurs during processes such as stretch flanging. Excessive wear and early chipping of trimming tools are also significant issues in mass production. This dissertation investigates these challenges by analyzing the sheared edge formability of DP980 and the durability of trimming dies using experimental, numerical, and fatigue modeling methods.

Edge quality was assessed based on burr height, burnish depth, fracture morphology, and microhardness mapping. Stretchability was evaluated through tensile, side-bending, and hole-expansion tests, demonstrating that edge quality significantly

affects the sheet's ability to withstand secondary deformation. Two DP980 materials were studied, showing different stretchability results and highlighting the variability within the same grade. A distinctive fracture mechanism was observed during trimming of DP980 steel, resulting in a burr at the final stage.

Finite element models were created using Abaqus/Explicit. Optimized meshes, kinematic contact algorithms, and appropriate fracture criteria enabled reasonable predictions of strain localization, fracture initiation, and punch load history, while also reducing the penetration issue between the die and sheet meshes. The simulation also provided stress data for fatigue analysis of the trimming tool.

This study also analyzed die wear and fatigue life over 230,000 cuts for D2 trimming inserts. Gradual tool wear decreased edge quality and stretchability, while localized chipping on inserts aligned with local burrs on the part edge. Fatigue modeling using the Goodman, Morrow, and Findley criteria showed that shear-based approaches best matched actual failure modes, supported by microstructural evidence of carbide-band effects.

Overall, the findings provide valuable metrics and predictive tools to optimize trimming processes, extend die life, and ensure reliable manufacturing of AHSS.

TABLE OF CONTENTS

LIST OF TABLES

LIST OF FIGURES

NOMENCLATURE

A, B	Coefficients of Rice-Tracey fracture criterion
C	Constant of the Cockcroft-Latham fracture criterion
D	Ductile fracture damage indicator
$D_1,\ D_2,\ D_3,\ D_4, D_5$	Damage constants of the Johnson-Cook fracture criterion
E	Young's modulus
K	Strength coefficient of material in power law
n	Strain hardening exponent
T^*	Absolute temperature
HV	Vickers Microhardness
t	Sheet thickness after deformation
t_0	Initial (as-received) sheet thickness
t_i	Sheet thickness after the i^{th} rolling step
$\varepsilon_1^{(i)}$	Through-thickness strain due to the i^{th} rolling step
r	Strain ratio (r-value – Lankford coefficient)
$\varepsilon_1, \varepsilon_2, \varepsilon_3$	Principal strains
$\bar{\varepsilon}$	Effective (equivalent) strain
$\bar{\varepsilon}_f$	Effective fracture strain
$\dot{\varepsilon}$	Strain rate
υ	Poisson's ratio
η	Stress triaxiality
σ_{flow}	Flow stress
$\bar{\sigma}$	von Mises equivalent stress

$\sigma_1, \sigma_2, \sigma_3$	Principal stresses
σ_m	Mean stress of the principal stresses
$\sigma_a = \Delta\sigma/2$	alternating (amplitude) normal stress
σ_{ar}	Corrected alternating stress
σ_y	Yield strength
σ_u	Ultimate tensile strength
σ_f	True fracture strength in the monotonic tension test
σ^*	Maximum principal stress in the Cockcroft-Latham criterion
R	Stress ratio ($\sigma_{min}/\sigma_{max}$)
τ	Shear stress
τ_m	Mean shear stress
τ_a=$\Delta\tau/2$	Alternating (amplitude) shear stress
τ_f^*	Fatigue shear strength coefficient
τ_f'	Shear fatigue limit
γ	Material constant for Walker fatigue model
N_f	Number of cycles to fatigue failure
σ_f'	Fatigue strength coefficient
b	Fatigue strength exponent
k	Material constant in the Findley fatigue model
S_f^*	Fatigue (endurance) limit
N_f^*	Number of cycles corresponding to the endurance limit
$\sigma_{n,max}$	Maximum normal stress
θ	Angle of the critical plane relative to the *x* principal axis
A_0	Initial cross-sectional area of tensile test coupon
A_f	Final cross-sectional area of tensile test coupon

RA	Reduction of area
τ_{af}	Fatigue limit in alternating torsion
σ_{af}	Fatigue limit in fully reversed bending
$\sigma_{H,max}$	Maximum hydrostatic stress
G	Shear modulus
γ_f	Ductility coefficient of shear fatigue strength
C_y	Exponent coefficient of shear fatigue strength
b_y	Exponent of shear fatigue strength
$\Delta\gamma$	Shear strain range
τ_{aeq}	Effective shear stress
τ_{μ}	Mesoscopic shear stress

LIST OF ABBREVIATIONS

AHSS	Advanced High-Strength Steels
AM	Additive Manufacturing
Al5182-H19	Aluminum Alloy 5182 in H19 condition
Al6022-T4	Aluminum Alloy 6022 in T4 condition
ALE	Arbitrary Lagrangian–Eulerian
ANN	Artificial Neural Network
ASTM	American Society for Testing and Materials
BH	Bake-Hardening Steel
CAD	Computer-Aided Design
CAE	Computer-Aided Engineering
CGA	Circle Grid Analyzer
CP	Complex-Phase Steel
DIC	Digital Image Correlation
DP	Dual-Phase Steel
DQSK	Deep-Draw Quality Special-Killed Steel
EDM	Electric Discharge Machining
EHT	Electrohydraulic Trimming
ESR	Electro Slag Remelting
EXP	Experimental
FE / FEA	Finite Element Analysis
FEM	Finite Element Method
FLD	Forming Limit Diagram

FLC	Forming Limit Curve
FSW	Friction Stir Welding
GISSMO	Generalized Incremental Stress-State-Dependent Damage Model
HAZ	Heat-Affected Zone
HET	Hole Expansion Test
HER	Hole Expansion Ratio
HSLA	High-Strength Low-Alloy Steel
IF	Interstitial-Free Steel
LD / TD / DD	Longitudinal, Transverse, and Diagonal Directions
LEFM	Linear Elastic Fracture Mechanics
M&C	Morrow and Coffin (fatigue models)
MART	Martensitic Steel
PM	Powder Metallurgy
SAZ	Shear-Affected Zone
SEM	Scanning Electron Microscope
SN	Stress versus Number of Cycles to Failure
SPH	Smoothed Particle Hydrodynamics
TE	Total Elongation
TRIP	Transformation-Induced Plasticity Steel
UE	Uniform Elongation
UHSS	Ultra-High-Strength Steel
UTS	Ultimate Tensile Strength
YS	Yield Strength
WPI	Wear Progression Index
XRD	X-ray Diffraction

CHAPTER ONE
INTRODUCTION

Products made of sheet metal are widely used in machines and structures. They include a broad range of consumer and industrial items, such as beverage cans, cookware, car bodies, file cabinets, metal desks, appliances, trailers, and aircraft fuselages. Sheet forming dates back to about 5000B.C., when household utensils and jewelry were made by hammering and stamping gold, silver, and copper [1]. The advantages of sheet metal forming include lightweight and versatile products, a high productivity rate, efficient material use, easy servicing of the machines used, and the ability to employ less skilled workers [1], [2].

Modern product design and manufacturing frequently use a variety of materials. Advanced high-strength steels (AHSS) are relatively new, and their use in the automotive industry is growing significantly because they offer key benefits such as weight reduction, better fuel economy, higher strength, improved crashworthiness, lower maintenance, and increased production efficiency.

1.1. Advanced High-Strength Steels

The trend toward more fuel-efficient and safer vehicles has increased interest in the latest generation of lightweight, higher-strength steel grades as an alternative to traditional milder steel sheets used in the automotive industry. Thinner sheet thickness can be used for weight reduction, and the increased energy absorption of these new steels meets safety requirements.

Advanced high-strength steels (AHSS) enable engineers to meet requirements for safety, efficiency, emissions, manufacturability, durability, and quality at a lower cost. AHSS is a newer generation of steel grades that offer extremely high strength and other advantageous properties while maintaining the high formability required for manufacturing [3], [4]. Figure 1.1 illustrates the strength and formability levels of AHSS compared to older grades of automotive steels [3], [5]. Conventional low- to high-strength steels have simpler one-phase structures and have been widely used for many years, while AHSS have multiple-phase microstructural features. The figure shows that ductility, as measured by percent total elongation, decreases with increasing ultimate tensile strength of steels.

The term “Advanced High-Strength Steels” generally implies a yield strength above 280/300 MPa and a tensile strength above 590/600 MPa at improved formability [6]. For tensile strengths exceeding 780 MPa, these steels are sometimes referred to as “Ultra High-Strength Steels” (UHSS).

Metallurgists classify AHSS into three generations. The first and most used generation of AHSS includes dual-phase (DP), complex-phase (CP), transformation-induced plasticity (TRIP), and martensitic (MART) steels. The second generation consists of those with a corrosion-resistant austenitic matrix, such as twinning-induced plasticity (TWIP) and lighter-weight steels with induced plasticity (L-IP). The third, recently developed generation includes multi- and nanophase materials. The AHSS derive superior mechanical and forming properties from their final micro-constituents (ferrite, bainite, martensite, and retained austenite). For example, DP steels derive their strength from the martensite phase and their ductility from the ferrite phase [7], [8].

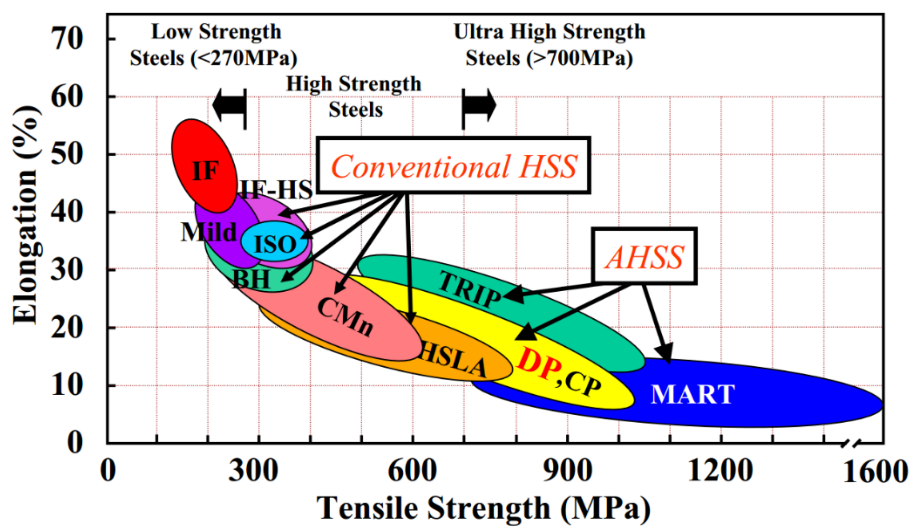

Figure 1.1. Total Elongation (%EL) vs. Ultimate Tensile Strength (UTS) “Banana Curve” of automotive steels [3]–[5].

To consistently distinguish steel grades, the international ultralight steel auto body (ULSAB) consortium adopted a classification system that defines both yield stress (YS) and ultimate tensile strength (UTS) for all steel grades [9]. In this nomenclature, steels are identified as “XX aaa/bbb,” where XX is the type of steel, aaa is the minimum yield strength in MPa, and bbb is the minimum ultimate tensile strength in MPa. The steel-type designator utilizes the classification shown in Table 1.1 [9].

For example, DP 590/980 refers to a dual-phase steel with a minimum yield strength of 590 MPa and a minimum ultimate tensile strength of 980 MPa. It's been commonly known as DP980, though.

Table 1.1. Steel type designator [9].

Designator	Classification	Designator	Classification
Mild	Mild Steel	**DP**	Dual Phase
IF	Interstitial Free	**CP**	Complex Phase
BH	Bake Hardenable	**TRIP**	Transformation Induced Plasticity
HSLA	High Strength Low Alloy	**MART**	Martensitic
ISO	Isotropic	**MnB**	Hardenable Manganese Boron

1.1.1. Dual Phase (DP) Steels

1.1.1.1. Microstructure of DP Steels

The microstructure of DP steel consists of a soft ferrite matrix and discrete hard martensitic islands, as shown in Figure 1.2. The ferrite is continuous for many grades up to DP780, but as the volume fraction of martensite increases (as might be found in DP980 or higher strengths), the ferrite may become discontinuous [3], [10]. The volume fraction of martensite determines the strength level of this steel. Specific heat-treating practices, including quenching and tempering, are employed to induce the martensite phase. The DP structure is produced by quenching low-carbon steels from the alpha + gamma phase region, resulting in a microstructure of martensite islands in a ferrite matrix [7]. The combination of hard and soft phases yields an excellent balance of strength and ductility. The soft ferrite in the final DP material is highly ductile. It absorbs strain around the martensitic islands, allowing for uniform elongation with a high work hardening rate and fatigue strength. Additionally, DP steels can absorb a significant amount of strain energy. Unlike conventional steels—including traditional BH steels—bake hardening in DP steels does not decrease with increasing pre-strain [3].

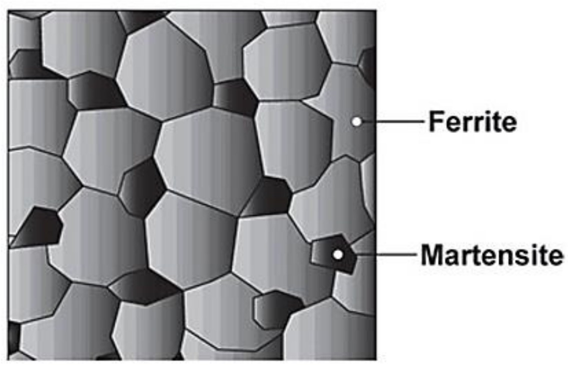

Figure 1.2. Schematic of a typical DP microstructure [3].

1.1.1.2. Application of DP Steels in Automobiles

DP steel is currently one of the most widely used AHSS materials. Automakers are increasingly using DP to improve the strength and reduce the weight of HSLA structural components. DP steels provide an excellent balance of strength and ductility due to their high strength, ductility, and hardenability, which gives them good capacity for strain redistribution [11]. For some applications, the initial yield strength of steels will be further increased by work hardening and the paint baking, so-called bake hardening (BH) process.

Steels with ferrite-martensite structures exhibit tensile strengths ranging from 490 to 1180 MPa, making them suitable for numerous car parts that require resistance to denting, fatigue, intrusion, impact, and other stresses – the high tensile strength results in excellent fatigue properties. The high strength and strain hardening capacity of these steels, combined with a strong bake hardening effect, gives them excellent potential for reducing the weight of structural and closure parts. Based on their high energy absorption capacity and fatigue strength, cold-rolled dual-phase steels are particularly well-suited for automotive structural and safety parts such as longitudinal beams, cross-members, and reinforcements [5].

DP is sometimes chosen for visible body parts and closures, such as doors, hoods, and front and rear rails. Other common applications include beams and cross-members, rocker, sill, and pillar reinforcements, cowl inner and outer panels, crush cans, shock towers, fasteners, and wheels [3]. An example of the application of DP steels in today's automobiles is illustrated in Figure 1.3 for a 2019 Chevrolet Silverado, in which the usage of dual-phase AHSS accounts for 12% of the total materials used for cabin, box, and closure components [12].

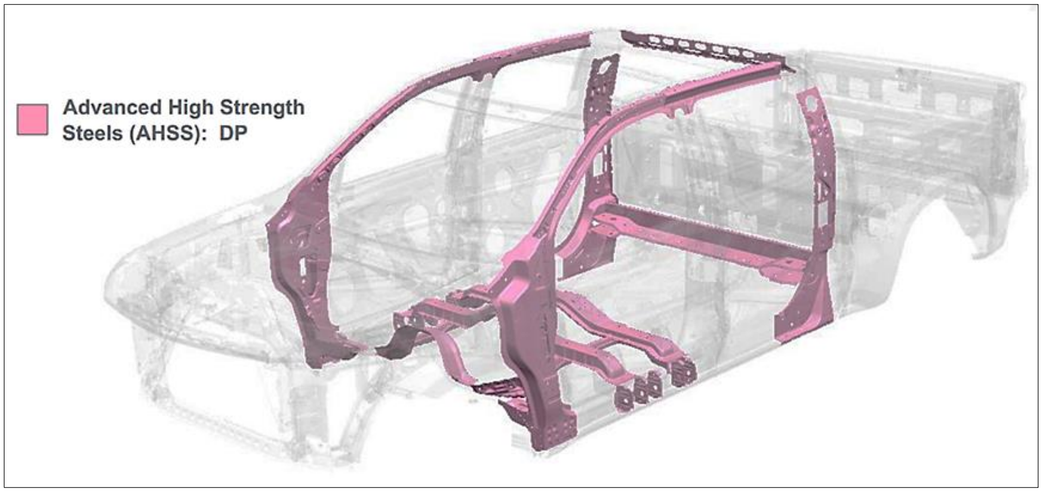

Figure 1.3. Application of dual-phase AHSS in the 2019 Chevrolet Silverado structure [12].

Table 1.2 summarizes the specifications, advantages, performances, and some typical applications of DP steels.

Table 1.2. Summary of specifications and applications of DP steels [3].

Microstructure features	Soft ferrite matrix, hard martensitic islands	**Typical additions**	C, Si, P strengthen but must be balanced for weldability, Mn, Cr, Mo, V, Ni increase hardenability
Formability	Excellent	**Weldability**	Good; at highest strengths requires careful selection of schedules

Advantage	**Performance**	**Application**
High bake hardening capability, high-strength	Resists fracture	Beams, cross-members and other structural components
High work-hardening rates and strain energy absorption	High UTS for given strength, delays necking	Crash energy absorption
Excellent elongation, weldability	Good manufacturability	Tailored blanks, hydroformed tubes

1.1.2. Significance of AHSS

High strength of AHSS - The significant advantage of AHSS over other lightweight materials is its wide range of strengths, extending from approximately 500 to 1700 MPa.

Weight reduction capability and high fuel economy - In most cases, high strength allows thicker-gauge components to be replaced by thinner-gauge ones while maintaining the same performance. The potential for weight reduction increases with an increase in the material's yield strength. Reducing vehicle weight lowers the inertial forces that the engine must overcome and reduces the power required to move the vehicle. An estimated 10% reduction in vehicle weight results in a 6-8% improvement in fuel economy [8].

Crash performance and energy absorption - The steel front-end structure absorbs a significant portion of the energy produced in a collision, as it deforms under impact. The structure is designed to collapse like an accordion to absorb the impacting load. A material’s ability to absorb an impact depends on its toughness, which is the product of strength and ductility. Also, a high strain hardening rate means the material becomes stronger on impact and absorbs more impact energy [8].

Material and cost savings - When AHSS is used, the mass reduction from downgauging results in less steel per car. This reduces the amount of steel that needs to be produced, thereby decreasing the demand for natural resources and the energy required to convert iron ore into steel [8]. Additionally, components made of AHSS are more durable and have lower maintenance costs.

1.1.3. Challenges in Stamping of AHSS

Despite the superior advantages of AHSS, there are some challenges associated with the implementation of AHSS, as follows:

1.1.3.1. Higher Press Load

The energy required to deform a steel sheet plastically is directly related to the area under its true stress–strain curve, which represents the material's plastic work per unit volume. Advanced High-Strength Steels (AHSS) often exhibit pronounced strain-hardening behavior, meaning their strength continues to increase with plastic deformation. This characteristic not only could contribute to higher formability but also provides valuable information for estimating the press capacity needed during stamping operations. Higher-than-normal binder pressure and press tonnage are also necessary with AHSS to maintain process control and prevent binder buckling. A double-action or hydraulic press cushion might be needed to generate the force necessary to control sheet metal flow into the die cavity. Air cushions or nitrogen cylinders may not provide enough force to set the draw beads or keep the binder sealed during AHSS stamping [7].

1.1.3.2. Inconsistency of Mechanical Properties

AHSS are performance-based steel grades. Although their chemical compositions may vary, several AHSS materials can meet the minimum strength requirements. Since different mills may use various production methods, even if their tensile properties are similar, other material parameters, such as elongation and weldability, might differ [13].

Figure 1.4 (a) shows the engineering stress-strain curves of the two DP980 sheets of steel. The UTS of these two materials is very similar, around 1000 MPa. Only based on the uniaxial tensile test results, one might expect that Material E has better formability than Material D in stamping trials. However, as shown in Figure 1.4 (b), the B-pillar made from Material D is formed successfully. In contrast, the part made from Material E has very long shear fractures along the bent corner regions [14].

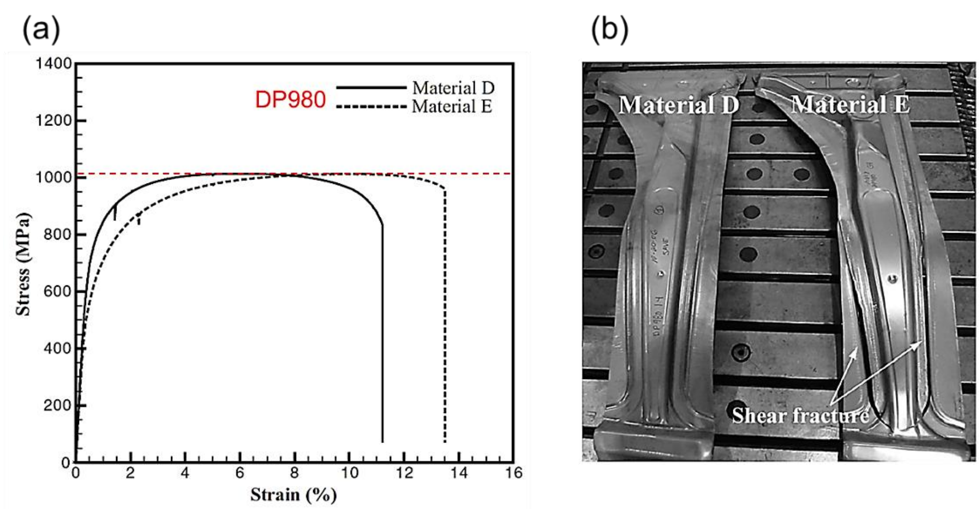

Figure 1.4. (a) Engineering stress-strain curves of the two DP980 steels, and (b) B-pillars stamped out of two DP980 steels [14].

1.1.3.3. Springback

Springback issues are much more significant for AHSS than for conventional HSLA. However, a more clear way to describe it is that the springback of AHSS varies from that of HSLA steels mainly due to the progressively higher initial yield strengths and the greater work hardening rate, which significantly increases the yield strength during forming. An example of this difference is shown in Figure 1.5. The two channels were made sequentially in a draw die with a pad on the post. The draw die was developed to attain part print dimensions with the HSLA 340/410 steel. The strain distributions between the two parts were very close, with almost identical line lengths. However, the stress distributions differed due to the differences in steel properties between DP and HSLA steels [4].

DP 350/600 **HSLA 350/450**

Figure 1.5. The springback difference between two channels made out of DP and HSLA steels [4].

1.1.3.4. Sheared Edge Cracking

After stamping, the excess material is trimmed off before operations such as flanging or hemming are performed. During these post-forming operations, tensile stresses develop in the trimmed edges, resulting in edge cracks [13], [15]. Some examples of sheared edge cracking of AHSS are shown in Figure 1.6.

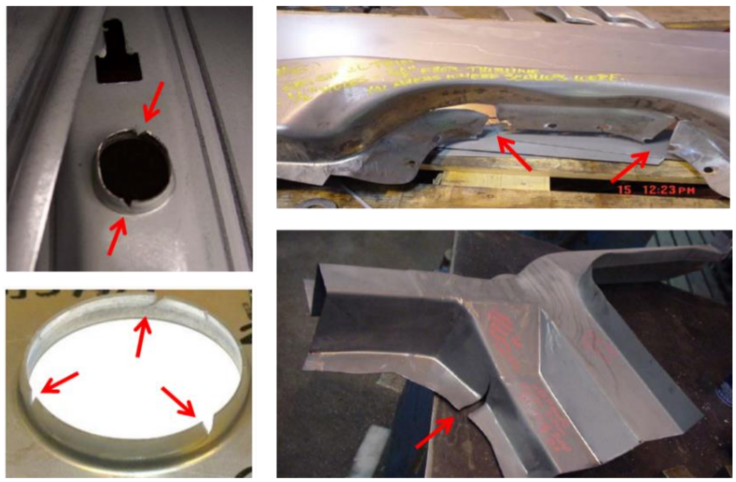

Figure 1.6. Sheared edge cracking of AHSS after (left) out-of-plane stretch flanging and (right) in-plane edge drawing [16], [17].

Several studies have demonstrated that FLD cannot predict edge cracks, and the reason is related to the quality of the sheared edge [4], [16], [18], [19]. The ability of an edge to stretch without failure can be measured by sheared edge stretchability tests, as detailed later in Section 1.3.1.

Smith [15] demonstrated the effect of burr formation on the sheared edge formability and introduced the stretchability graph, as shown in Figure 1.7. The graph indicated that burr formation requires cold working of the metal, which reduces the material's formability limit and leaves the edge with decreased formability.

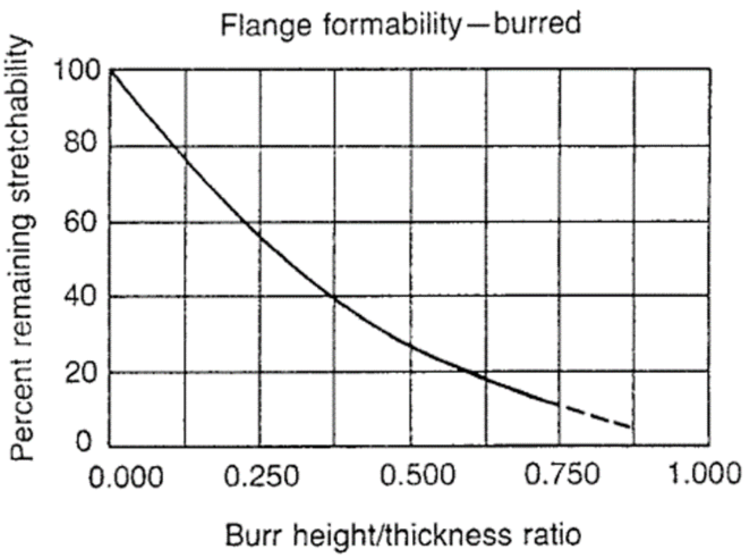

Figure 1.7. The effect of burr height on the sheared edge formability [15].

1.1.3.5. Tool Wear

Forming of AHSS involves higher contact pressures and temperatures at the tool-sheet interface compared to forming mild steel, due to the higher strength and higher strain-hardening behavior of AHSS. These conditions lead to galling, chipping, abrasive and adhesive wear in the tool, and significantly reduce tool life. Tool failure mechanisms for cutting AHSS are discussed in detail in Section 1.4.2.

1.2. Shearing Process

All sheet metal working processes can be divided into two main groups: plastic deformation and shearing.

The sheet metal shearing process involves cutting material by subjecting it to shear stress, usually between a punch and die or between the blades of a shear. Different blades or cutters may do the shearing in special machines driven by mechanical, hydraulic, or pneumatic power. Generally, the operations consist of holding the sheet metal blank rigidly while it is severed by the force of an upper sharp tool as it moves down past the stationary lower tool [20]. The punch and die may be of any shape, and the cutting contour may be either open or closed (Figure 1.8). If the entire cutting line lies within the sheet strip, not cutting the edges, it is a closed or otherwise open cut [21]. The plastic deformation and fracture theory applies to all operations in sheet metal cutting processes.

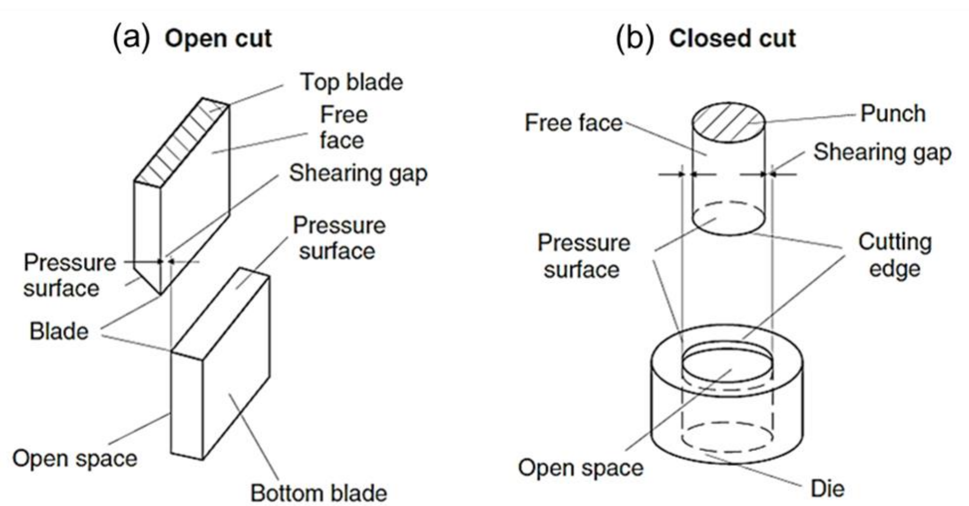

Figure 1.8. (a) Open and (b) closed cuts in shearing [21].

Trimming is classified as an open-cut shearing process. The tooling setup for a trimming process is illustrated schematically in Figure 1.9 (a). During the shearing process, three phases are commonly described as follows [2].

Phase I – Plastic deformation: As the upper blade begins to push into the work material, plastic deformation occurs on the sheet's surfaces, as shown in Figure 1.9 (b).

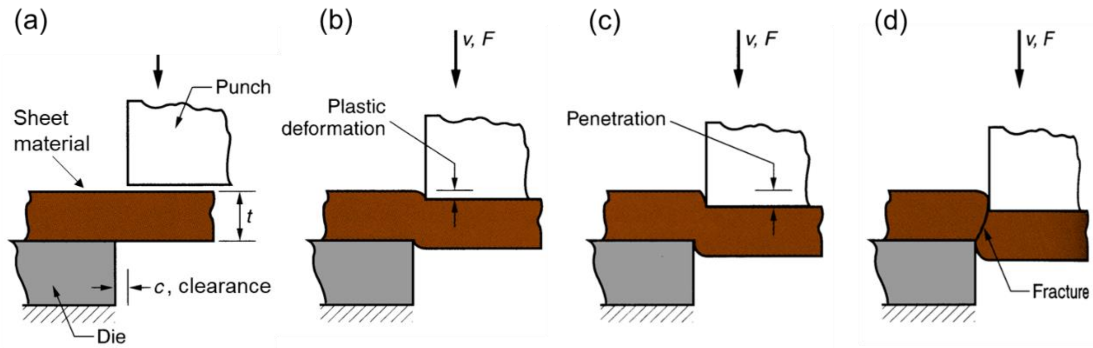

Figure 1.9. (a) General positioning of tools in a shearing process, (b) initial cutting occurring by plastic deformation, (c) shearing during punch penetration, and (d) fracture following shearing, adopted after [22].

Phase II – **Penetration:** As the blade moves downward, penetration occurs in which the blade compresses the work material and cuts into the metal (Figure 1.9 (c)).

Phase III – **Fracture:** As the blade continues to travel into the work material, fractures are initiated at the two cutting edges. If the clearance between the blades is correct, the two fracture lines meet, separating the work material into two parts (Figure 1.9 (d)). Once the shearing action causes a fracture of the sheet, the punch force, F, quickly drops to zero [22]. The thickness through which each shearing mechanism occurs depends on the punch-die clearance, cutting angle, cutting speed, and material thickness and properties.

1.2.1. Sheared Edge Profile

The characteristic sheared edge of sheet metals has four typical zones, including rollover, burnish, fracture, and burr, as illustrated in Figure 1.10. In some cases, these features are found on both the edge of the cut-off piece and the clamped piece, but in alternate orientations [3], [23]. Rollover represents a transition zone between severely deformed material and the non-deformed sheet. With a sharp cutting tool edge, the tool creates a shiny, vertical edge identified as the burnish zone. The rough fracture area is a steep transition from the smooth burnish zone. The burr is usually caused by excessive clearance, dullness of the cutting tools, or both. The term penetration refers to the sum of rollover and burnish heights. These features result from two consecutive stages in the shearing process, including cutting and fracture [24]. In general, many factors could affect the configuration of the sheared edge, such as the clearance between the upper and lower cutting blades (i.e., the cutting clearance), cutting angle, the degree of sharpness of the cutting blades, cutting speed, lubrication, sheet material parameters, strain rate, etc. [25]–[27].

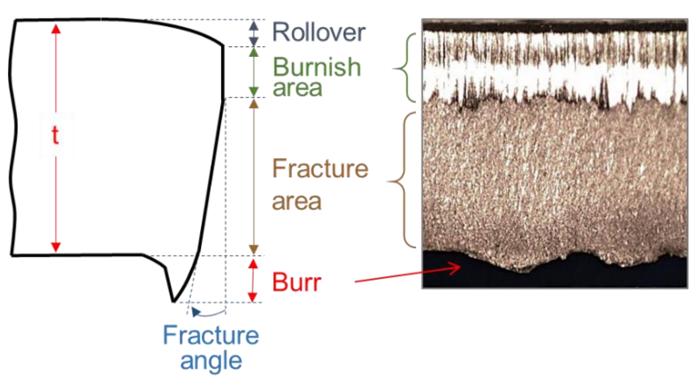

Figure 1.10. Typical features of a sheared edge.

1.2.2. The Cutting Clearance

Figure 1.11 (a) and (b) show a schematic of the trimming and punching processes. The clearance is the horizontal distance between the upper and the lower shearing edges in trimming, and the radial distances between the round punch and die in hole punching.

The clearance is a significant factor in determining the shape and the quality of the sheared edge. However, no absolute rules govern the clearance amount between the cutting tools [28].

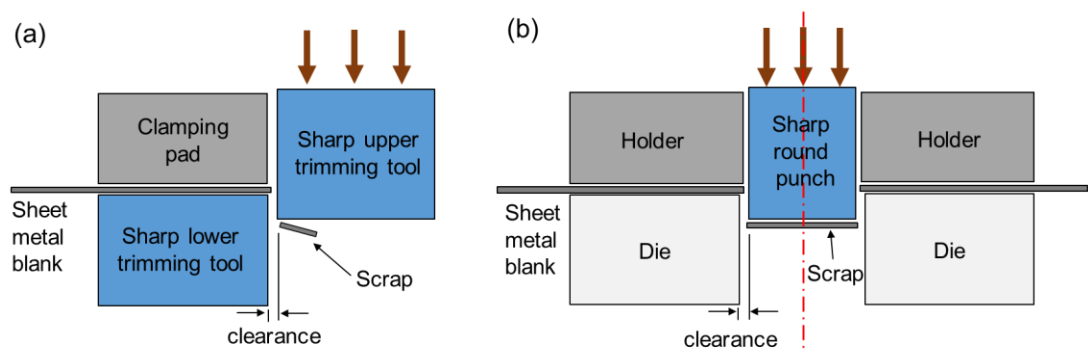

Figure 1.11. Schematic of (a) the Trimming process, (b) the punching process of a round hole.

Clearance is typically expressed as a percentage of the sheet metal thickness gap. Optimizing the amount of die clearance to suit the material being cut best may require some experimentation to minimize the condition of an uneven, fractured edge.

According to Spitler et al. [28], tight clearances, generally in the range of 3-5%, will result in a sheared surface with a high ratio of burnish to fracture, and a reduced burr on the sheared edge, at the expense of accelerated tool wear and higher cutting forces.

When there is insufficient clearance, the fracture, which starts from each side, may not meet evenly, as shown in Figure 1.12, and a double-burnish appearance may happen, especially in thick materials.

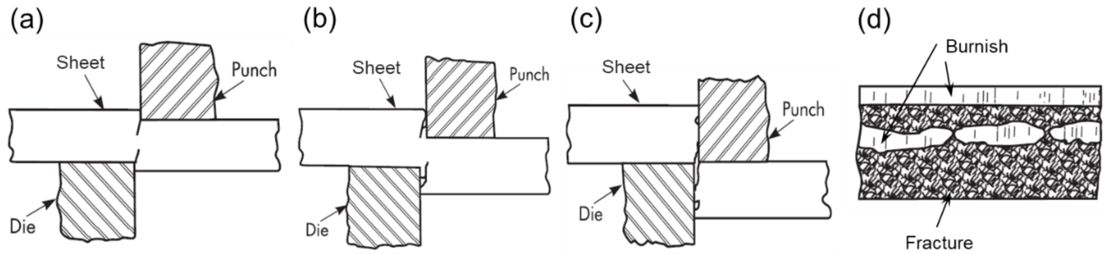

Figure 1.12. Shearing with insufficient clearance: (a) fracture initiation, (b) multiple fracture paths, (c) complete separation, and (d) sheared surface with a double-burnish area [28].

As larger clearances generally in the 10-20% range are used, the cutting force is lower, the life of the punch and die is longer between resharpening, and the sheared edge shows all features, including rollover, burnish, fracture, and burr. In the case of relatively large clearance, as demonstrated in Figure 1.13, the sheared edge may have a pronounced taper in the fracture area, and rollover depth and burr height also may be more prominent [28].

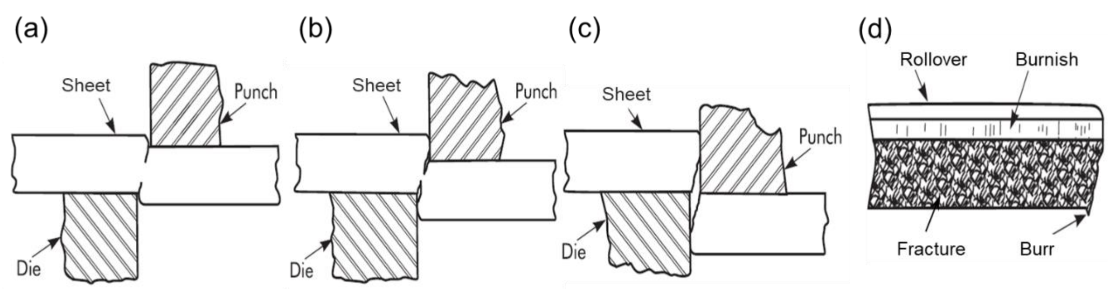

Figure 1.13. Shearing under a relatively large clearance: (a) fracture initiation, (b) crack growth, (c) complete separation, and (d) all sheared edge features on the edge [28].

If the clearance is very large, forces may be required that exceed regular forces. The burr height will be substantially higher in most materials. Large clearances also result in high lateral force on the punch and die, which can shorten tool life.

As the clearance increases, the zone of deformation (Figure 1.14 (a)) becomes larger, and the sheared edge becomes rougher. The sheet tends to be pulled into the clearance region, and the perimeter or edges of the sheared zone become rougher. Unless such edges are acceptable as produced, secondary operations may be required to make them smoother (which will increase the production cost). Figure 1.14 (b) shows that sheared edges can undergo severe cold working due to the high shear strains [29]. Work hardening of the edges will then reduce their ductility, thereby adversely affecting the formability of the sheet during subsequent operations, such as bending and stretching.

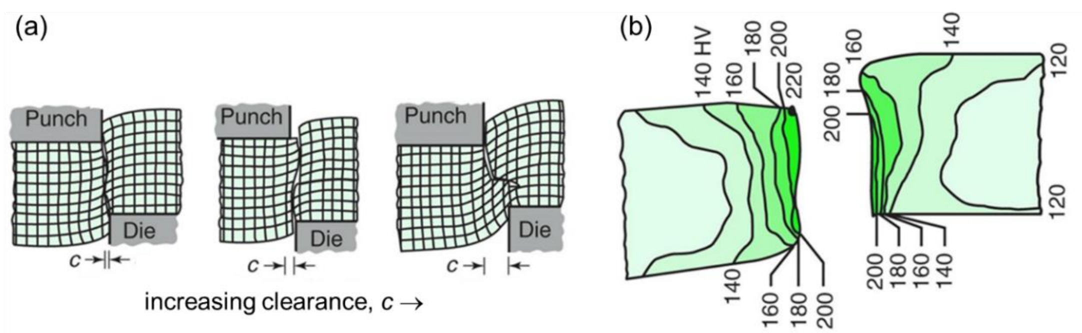

Figure 1.14. (a) Influence of clearance on the deformation zone in shearing, and (b) microhardness (HV) contours for a 6.4-mm AISI 1020 hot-rolled steel in the sheared zone at a cutting clearance of 11% [29].

1.2.3. Forces and Moments during the Shearing Process

The cutting force is crucial when shearing high-strength sheet materials, such as

AHSS and UHSS. The force significantly influences the tool's performance, as well as factors such as the noise level in the workshop. When making an interrupted cut, such as when trimming or punching, higher forces involved will usually result in noisier operations [30]. The forces necessary for the cutting process must be calculated for the tool design and to estimate the production press in advance. Parameters affecting the magnitude and profile of cutting forces include the shear strength of the material, sheet thickness, length, and geometry of the cutting line, cutting clearance, tool wear, tool surface quality, tool coating, and lubrication [21].

The magnitude of the maximum cutting force is directly proportional to the work material's strength and the area to be cut. The maximum cutting force for a straight-line shearing process can be estimated using Equation (1.1) [2], [21], [24].

$$F_{S\,max} = l \cdot t \cdot k_S \tag{1.1}$$

Where l, t, and k_S are the cutting line length, sheet material thickness, and material shear strength, respectively. The cutting force F_{Smax} required for the cutting process consists of various force components that act between the lower die, sheet material, and punch in the shear-affected zone (Figure 1.15).

According to Kopp et. al. [31], the main part of the cutting force F_{Smax} is the vertical force F_V, which acts on the cutting punch. It is assumed that the highest surface pressures on the punch end surface occur in a region near the cutting edge and fall off with increasing distance to the cutting edge. The distance between the forces F_V and F'_V causes a bending moment that bends or tilts the sheet metal blank. This moment must be compensated for by a counter-bending moment created by bending and horizontal normal stresses between the sheet and tool. Horizontal forces, F_H and F'_H, between the sheet material and the tool's lateral surfaces cause a sliding movement, depending on the coefficient of friction μ and the tool's rigidity. The forces acting on the cutting punch are in the opposite direction to those acting on the lower die due to the balance of forces.

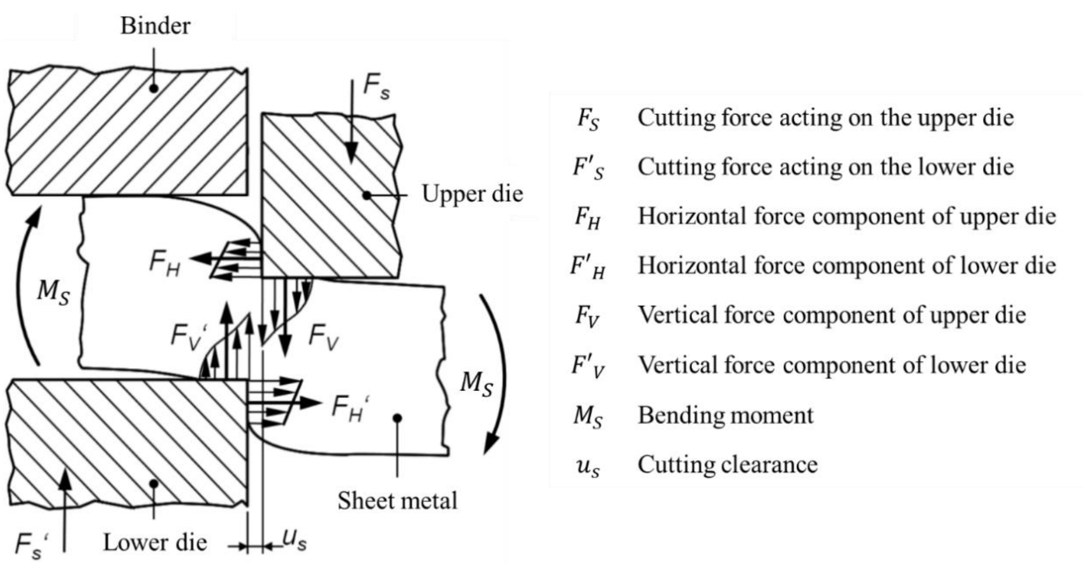

Figure 1.15. Forces and moments acting on the sheet metal [31].

Once the shearing action causes the fracture completion and complete separation of the sheet material, the punch force, F_S, quickly drops to zero. The thickness through which each shearing mechanism occurs depends on the cutting clearance. The optimum clearance will cause a fracture when the punch penetrates halfway through the sheet. Therefore, the shearing force increases until a fracture occurs and then rapidly drops to zero, as shown in Figure 1.16 (a). Improper clearance (Figure 1.16 (b)) will require greater energy for shearing (energy is the area below the force-distance plot) and will cause excessive burr formation on the sheared edge [22].

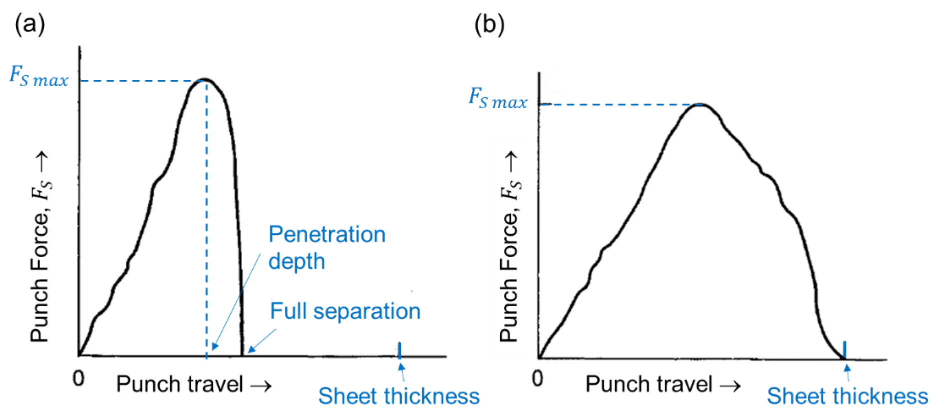

Figure 1.16. Punch force required for shearing with (a) optimum clearance and (b) improper clearance, adopted after [22].

1.2.4. Geometry and Position of Shearing Tools

If the surfaces of both punch and die are flat, as shown in Figure 1.11, the punch force increases rapidly during shearing because the entire thickness of the sheet material is sheared simultaneously. The demand for lower cutting force can be met through a suitable geometry of the cutting elements. Given an open cutting line (Figure 1.8 (a)), if the cutting edge of a shearing tool tilts at the shear rake angle, θ_3, as shown in Figure 1.17 (b), the cutting force is reduced because not the entire sheared edge is separated simultaneously [32]–[34]. However, a disadvantage is that the cutting path becomes larger, resulting in distortion of the sheet metal blank.

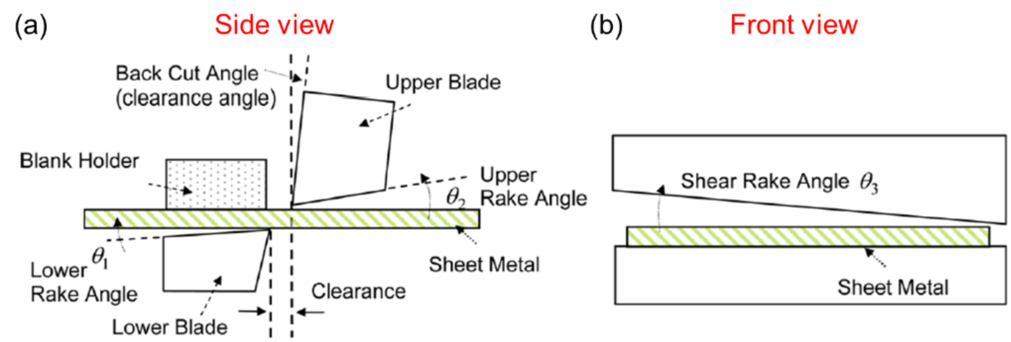

Figure 1.17. Schematic of shearing tools with adjustable shearing angles (a) side view, and (b) front view [32]–[34].

When piercing, the cutting force can be lowered if the end face of the punch is beveled (Figure 1.18). This way, while the piercing scrap is deformed, it prevents it from being torn when the punch is retracted. Such measures can significantly reduce the cutting force. Beveling is primarily suitable for shearing thick sheets, as it reduces the force at the beginning of the stroke. It also decreases the operation’s noise level because it is smoother. A beveling at twice the sheet thickness height can lower the maximum cutting force to 30% of the value yielded if the entire cutting line is engaged from the start of cutting (Figure 1.19). The cutting force reduction caused by the beveled cutting elements is associated with a greater cutting path [21].

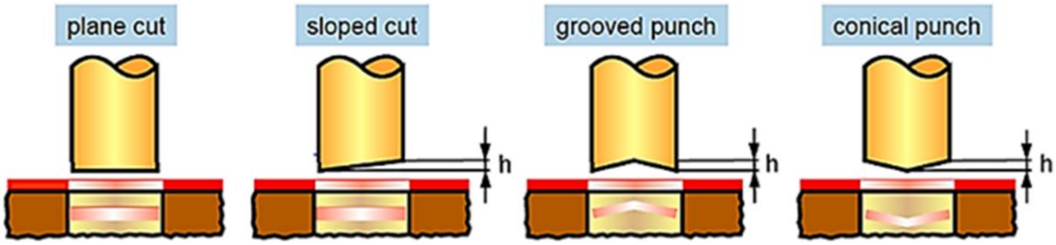

Figure 1.18. Modified punch and die shape for cutting force reduction [35].

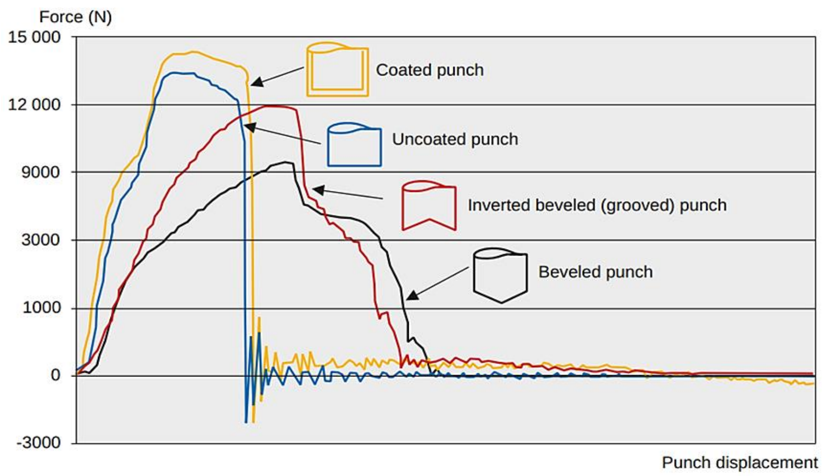

Figure 1.19. Blanking/punching force when punching a 5-mm hole in a 1-mm-thick Docol 1400M sheet metal at 10% cutting clearance [18].

1.3. Stretchability of Sheared Edge

During post-shearing operations, such as stretch-hemming and stretch-flanging, tensile stresses develop in the sheared edges, leading to edge cracking. A substantial question would be how much stretch can be imposed on the sheared material, which is already fractured and severely deformed in the burr zone. Thus, a simulative experiment is needed to quantify the sheared edge stretchability of various sheet materials, to provide data for numerical analysis, and to aid in material selection during the design stage [36].

1.3.1. Sheared Edge Stretchability Test Methods

The stretchability of a sheared edge for a known material can be assessed by four different test methods as follows:

1.3.1.1. Sheared Edge Tensile Test

The edge formability can be evaluated in the form of the total elongation of sheet metal under stretching conditions. The stretching condition can be provided by tensile testing of half-a-dog bone specimens or narrow metal strips, with one side representing the sheared edge [37]. A schematic representation of the sheared edge tensile test is shown in Figure 1.20.

In addition to the total elongation data, the local strains near the fracture area and adjacent to the sheared edge are measured using grid analysis and digital image correlation (DIC) methods to determine the stretchability of the edge. The quality of the sheared edge depends on several parameters, including shear tool geometry, punch/die clearance, sheet material type, and thickness. The tensile test can provide a comparative study on the influence of each parameter on the fracture strain, serving as a measure of stretchability under different conditions. There is no contact between the tools and the edge in this test, so any possible effect of friction is omitted. There would be necking strain included in the corresponding strain measurements; however, AHSS demonstrates limited diffuse necking before failure in the edge tension test, making this method the proper selection for the stretchability analysis of AHSS [33].

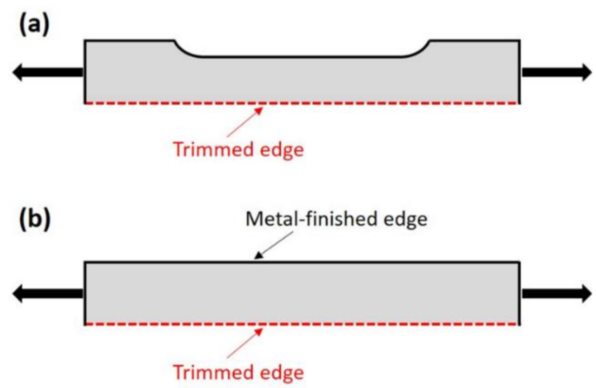

Figure 1.20. Tensile testing of trimmed specimens: (a) half-a-dog bone specimen and (b) sheet metal strip with one edge trimmed and the other edge polished.

1.3.1.2. Side-bending Test

The schematic representation of the side-bending test and a tested specimen are shown in Figure 1.21. In this test, the metal strip specimen is clamped to prevent buckling in the planar areas. The specimen with the trimmed edge on the outer side is bent about the rolling pin until the first crack is detected on the edge [38]. Two high-speed DSLR cameras, positioned to face the edge and planar areas, capture the edge fracture event. The fracture initiation and through-thickness fracture strains are measured by the pixelation method. The side-bending test is a unique method that produces a strain similar to that in the uniaxial direction on the edge but reduces the effect of necking, resulting in more accurate fracture strain measurements [39].

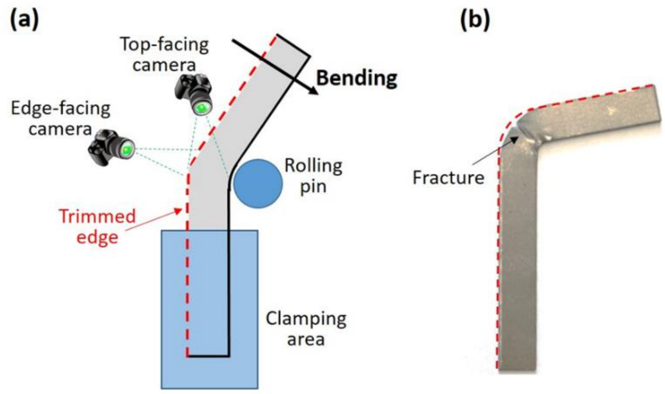

Figure 1.21. (a) Schematic of side-bending testing of a trimmed specimen and (b) bent and fractured specimen.

1.3.1.3. Hole Expansion Test

The hole expansion test was developed to evaluate the edge formability (i.e., edge stretchability or stretch flangeability) of sheet materials and has been widely used in the industry [40]. Figure 1.22 (a) shows the hole expansion test setup. A 10 mm diameter punched hole undergoes an axisymmetric hole expansion with a 60˚ conical punch until a crack is observed at the edge, extending through the material thickness. The hole expansion ratio (HER) is defined by Equation (1.2).

$$HER = \frac{D_h - D_0}{D_o} \times 100 \tag{1.2}$$

Where D_0 and D_h are the initial hole and inner diameter at the first crack initiation (Figure 1.22 (b)). For the tests conducted according to the ISO 16630 Standard [40], the burr side of the blank needs to be placed on the opposite side of the punch (burr-up position).

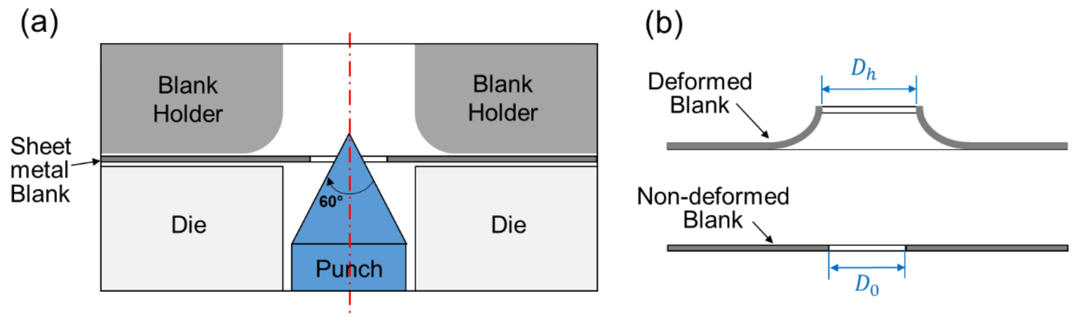

Figure 1.22. (a) Schematic of hole expansion test, (b) measurements for the hole expansion ratio.

The hole expansion test generally applies to closed-line cutting, such as punching and piercing, and does not reflect the actual cutting conditions in blanking or trimming dies. The main difference lies in the ability to bend sheet material during trimming, as opposed to minimal bending in hole punching. Friction also influences this method because the punch is in direct contact with the sheet material; additionally, the burr-up configuration produces different results than the burr-down configuration [41]. Lastly, maintaining a uniform punch/die clearance along the tool's perimeter is challenging due to tool misalignment or deflection during the punching operation.

1.3.1.4. Half-Specimen Dome Test

A half-specimen dome test is developed to evaluate the stretchability of the sheared edge in a 3-dimensional forming and flanging mode [33]. As demonstrated in Figure 1.23 (a), the as-sheared edge of the rectangular-shaped specimen is carefully aligned along the centerline of the die, which is usually used for the limiting dome height (LDH) test. A hemispherical punch strains the clamped specimen until the first crack appears on the edge of the specimen, as shown in Figure 1.23 (b). Strain or thinning at fracture can be assessed as the edge stretchability measure using grid analysis or digital image correlation methods. Accurate alignment of the specimen with the punch and die is a critical factor in this test. An appropriate lubricant between the punch and specimen is also necessary to reduce the frictional effects [33].

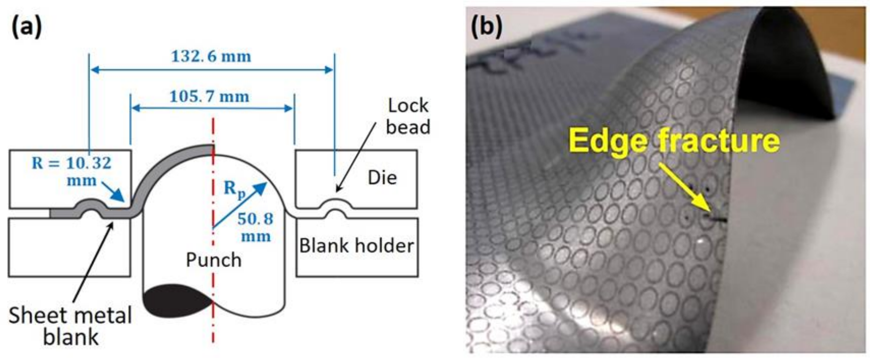

Figure 1.23. (a) Configuration of half-specimen dome test (b) bulged and fractured specimen [33].

1.3.2. Measuring Local Strains

1.3.2.1. Grid Measurement Method

Local strains are measured by marking the surface and comparing the condition after forming to that before forming. These markings can be created by painting or chemically etching grids. Etching supplies very robust markings, but the procedure takes more effort. Also, a deep etching may act as a stress concentrator, initiating early failure [42].

An original square grid on the surface is changed into a different shape, such as a rectangle, trapezoid, or larger square, during the forming operation, as shown in Figure 1.24 (a). Similarly, a circular grid is altered into an ellipse during the deformation, as demonstrated in Figure 1.24 (b).

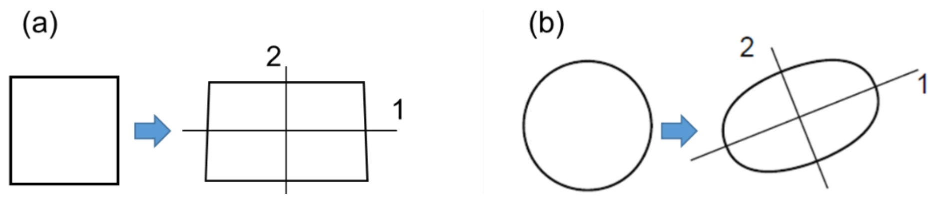

Figure 1.24. (a) A square grid changes to a trapezoid, and (b) A circle grid changes into an ellipse after deformation.

The lengths of the two axes immediately indicate the major and minor strains, while the orientation of the axes shows the principal direction of strain on the surface. Therefore, marking a set of circles on the surface seems appropriate, and this approach has long been widely accepted as a method for creating measurement grids. Since automatic measurement methods and equipment are available, various grids have been developed, including separate and intersecting circles, square grids, dots, and more (Figure 1.25). These regular grids have the advantage that they can be applied in the laboratory, are not limited by sheet size, and can be measured in the laboratory after having been pressed elsewhere. A limitation is that they rely on a perfect grid – any irregularities in the grid result in minor errors in the final results. Consequently, the resolution is limited, and small strains are difficult to measure.

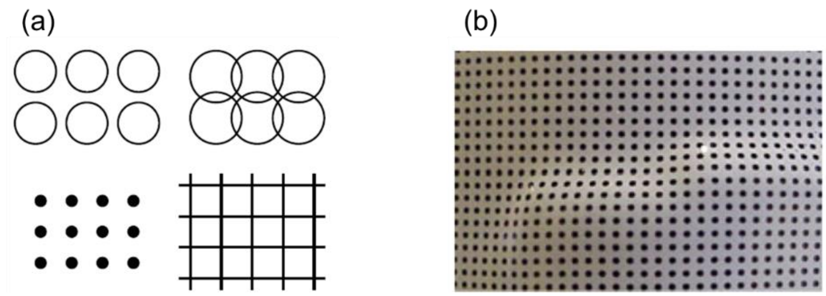

Figure 1.25. (a) Different types of grids, and (b) an example of an actual grid on a product surface [42].

1.3.2.2. Pixelation Method

An innovative approach uses very fine dots as a real-time index of local strain [43]. To do so, the sheet metal surface is painted with very fine black dots and a traceable coordinate system before deformation. The geometrical changes in the shape of dots due to deformation, which eventually lead to fracture, are tracked and measured (Figure 1.26). Observing the process using a camera to assess the strain at various time intervals throughout the deformation is necessary. This limitation restricts the applicability, but it allows for the measurement of tiny strains, and the progress during all intermediate stages can also be studied.

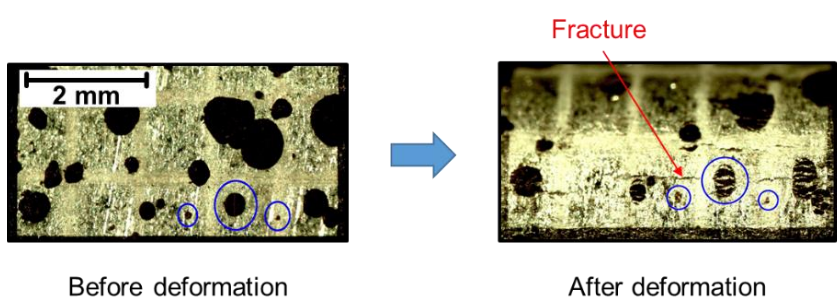

Figure 1.26. Pixelation method for the strain measurement.

1.4. Cutting Tools

1.4.1. Cutting Tool Steels

Tool steels are either unalloyed or alloyed and are used for applications with surface temperatures below 200 °C [44]. They can be produced by conventional melting processes followed by refining steps, or by powder metallurgy. The requirements for cold-work tool steels used in cutting tools focus on minimizing abrasive and adhesive wear while reducing the risk of breakouts at the cutting edges. Therefore, a balance must be maintained between wear resistance gained through high hardness and adequate toughness to prevent breakout. Figure 1.27 illustrates the typical trade-offs between high hardness and toughness in conventional cold-work steels [45].

Cold work tool steels for stamping applications typically contain 5-20% of Si, Mn, Cr, Mo, W, and V, and 0.6 - 3%C. The steels are hardened and tempered to a range of 56-66 HRC, providing an optimal combination of properties, including wear and indentation resistance, toughness/ductility, hardenability, temper resistance, surface hardening characteristics, weldability, machinability, and grindability [46]. The microstructure may vary from a plain martensitic microstructure to one that contains nearly 30% of hard and wear-resistant carbides/nitrides. Depending on the properties profile, the production route is either conventional ingot casting, with or without electro slag remelting (ESR), or powder metallurgy (PM). They are increasing the solidification rate, enabling the manufacture of alloys with more carbide-forming elements, increased homogeneity, and advanced properties. Table 1.3 presents potential tool steel grades for stamping applications [47].

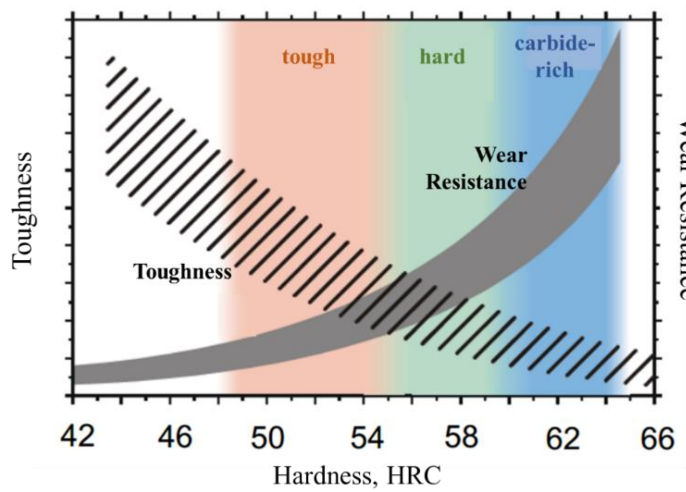

Figure 1.27. Properties of conventionally produced cold work tool steels, adopted after [45].

Table 1.3. Potential tool steel grades for stamping applications [30].

Steel grade	Process	%C	%Si	%Mn	%Cr	%Mo	%W	%V	%Co
AISI A2	Conventional	1,0	0,2	0,8	5,3	1,1	-	0,2	-
AISI D2		1,5	0,3	0,4	12	0,8	-	0,8	-
Carmo/Calmax		0,6	0,4	0,8	4,5	0,5	-	0,2	-
Sleipner		0,9	0,9	0,5	7,8	2,5	-	0,5	-
Caldie	Conv. +ESR	0,7	0,2	0,5	5,0	2,3	-	0,5	-
Vanadis 4	PM	1,5	1,0	0,4	8,0	1,5	-	4,0	-
Vanadis 4 Extra		1,4	0,4	0,4	4,7	3,5	-	3,7	-
Vanadis 6		2,1	1,0	0,4	6,8	1,5	-	5,4	-
Vanadis 60		2,3	0,6	0,3	4,2	7,0	6,5	6,5	10,5
Vancron 40		1,1C/ 1,9N	0,5	0,4	4,5	3,2	3,7	8,5	-

High-carbon, high-chromium cold-work tool steel D2 is one of the most widely used grades, often employed for dies in blanking, trimming, forming, and calibration.

With a long history spanning many decades, AISI D2 offers a strong combination of properties, including excellent wear resistance and toughness, while maintaining a favorable cost balance. The steel's 12% chromium and 1.5% carbon content produce a significant amount of chromium-rich carbides, mainly M_7C_3, which improve its wear resistance and hardness. However, the amount, distribution, and orientation of these carbides can influence the steel's toughness and fatigue resistance [48].

Reducing die maintenance costs and press downtime is crucial for cutting overall production expenses. Achieving optimal tooling economy, which involves minimizing the cost per part produced, depends on selecting the right tool steels for various stamping operations based on factors such as sheet material strength, design considerations, press tool manufacturing methods, expected production volume, and the cost and availability of die material.

1.4.2. Cutting Tool Failure

Since the dimensional and shape accuracy of the workpiece is determined by the quality of the tool used, the tool must be kept in decent shape. The loads applied during the cutting process cause the tools to wear and fail, harming the quality of the blanked parts and the required cutting work. If the extent of wear is excessive, the tool must be replaced or resharpened to maintain the required tolerance.

Table 1.4 summarizes the different types of tool failure that can occur during sheet metal stamping, including those for AHSS. It also illustrates the mechanism of each failure type, the potential cause, and the steps that could help to prevent these failures.

Table 1.4. Tool failure mechanisms, sources, and recommended solutions to prevent each one [24], [35], [49].

Tool Failure	**Mechanism**	**Source**	**Changes in Tool**	
			Increase	**Decrease**
 Wear	Abrasive-adhesive or mixed	Sliding contact	- Hardness - Ductility	- Friction coefficient
 Plastic Deformation	Exceeding of yield strength locally	Contact pressure	- Hardness - Yield stress	- Local die pressure
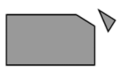 Chipping	Cracking at cutting edges and surfaces	Fatigue	- Toughness - Ductility	- Sharp corners
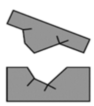 Cracking	Total cracking of the tool	Fatigue	- Fracture toughness	- Hardness - Sharp corners
 Galling	Material pick up; Same as adhesive wear	Sliding contact	- Surface hardness	- Friction coefficient

1.4.2.1. Tool Wear

Wear is damage to a solid surface involving loss or displacement of material. It is caused by sliding contact between the workpiece and the tool [18], [50], [51]. There are two main types of wear, including abrasive and adhesive wear. Abrasive wear is caused by hard particles forced against and moving along a solid surface. Adhesive wear occurs due to localized bonding between contacting solid surfaces, resulting in material transfer between the two surfaces or loss from either surface.

During the trimming of AHSS, the contact pressure between the workpiece and the tool surface increases, increasing tool wear [24], [52]–[55]. Wear is a dynamic and complex process that may be studied as a function of materials involved, local working load and stresses, shape and geometry of die and part, surface finish, surface hardness, lubrication, and other process parameters (see Figure 1.28). The complexity of having a vast array of process parameters, material properties, and their combined effect poses difficulties in accurately predicting wear loss in tools. For a robust trimming operation of AHSS, it is essential to understand the wear mechanism and develop a methodology for predicting the magnitude of wear on the die surface. This understanding, along with a wear model, will enable tooling engineers to implement tool wear reduction techniques on specific tooling surfaces with severe wear. The enabling technologies designed to reduce die wear include optimization of tooling geometries, improved heat and surface treatments, and tool steel alloy optimizations for advanced die materials [56].

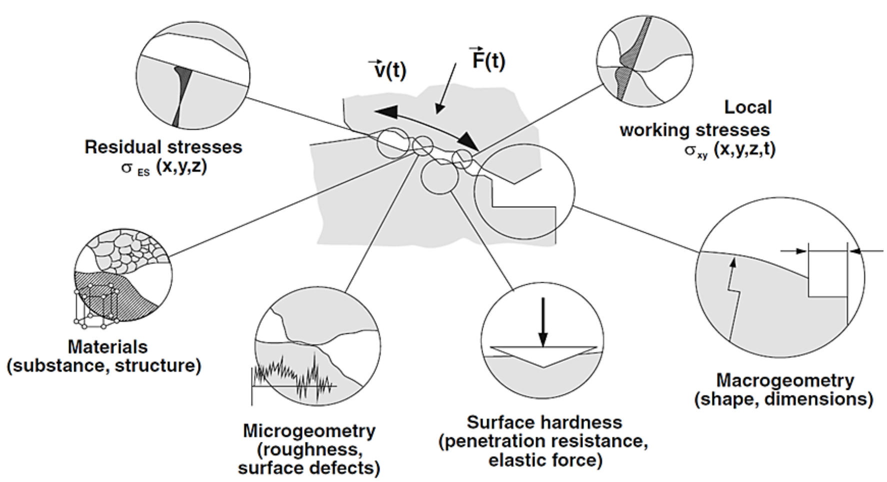

Figure 1.28. Parameters influencing die wear as a tribological system's behavior [21].

Wear mechanisms should be divided into four basic fundamental phenomena, as depicted in Figure 1.29 [35]:

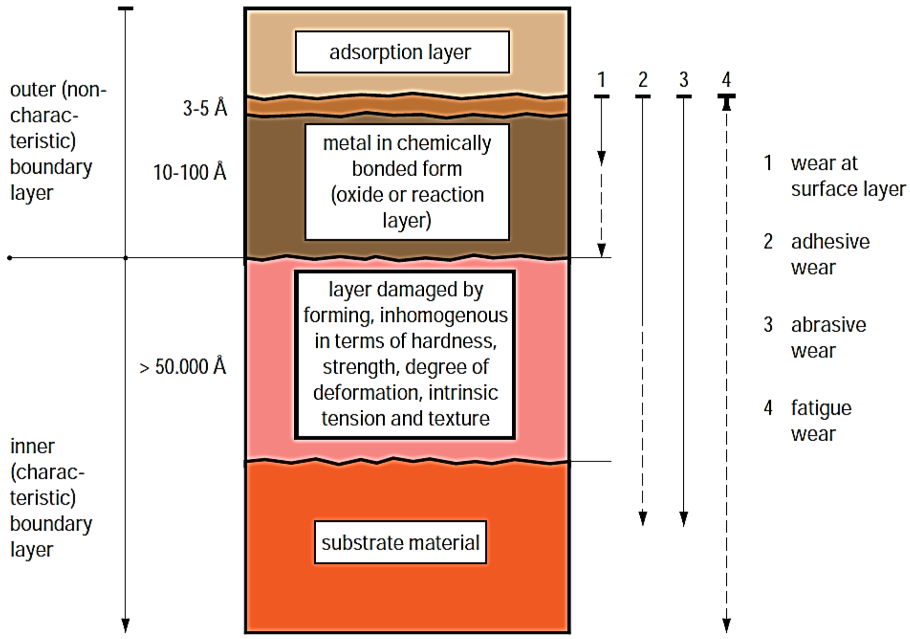

Figure 1.29. Depth effect of wear mechanisms on metallic surfaces [35].

Wear at surface layer – The application of load, frictional heating, lubricant, and the surrounding medium leads to the build-up of an interface layer at the die/material interface. The shear strength of the interface layers is less than that of the metals, so they are easily removed under frictional shear stresses.

Adhesion – Adhesion, also called cold welding, occurs due to nuclear adhesive forces between the frictional partners. The emergence of adhesive forces presupposes the following:

- Plastic deformation at the peaks of the roughness of contacting surfaces (sheet and die),

- Surface expansion brought about by the forming process, which removes the adhesion-presenting boundary layers and brings bright metal surfaces in contact with one another,
- Similar material structures of the frictional partners. The more significant the difference between the frictional partners, the lower the tendency to develop cold welding.

Abrasion – Abrasive wear includes all processes of parting or separation at the interface of frictional partners, where material is released in submicroscopic particles through a material removal process. The difference in the hardness between the two surfaces of frictional partners is a critical factor for assessing abrasive friction. Abrasive wear represents a generally inevitable long-term wear effect on the die.

Surface fatigue – Fatigue wear is the separation of micro- and macroscopic material particles. This separation is caused by fatigue cracking, progressive cracking, and residual fracture resulting from mechanical, thermal, or chemical stress-related conditions, as well as repeated impact loads. Generally, surface fatigue plays a minor role in forming dies. However, fatigue is common in cutting tools, such as those used for trimming, blanking, and piercing, where an increasing normal tensile stress is applied to the front surface in addition to a variable frictional shear stress that exists over the entire external surface area [35]. A more detailed explanation of fatigue failure and the methods for fatigue assessment is provided in section 1.4.2.2.

When shearing AHSS, if the imposed stresses exceed the fatigue strength of the tool material, microcracks develop on the face of the punch edges, as shown in Figure 1.30 (a). When these cracks propagate further during shearing, the punch edges produce micro-chipping and chipping (Figure 1.30 (b) and (c)). Further cracking leads to macro-fracture and gross fracture (Figure 1.30 (d)).

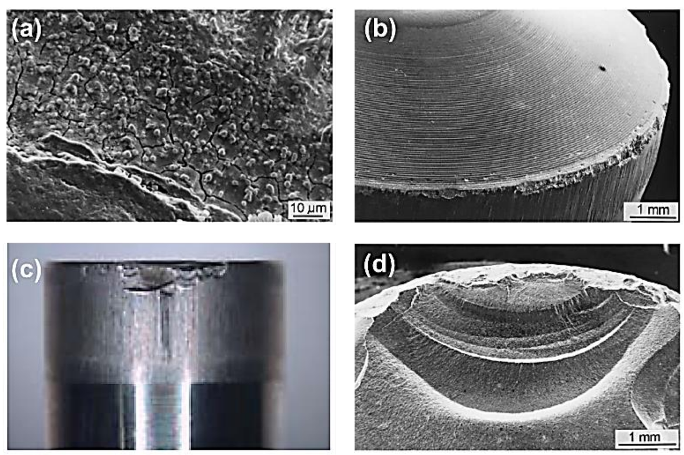

Figure 1.30. (a) Micro-cracks produced on the face of the worn cutting edge, (b) micro-chipping on the punch edge, (c) chipping wear on the punch cutting edge, and (d) gross fracture on the worn cutting edge [18], [57].

Depending on the location of wear on the tool, wear can be categorized as side wear and face wear, as shown in Figure 1.31.

Side wear – In this case, the vertical wall of the die or punch is worn during the shearing process. It is also called flank wear and results from the combination of adhesive, fatigue, and abrasive wear. Side wear increases the clearance between the punch and the die, as well as the workpiece's deformation (edge draw-in), during the shearing process.

Face wear – face wear results from abrasion and micro-chipping, making the punch and die edges round and dull. It reduces the sharpness of the punch during shearing and increases the deformation of the blank. As a result, the burr height on the sheared edge becomes more prominent, and more noise is produced in the press [57]–[59].

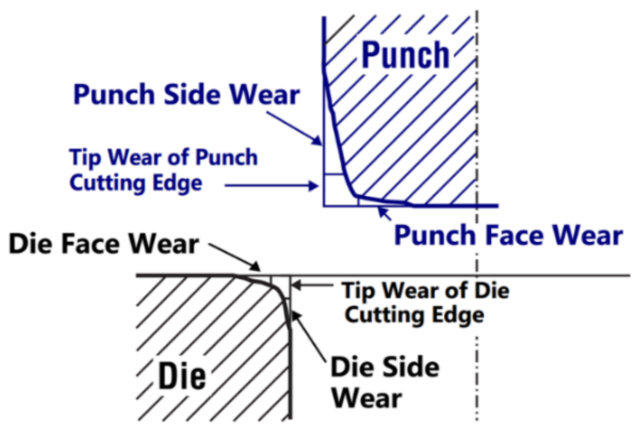

Figure 1.31. Schematic illustration of side and face wear in cutting tools [60].

1.4.2.2. Fatigue Failure

Fatigue failure is a slow and localized form of structural deterioration that occurs when a material is subjected to repeated or cyclic loading. Unlike static failure, which occurs when the applied load exceeds the material's yield strength, fatigue failure can happen at stress levels well below the yield strength due to the repetitive nature of the cycles. Fatigue failure is particularly dangerous because a component can appear to function normally until it suddenly breaks, often without any prior visible signs of deformation [61], [62].

The process of fatigue consists of three stages: crack initiation, crack propagation, and final fracture. In the initial phase, stress concentration at specific points causes localized plastic deformation, which leads to the formation of microcracks. Microcracks typically originate from microscopic defects, such as inclusions, surface scratches, or sharp corners. As cyclic loading progresses, these microcracks begin to grow, or propagate, until the remaining uncracked section of a part becomes too weak to withstand the applied loads. Eventually, this results in a sudden fracture of the weakened section. Various environmental factors, including temperature, corrosion, and surface condition, can significantly impact overall fatigue performance [63].

Trimming tools used in sheet metal forming are exposed to repeated and localized high stresses at the cutting edges. These tools often work under cyclic loading conditions with each press stroke. Over time, the repeated contact with sheet metal causes fatigue damage, especially when stress concentrators are present at the trimming edge, along with microstructural defects or surface roughness from wear or improper machining.

Fatigue failure in trimming tools appears as microcracking and chipping along the cutting edge. These tools are typically designed to withstand thousands to millions of cycles before they need regrinding or replacement, highlighting the importance of fatigue resistance for tool durability and maintenance intervals. Insufficient fatigue resistance can lead to early tool failures, compromising cut quality, increasing downtime, and potentially damaging stamping presses or dies. This problem is especially critical when working with ultra-high-strength steel (UHSS) materials, as they impose greater mechanical and thermal demands on the tools.

Therefore, understanding the fatigue mechanism and improving the fatigue resistance of trimming tool steels is crucial for ensuring cost-effective and continuous operation in the automotive and high-volume manufacturing industries. This process involves the careful selection of tool materials, controlling microstructural features (such as carbides and inclusions), and optimizing heat treatment processes to achieve a good balance between hardness, toughness, and fatigue strength. Additionally, fatigue analysis methods can be employed in tool design or simulation to more accurately predict the service life under actual operating conditions.

CHAPTER TWO
LITERATURE REVIEW

Before discussing the current research, it is essential to review earlier work by other researchers to gain a deeper understanding of the shearing of AHSS sheet materials. This chapter provides an overview of the relevant literature, organized into six main sections. The first section provides a brief description of the experimental work conducted to analyze the sheared edge profile and its key parameters. The next section reviews studies on the experimental investigation of sheared edge stretchability. The third section examines research on the numerical simulation of sheet metal shearing processes. The fourth section discusses previous efforts related to shearing tool wear. The fifth section summarizes studies on the impact of compressive mean and shear stress, as well as other researchers' work on estimating fatigue life in tooling materials. The final section highlights research gaps and presents the framework of the current thesis.

2.1. Experimental Works on Sheared Edge Characterization of AHSS

Numerous studies have been conducted on shearing processes and the characterization of the sheared edge. Weaver and Weinmann [29] investigated the stages of sheared edge formation and the effects of clearance, tool dullness, and other parameters. They demonstrated that the nature of the shearing process leads to extremely high levels of work hardening in the shear-affected zone.

Li [64] experimentally studied the influence of the clearance, the shear rake angle, and the sharpness of the tool on the trimmed surface, burnish depth, and burr height, and presented the micro-mechanisms of fracture and deformation in the trimming of aluminum alloys.

Johnson and Slater [65] investigated the effect of punch-die radial clearance on the sheared edge finish obtained under different experimental conditions. A series of punches with various diameters and punch-die radial clearances was used to study their impact on the sheared surface quality. It was concluded that, as the radial clearance increases, the level of plastic deformation decreases, but the burr height increases for mild steel and aluminum.

Jana and Ong [66] studied the effect of high-speed blanking on the sheared edge. Their investigations revealed that higher press speeds generally yield an improved surface finish compared to those obtained at lower speeds.

The part edge quality also depends on the material anisotropy of the trimmed sheet. Le et al. [23] conducted an experimental study on a widely used aluminum alloy, 6111-T4, illustrating the effects of cutting clearance on the trim line's longitudinal, transverse, and diagonal orientations relative to the rolling direction. Ilinich et al. [67] determined the influence of material anisotropy and trimming method on the total elongation of the trimmed edge of DP500 sheet steel, showing that the total elongation in DP500 steel exhibits significant sensitivity to specimen orientation with respect to the rolling direction and trimming method employed. In a work by Wu et al. [25], the effect of punch-die clearance, material strength, and sheet orientation in RD and TD on the relative edge zone heights was obtained.

Over the last two decades, a significant effort has been made to develop trimming methods for AHSS and UHSS, as well as to characterize them. According to Chintamani and Sriram [68], the limited quality of the sheared edge is one of the obstacles to the extensive application of AHSS in the automotive industry due to the formation of splits and burrs from the sheared surface. Among the parameters studied, burr height is significantly influenced by other edge parameters and is a practical parameter that can be monitored easily to track the performance of trim dies. For all materials studied, including BH210, DQSK, and DP500, increasing the die clearance results in an increase in burr height.

Wiedenmann et al. [69] conducted a blanking study on 1.4 mm-thick DP590 and examined the effect of clearances in the range of 5% -20% on part edge quality after blanking of 10 mm-diameter holes. They showed that rollover and fracture depths increase with clearance while the burnish zone decreases.

Mori et al. [70] developed a punching process using local resistance heating of a shearing zone to shear UHSS sheets. As a result, the punching load decreased, and the burnish surface of the sheared edge increased.

To eliminate slivers and burrs, Golovashchenko [71] modified the conventional shearing process by using a scrap support underneath the blank along with a dull upper trimming tool. In this so-called “robust” trimming process, the preferential mechanism of fracture development from the lower trim edge was promoted. Accordingly, a higher-quality sheared edge has been achieved, and burrs have been reduced across a wide range of clearances without compromising the total elongation or edge stretchability. Even though the elongation for DP500 and DP600 was lower in some cases than that observed from the conventional trimming process, it has not deteriorated.

Golovashchenko [71]–[73] also employed this robust trimming method for aluminum AA6111-T4 sheet metal blanks and showed that almost no burr was formed on the part edge, even with a relatively wide clearance of 107% of the sheet thickness. He also revealed that the presence of hairline slivers generated during conventional trimming, which can be attributed to fracture development from the upper trim die and the bending of the scrap, can be prevented.

2.2. Research on the Sheared Edge Stretchability of AHSS

As described in section 1.1.3.4, the traditional Forming Limit Diagram approach [74] does not apply to sheared edges due to the significant strain in the sheared affected zone, resulting in steep strain gradients. A substantial question would be how much stretch can be imposed on the material, which is already fractured or severely deformed in the burr zone. Thus, a simulative experiment is generally used to compare edge formability, to provide data for numerical analysis, and to help in the material selection. The most common method of characterizing the stretchability of the sheared edge is the hole expansion test described by ISO Standard [40], in which a 10 mm in diameter punched hole undergoes an axisymmetric hole expansion with a 60˚ conical punch.

In an early work by Adamczyk and Michal [75], the edge formability of a spectrum of high-strength cold-rolled steels was evaluated using the hole expansion test, and the effects of edge condition, microstructure, and tensile properties on hole expansion performance were determined. They showed that deformation modes generated in a hole expansion test were drawn near the hole edge and stretched farther from the edge.

In work conducted by Mori et al. [76], the stretch flangeability of different ultra-high-strength steel sheets, including DP590, DP780, and DP980, was examined using a hole expansion test. It was revealed that the blanked edge quality plays a crucial role in the hole flangeability of the sheet material. Then, a secondary smoothing operation was used to improve the formability of the punched hole. The uneven surface on the sheared edge was smoothed by applying shear and compressive deformation with the conical punch having an angle of 30°. Applying higher smoothing loads resulted in a higher limiting expansion ratio. They showed that the limiting expansion ratio for DP980 sheet material can be increased by 40% by smoothing the sheared edge.

In AHSS, the microstructure plays a vital role in determining the quality of the sheared edge due to the high volume fraction of hard phases. Hasegawa et al. [77] indicated that the difference in phase strengths is the main factor influencing the crack path and edge stretchability. It is shown that the "four-zone" edge feature (rollover, burnish, fracture, and burr) is not consistently observed on the sheared edges of the AHSS. These findings suggest that measuring the edge geometric feature is insufficient to determine the AHSS edge quality, and further investigations are necessary to characterize the AHSS sheared edge.

Wiedenmann et al. [69] performed experimental work on the hole expansion of DP590 sheet material punched at four different clearances (5 to 20%), using two different punch geometries (conical and spherical) and two different positions of burr-up and burr-down. They also conducted a numerical simulation. It was found that the outer edge always experiences more significant stretching for the conical punch. In the burr-up case, the fracture zone is located at the outer edge and is likely to fracture earlier than in the burr-down case. The spherical punch yields a more uniform distribution of damage value along the sheared edges. Thus, the influence of burr orientation on HER is less significant for this punch geometry.

Empirical formulas predicting the hole expansion ratio were developed by Comstock et al. [78] for different grades of steels, including ferritic, ferritic stainless, and austenitic stainless steels. Similarly, Stanton et al. [79] developed empirical formulas to calculate the hole expansion ratio for 6xxx and 5xxx aluminum alloys. Their methodology was based on the approach introduced by McEwan et al. [80] to incorporate the hole expansion test results into the Forming Limit Diagram (FLD), assuming that the deformation mode in hole expansion is uniaxial tension only. However, this approach did not account for punching process parameters, which critically affect the hole expansion ratio, and assumed only optimal cutting clearance conditions.

In work done by Konieczny and Henderson [41], the effect of blanking clearance and various edge morphology parameters on the formability of various AHSS was investigated. They demonstrated that positioning the burr in contact with the punch results in a higher hole expansion ratio. Results revealed that the hole expansion ratio (HER) was highest for all materials with reamed-edge holes and second highest for laser-cut holes, except for DP780 and DP980 steels, where the HER values for laser-cut holes were highest.

Levy and Van Tyne [74,75] conducted a detailed analysis of the strain path in the hole expansion test with both conical and flat punches. They indicated that more stretching occurs if the flat punch is employed. They called the hole expansion test with the conical punch hole extrusion, while the process with the flat punch was called hole expansion. They concluded that the shape of the expanding punch is a critical factor that may affect the experimental results.

Chiriac and Shi [81], [82] studied the effect of the prior deformation on the edge stretching limit and performance of DP780 and DP980 sheets experimentally. They concluded that if a conical punch is used for the hole expansion test, the strain distribution along the hole circumference is uniform, and the HER is the same across various pre-strained samples. However, when a flat punch is used for the hole expansion test, the strain distribution around the hole circumference is highly concentrated, and the HER decreases with increasing pre-strain levels.

Karelova et al. [83] reported the experimental evaluation of the edge stretchability of AHSS in standard punched, laser-cut, and drilled holes. They revealed imperfections and damage introduced during drilling and punching operations. They concluded that the edge stretchability could be substantially improved by applying a more effective shearing process. Results also showed a higher hole expansion ratio for the complex-phase CP800 than for the dual-phase DP800.

Hance et al. [84] assessed the edge stretching performance using the hole expansion test for a variety of automotive sheet steels, including ultra-low carbon IF steel, dual-phase DP980, an austenitic stainless steel (204), an annealed martensitic stainless steel (410 AN), and a ferritic stainless steel (429 MOD). They compared punching results to other hole fabrication methods such as machining, water jet, and laser cutting.

Shih et al. [32]–[34] developed an adjustable straight-edge shearing device enabling variable angles of shear rake angle, lower rake angle, and back cut angle, as shown in Figure 1.17. They identified the optimal shearing conditions, including rake angle combinations, shearing speeds, and cutting clearances, which resulted in the best sheared edge stretching performance for DP600 and DP980 sheet materials. Based on their work, an optimal combination of all three shear angles with 15% die clearance was recommended for the production trimming setup of AHSS. The half-specimen dome test was employed to measure the strain at failure adjacent to the sheared edge, serving as an index of edge stretchability. They also investigated the edge stretchability of the sheared DP980 specimens produced via different cutting methods. They demonstrated that high-energy techniques, including laser cutting, milling, and waterjet cutting, tend to produce total elongation that is significantly higher than that of mechanical shearing.

Based on previous research, advanced and high-energy cutting methods yield a better sheared edge in terms of both quality and performance [33], [41], [68], [83]. However, in large-volume sheet metal stamping, especially for automotive applications, part edges are typically trimmed, blanked, or punched.

Atkins et al. [85] conducted an analytical and experimental study on the hole expansion of aluminum sheets, indicating that multiple necks and cracks formed along the hole's perimeter. These results correlate with observations by Chiriac [86] and provide evidence that the hole expansion ratio is substantially more significant than the total elongation in the tensile test, where only one neck usually occurs.

According to Wang et al. [87], the hole expansion (HE) test was developed to evaluate the edge formability (i.e., edge stretchability or stretch-flangeability) of hot-rolled steels and has been widely used in industrial practice. However, although it is useful as a comparative measure, the HE test does not mimic the actual mechanical conditions during blanking or trimming. In trimming operations, the sheet experiences localized bending and complex shear–tensile stress interactions near the cutting edge, whereas the hole punching involved in the HE test involves minimal bending and a more uniform stress state. This key difference restricts the direct application of HE test results to real trimming situations.

Golovashchenko and Ilinich [37], [67], [73] presented edge formability in the form of total elongation of sheet metal under stretching conditions. They introduced tensile testing of half-dog-bone samples, with one side representing the sheared edge for DP500 and DP600. In addition to the edge-stretching limit, they studied the influence of trimming clearance on the fracture mode during tensile testing. They showed that small clearances promote ductile failure modes along trimmed edges, and larger clearances promote brittle (less desirable) failure modes.

The sheared edge tension test was also successfully applied by Wang et al. [87] to investigate the formability of the sheared edge of several AHSS sheet materials, including DP590, DP780, PM780, TRIP780, and DP980. The results showed that AHSS exhibited limited diffuse necking before failure in edge-tension testing. They demonstrated that sheared edge tension testing can serve as an alternative method for evaluating edge formability and can be easily implemented for product quality assurance.

Le et al. [23] performed the tensile testing of half-a-dog bone sheared samples to characterize the edge stretchability of aluminum alloy 6111-T4 sheet material. They measured the fracture strain near the sheared edge as the limit of edge stretching. They investigated the effects of trimming process parameters (clearance and angle), the orientation of the trimming line to the rolling direction, and pre-strain deformation. They demonstrated that for all sheet orientations, increasing the cutting clearance led to a substantial reduction in material stretchability along the sheared edge. The analysis of material pre-strain on sheared edge stretchability for various combinations of minor and major strains revealed that, for the widely accepted industry-standard gap of 10% of the material thickness, pre-strain has a significant effect on stretchability, which intensifies with increased thinning of the sheet during pre-straining. With an extended clearance of

40%, the effect of pre-strain was less pronounced, indicating that the sheared edge had a greater impact on these cutting conditions than pre-strain. Analysis of the effect of the cutting angle on stretchability revealed that higher elongations were observed at 10° and 20° cutting angles with a widely used 10% clearance, compared to orthogonal cutting with the same clearance.

Later, Wang and Golovashchenko [88], [89] investigated the mechanisms of fracture of the aluminum AA6111-T4 blank subjected to shearing and stretching along the sheared edge. They showed that early fracture during stretching of the sheared edge originates from the burr tip and propagates perpendicular to the sheared surface. Multiple small cracks originate from the tip of the burr, indicating that there is no single local defect that leads to reduced material elongation of the sheared surface. They also demonstrated that deburring or solution heat treatment of AA6111-T4 samples can increase edge stretchability.

More recently, Nasheralahkami et al. [90]–[92] conducted an experimental study on the effect of clearance and tool wear on the trimmed edge quality and stretchability of DP980, comparing it with other steel sheets of varying strength levels, including HSLA340 and BH210. Nasheralahkami et al. [36] also performed a finite element study on the trimming process of DP980. They experimentally investigated how fractures were initiated and propagated during the tension test of the sheared edge.

2.3. Finite Element Modeling of Shearing Process

One of the earliest research works was done by Popat et al. [93], who studied the optimal punch-die clearance and punch penetration using finite-element modeling. Results showed that the optimum punch-die clearance strongly depended on the local fracture strain of the material. The percentage of punch penetration when the crack initiated at the optimum punch-die clearance did not depend on parameters such as sheet thickness, work-hardening exponent, and ductility.

Singh et al. [94] studied the design of various punches using finite element simulation. They demonstrated that the clearance between the punch and die affects both the punching force and the quality of the finished product. Their analysis also indicated that punches with balanced convex and concave shear faces require a lower punching force and have a reduced noise level.

Goijaerts et al. [95], [96] conducted experimental and finite element analysis on the blanking of X30Cr13 stainless steel with varying punch-die clearance ranging from 1% to 15%. Simulations were performed using different ductile fracture models, including plastic work criteria, Cockroft and Latham, Rice and Tracy, and Oyane et al.'s damage criteria. Authors later adopted the Rice & Tracy criteria, changed a constant parameter within the damage formula, and showed that these adopted criteria correlate very well with the experimental results.

Sartkulvanich et al. [26] studied the blanking of AHSS DP590 with four punch-die clearances. Different fracture criteria were evaluated for FE modeling of blanking, and the results were compared with experimental data. The adapted Rice & Tracy criterion is shown to give the closest results when comparing the simulated part edge measurements to the experimental results. Additionally, the results of this criterion for hole expansion simulations with a spherical punch demonstrated that the predicted hole radii at fracture align well with experimental results.

Hu et al. [97] examined the traditional and advanced trimming of AA6111-T4 aluminum sheets using finite element simulations. The Rice-Tracy damage model was employed for the simulation, and damage parameters were estimated from experimental observations of the grain aspect ratio near the fracture surface of trimmed parts. Fine meshes at the shearing zone, adaptive meshing, and adaptive contact techniques accurately capture the contact interactions between the sharp corners of the trimming tools and the blank to be trimmed. FE Results showed that the crack initiation location was shifted to the sharp corner of the lower trimming, leading to the formation of burrs on the scrap side. Therefore, the part side showed significantly improved blanking quality in the robust trimming process.

In another work done by Hu et al. [98], a finite element model was developed to predict the trimmed edge tensile stretchability of AA6111-T4 sheets by incorporating the burr geometry, damage, and plastic strain from trimming simulations into subsequent tensile stretchability simulations. Simulation results were shown to successfully capture experimentally observed variations in edge crack initiation and failure modes for different trimming clearances.

2.4. Tool Wear for Shearing AHSS

Extensive research involving both numerical simulation and experiments has been conducted to study and predict tool wear in general sheet metal stamping. It is helpful to briefly review the development of wear models that describe the quantification of wear loss and the wear mechanisms during the sliding wear of AHSS sheet materials.

Archard [99], [100] pioneered studies to quantify wear loss and proposed that wear was proportional to the applied stress and hardness of the material. Lim and Ashby [101], [102] worked under the assumption that the wear coefficient was dependent on sliding speed and applied load, and constructed wear maps for steel based on wear rate calculations and wear mechanisms. Hoffman et al. [103] presented a combination of classical wear equations developed by Archard and a finite element simulation model to predict die wear. Progressive die wear, determined by measuring the volume loss, was observed with an increase in the die radius. Ersoy-Nurnberg et al. [55] studied the numerical simulation of tool wear during the sheet metal drawing process, applying the modified Archard model. A correlation was established between the wear coefficient and volume loss, with the dissipated energy attributed to the phase changes of the workpiece during the stamping processes.

Pereira et al. [104], [105] demonstrated a qualitative description of the evolution and distribution of contact pressure at the die radius for a typical channel-forming process. They analyzed the deformation conditions, contact phenomena, and underlying mechanics, identifying three distinct phases. The initial and intermediate stages resulted in severe and localized contact conditions, with contact pressure values significantly exceeding the yield strength of the blank material. The final phase corresponded to a larger contact area with steady and reduced contact pressure. The proposed contact pressure model was compared to existing results and discussed in relation to tool wear. Palanisamy et al. [106] focused on predicting tool wear using two models, including regression and artificial neural networks.

Ko and Kim [107] suggested an analytical scheme for predicting tool wear in the shearing process utilizing the finite element method and a wear model. They claimed that the need for regrinding of the shearing tool could be determined for an allowable burr height using the suggested scheme. They performed the pin-on-disk wear test, and the wear coefficient was determined using Archard's wear model. It was demonstrated that the wear coefficient increased as both velocity and load increased during the wear test.

Ko et al. [108] conducted a finite element analysis to investigate the wear mechanism and predict the wear profile of the Ti-N-coated tool in the piercing process as a function of the production volume.

Hambli [109] proposed a wear model for the sheet metal blanking process based on a finite element code. The tool wear was considered a function of normal pressure and material properties. The tools, however, were modeled as rigid bodies, and the wear variables were computed by considering the contacting elements.

In work by Husson et al. [110], the effect of tool wear was simulated by assuming different punch corner radii. It was shown that tool wear leads to the formation of burrs, and burr height increases as the cutting clearance increases. It was also observed that the effect of tool wear is more pronounced at higher blanking clearances.

Makich et al. [111] proposed a method using 3D topographical images to measure the volume of a burr in a blanking operation and to correlate it with punch wear. They demonstrated that the overall trend is an increase in burr volume as the number of press strokes increases, with a higher rate of growth up to 100,000 strokes. This pattern and the volume of generated burr are shown to depend on the sheet material.

Luo [57], [112] investigated the worn behaviors of the punch in piercing a hole in a larger thickness plate of AISI 52100 steel using two kinds of convex double shear angles. Hernandez et al. [60] presented a theoretical model of the effects of tool wear on the shearing mechanism and resulting form errors, as well as an experimental study of edge draw-in, depth of crack propagation, and burr height for AISI 304 stainless steel sheet.

Cora and Koç [113] investigated and compared the wear performances of different, uncoated die materials (AISI D2, Vanadis 4, Vancron 40, K340 ISODUR, Caldie, Carmo, 0050A) for punching AHSS DP600 sheet material. They investigated the impact of the die material, surface roughness, and plastic deformation on wear performance.

Krause and Bell [114] conducted a die wear study up to 200,000 strokes on PM 4%V, 60 HRC punch for punching a 1-mm-thick 1400 MPa grade steel sheet. They examined three different clearances – 6%, 10%, and 14% – and concluded that the lower clearance caused galling. In comparison, higher clearance caused high bending stresses in the cutting edge, increasing the risks of edge chipping. They found that 10% is the optimum clearance for the material studied, resulting in minimal tool wear.

Högman [30] studied the influence of punch-die clearance on the punch life for blanking a rectangular-shaped part out of 1mm-thick Docol DP800 sheet material. The tool material was Vanadis 4, with a hardness of 60 HRC. The results showed that the punch with a punch-die clearance of 10% at the rectangle corner lasted 40,000 strokes before chipping, while the punch with a punch-die clearance of 20% at the rectangle corner lasted 200,000 strokes without chipping.

Zeidi et al. [115] studied the failure mechanisms of AISI D2 punch heads, focusing on damage caused by wear and fatigue. Using microscopic evaluation and microhardness testing, they identified three main types of damage: swollen, mated, and cracked punches. They found that uneven chromium carbide distribution and microstructure inconsistencies were the main reasons for material failure and cracking. Three types of chromium carbides were present in the D2 punch material, including coarser Cr_7C_3 and smaller $Cr_{23}C_6$ and Cr_3C_2 carbides. Cracks began at the punch surface and gradually extended inward. Both abrasive wear and fatigue played significant roles in the development of larger cracks; additionally, layers accumulated on the punch surface over time.

Among the limited studies addressing trimming tool failure in dual-phase steels, the work of Choi et al. [116] stands out as the most relevant to DP980 material. Their combined experimental and finite element analyses revealed that burr height progressively increased with the number of strokes due to tool failure under high contact pressure. Furthermore, a negative die inclination angle (−10°) improved sheared edge quality by reducing trimming load and mitigating stress concentration at the die edge, whereas a positive inclination (+10°) promoted tool damage and burr formation. The FE results also indicated that at clearances between 12% and 21%, hydrostatic compressive stresses at the lower die corner suppressed crack initiation from the bottom side, leading instead to crack initiation from the upper tool edge under tensile stress.

Despite its importance, this study had several limitations. No results were presented for clearances larger than 21%. Moreover, the authors did not investigate the post-trimming performance or stretchability of the sheared edges – an essential factor for forming operations that follow trimming. While Choi et al. [116] reported no significant burr formation in their tests, our experiments on DP980 revealed distinct burr formation and subsequent burr break-up, leaving the trimmed edge nearly burr-free.

2.5. Fatigue Analysis of Tool Materials

In practical engineering situations, components rarely experience idealized loading cycles; instead, they are often subjected to fluctuating loads that introduce a mean stress component to the stress cycle. In our case, trimming tools mainly undergo compressive and shear stresses during the sheet metal cutting process, especially in the early stages before fracture initiation. Therefore, understanding how compressive mean stress and shear stress influence fatigue life is crucial for our broader analysis.

2.5.1. Mean Stress Effect

Mean stress occurs when the loading conditions are not fully reversed, resulting in a difference in magnitude between the maximum and minimum loads. Numerous mechanical designs experience cyclic loading, where the applied loads are asymmetrical. It has been understood for a long time that non-zero mean stress can affect the fatigue behavior of materials. It is widely accepted that compressive mean stress is advantageous, while tensile mean stress is harmful to fatigue performance [117].

The mean stress, σ_m, is the algebraic average of the maximum stress, σ_{max}, and the minimum stress, σ_{min}, in one cycle, as written in Equation (2.1):

$$\sigma_m = \frac{\sigma_{max} + \sigma_{min}}{2} \tag{2.1}$$

The stress amplitude, σ_a, is one-half the range of stress, as Equation (2.2)

$$\sigma_a = \frac{|\sigma_{max} - \sigma_{min}|}{2} \tag{2.2}$$

Also, the stress ratio, *R*, is given by Equation (2.3)

$$R = \frac{\sigma_{min}}{\sigma_{max}} \tag{2.3}$$

Several models have been proposed to explain how mean stress affects fatigue behavior. Some of the most commonly referenced stress-based mean stress equations in the literature include the Modified Goodman, Morrow, Soderberg, Smith-Watson-Topper, Gerber, and Walker equations.

The Modified Goodman equation is given by Equation (2.4) [118]:

$$\frac{\sigma_a}{\sigma_{ar}} + \frac{\sigma_m}{\sigma_u} = 1 \tag{2.4}$$

Where σ_{ar} and σ_u are the corrected alternating stress and the material's ultimate tensile strength, respectively. The Modified Goodman model suggests that as the ultimate strength of a material increases, σ_{ar} becomes less sensitive to mean stress.

Morrow [119] suggested modifying the Goodman relationship by employing the true fracture strength instead of tensile strength, as shown in Equation (2.5):

$$\frac{\sigma_a}{\sigma_{ar}} + \frac{\sigma_m}{\sigma_f} = 1 \tag{2.5}$$

Where σ_f is the true fracture strength in the monotonic tension test. For materials with low necking, the gap between tensile strength and true fracture stress is small; therefore, the Morrow and Modified Goodman equations produce similar results. In contrast, for materials that show high necking, the difference between tensile strength and true fracture stress can be considerable.

The Soderberg [120] line equation is similar to the Modified Goodman line equation, with yield strength, σ_y, substituting the ultimate tensile strength:

$$\frac{\sigma_a}{\sigma_{ar}} + \frac{\sigma_m}{\sigma_y} = 1 \tag{2.6}$$

The Soderberg method is viewed as more conservative than the Goodman and Morrow models.

Another popular equation is the Gerber parabola, as represented by Equation (2.7):

$$\frac{\sigma_a}{\sigma_{ar}} + \left(\frac{\sigma_m}{\sigma_u}\right)^2 = 1 \tag{2.7}$$

This method tends to overestimate fatigue lives and is only valid for tensile mean stresses, as it inaccurately predicts a harmful effect of compressive mean stresses [121].

Regarding tensile mean stresses, the Goodman and Soderberg models tend to give conservative predictions, while the Gerber model produces non-conservative results. Conversely, for compressive mean stresses, the Goodman and Soderberg models may offer non-conservative estimates, and the Gerber model might not be suitable [122].

Another fatigue model is the Smith, Watson, and Topper (SWT) [123]. Three equivalent forms of this model are shown in Equation (2.8).

$$
\begin{aligned}
\sigma_{ar} &= \sqrt{\sigma_{max}\sigma_a} && \text{(a)} \\
\sigma_{ar} &= \sigma_{max}\sqrt{\frac{1-R}{2}} && \text{(b)} \\
\sigma_{ar} &= \sigma_a\sqrt{\frac{2}{1-R}} && \text{(c)}
\end{aligned}
\tag{2.8}
$$

The SWT model has the advantage of not relying on any material constant and has been shown to give acceptable and consistent results for various materials [121].

Walker [124] used a similar approach, introducing a product of the maximum stress and the stress amplitude with an exponential parameter γ to predict the fatigue life under non-zero mean stress conditions. Three corresponding equivalent forms are given in Equation (2.9).

$$
\begin{aligned}
\sigma_{ar} &= \sigma_{max}^{1-\gamma}\,\sigma_a^{\gamma} && \text{(a)} \\
\sigma_{ar} &= \sigma_{max}\left(\frac{1-R}{2}\right)^{\gamma} && \text{(b)} \\
\sigma_{ar} &= \sigma_a\left(\frac{2}{1-R}\right)^{1-\gamma} && \text{(c)}
\end{aligned}
\tag{2.9}
$$

Note that $\sigma_{max} = \sigma_m + \sigma_a$, so that Equations (2.8) and (2.9) also provide the general function of $\sigma_{ar} = f(\sigma_a, \sigma_m)$.

Values of γ for Equation (2.9) can vary from 0 to 1, but metals are usually 0.4 to 0.8. If $\gamma = 0.5$, Equation (2.9) reduces to Equation (2.8). The term $(1 - \gamma)$ can be considered a measure of the material's sensitivity to mean stress; lower γ means more sensitivity to mean stress than higher values [125].

Figure 2.1 displays a schematic diagram comparing the described models. The Goodman relationship focuses on mathematical simplicity and applies to brittle materials. In contrast, the Soderberg equation is typically applied to ductile materials due to its conservative values. Additionally, the Gerber model is commonly used for ductile materials ($\sigma_f > \sigma_u$). The Morrow and Goodman theories are also comparable for brittle steels. Furthermore, multiple S-N curves, known as mean stress curves, can be constructed if test results are available [126].

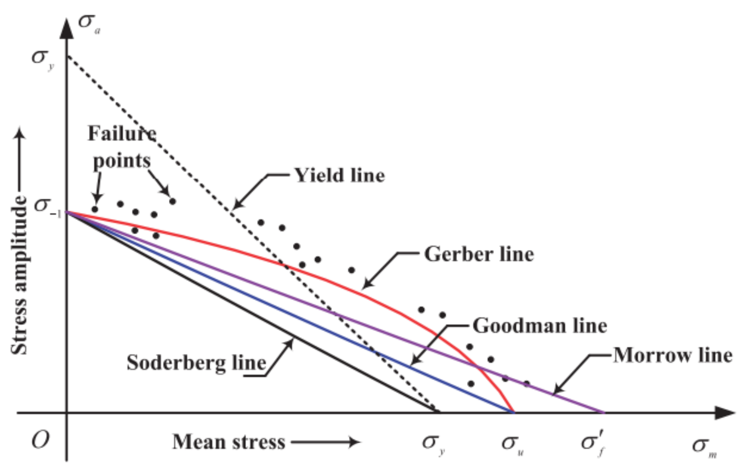

Figure 2.1. Schematic of Soderberg, Gerber, Goodman, and Morrow diagrams [127].

Most of these fatigue models were first introduced for tensile mean stresses;

however, some have been extended to the compressive mean stress domain and have been applied in the literature.

It is often reasonable to extrapolate the correction line for compressive mean stresses, as illustrated by the dashed lines in Figure 2.2 [128]. Many experiments have shown that it is safe [129]. According to Schijve [129], a crack opening requires a larger stress amplitude if a negative mean stress is present. In practice, it implies that fatigue is rarely a problem for a negative mean stress.

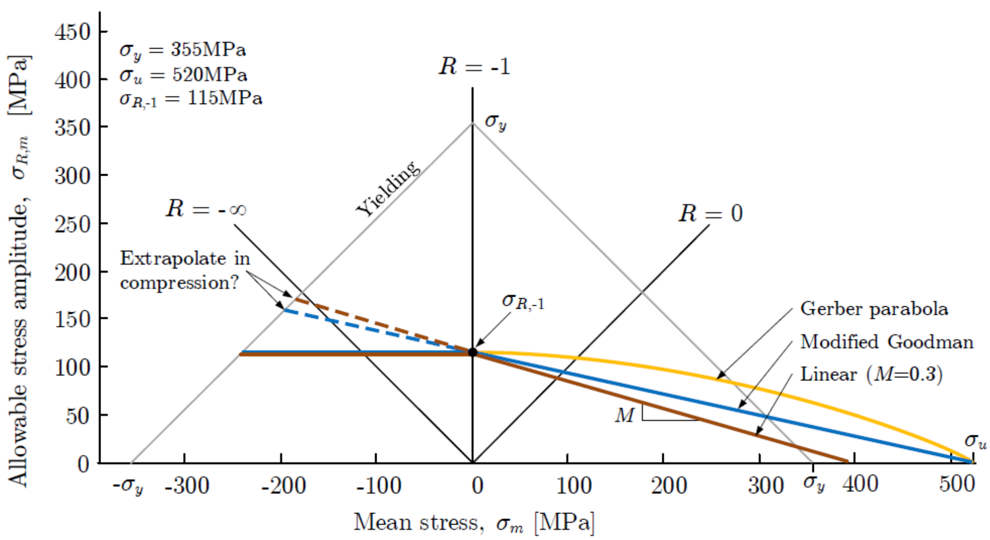

Figure 2.2. Haigh diagram showing different mean stress corrections in the compressive mean stress region [128].

Dowling [130] demonstrated a good correlation between Goodman's life correction and experimental data for both tensile and compressive mean stresses for AISI 4340 steel grade. Meyer [131] showed that the modified Goodman method provides good data correlation for smooth specimens under compressive mean stress. However, for notched specimens, it tends to be overly conservative regarding compressive mean stress data while being non-conservative for tensile mean stress data.

Dowling et al. [125] used Goodman's method and demonstrated that, for compressive mean stresses, the calculated stress amplitude is slightly lower and predicts a longer life than experimental results for selected steel grades. They also applied Morrow's model across the full range from compressive to tensile mean stress for two steel grades, showing that the theoretical predictions closely matched the experimental data.

Meyer [131] used the SWT equation to calculate the average compressive and tensile stresses for fatigue analysis of cast iron. He showed that SWT offers more accurate fatigue predictions for notched specimens than for smooth ones, across both tensile and compressive mean stress ranges. Dowling demonstrated that SWT is a reliable method for predicting fatigue in aluminum alloys. However, tested steel grades give non-conservative estimates of compressive mean stresses [130].

According to Meyer, the Gerber equation is highly non-conservative and cannot account for compressive mean stress [131]. The Gerber equation is limited to tensile mean stresses, as it incorrectly predicts a harmful effect of compressive mean stresses [121], [125].

da Silva et al. [132] investigated the impact of mean stress on the fatigue behavior of hard carburized steels with a Rockwell C hardness of 58-63 and ductile pre-stressing wire steel. They compared their experimental results with several commonly used mean stress correction models, including the Goodman/Morrow, SWT, and Walker relations. The findings demonstrated that these models provided a reasonable fit to the experimental data for tensile mean stresses in hard steels. However, the study found that the experimental data did not align well with these traditional models for compressive mean stress conditions, indicating a need for further research to develop more accurate predictive models for such scenarios. As a result, the authors proposed a new mean stress model that combines the Morrow rule for positive mean stresses and equates the maximum stress in a fatigue stress cycle to the fully reversed constant amplitude stress for negative mean stresses. This new model has proven effective in providing accurate predictions for hard carburized steels in both tensile and compressive mean stress regions.

2.5.2. Multiaxial Fatigue Models

Predicting fatigue behavior under complex, multiaxial, and often non-proportional loading conditions requires models that incorporate both shear-driven damage mechanisms and the influence of normal stress. One approach to extend continuum-based uniaxial damage formulations to multiaxial fatigue is through critical plane analysis. In this approach, a fatigue damage parameter is calculated on multiple planes with various orientations, and the plane showing the maximum damage parameter is identified as the critical plane where failure is most likely to occur. Under in-phase loading, the orientation of this plane remains constant, while for constant-amplitude loading, the damage accumulation rate on that plane remains constant [133].

Depending on the applied stress state, environmental factors, component geometry, and stress amplitude, fatigue damage may be dominated by crack initiation along planes of either maximum shear stress or maximum normal stress [134]. Models based on the critical plane analysis are therefore especially effective, as they explicitly consider the stress or strain histories acting on these physically meaningful planes—those on which fatigue cracks originate and subsequently propagate. The idea of combining normal and shear stresses on a specific plane within a material was first suggested by Stanfield [135] and later developed and extended by other researchers. In this section, some of the most popular multiaxial fatigue models are briefly discussed.

Findley [136] proposed a model considering the effect of the mean stress value, where the equivalent amplitude of shear stress on the critical plane (shear plane in this case). He suggested that the normal stress, σ_n, acting on a shear plane might have a different linear influence on the allowable shear stress amplitude, $\frac{\Delta\tau}{2}$. According to this criterion, fatigue failure starts from the plane on which the left term in Equation (2.10) is maximized.

$$(\frac{\Delta\tau}{2} + k\sigma_n)_{max} = f \qquad (2.10)$$

Parabolic forms were examined, but Findley concluded that a linear model was adequate to describe the experimental data. In this context, k is a material constant linked to the material's sensitivity to normal stresses, and f directly correlates with the material's fatigue strength.

Dang Van [137] proposed a multiaxial fatigue criterion based on mesoscopic (grain boundary) stress observation. The Dang Van criterion assumes that fatigue failure does not occur if all grains within the material reach a stable elastic state. In other words, after an initial transient period lasting a few load cycles, the material undergoes isotropic hardening, after which the stress–strain response remains within the elastic domain. The mesoscopic shear stress, τ_{μ}, combined with the hydrostatic stress, $\sigma_{H,max}$, controls the onset of critical deformation. The maximum mesoscopic shear stress value is determined based on principal stresses.

The stresses discussed above are combined using a linear function that defines effective shear stress, τ_{aeq}:

$$\tau_{aeq} = |\tau_{\mu}| + k\sigma_{H,max} \qquad (2.11)$$

The parameter k is determined by Equation (2.12) as a function of fatigue limits in alternating torsion, τ_{af}, and fully reversed bending, σ_{af}.

$$k = \frac{\tau_{af} - {\sigma_{af}}/{2}}{{\sigma_{af}}/{3}} \tag{2.12}$$

Another multiaxial model based on critical plane theory was presented by Fatemi and Socie [138] in 1988. The model is as follows:

$$\frac{\Delta\gamma}{2}\left(1 + k\frac{\sigma_{n,max}}{\sigma_y}\right) = \frac{\tau_f}{G}(2N)^{b_\gamma} + \gamma_f(2N)^{c_\gamma} \tag{2.13}$$

The shear strain range, $\Delta\gamma$, and the maximum normal stress in a plane, $\sigma_{n,max}$, are the two parameters considered in this model. Shear loading is required for crack initiation since fatigue cracks begin on high-shear planes. Normal stress is also significant. In Equation (2.13), τ_f is the coefficient of shear fatigue strength, b_γ is the exponent of shear fatigue strength, γ_f is the ductility coefficient of shear fatigue strength, c_γ is the exponent coefficient of shear fatigue strength, G is the shear modulus, and k is a normal stress sensitivity parameter.

Next, previous research on the fatigue life prediction of tool steels has been reviewed, as the durability and lifespan estimation of metalworking tool materials have been investigated in several studies.

Fu et al. [139] presented a simulation-based methodology for evaluating and enhancing the fatigue life of M2 tool steel in the gear forging operation. The authors employed stress-life and strain-life approaches to predict tool fatigue life, integrating finite element analysis (FEA) to simulate the stress and strain distributions during operation. They identified potential fatigue locations in the punch and die, where the maximum principal strains and maximum principal stresses are the greatest, respectively. Then, the punch and die fatigue life was estimated using the strain-life and stress-life diagrams for M2 tool steel.

Another study by Tong et al. [140] proposes a similar approach to the CAE-enabled die fatigue life analysis and improvement methodology. The Goodman mean stress correction is used to represent the relationship between die stress and its corresponding fatigue life, leading to the construction of a Haigh diagram for M2 tool steel. Once the potential areas of fatigue and the variations in loading cycles are identified, the stress panorama and the maximum and minimum principal stresses are identified. Finally, the die fatigue life has been estimated.

Long et al. [141] examined the fatigue performance of H13 steel tools used in Friction Stir Welding (FSW) of aluminum alloys. The researchers demonstrated that during steady-state FSW, the welding tool experiences multiaxial stresses, including tension, compression, torsion, and bending. These conditions can lead to multiaxial fatigue. For this analysis, the maximum principal stress of the tool was used as the fatigue analysis stress for the S-N curve, simplifying the calculation model. The stress analysis of the welding tool indicated that all average stresses at the pin root of the tool are tensile. As a result, the corresponding S-N curve for the tool is lower than the standard S-N curve. The standard S-N curve for H13 steel, constructed using the Basquin model, was applied to analyze and predict fatigue life.

In studies conducted by Skov-Hansen and his team [142], [143], low-cycle fatigue analysis and fatigue crack growth testing were performed on cold-forging tool materials. These tests were combined with finite element modeling to predict the tool's lifespan. The models first calculated the number of forming cycles required for crack initiation, subsequently leading to catastrophic failure during the crack growth phase. By applying the strain levels identified through finite element analysis, the researchers could estimate tool life by comparing these predictions with the actual lifespan measurements obtained from the material tests. They utilized the Modified Goodman model to account for the effects of mean stress on fatigue life.

Alimov et al. [144] employed the Manson-Coffin-Basquin equation, with Morrow's mean stress correction, implemented in QForm finite element software, to predict the fatigue life of hot-forging dies made from AM-processed 17-4PH steel. Due to the absence of any considerable plastic strains up to the last few cycles before failure, the strain term in the fatigue equation was neglected. They simulated the distribution of the first principal stress surface during the forging process for all die elements and then calculated the corresponding fatigue life for each element.

Ab-Kadir et al. [145] developed an integrated approach combining Finite Element Analysis (FEA) and the stress-life method to estimate the fatigue life of cold forging punches used in fastener production. The study examined stress distribution, elastic deformation, and forging load to identify potential areas prone to fatigue. Using DEFORM F3 software, four punch designs with varying corner radii were analyzed. The stress-life approach was employed to predict fatigue life while incorporating modification factors to enhance punch performance. Simulation results confirmed that increasing the corner radius of the punch reduced stress concentration, elastic deformation, and forging load. The largest corner radius design demonstrated the lowest stress, minimal elastic deformation, and the longest fatigue life. These results highlight the need to optimize punch geometry to improve durability and efficiency, offering a method to refine die designs.

Salunkhe et al. [146] presented an Artificial Neural Network (ANN) model to predict the life of compound dies used in sheet metal forming. The model considered key die components (die block, punches, and stripper) and factors like punch force, stripping force, and material properties. Finite Element Analysis (FEA) was employed to determine stress values, and fatigue life was estimated using the S-N curve and Goodman's equation. However, the proposed model includes several simplifications – such as assuming uniform loading conditions, ignoring local stress concentrations, and limiting consideration of microstructural effects – which restrict its applicability to specific die geometries and operating conditions, thereby reducing its overall validity for complex industrial situations.

To the author's knowledge, there are few scientific publications on the fatigue analysis and life estimation of trimming dies used for AHSS. However, the work done by Picas [147] is the most relevant in this area. This work provided a detailed analysis of the microstructural, mechanical, and tribological properties of various cold-work tool steels, including 1.2379 (D2 equivalent), K360, UNIVERSAL, and HWS, used in UHSS and PHS trimming and punching applications. Picas examined crack nucleation and growth under both monotonic and cyclic loads, finding that crack initiation typically originates from carbide cleavage or inclusion particles once the surrounding matrix yields. The work also showed that traditional Linear Elastic Fracture Mechanics (LEFM) models, such as those based on Paris' law, have limitations in predicting tool life because they assume pre-existing cracks and ignore nucleation and surface changes caused by wear and plastic deformation.

Building on these findings, Picas reviewed several fatigue life prediction models and categorized them by their approach. Fracture-mechanics-based models linked fatigue limits to carbide or inclusion size distributions using probabilistic methods. Meanwhile, other studies introduced finite element (FE)–based algorithms to simulate wear and fatigue by incorporating fracture parameters. Despite these advances, none could accurately describe fatigue failure in UHSS shearing tools, largely because of the complex interactions among microstructural anisotropy, cyclic contact stresses, and surface wear. To address these limitations, Picas proposed a new micro-mechanical damage model that links the degradation of the elastic modulus (*E*)

to the applied stress and the number of loading cycles. This approach was claimed to enable tool-life prediction based on the progressive softening of the metallic matrix, rather than relying on predefined crack geometry or propagation criteria. However, she did not further develop or validate this concept within her work, leaving it as a theoretical framework and a suggestion for future research.

2.6. Summary and Research Needs

To summarize the key findings from the reviewed literature, two tables were prepared: one listing studies conducted on materials other than DP980, and another dedicated exclusively to research on DP980 sheet steel. Table 2.1 summarizes the works on other materials, while Table 2.2 focuses on DP980.

Table 2.1. List of studies on the shearing of other materials.

Author(s)	**Materials**	**Topic**	**Method**	**Key findings/contributions**
Weaver & Weinmann [29]; Johnson & Slater [65]; Jana & Ong [66]	Mild steel, Al	Sheared edge features Variables: clearance, tool sharpness, speed	Exp	↑Clearance → ↓plastic deformation but ↑burr; high-speed blanking improves edge finish.
Li [64]	Al 6xxx	Trimming parameters Variables: clearance, angle, sharpness	Exp	Links clearance/rake to burnish depth & burr; micro-mechanisms of trim fracture.

Table 2.1. – Continued

Author(s)	Materials	Topic	Method	Key findings/contributions
Le et al. [23]	Al 6111-T4	Trimming parameters: Sheared edge tension – variables: clearance, cut angle, RD/TD orientation, pre-strain	Exp	↑Clearance → ↓edge stretchability; 10–20° cut angles at 10% clearance improved elongation; pre-strain effects depend on clearance
Ilinich et al. [67]; Wu et al. [25]	DP500; DP steels	Sheared edge features – variables: material strength, clearance, RD/TD orientation	Exp	Elongation sensitive to orientation & method; zone heights tied to clearance / strength / orientation
Chintamani & Sriram [68]	BH210, DQSK, DP500	Burr as a QC metric vs clearance	Exp	Burr height tracks die performance; ↑Clearance → ↑burr
Wiedenmann et al. [69]	DP590	HER & edge geometry – variables: clearance, punch shape, burr up/down	Exp + FE	↑Clearance → ↑rollover/fracture, ↓burnish; spherical punch reduces burr-orientation effect on HER
Golovashchenko [71-73]	Al 6111-T4 DP500/ DP600	"Robust" trimming (scrap support + dull upper)	Exp	Significant burr reduction; maintains edge stretchability; prevents hairline slivers
Adamczyk & Michal [75]; Comstock et al.[78]; Stanton et al. [79]; McEwan et al. [80]; Karelova et al. [83]; Hance et al. [84]; Atkins et al. [85]; Chiriac [86]	Steels & Al	Hole expansion test Edge prep effect; empirical HER models	Exp	HER is highly edge-condition dependent; empirical HER formulas (steels, Al); HER test stress state differs from trimming

Table 2.1. – Continued

Author(s)	**Materials**	**Topic**	**Method**	**Key findings/contributions**
Golovashchenko [37-39]; Wang et al. [87]	Several AHSS	Sheared edge tension alternative to HER; localized strain	Exp	Small clearances favor ductile edge failure; simple QA methods for sheared edges
Popat et al. [93]; Singh et al. [94]; Sartkulvanich et al. [26]; Goijaerts et al. [95, 96]; Hu et al. [97, 98]	Various metals	Finite Element Modeling (FEM) of blanking/ trimming; Influence of clearance, mesh size, fracture criteria	FE	Rice–Tracy and related criteria frequently best fit; robust trimming shifts crack/burr to scrap; integrated trim→tension sims predict edge stretchability

Table 2.2. List of studies on the shearing of DP980 steel.

<table>
<tr><th>Author(s)</th><th>Topic</th><th>Method</th><th>Variables/ metrics</th><th>Key findings</th><th>What is Missing?</th></tr>
<tr><td>Mori et al. [76]</td><td>Hole expansion/ edge smoothing</td><td>Exp</td><td>Conical punch; post-punch smoothing loads</td><td>Smoothing raised DP980 HER by ~40%</td><td rowspan="3">• Experimental punching and HER only
• Punching is not directly reflective of trimming
• No modeling work</td></tr>
<tr><td>Chiriac et al. [81, 82]</td><td>Edge stretchability with pre-strain (flat vs conical punch)</td><td>Exp</td><td>Pre-strain; punch shape</td><td>Conical → uniform edge strain, HER insensitive to pre-strain; Flat → localized strain, HER decreases with pre-strain</td></tr>
<tr><td>Hance et al. [84]</td><td>Edge preparation methods vs HER</td><td>Exp</td><td>Punching vs machining, waterjet, laser</td><td>Non-mechanical cutting improves HER vs punching for DP980</td></tr>
</table>

Table 2.2. – Continued

Author(s)	Topic	Method	Variables/ metrics	Key findings	What is Missing?
Shih et al. [32, 34]	Adjustable straight-edge shearing for AHSS, Stretchability by half-specimen dome test	Exp	Shear rake, lower rake, and back-cut angles, clearance	Optimal angle combo + 15% clearance improved DP980 edge stretchability; laser/mill/waterjet > mechanical shearing	• Novel stretchability method. • Complex three-angle cutting does not seem practical in real production!
Wang et al. [87]	Sheared edge tension test	Exp	Half-dog-bone with one sheared edge	AHSS incl. DP980 shows limited diffuse necking; simple QA test for edge formability	• Experimental work only • Two clearances only
Cheng et al. [161]	Post-necking grid-size-dependent fracture model for trimming of DP980	FE	Microstructure-based model	Calibrates grid-size-dependent fracture strains for accurate DP980 failure prediction	• Some assumptions • No physical validation • Used the extrapolated SS curve
Choi et al. [116]	DP980 trimming, focusing on tool failure Tool: Hardened cast-tool steel 57-58 HRC	Exp + FE	Burr vs strokes; die inclined angle; edge profile	Number of strokes↑ → burr ↑ -10º angle → tool failure↓ & burr↓ FE results: compressive stress at lower → no crack from lower die corner → no burr, but for lower clearances only	• No study for clearances larger than 21% • Up to 20,000 cuts only • No part stretchability evaluation • No tool failure mechanism

Despite significant progress in understanding the shearing and trimming of AHSS, important gaps still exist—especially for ultra-high-strength grades like DP980. While earlier studies have examined the effects of cutting clearance, tooling geometry, and post-trimming stretchability (mainly through hole expansion tests), critical issues related to tool life, fatigue failure mechanisms, and edge formability under industrial trimming conditions remain less explored.

Specifically, limited attention has been given to:

- The fracture behavior of DP980 during trimming, especially when burr-free edges form at large clearances.
- The post-trimming stretchability and cracking behavior of sheared edges during subsequent forming operations.
- The degradation and fatigue-related failure of D2 trimming dies after very high stroke counts typical of industrial use.
- The lack of predictive frameworks for trimming tool life, especially those that combine experimental data with simulation-based approaches.

These gaps highlight the need for a comprehensive investigation combining experimental and numerical methods to better understand and predict DP980's trimming behavior, improve edge quality, and increase tool durability. The next chapter details the specific objectives and methodologies used to address these research needs.

CHAPTER THREE
RESEARCH OBJECTIVES AND APPROACHES

The motivation for this research came from early production experiences with ultra-high-strength DP980 steel, which exhibited minimal burr formation even at large clearances. Although trimmed DP980 edges often displayed unusually small burrs – especially when compared to lower-strength grades like BH, HSLA, DP500, or DP600 – these burr-free edges still tended to crack prematurely during forming operations. This observation for DP980 contradicts the well-established relationship between stretchability and burr height, illustrated in Figure 1.7. Simultaneously, trimming tools used for high-volume DP980 stamping were found to suffer from excessive wear and chipping, particularly after extended use, raising concerns about tool durability and the ability to maintain consistent edge quality.

The current research seeks to address these knowledge and application gaps by focusing on the following main objectives:

1. Improve the sheared edge quality and performance of UHSS DP980, which has high potential for reducing weight in automotive structures.
2. Understand the main impact of the fracture mechanism on edge stretchability when there are no large burrs on the sheared edge DP980.

3. Develop a numerical model predicting the trimming process with a deformable die.
4. Make maintenance of trim dies predictable and prevent catastrophic die failures during high-volume trimming operations.

The following approaches are employed to achieve the above objectives:

1. Analyze the trimming mechanism in DP980 – Develop a fundamental understanding of how ultra-high-strength steel is trimmed and explain why the trimmed parts have reduced edge stretchability.
2. Cutting parameter optimization – Identify trimming conditions, especially cutting clearance, that create advantageous sheared edge morphologies and enhance the stretchability of DP980 during downstream forming.
3. Development of diagnostic tools for edge quality – Based on analyzing sheared edge parameters under various cutting conditions, develop a non-destructive quality control method that enables early detection of declining quality in trimmed parts.
4. Tool wear characterization and maintenance criteria – Analyze the progression of tool wear and chipping over high stroke counts using profilometry and optical methods, and establish thresholds for predictive maintenance.

5. Fatigue-based life prediction of trimming tools – Use experimental data and finite element modeling to simulate the fatigue life of broadly used D2 trimming inserts, incorporating existing fatigue models and real-world loading histories.

Together, these approaches will provide an integrated experimental–numerical framework for enhancing trimmed edge performance, extending tool life, and reducing downtime and costs in the mass production of automotive UHSS components.

CHAPTER FOUR
SHEARING PROCESS AND CHARACTERIZATION OF THE SHEARED EDGE OF DP980

This chapter details the materials used in this study, the experimental procedure of trimming and punching operations, and the results of the sheared edge characterization.

4.1. Materials

Ultra-high-strength dual-phase steel (DP980) was selected as the primary sheet material for this study. For comparison, several other sheet steels with different strength levels were also examined:

- High-strength low-alloy (HSLA 340/410), 1.4 mm thick
- Bake-hardenable (BH 210/340), 0.55 mm thick
- Interstitial-free (IF) mild steel, 1.2 mm thick

Two commercial DP980 steels from different suppliers were examined. Their nominal chemical compositions, based on mill certificates, are listed in Table 4.1.

Table 4.1. The chemical composition of the studied DP980 sheets.

Material index	Supplier	Chemical composition (%wt.)									
		C	Mn	P	S	Si	Ni	Cr	Mo	Al	Nb
DP980-1	Supplier 1	0.154	1.89	0.019	0.003	0.527	0.01	0.04	0.004	0.048	0.002
DP980-2	Supplier 2	0.10	2.32	0.012	0.002	0.117	0.014	0.583	0.097	0.033	0.037

The mechanical properties of the two DP980 sheets are presented in Table 4.2.

Table 4.2. The mechanical properties of DP980 sheets.

Material index	As-received thickness (mm)	Yield strength (MPa)	Tensile strength (MPa)	Uniform elongation (%)	Total elongation (%)	n-value (4-6%)
DP980-1	1.45	786	1004	7.3	13.5	0.078
DP980-2	1.50	696	1027	9.2	13.7	0.085

From the name designation, both DP980-1 and DP980-2 are dual-phase steels with a minimum ultimate tensile strength (UTS) of 980 MPa. Even though their chemical compositions are similar, their mechanical behavior may differ. Tensile test results of these two DP steels are shown in Figure 4.1 for different directions relative to the rolling direction, and the results of the longitudinal direction are marked in the graphs for comparison purposes. With a similar ultimate strength level, DP980-1 exhibits significantly lower uniform elongation compared to DP980-2, but displays noticeably higher post-necking deformation.

The scanning electron microscopy study was performed to analyze the microstructure and grain morphology of two DP steels, and the microstructures are illustrated in Figure 4.2. The figure shows that the studied steels have different grain sizes of martensite and ferrite phases. The average grain size in DP980-2 is about one-third of that in DP980-1. This could explain why the amount of uniform elongation in DP980-1 is much smaller than in DP980-2.

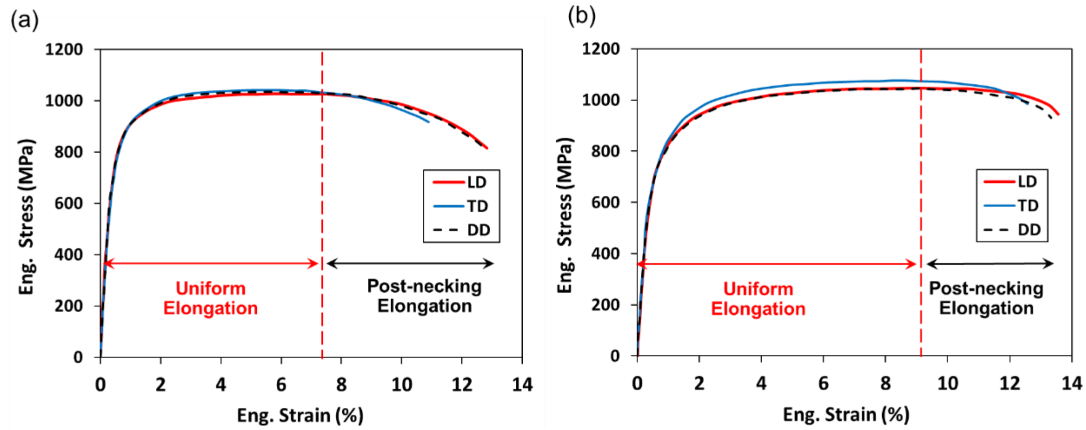

Figure 4.1. Engineering stress-strain curves for (a) DP980-1 and (b) DP980-2 sheets. LD, TD, and DD denote the longitudinal, transverse, and diagonal directions, respectively. Marked uniform and post-necking elongations are related solely to LD.

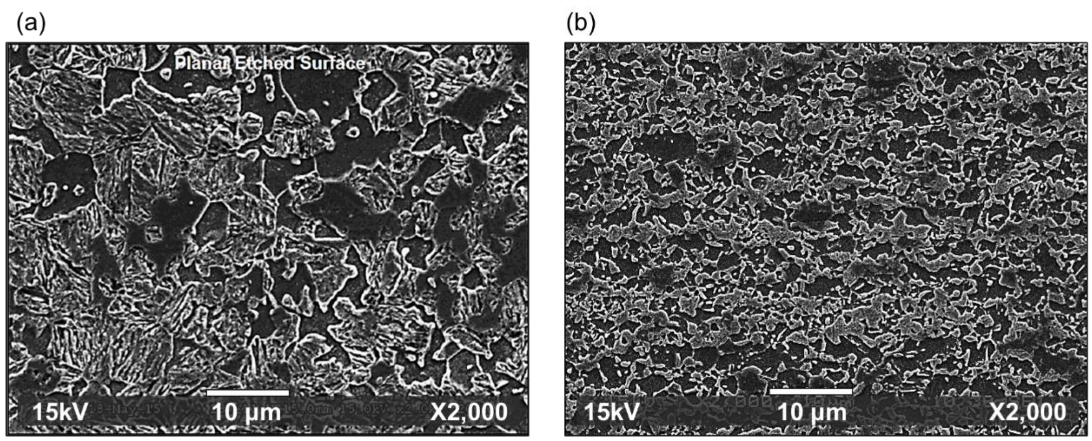

Figure 4.2. Scanning Electron Microscopy microstructure of (a) DP980-1 and (b) DP980-2 steel sheets.

4.2. Trimming Operation

A schematic of the mechanical trimming processes employed in this study was shown earlier in Figure 1.11 (a). The clearance is the horizontal distance between the upper and lower trimming tools. In our trimming experimentation, clearance was precisely controlled and varied using a set of shims, as shown in Figure 4.3. Significant attention was paid to providing the experimental die with substantial stiffness to avoid clearance variation during the cutting process. This dissertation expresses the percent clearance ratio of this distance to the sheet thickness. In the trimming experiment, the upper and lower cutting inserts were made of D2 high-carbon, high-chromium cold-work steel. The typical chemical composition of D2 tool steels is 1.55 wt.% C, 11.5 wt.% Cr, 0.8 wt.% Mo, 0.9 wt.% V, 0.3 wt.% Mn, and 0.4 wt.% Si [148]. Both inserts had sharp trimming edges with a zero-degree cutting angle.

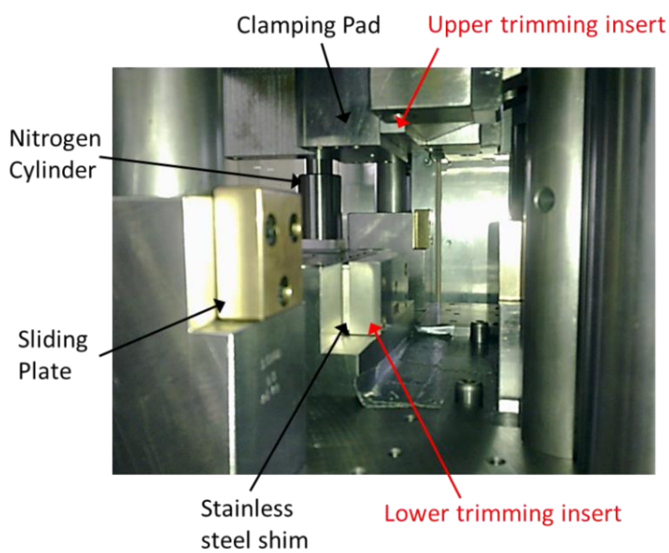

Figure 4.3. The experimental trimming tool.

The trimming line for cutting specimens included a decoiler, straightener, automatic feeder, and a 65-ton Minster mechanical press, as shown in Figure 4.4. The specimens were trimmed at a speed of 45 strokes per minute. The schematic diagram, as shown in Figure 4.4 (d), provides an overview of the trimming line's functional layout, showing the material flow from the coil through leveling, feeding, and shearing stages. This setup ensures a consistent and repeatable environment for evaluating tool durability and sheared edge formability under production-like conditions.

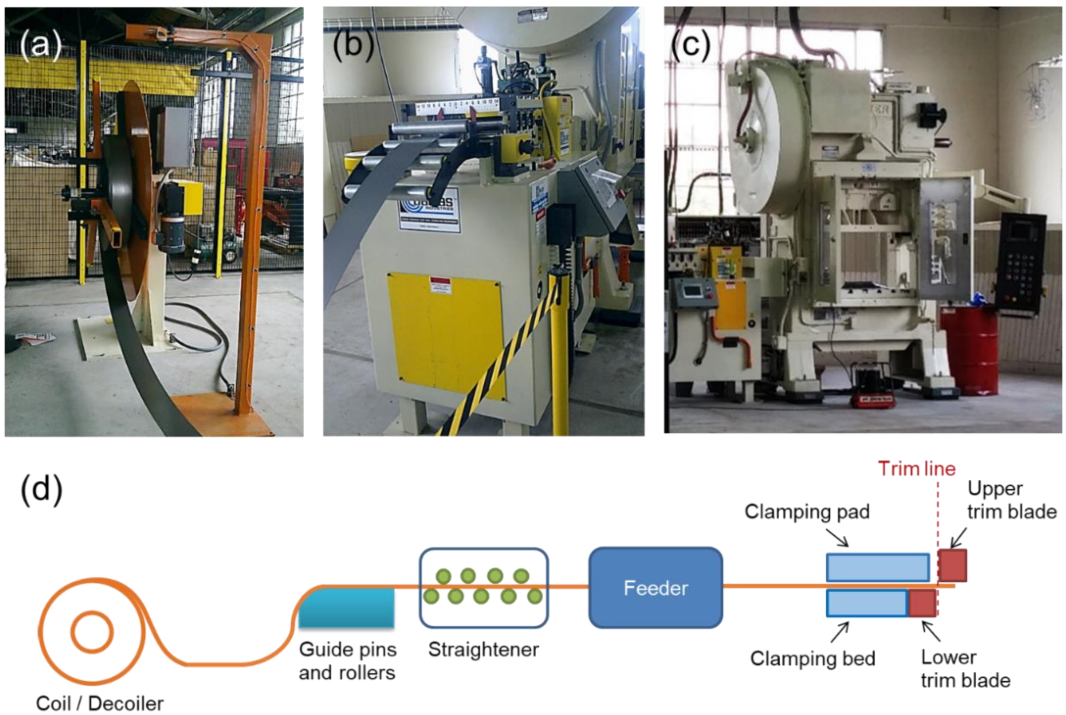

Figure 4.4. The trimming line consists of (a) decoiler, (b) Dallas Industries straightener and automatic feeder, (c) 65-ton Minster mechanical press, and (d) schematic representation of trimming line.

Trimming clearance was varied using precision shims, as detailed in Table 4.3, for each sheet of material.

The dimensions of the trimmed specimen are shown in Figure 4.5 (a). To study the effect of material orientation on the sheared edge quality, shearing operations were done on sheets with different cutting directions with respect to the rolling direction, as shown in Figure 4.5 (b). Based on the orientation of the trim line to the rolling direction, we will have longitudinal (LD), transverse (TD), and diagonal (DD) trimmed specimens.

Table 4.3. Variation in trimming clearance by material type.

Material Type	**Sheet Thickness (mm)**	**Trimming clearance (%t)**					
DP980	1.45	4	10	17	20	30	40
HSLA340	1.4	4	11	18	21	32	43
BH210	0.55	-	12	18	27	36	45.5
IF	1.2	5	12.5	17	21	25	37.5

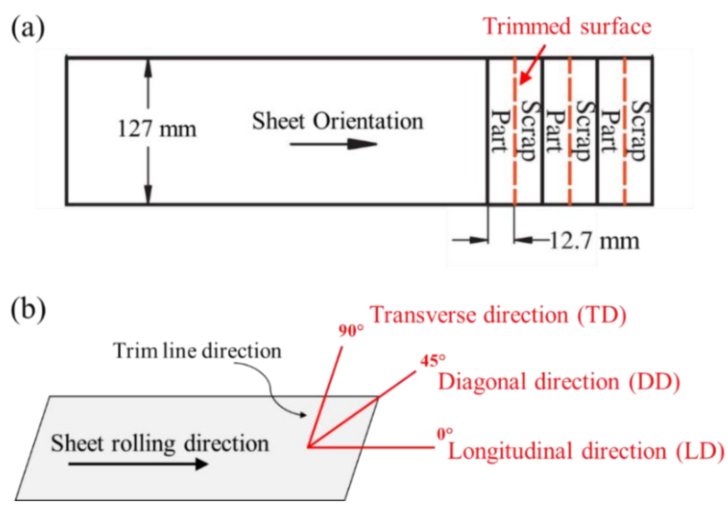

Figure 4.5. (a) Dimensions of trimmed specimen, (b) trim line direction with respect to the rolling direction.

4.3. Measurements of Sheared Edge Features

Measurement of the burr height of the trimmed specimens was carried out using a Mitutoyo MDC-1" SXF digital micrometer, Figure 4.6 (a). Five repeated tests were conducted for each test condition, and measurements were taken at ten locations on each specimen. The experimental results in this study are presented as averaged values with their standard deviations, based on 50 measurements. To measure the rollover, burnish, and fracture zones of the trimmed specimens, the specimens were photographed under a Nikon SMZ745T microscope, and MATLAB software [149] was used for image processing (Figure 4.6 (b) and (c)). The difference between the thicknesses at the edge measured by the microscope and by the micrometer was taken as the rollover length.

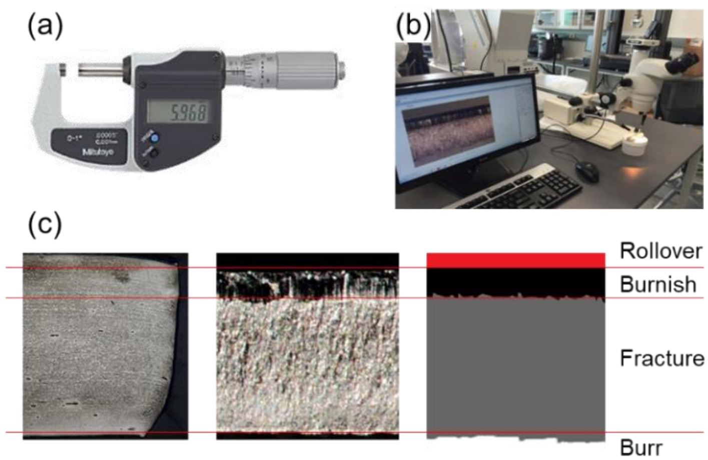

Figure 4.6. Measurement tools including (a) digital micrometer, (b) Nikon Microscope, and (c) Matlab measurement scheme.

4.4. Influence of Trimming Clearance on Sheared Edge Quality

As previously defined by published literature, the most critical factor influencing trimming quality is the clearance between the cutting edges. Figure 4.7 shows the experimental plot representing the effect of trimming clearance on the depth of rollover, burnish, and fracture zones, and the height of burr for DP980-1 sheet material. Figure 4.8

shows trimmed surfaces and cross-sections of DP980-1 as well. Similarly, for DP980-2 sheet material, the effect of trimming clearance on the sheared edge features is shown in Figure 4.9, and surfaces and cross-sections of trimmed edges are shown in Figure 4.10.

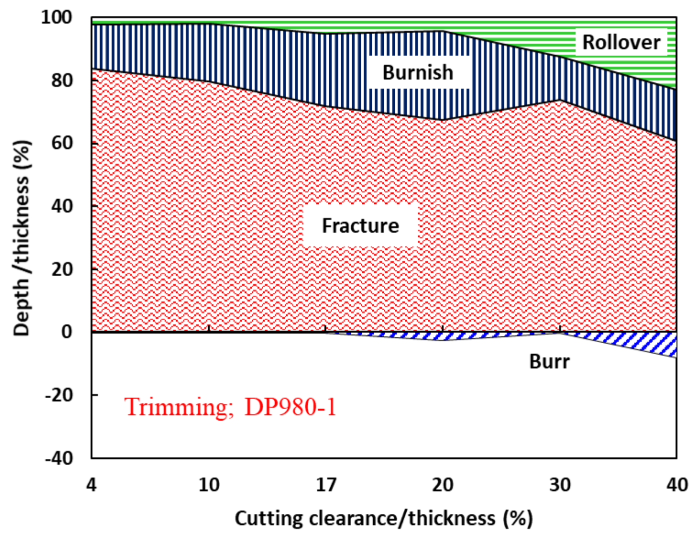

Figure 4.7. The effect of trimming clearance on the sheared edge features of DP980-1.

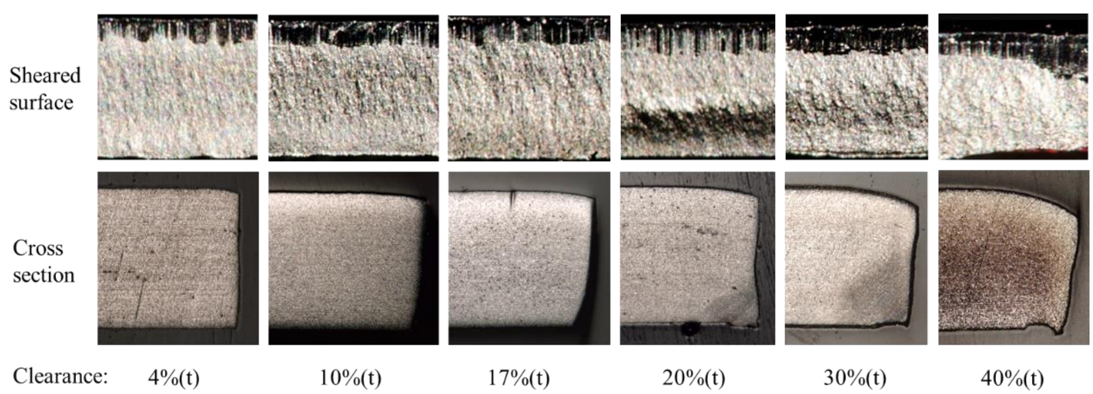

Figure 4.8. The surface and cross-section of trimmed DP980-1 sheet material for different trimming clearances.

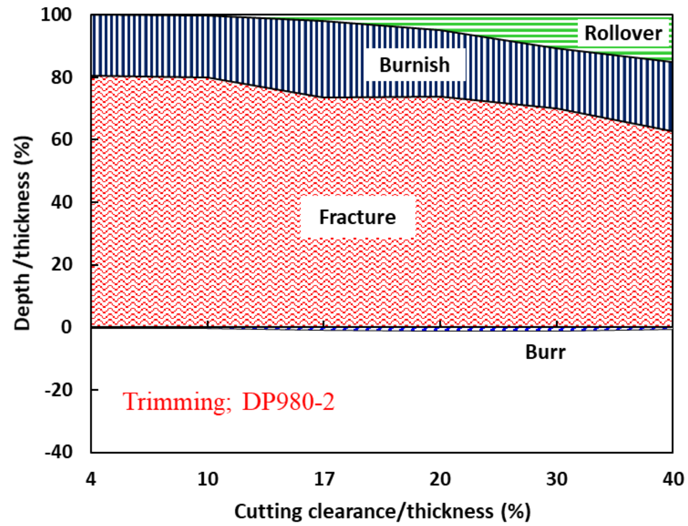

Figure 4.9. The effect of trimming clearance on the sheared edge features of DP980-2.

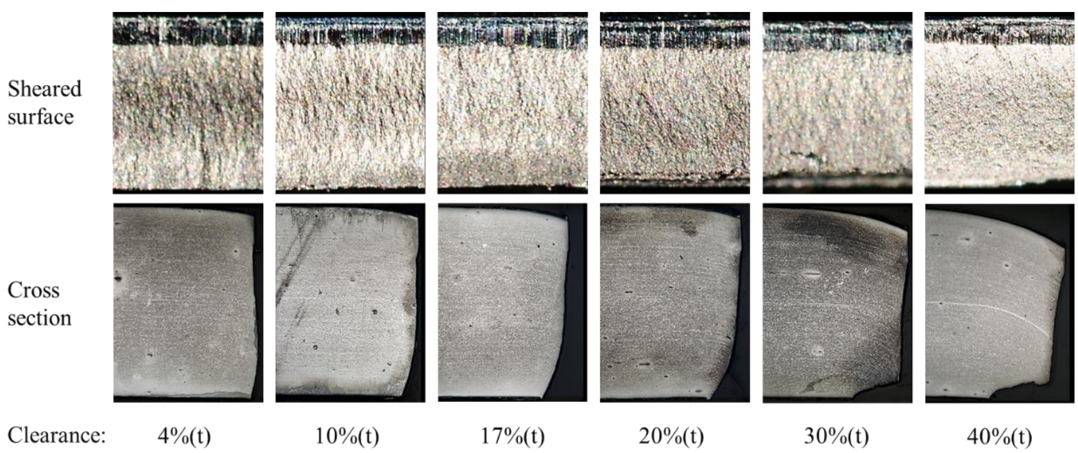

Figure 4.10. The surface and cross-section of trimmed DP980-2 sheet material for different trimming clearances.

4.4.1. Rollover Depth Analysis

The rollover region undergoes an increase in bending deformation. The overall trend for this region is that it increases with clearance due to larger bending moments, as observed in Figure 4.7 through Figure 4.10, for both DP980 steels.

4.4.2. Burnish Depth Analysis

The burnish area, also known as the shear area, is the smooth and shiny region formed during the shearing of material. Along with the rollover area, it indicates the penetration depth before fracture begins. Generally, more ductile materials tend to have larger burnish areas. Hydrostatic pressure within the sheared zone increases in smaller clearances, which enhances the material's ductility and enlarges the burnish zone. As a result, the burnish depth is greater in smaller clearances compared to larger ones. This effect is more pronounced in relatively ductile materials [116].

Well-known fine blanking processes are based on increased hydrostatic pressure, which allows the burnished zone to propagate through the entire thickness. However, a different behavior was observed during the trimming of DP980. In this case, increasing the clearance to 20% resulted in an increased burnish depth, followed by a decrease at larger clearances for DP980-1. For DP980-2, the same trend was observed, but the maximum burnish occurred at 17% clearance. Graphs of burnish depth versus trimming clearance for these two steels are shown in Figure 4.11.

4.4.3. Fracture Area Analysis

The fracture and burnish areas cover most of the sheared surface, and when the rollover depth is included, it equals the original sheet thickness. The depth of the fracture area for trimmed DP980 materials is shown in Figure 4.7 through Figure 4.10, decreasing with clearance due to the increased sum of rollover and burnish.

According to Wu et al. [25], the actual edge profile of the fracture zone can be a combination of multiple micro-cracking progressions, so that the detected rough surface can be the summation of various micro-cracks at different length scales within the lattice, between grain and phase particles, and among martensite clusters.

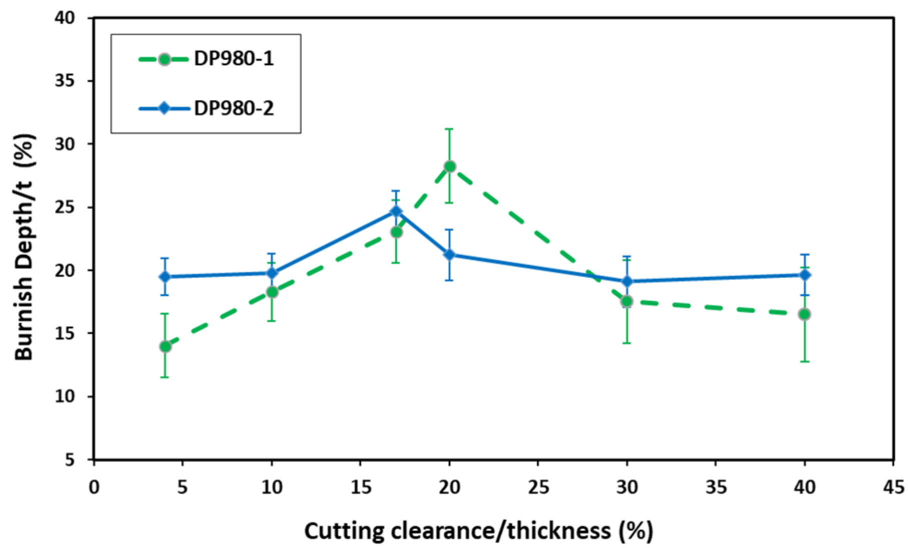

Figure 4.11. Burnish depth as a function of trimming clearance for two different DP980 materials, trimmed in the transverse direction.

4.4.4. Burr Height Analysis

Figure 4.12 shows the graphs of burr height versus the cutting clearance for two DP980s. For DP980-1, as the clearance increased from 4% to 17%, no visible burr was observed; however, the average burr height increased above the 17% clearance. However, burr height for DP980-2 was noticeably less sensitive to the clearance than DP980-1 and showed almost no considerable burr for all clearances ranging from 4% to 40%.

The fracture mechanism of the DP980 sheet material during the trimming process is described later in Section 6.4. As a result of this mechanism, the heavily deformed burr is removed from the trimmed edge at the final stage of trimming, leaving the part side with no noticeable burr, despite having large clearances.

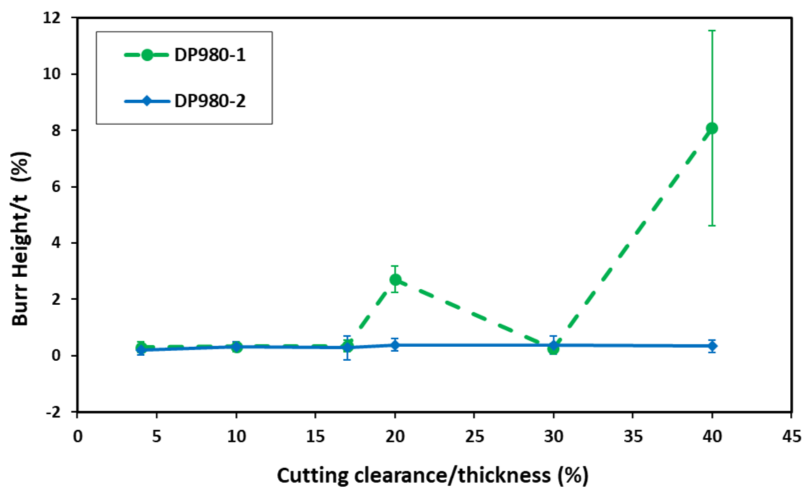

Figure 4.12. Burr height as a function of trimming clearance for two different DP980 materials, trimmed in the transverse direction.

Although the cutting force applies vertically on the blank and produces a corresponding vertical reaction force on the tools, a horizontal force component tends to increase the clearance between the tools. During the design and manufacturing of the experimental die, considerable attention was given to ensuring substantial stiffness and preventing clearance variation during trimming. A simple way to verify the clearance after trimming is to measure the distance (c), as shown in Figure 4.13. The actual clearance percentage is then calculated as (c/t) ×100. By taking these measurements at cross-sections of Figure 4.13 for DP980-1, the actual clearances are 4.7%, 10.6%, 17.7%, 20.8%, 30.9%, and 40.6% for the nominal clearances of 4%, 10%, 17%, 20%, 30%, and 40%, respectively. Thus, the clearance remained relatively close to the target values during the trimming experimentation.

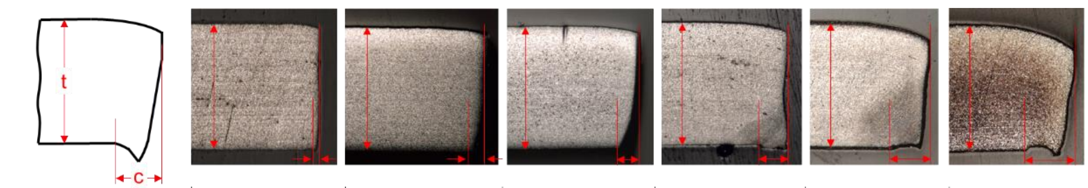

Nominal clearance	4%	10%	17%	20%	30%	40%
Calculated clearance $\left(\frac{c}{t} \times 100\right)$	4.7%	10.6%	17.7%	20.8%	30.9%	40.6%

Figure 4.13. Calculation of actual clearance for DP980-1.

4.5. Influence of Material Type on Sheared Edge Quality

The part edge quality also depends on the material being sheared [41], [68], [111]. Materials with high ductility, low yield strength, and homogeneity will produce better sheared edge quality and tighter dimensional tolerances. It can also be expected to have a longer tool life, based on the expectation of increased fatigue life under lower loads [24].

Burr height results with respect to the trimming clearance for different sheets, including mild steel (IF), bake hardenable steel (BH210), high strength steel (HSLA340), and DP980-1, are plotted in Figure 4.14.

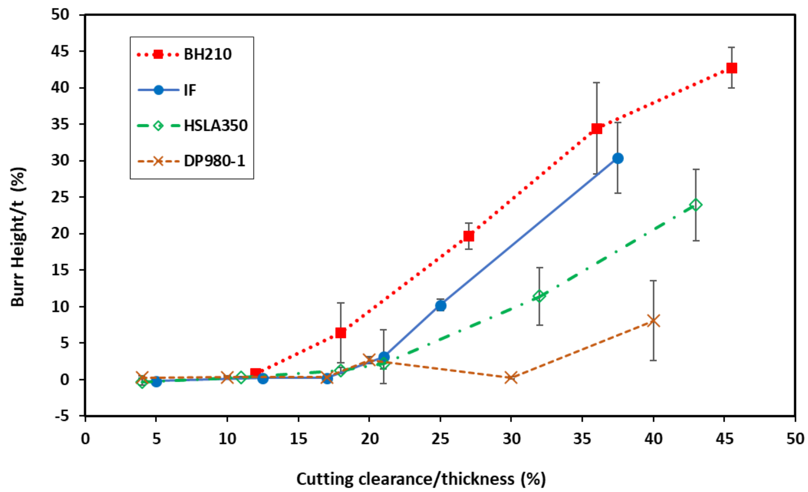

Figure 4.14. Burr height as a function of trimming clearance for different sheet materials trimmed in the transverse direction.

All four sheet materials exhibit the same trend in response to increased clearance, characterized by growth in burr height [90]. Pretty similar to DP980, for smaller clearances up to 15%, the formed burr for BH, HSLA, and IF steels is very small and negligible. At higher clearances, BH210, widely used for exterior panel applications, exhibits a visibly larger burr height than other materials. IF steel has a higher burr than HSLA and DP980 steels. These differences in burr height are related to the materials' ductility, with more ductile materials showing more burrs.

4.6. Influence of Material Anisotropy on Shear Edge Quality

As other researchers in the literature review showed, the material anisotropy may affect the part edge quality [67].

Burr height results concerning the trimming clearance for two different DP980 and different trim line orientations relative to the rolling direction are plotted in Figure

4.15. As described previously, all configurations exhibit the same trend with increasing clearance, characterized by an increase in burr height. From the influence of material anisotropy, DP980-2 exhibits relative isotropy and minimal sensitivity to clearance. However, DP980-1 shows some anisotropy in burr height; TD is more sensitive to the clearance than LD. In other words, anisotropic effects on trimmed edges become more dominant with increasing trimming clearance, and interaction between trim edge quality and anisotropy exists for DP980-1.

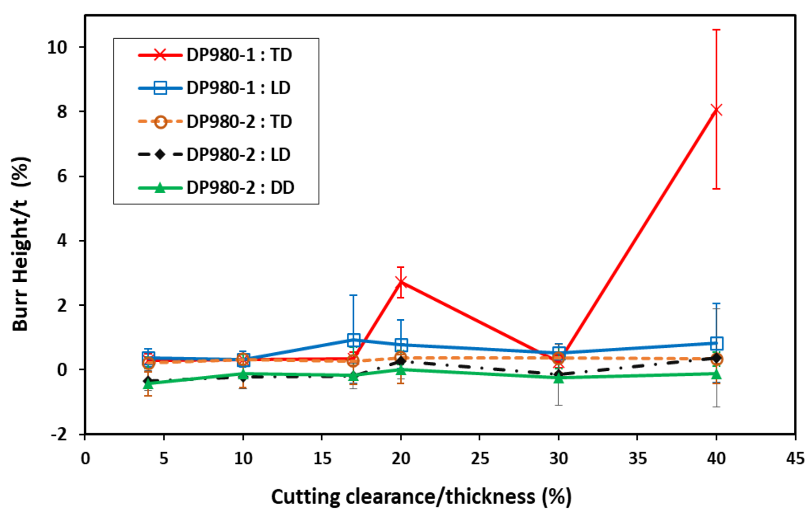

Figure 4.15. Burr height as a function of trimming clearance for two different DP980 and different trim line orientations relative to rolling direction.

The influence of material cutting direction for IF, BH210, and HSLA340 sheets is shown in Figure 4.16, Figure 4.17, and Figure 4.18, respectively. For all materials and directions, burr height increases with trimming clearance. Also, as a general trend, the burr height increases slightly with shearing orientation relative to the rolling direction, i.e., burr height in TD is larger than in DD and then in LD cuts.

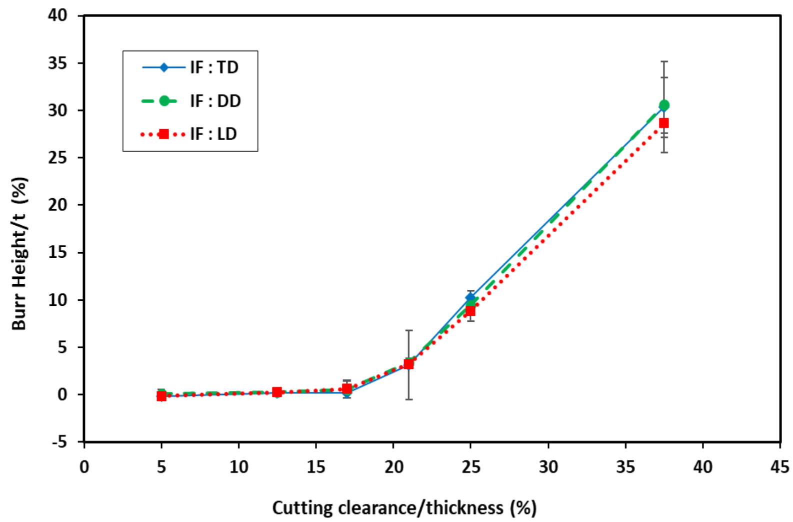

Figure 4.16. Burr height as a function of trimming clearance and different trim line orientations relative to the rolling direction for IF sheet material.

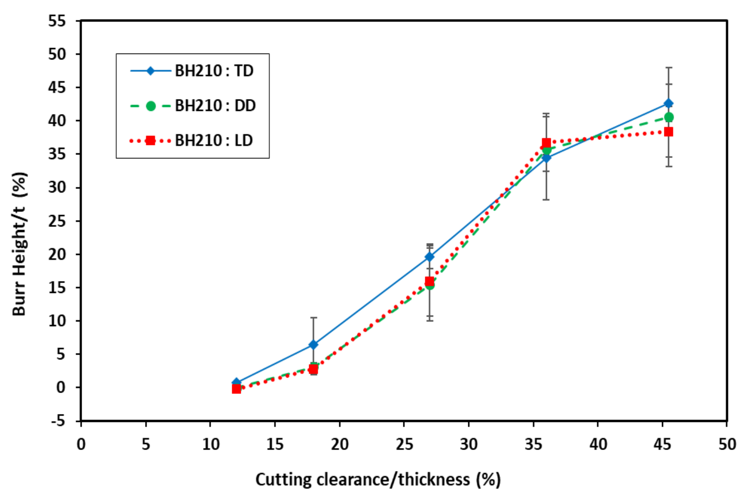

Figure 4.17. Burr height as a function of trimming clearance and different trim line orientations relative to the rolling direction for BH210 sheet material.

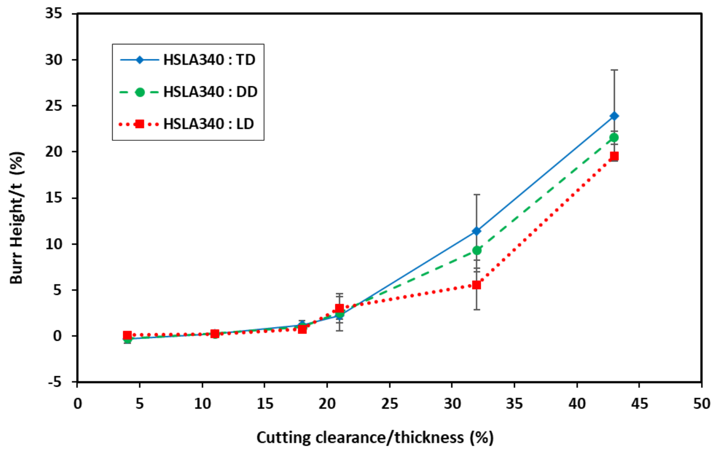

Figure 4.18. Burr height as a function of trimming clearance and different trim line orientations relative to the rolling direction for HSLA340 sheet material.

4.7. Microhardness Gradient Characterization Across the Sheared Edge

The hardness distribution near the sheared edge was characterized using a Wilson VH3100 microhardness tester with a diamond Vickers indenter (Figure 4.19). An applied load of 300 mN was selected according to ASTM E-140 guidelines [150], to ensure consistent indentation size and minimize interaction between neighboring indents. A rectangular measurement grid was mapped across the sheared edge area, including 65-85 measurement points arranged systematically. Each indentation was carefully spaced to record the hardness gradient from the edge to the bulk material. The collected data were compiled and processed to generate a two-dimensional hardness contour map, revealing local variations in hardness caused by the shearing process at the different trimming clearances. The actual measurement data for each point are detailed in Appendix A.

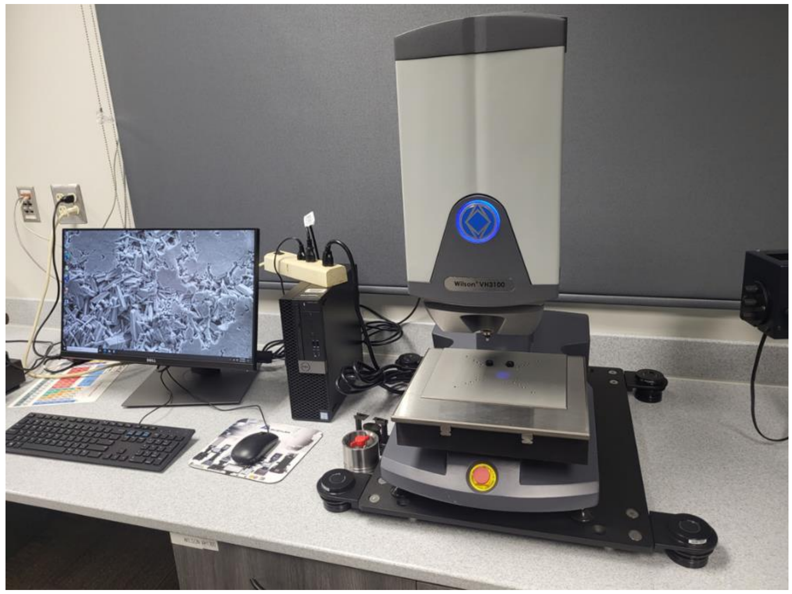

Figure 4.19. Wilson VH3100 Microhardness Tester

At the smallest clearance of 4%, the sheared region showed a significant increase in hardness, with localized values exceeding 335 HV near the cut edge, as shown in Figure 4.20. This strong hardening effect can be attributed to substantial plastic deformation caused by shearing at tight clearances. The deformation zone is highly narrowed, resulting in significant strain hardening, but it may also cause embrittlement near the edge due to excessive strain localization.

The hardness maps for clearances of 10%, 17%, and 20% are illustrated in Figure 4.21, Figure 4.22, and Figure 4.23, respectively. At 10% clearance, the hardened area was still visible but had spread across a wider zone, with peak hardness values exceeding 395 HV in some areas. This indicates that an increase in clearance creates a larger shear-affected zone. By 17% and 20% clearance, the hardness maps revealed a larger area with values closer to those of the bulk material (275–325 HV). This suggests reduced strain hardening compared to smaller clearances, reflecting a more balanced fracture-dominated shearing mechanism that appears at intermediate clearances.

For large clearances of 30% and 40%, as illustrated in Figure 4.24 and Figure 4.25, respectively, the hardness distribution showed a clear asymmetry: highly hardened areas were concentrated in specific regions of the sheared edge, especially in the burr tip and fracture zones with hardness exceeding 395 HV. However, large parts of the sheared surface exhibited hardness levels comparable to those of the base material. This unevenness indicates that at excessive clearances, deformation becomes focused in localized zones, resulting in inhomogeneous edge properties. Such conditions may decrease overall edge quality and create weak points that can initiate cracks during subsequent forming or cyclic fatigue loading.

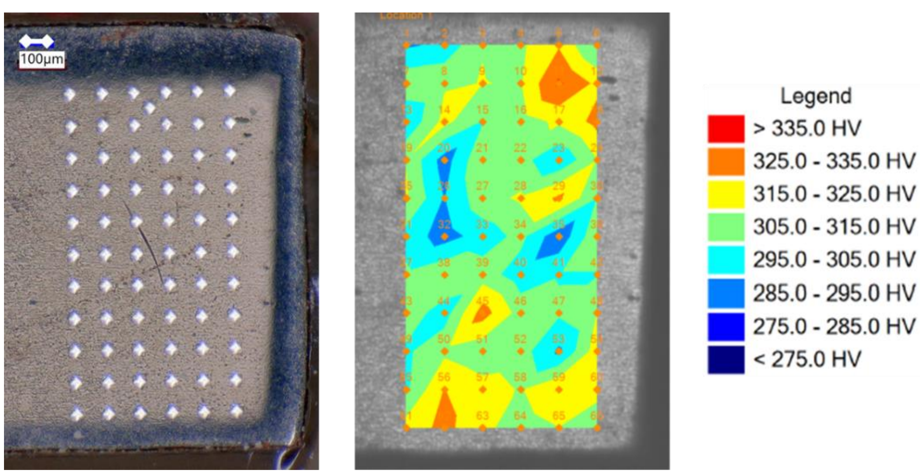

Figure 4.20. Vickers microhardness contour maps of the sheared edge profile of DP980-1, trimmed at 4% clearance, at 150x magnification.

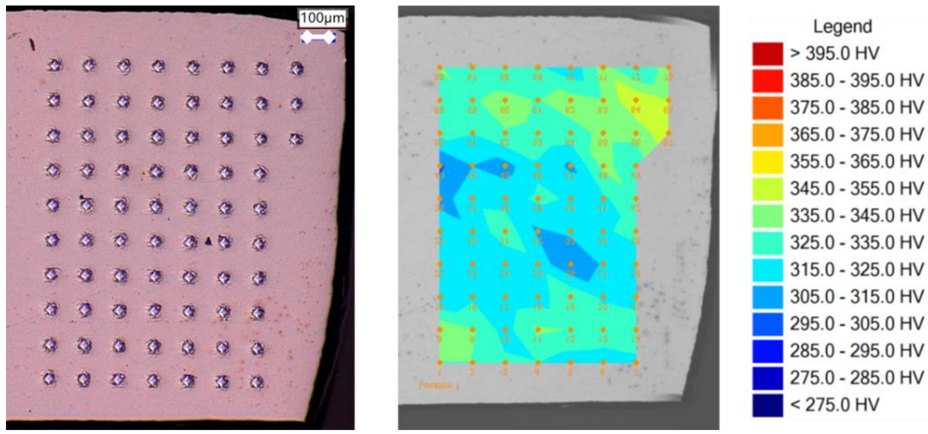

Figure 4.21. Vickers microhardness contour maps of the sheared edge profile of DP980-1, trimmed at 10% clearance, at 150x magnification.

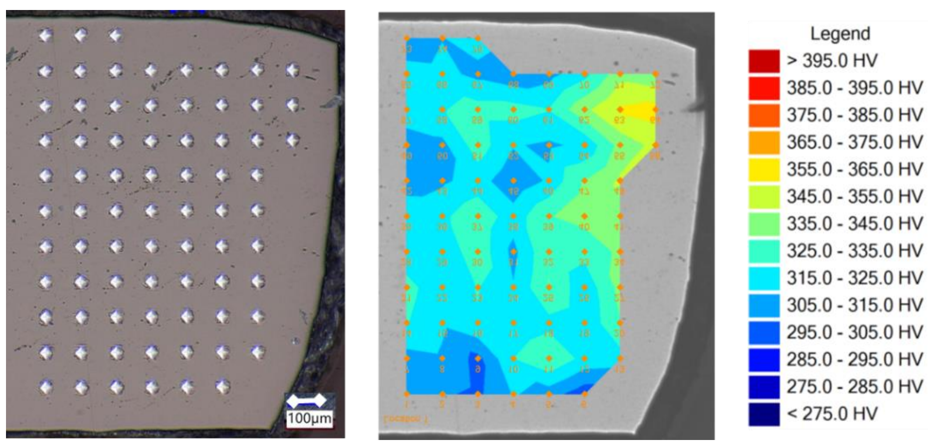

Figure 4.22. Vickers microhardness contour maps of the sheared edge profile of DP980-1, trimmed at 17% clearance, at 150x magnification.

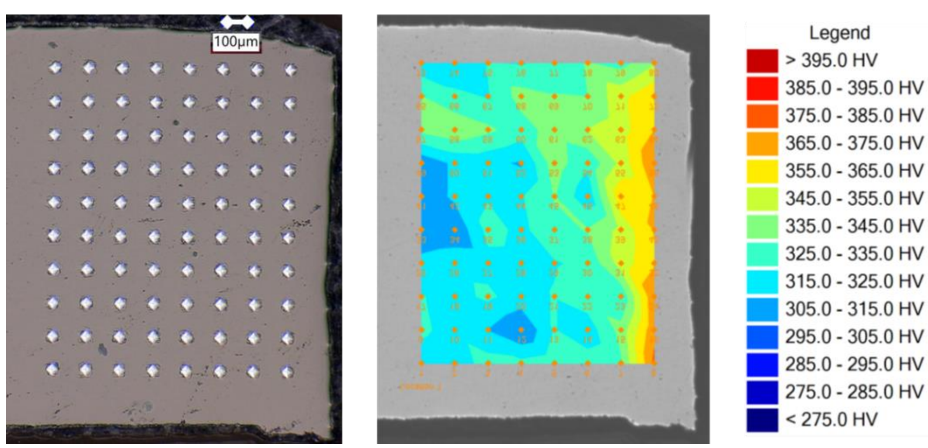

Figure 4.23. Vickers microhardness contour maps of the sheared edge profile of DP980-1, trimmed at 20% clearance, at 150x magnification.

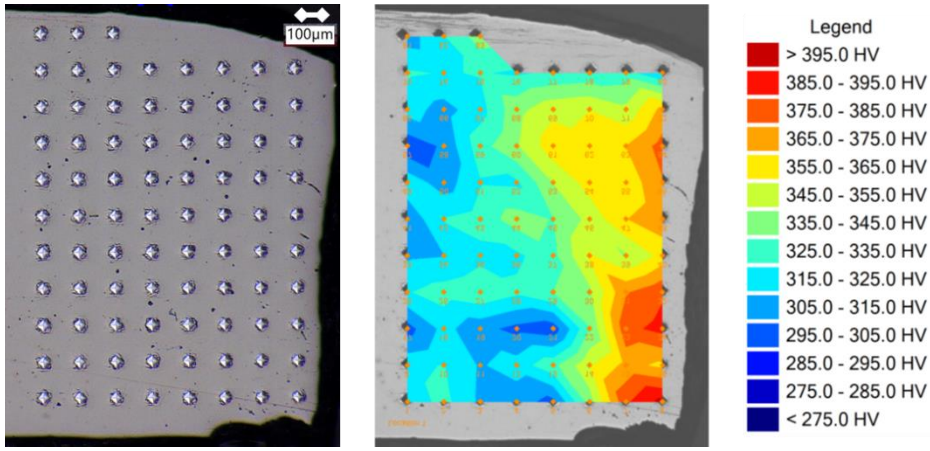

Figure 4.24. Vickers microhardness contour maps of the sheared edge profile of DP980-1, trimmed at 30% clearance, at 150x magnification.

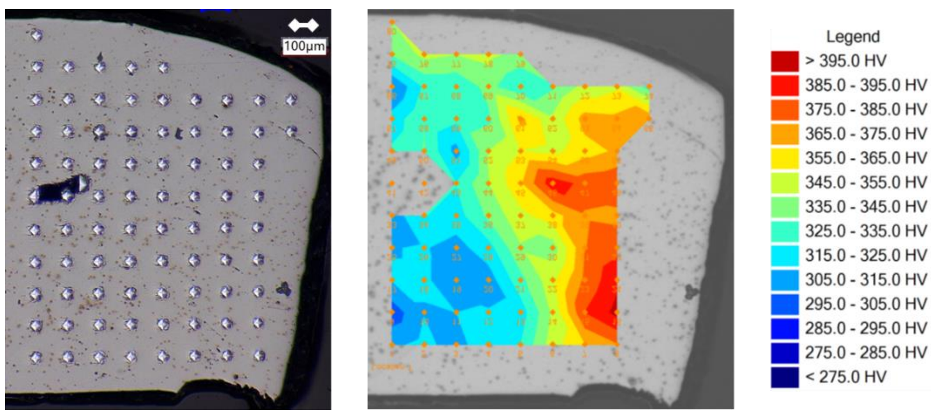

Figure 4.25. Vickers microhardness contour maps of the sheared edge profile of DP980-1, trimmed at 40% clearance, at 150x magnification.

Overall, the results demonstrate a clear relationship between punch-to-die clearance and the hardness gradient near the sheared edge. A small clearance of 4% causes a high work hardening in a narrower shear-affected zone, while large clearances, over 30%, lead to highly localized hardening and uneven edge properties. Intermediate clearances (~17–20%) offer a balance, with moderate hardening and a relatively uniform hardness distribution, which may be beneficial for achieving both good edge quality and resistance to crack initiation.

The microhardness profiles measured with the Future-Tech FM-700 hardness tester further emphasize how punch-to-die clearance influences deformation-induced hardening in both the burnish and fracture zones of the sheared edge. In the burnish zone (Figure 4.26), the hardness values near the edge were consistently higher than the bulk hardness, indicating severe plastic deformation in this area. The highest hardness levels, close to 390 HV, appeared at the smallest distances from the edge for the largest clearances (30% and 40%). These values gradually decreased with increasing distance from the edge, stabilizing around approximately 325 HV beyond roughly 1500–2000 μm. In contrast, smaller clearances (4% and 10%) resulted in lower peak hardness near the edge (~350–360 HV), with a quicker decline toward the bulk hardness. This shows that larger clearances lead to more intense strain hardening in the burnish zone, though with a broader and less uniform distribution.

In the fracture zone (Figure 4.27), a similar trend was observed, although the overall hardness values were generally lower than in the burnish zone. The highest hardness levels near the edge were observed at large clearances (30% and 40%), exceeding 370 HV in some areas. These hardness levels decreased more gradually with distance, indicating that fracture at high clearances causes a deeper, more penetrating strain gradient. Conversely, at smaller clearances (≤10%), the fracture zone showed lower hardness (~320 HV at the edge), with only a slight gradient toward the bulk. The softening at low clearance may be due to the predominance of plastic compression and uniform deformation rather than localized hardening from burr breakage, as discussed further.

Together, these findings support the fact that clearance has a significant influence on the mechanical state of the sheared edge. Small clearances promote uniform deformation with minimal edge hardening, while large clearances lead to concentrated strain hardening that extends further into both the burnish and fracture zones.

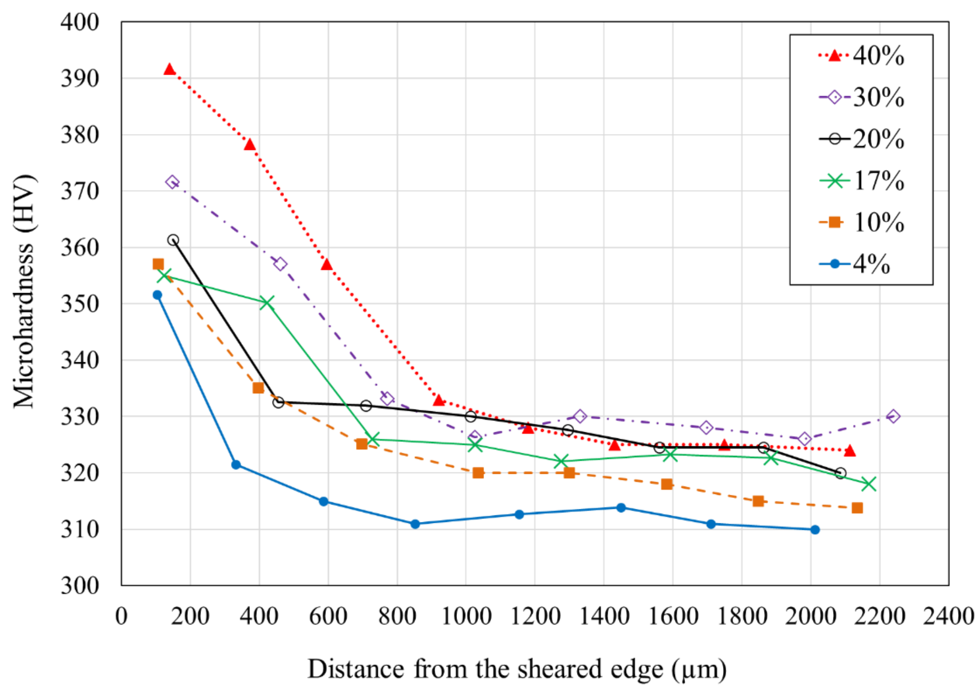

Figure 4.26. Microhardness profile in the burnish zone for different trimming clearances.

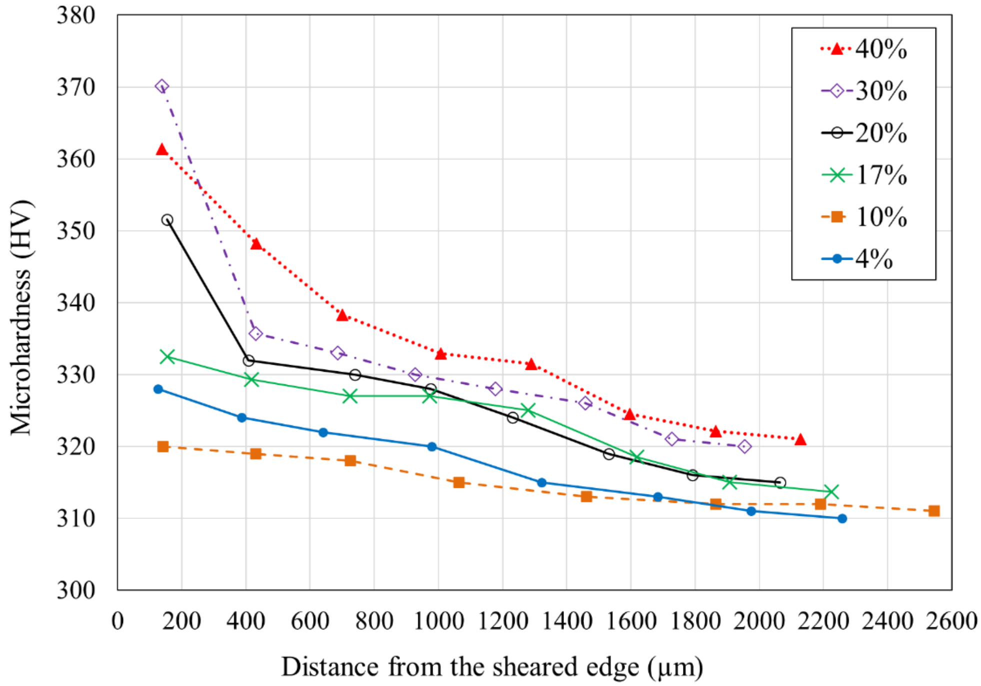

Figure 4.27. Microhardness profile in the fracture zone for different trimming clearances.

4.8. Correlation Between Microhardness and Strain Levels

A novel method was developed to estimate local equivalent stress and strain levels based on measured Vickers microhardness values. This correlation enables quantification of deformation histories in specific regions, such as sheared edges, where direct strain measurement is challenging. To establish this relationship, 13 sequential rolling operations were performed on DP980-1 steel samples, each resulting in an incremental thickness reduction of about 0.1 mm. For DP980-1, the initial sheet thickness, t_0, was 1.45 mm, corresponding to zero pre-strain, and the rolling process was continued until the minimum thickness of 0.24 mm was reached.

Assuming the r-value of material is equal to one, the equivalent true strain level for the i^{th} thickness, ε_i, was calculated using Equation (4.1) as follows:

$$\varepsilon_i = -\frac{2}{\sqrt{3}} \cdot ln \frac{t_i}{1.45} \tag{4.1}$$

Where t_i is the current sheet thickness after rolling, this equation, derived from volume constancy and the assumption of plane-strain deformation in rolling operation, is explained in more detail in Section 6.1.7.3. The rolled specimens were sectioned, mounted, and polished, and the Vickers microhardness measurements were undertaken using a Wilson VH3100 automated tester. For each strain level, five indentations were performed to ensure statistical reliability. The measured average microhardness and corresponding standard deviations are summarized in Table 4.4.

Table 4.4. Microhardness and strain levels of rolled DP980-1 samples.

Thickness, mm	**True strain level**	**Average Microhardness, HV**	**Std. deviation**
1.45	0	329	8
1.3	0.086	340	12.1
1.2	0.18	355	7.1
1.1	0.28	376	4.9
1	0.39	380	9.7
0.9	0.51	368	5.4
0.8	0.65	391	4.3
0.7	0.82	395	6
0.6	0.99	401	8.5
0.5	1.19	417	3.9
0.4	1.45	426	9.1
0.29	1.86	431	7.2
0.24	2.04	435	12.6

The correlation between average microhardness and strain level is illustrated in Figure 4.28. The measured data (blue line with error bars) show a general increase in hardness with increasing strain, consistent with the strain-hardening behavior of dual-phase steels. A second-order polynomial trendline (red dashed curve) was fitted to the data, resulting in the regression Equation (4.2):

$$HV = -22.69\varepsilon^2 + 93.52\varepsilon + 336.84 \tag{4.2}$$

With a strong positive correlation between hardness and strain level up to approximately 2.0. Despite local variations around 0.3-0.5 strain, the overall trend reflects continuous work-hardening throughout the rolling process.

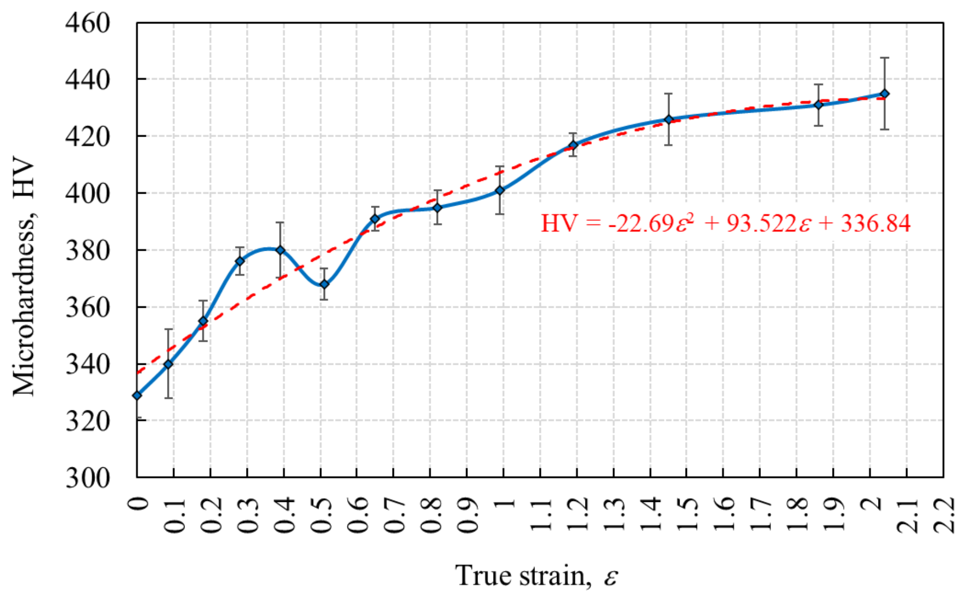

Figure 4.28. Measured HV Microhardness versus true strain level for rolled samples of DP980-1.

This empirical relationship enables an indirect estimate of plastic strain from hardness measurements at any location, especially along sheared or deformed regions of trimmed edges. Once the strain level is obtained from microhardness, the corresponding equivalent stress can be calculated using the true stress–strain curve of the material, allowing for a complete reconstruction of the local stress–strain state. This method offers a valuable tool for validating numerical simulations, assessing localized deformation in high-strain areas, and evaluating material response near fracture or fatigue-sensitive zones in advanced high-strength steels.

4.9. Punching Operation

In addition to the trimming, punching experiments were performed on DP980-1 and DP980-2 sheet materials using a 10 mm punch and six different die diameters to provide clearances of 6, 10, 17, 24, 34, and 46 % of the sheet thickness. A schematic of the punching processes employed in this study was shown earlier in Figure 1.11 (b).

4.10. Influence of Punching Clearance on Sheared Edge Quality

Similarly, the hole-punched specimens were measured for rollover, burnish, and burr heights. As shown in Figure 4.29, each punched specimen was divided into eight zones, and averages of these eight zones are reported as the height or depth of each edge feature. Each zone was photographed under the microscope, and the burnish and fracture height were measured by pixel counting. The thickness and burr height were measured by a Mitutoyo PMU150-25MX sheet metal micrometer with a deep-throated frame. The difference between the thicknesses at the edge measured by the microscope and by the micrometer was taken as the rollover length.

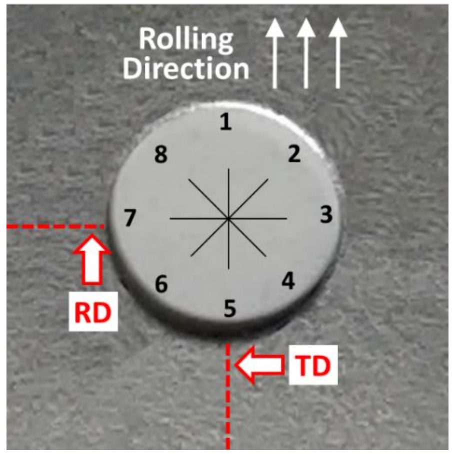

Figure 4.29. Measurement locations on the punched hole and locations of RD and TD cross-section samples.

Figure 4.30 shows the results of punching experiments expressing the effect of punching clearance on the depth of rollover, burnish, and fracture zones, and the height of the burr for DP980-1. Also, the cross-sections of the sheared edge in transverse and rolling directions for DP980-1 after the hole punching are shown in Figure 4.31.

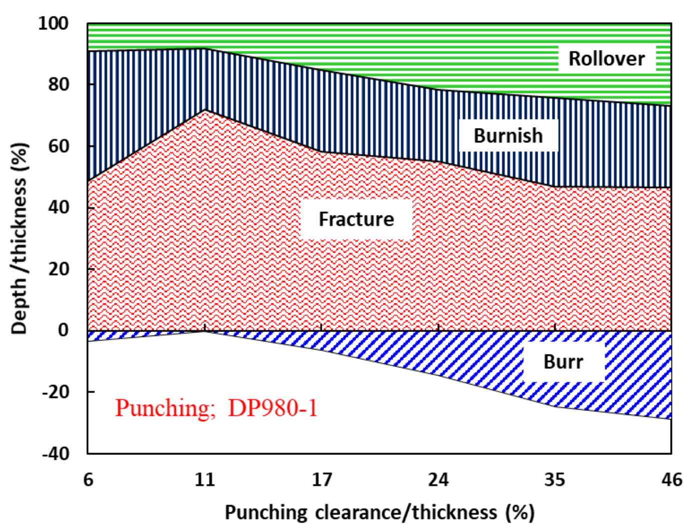

Figure 4.30. The effect of punching clearance on the sheared edge features of punched DP980-1.

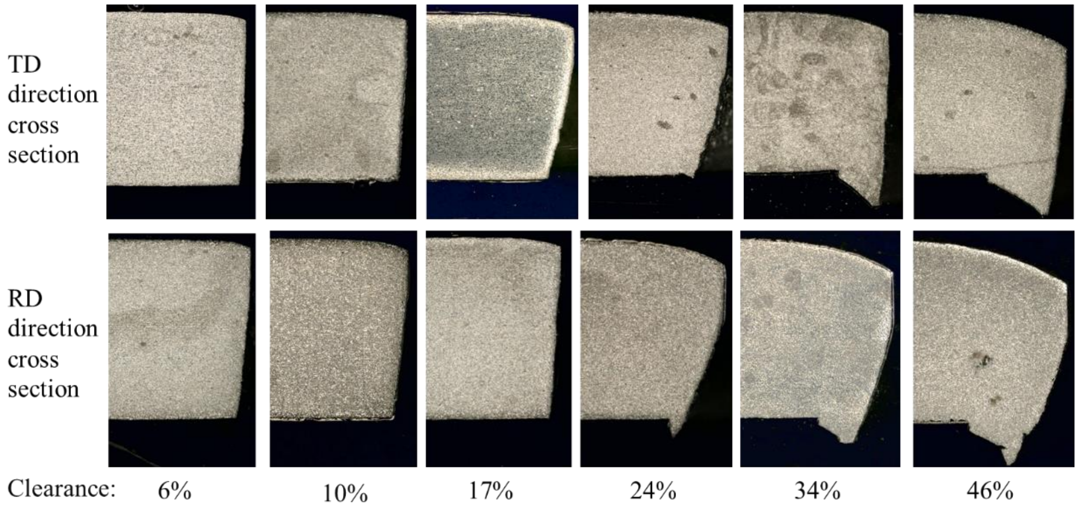

Figure 4.31. The cross-section of punched DP980-1 sheet material in the transverse and rolling directions for various punching clearances.

A stacked area chart of the sheared edge features of DP980-2, showing changes to the punching clearance, is depicted in Figure 4.32, and corresponding cross-section images in rolling and transverse directions are shown in Figure 4.33 as well.

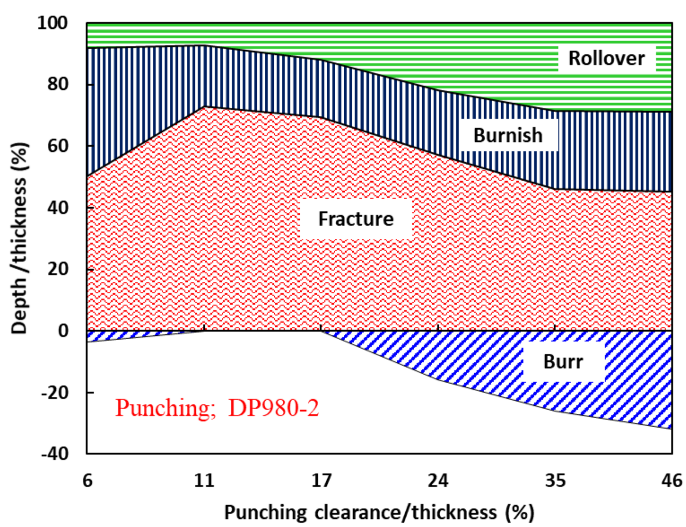

Figure 4.32. The effect of punching clearance on the sheared edge features of punched DP980-2.

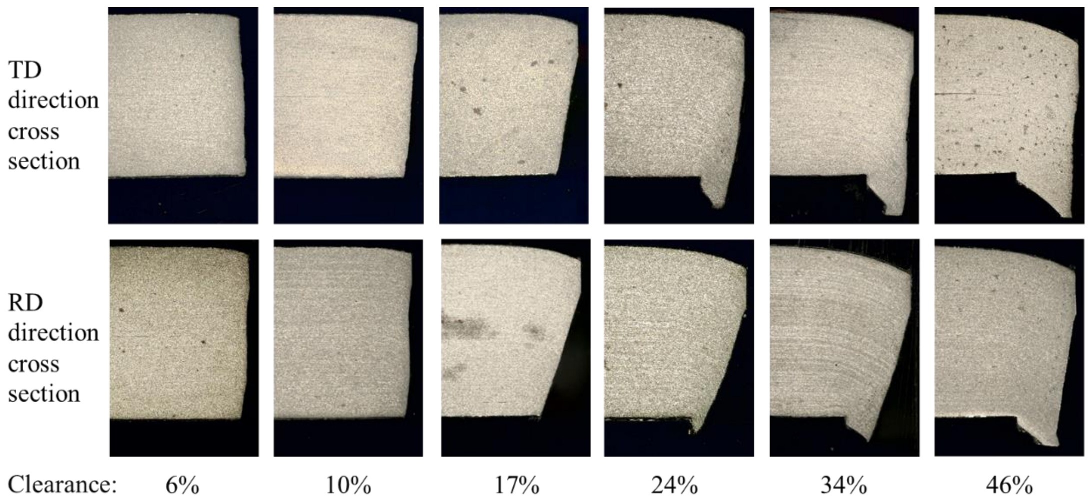

Figure 4.33. The cross-section of punched DP980-2 sheet material in the transverse and rolling directions for various punching clearances.

For the punching process of the DP980, the burr removal mechanism observed during trimming did not occur due to the very limited bending. In this process, burrs were easily formed and increased significantly with clearance, as shown in Figure 4.31 and Figure 4.33.

Burnish depth for both punched DP980s was the highest for the smallest clearance (6%) and decreased substantially for 10% clearance, then slightly increased up to the clearance of 46%. As described before, the highest hydrostatic pressure for the smallest clearances in the sheared zone generally increased the material's ductility and burnish area. The indentation height increased for the clearances larger than 10%, indicating that the fracture was initiated at a higher punch penetration depth.

In Figure 4.34, burr height and rollover depth are compared for trimmed and punched DP980 steels. It is observed that the hole-punched specimens have a higher rollover and burr compared to the trimmed samples. This behavior significantly differs from previous studies conducted on DP500 [67].

The difference in results between the trimming and hole punching processes can be explained by the variation in cutting conditions when punching a 10 mm diameter hole versus cutting along a straight line. In punching, the scrap button experiences an axisymmetric membrane constraint, but the scrap is free to move and bend during the process of trimming.

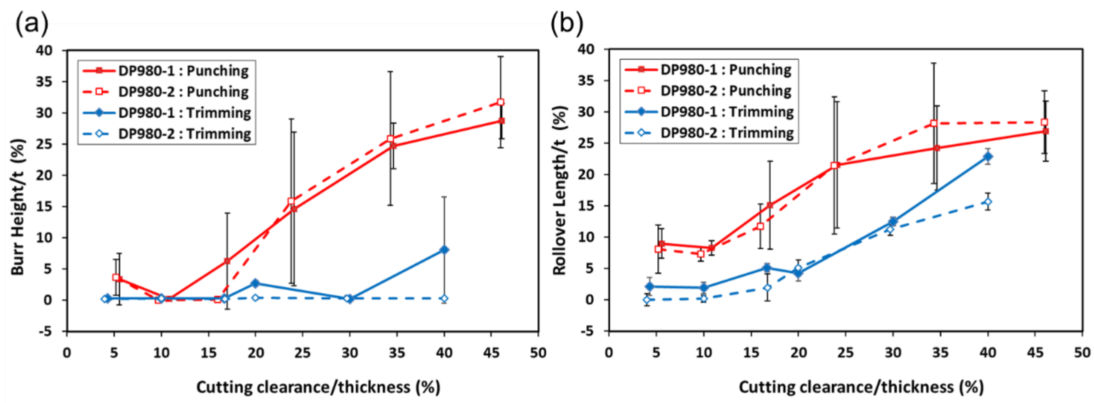

Figure 4.34. Comparison of trimmed to punched edge features for two DP980 sheets: (a) burr height and (b) rollover length.

4.11. Summary

This chapter examined the trimming and punching behavior of DP980 steels, emphasizing how clearance, material properties, and anisotropy influence the sheared edge. Two commercial grades of DP980 were compared with HSLA340, BH210, and IF steels. Trimming was carried out using D2 steel dies with clearances from 4% to 40% of the sheet thickness. Burr height, burnish depth, rollover, and fracture zones were measured to evaluate edge quality.

Among the DP980 steels, DP980-2 exhibited superior edge quality and was less prone to burr formation, likely due to its finer microstructure and more isotropic properties. In contrast, DP980-1 experienced greater burr growth, stronger anisotropy, and more variable rollover. Across all materials, burr height increased with increasing clearance, while burnish and fracture zones showed material-dependent trends. Notably, DP980-1 and DP980-2 had a peak in burnish depth at intermediate clearances (~17–20%) before decreasing at higher values.

Shearing direction also influenced edge quality, especially for DP980-1, where burr height varied with cutting orientation relative to the rolling direction. This effect was less significant in more isotropic materials like DP980-2. Comparing with IF, BH210, and HSLA steels showed that more ductile materials tend to produce larger burrs, even at small clearances.

Microhardness mapping around the sheared edge provided valuable insights into deformation-induced hardening. At low clearances, work hardening was more evenly distributed, while high clearances caused localized hardening near fracture tips and burrs. Intermediate clearances produced a more balanced hardness profile with less strain concentration—suggesting they may offer the best compromise between edge quality and fatigue resistance. Additional microhardness profiles taken in both burnish and fracture zones supported these findings and showed how clearance choice affects the subsurface mechanical properties state.

Additionally, punching experiments resulted in noticeably different edge features compared to trimming for DP980. The axisymmetric nature of punching led to more pronounced burr formation and deeper rollover depths, even at similar clearances.

The findings in this chapter provide an essential experimental baseline for analyzing edge fracture and assessing sheared edge performance in the next chapter.

CHAPTER FIVE
SHEARED EDGE STRETCHABILITY

In addition to the quality of the sheared edge, the performance and formability of the sheared edges must be understood for the efficient implementation of UHSS steels and other advanced materials. Sheared edge stretchability tests can measure the ability of edge stretching without failure, which is needed for final stamping and subassembly processes. In this chapter, the three stretchability tests employed in the present study will be explained individually: tension, side bending, and hole expansion tests.

5.1. Sheared Edge Stretchability by Tensile Testing

The basics of this method were explained earlier in Section 1.3.1.1. Trimmed specimens of DP980, HSLA, BH, and IF were examined by tensile testing.

First, 12.7 mm wide and 127 mm long specimens were trimmed on the mechanical press. To eliminate the effect of the scrap portion of the sheared edge, the scrap side was carefully metal-finished to remove the shear-affected zone, while the part side of the trimmed specimens was left untouched. The efficiency of the metal finish procedure was validated by checking the fracture propagation either by necking through the whole width of the sample or by initiating from the sheared edge.

Then, one surface of the specimens was electro-etched to obtain 1 mm square grids to measure local deformations after stretching. Tension tests of the prepared specimens were performed using an Instron 5982 universal testing machine equipped with a 100 KN static load cell, hydraulic grips, and the Advanced Video Extensometer (AVE 2.0), as shown in Figure 5.1 (a).

Finally, local strain measurements of fractured specimens were performed using an automated FMTI grid analyzer series 100U (Figure 5.1 (b)), and the results were reported.

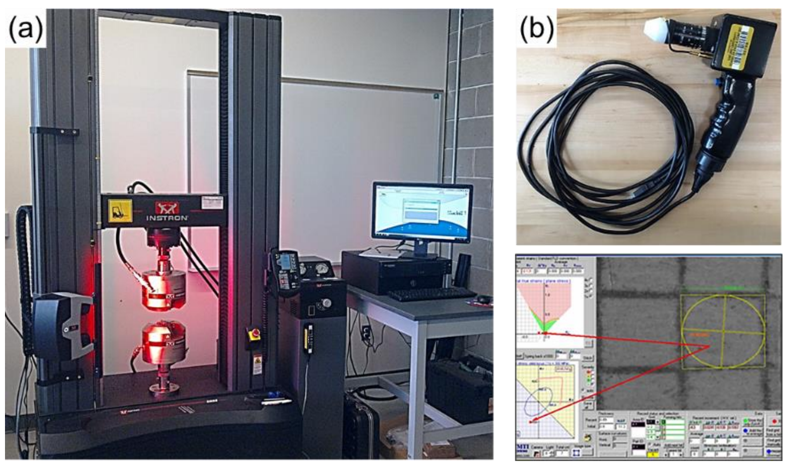

Figure 5.1. (a) Instron 5982 tensile frame with video extensometer and hydraulic grips, and (b) FMTI grid analyzer.

The approach used in this study is based on the method developed by Hecker [151] for building forming limit diagrams. This method was later successfully applied by Le et al. [23], in which, depending on the distance of the grid from the fracture, the measured local strains are categorized as fractured, safe, and outside necking. Their results revealed that aluminum alloys typically have a relatively small necking portion of the elongation in the tensile test, and splits from the sheared edge occurred substantially earlier than necking initiation. In this deformation mode, sheared edge stretchability and necking did not interfere with each other.

Unlike aluminum alloys, UHSS used in this study has a relatively low work-hardening exponent, which limits the uniform elongation portion of the tensile test and often results in a substantial portion of the tensile test in the necking phase. Accordingly, splitting from the sheared edge occurs during the necking stage of the tensile test for UHSS DP980. Therefore, it is necessary to use finer grids that can provide data on strains along the sheared edge near fracture initiation within the diffuse neck. For this reason, a 1 mm square grid was chosen for strain measurements.

In all measured cases, cracks propagated through one of the grids, as shown in Figure 5.2. The grid analyzer could stitch the fractured grid to measure the fracture strain. These fracture-strain data points are shown in red. Safe measurements, illustrated with green color in graphs, correspond to the maximum strain on the sheared edge where fracture did not happen. Usually, these measurements were performed adjacent to fracture zone grids. In addition, measurements were taken outside the necking area, approximately 15mm from the fracture zone.

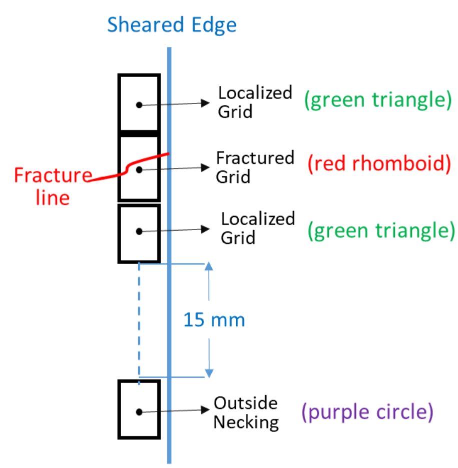

Figure 5.2. Measurement of local strains adjacent to the sheared edge.

5.1.1. Influence of Trimming Clearance on Sheared Edge Stretchability

The stretchability results in the form of major local strains are plotted versus the trimming clearance for DP980-1 and DP980-2 in Figure 5.3 and Figure 5.4, respectively. In these graphs, the lowermost boundary of all fractured data points represents the fracture limit (dotted red line), and the uppermost boundary of all safe data points represents the safe forming limit (solid green line). Additionally, the trend line of strains outside the necking area, crossing the averages, is plotted for further discussion. In addition to the local strain measurements, the extensometer data on total elongation are plotted as a potential parameter indicating the sheared edge stretching performance, with an initial gauge length of 50 mm. The strain values are engineering strain in percentage, comparable to the total elongation.

The stretchability of a trimmed surface is essential for processes such as stretch-hemming and stretch-flanging, which are typically performed after trimming. The general trend observed in both DP980 materials was that higher clearances showed less stretchability than smaller clearances.

Comparing the two materials, DP980-2 had much lower local strains for all trimming clearances than DP980-1. Also, DP980-2 exhibited substantially different behavior: a visible effect of the cutting clearance was seen for the clearances larger than 17%, as illustrated in Figure 5.4. Further increasing the clearance led to a more substantial reduction in the uniform elongation of samples and in the fractured and safe strains. For 40% clearance, the uniform elongation of DP980-2 was significantly below the n-value. More attention should be paid to aligning the trimming dies when stamping this material to avoid unexpected splits from the sheared edge.

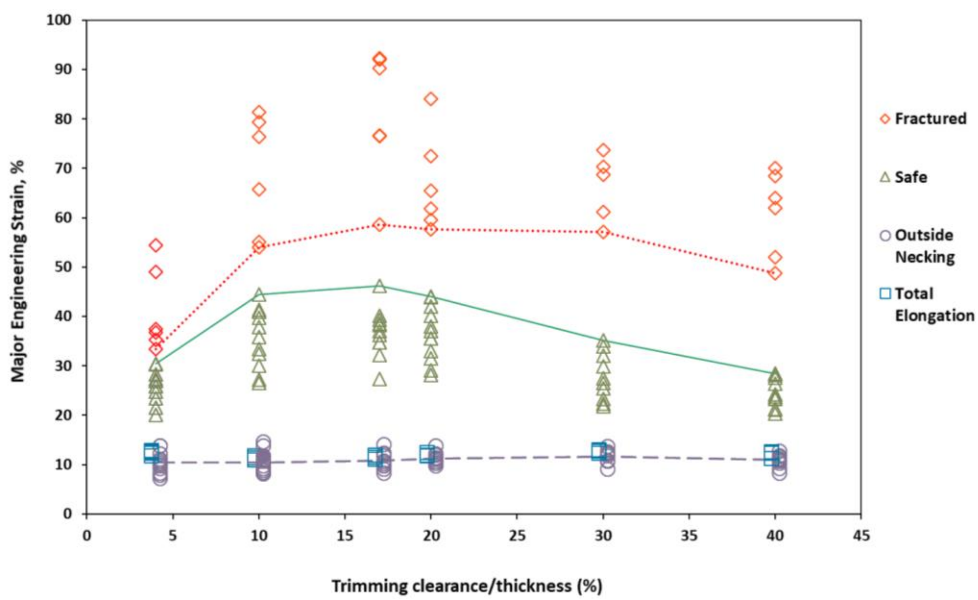

Figure 5.3. Results of the sheared edge stretchability of DP980-1 as a function of cutting clearance, using square grid analysis.

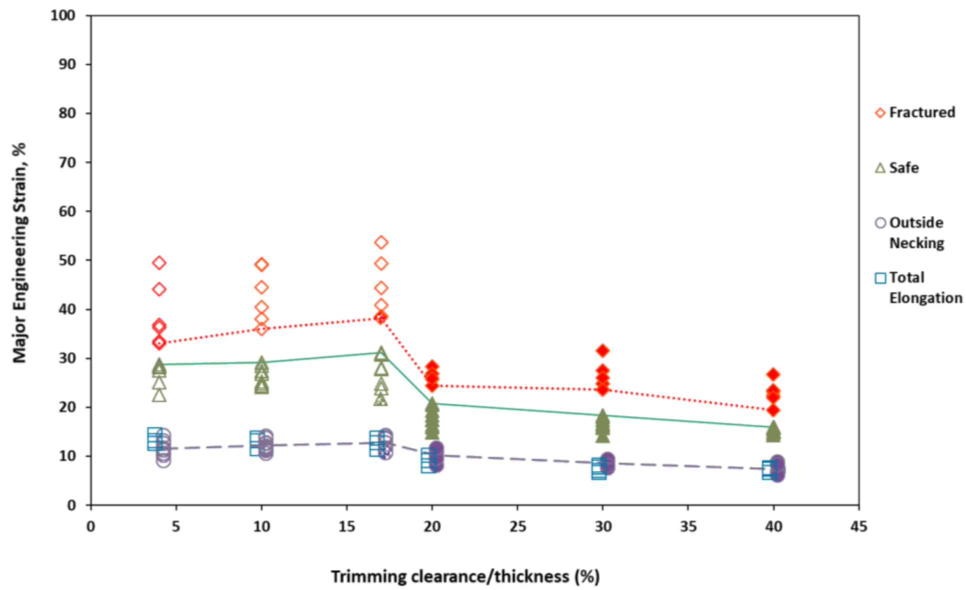

Figure 5.4. Results of the sheared edge stretchability of DP980-2 as a function of cutting clearance, using square grid analysis.

Data points related to measurements outside the necking area mostly showed uniform elongation of the sample, provided that fracture from the sheared edge did not occur before diffuse neck formation. In a tensile test, the material is expected to enter the diffuse necking deformation mode at true strains close to the n-value at the uniform elongation, assuming the power law approximation is valid, and the thickness is uniform [152]. Therefore, the strain measured away from the necking area should be near the uniform elongation. For DP980-1, this is 7.3% engineering strain. Strains measured outside necking in Figure 5.3 are near 7.3%, indicating that fracture from the sheared edge was initiated at strains above the n-value. Similarly, the uniform elongation for DP980-2 is 9.2% engineering strain, and all measured strains outside necking for smaller clearances in Figure 5.4 are close to this value. However, at 30 and 40% clearances for

DP980-2, where the trimmed edge has a significant influence, the measured strains outside necking are lower than those for smaller clearances.

In summary, both DP materials have very similar fracture initiation strains measured by square grid analysis; however, it takes longer for a crack to propagate through the DP980-1 than through the DP980-2 sample from the moment of initial crack formation until through-thickness cracking. The stress–strain curves for these materials show that DP980-2 exhibits less post-necking deformation than DP980-1. Failure in tensile tests often results from the onset of instability (necking), and many void formation and linkage processes occur after instability (post-necking). This aligns with previous findings that void nucleation, growth, and coalescence are strongly concentrated within the localized necking region, where stress triaxiality rapidly increases [153], [154]. One simple explanation could be that void nucleation and propagation leading to fracture in a fine-grain microstructure are easier, so the post-necking region (the length of this area) is shorter. Finer ferrite–martensite spacing promotes earlier void interaction and coalescence, which speeds up post-necking failure and reduces the post-uniform deformation elongation [154], [155].

Figure 5.5, Figure 5.6, and Figure 5.7 show graphs of sheared edge stretchability for IF, BH210, and HSLA340 sheet materials, respectively. All three steels exhibit a trend similar to that of DP980 steels: a decrease in edge stretchability as clearance increases. Among these materials, HSLA exhibits the greatest sensitivity to variations in cutting clearance, resulting in the largest drop in all strain measurements, including fractured, safe, and outside necking.

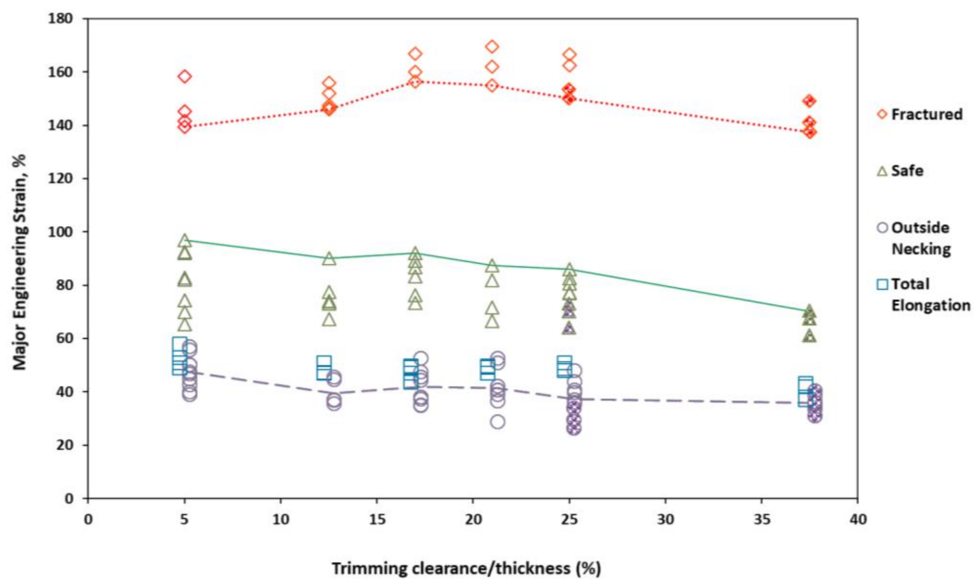

Figure 5.5. Results of the sheared edge stretchability of IF sheet material as a function of cutting clearance, using square grid analysis.

Based on Figure 5.5 for IF material, 18% clearance exhibits the best stretchability results with the highest strain levels, although it showed about 5% burr formation. (Figure 4.17). The large band between fractured and safe strains can be attributed to large localized necking deformation of ductile IF steel sheet. IF steel's total and uniform elongations are 45% and 27%, respectively, with an n-value of 0.24. Measured strains for outside necking points in Figure 5.5 are very close to the total elongation, which means that at a 15 mm distance from the fracture line, we are still within the necking area, and the term “outside necking” needs to be redefined for IF sheet material.

Measured outside necking strains are shown in Figure 5.6 and Figure 5.7 are close to uniform elongations of 22% and 18% for BH and HSLA, respectively. BH steel's best stretchability is achieved at 18% clearance, with quite a bit of localized necking before fracture, leading to higher local elongation than the outside necking strain. As the clearance increases beyond 18%, the safe strain decreases, indicating that edge stretchability decreases even as fractured strains increase.

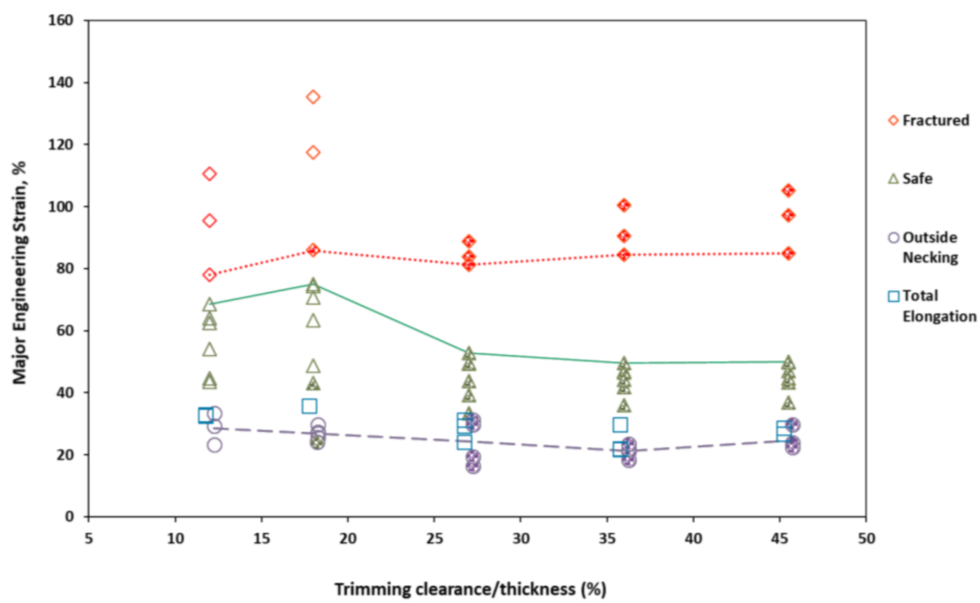

Figure 5.6. Results of the sheared edge stretchability of the BH210 sheet material as a function of cutting clearance, using square grid analysis.

HSLA specimens trimmed at 11% exhibit the best stretchability results, and for larger clearances up to 32%, all strains of fractured, safe, and outside necking decrease noticeably. Strain levels have increased slightly from 32% to 43%. At 43% clearance, a relatively thick and uniform burr layer, over 40% of the sheet thickness, forms on the part edge, which could reinforce the part.

Another reason measured total elongations are larger than outside necking strains for IF, BH, and HSLA is that total elongation averages over all square and rectangular grids and accounts for strain localization in both diffuse and localized necking.

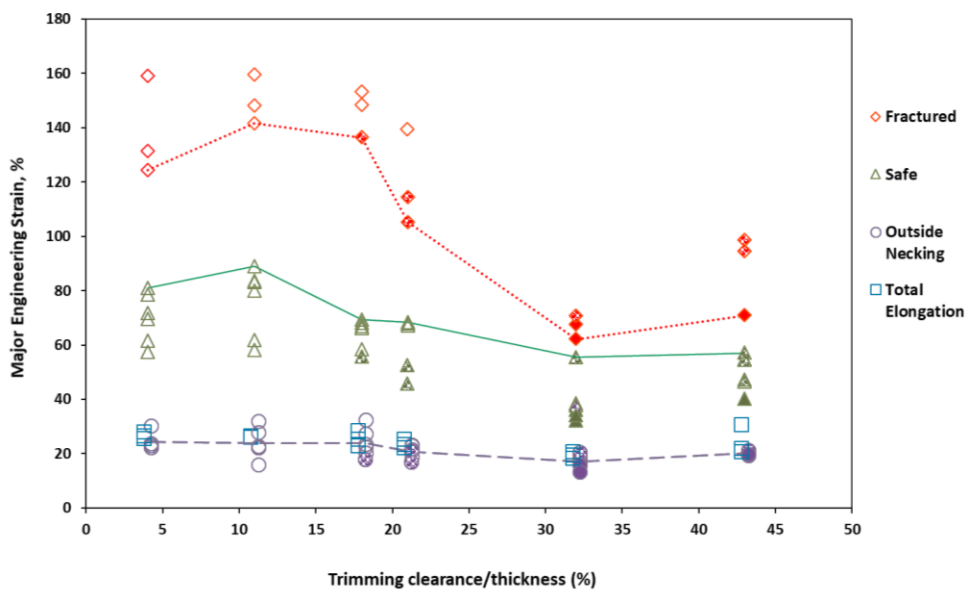

Figure 5.7. Results of the sheared edge stretchability of HSLA340 sheet material as a function of cutting clearance, using square grid analysis.

5.1.2. Influence of Trimming Clearance on Fracture Mode

One interesting observation in the tensile tests of trimmed specimens is their fracture mode. Golovashchenko [73] initially introduced three different failure mode types, which are depicted in Figure 5.8 and include:

- Mode 1 was typically characterized by a localized necking happening simultaneously through the specimen width and was commonly observed while strain localization occurred at failure. Mode 1 was a high elongation fracture mode.

- Mode 2 was a horizontally propagated cracking through the specimen section without having a localized neck. This failure is usually initiated at the sheared edge, resulting in a substantially lower elongation-to-fracture than in mode 1.
- Mode 2+1 was simply a combination of modes 2 and 1. The initial crack started perpendicular to the tensile direction in mode 2, and then the localized necking and the diagonal cracking occurred, similar to mode 1. This failure featured intermediate stretchability.

In all stretchability graphs of Figure 5.3 to Figure 5.7, the unfilled, partially filled, and solid-filled data points represented specimens that failed in mode 1, mode 2+1, and mode 2, respectively.

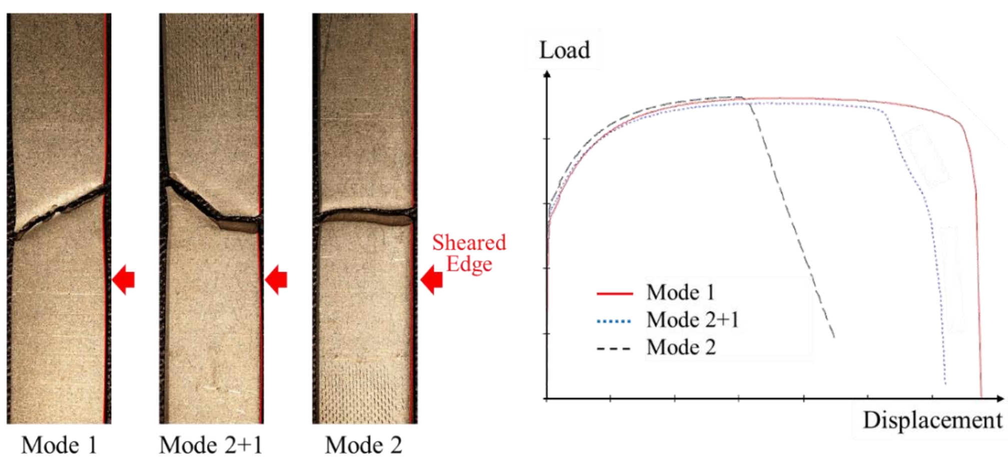

Figure 5.8. Failure modes of tensile test specimens.

As shown in Figure 5.3 for DP980-1 sheet material, the predominant failure mode in most cases is mode 1, in which the sheared edge has almost no influence on the fracture that occurred. However, a different trend was observed for DP980-2, as shown in Figure 5.4, i.e., with increasing clearance, the failure mode changes from mode 1 to modes 2+1 and 2. Lower fracture strains were observed for larger clearances, and failure mode 2 is the dominant one. As clearance increases, the burr and stress concentration sites on the sheared edge grow. For larger clearances, fracture always initiates from the sheared edge and leads to failure modes 2 and 2+1.

As demonstrated in Figure 5.5 to Figure 5.7, a similar trend was observed in the IF, BH, and HSLA graphs. With increasing the clearance, the failure mode changes from mode 1 to modes 2 and 2+1. Notably, HSLA exhibits high sensitivity to variations in cutting clearance, with failures predominantly occurring at mode 2 for clearances exceeding 32%.

Generally, when observing mode 1, the condition of the trimming process does not affect the material's formability, at least within the tested deformation mode. Therefore, it is recommended to avoid conditions that lead to failure modes 2 and 2+1 at sheared edge endings rather than failure mode 1.

5.1.3. Load-Displacement during the Stretchability Test of DP980

Load versus displacement data were captured during the tensile testing of trimmed specimens. The distance between grips was set at 90 mm for 127 mm-long sheared strips. In Figure 5.9 to Figure 5.14, load-displacement curves for DP980-1 are plotted for different cutting clearances, along with pictures of corresponding specimens. Notably, only specimens fractured within the extensometer are shown and plotted.

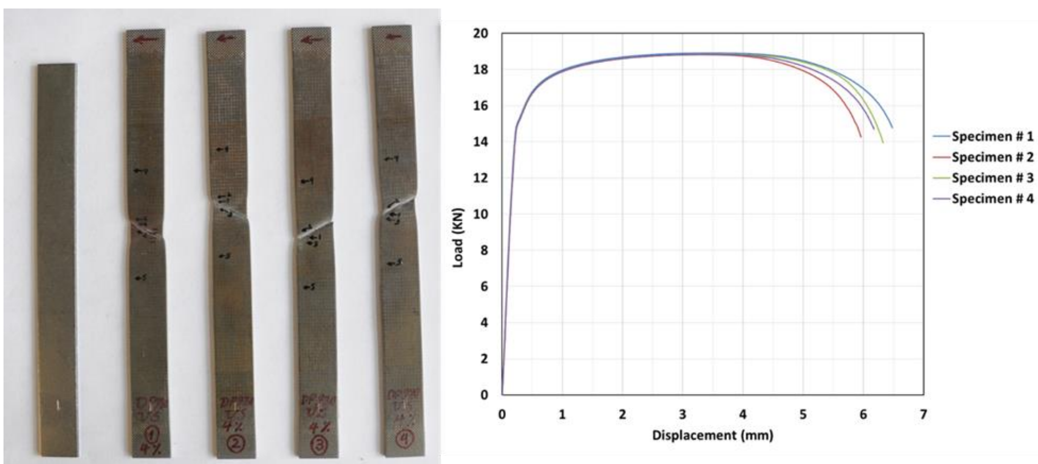

Figure 5.9. Load-displacement curve during tensile testing of DP980-1 specimens trimmed at 4%t clearance.

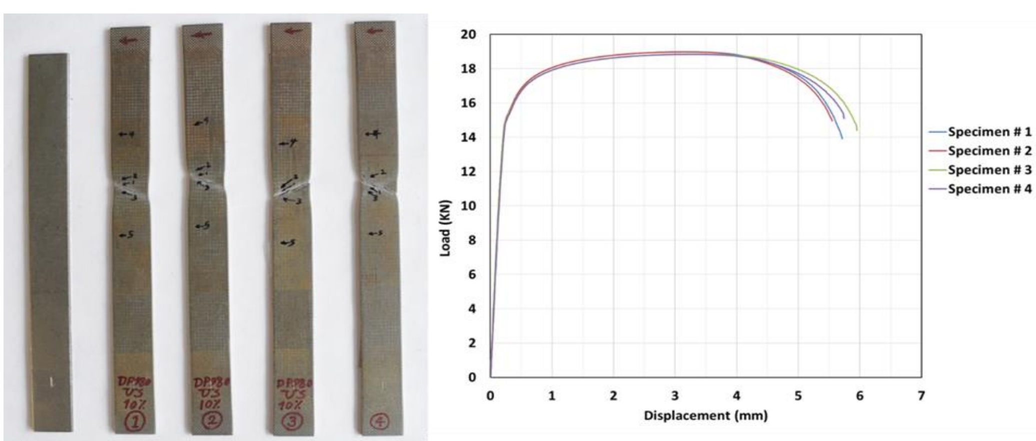

Figure 5.10. Load-displacement curve during tensile testing of DP980-1 specimens trimmed at 10%t clearance.

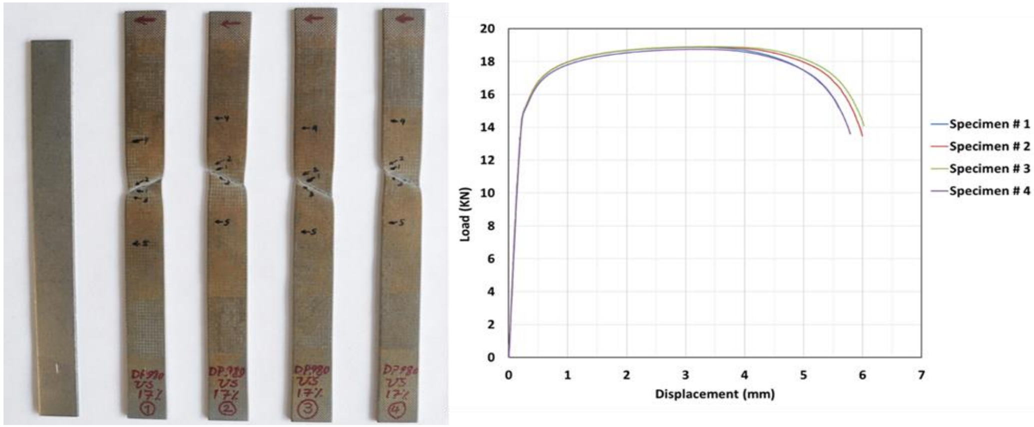

Figure 5.11. Load-displacement curve during tensile testing of DP980-1 specimens trimmed at 17%t clearance.

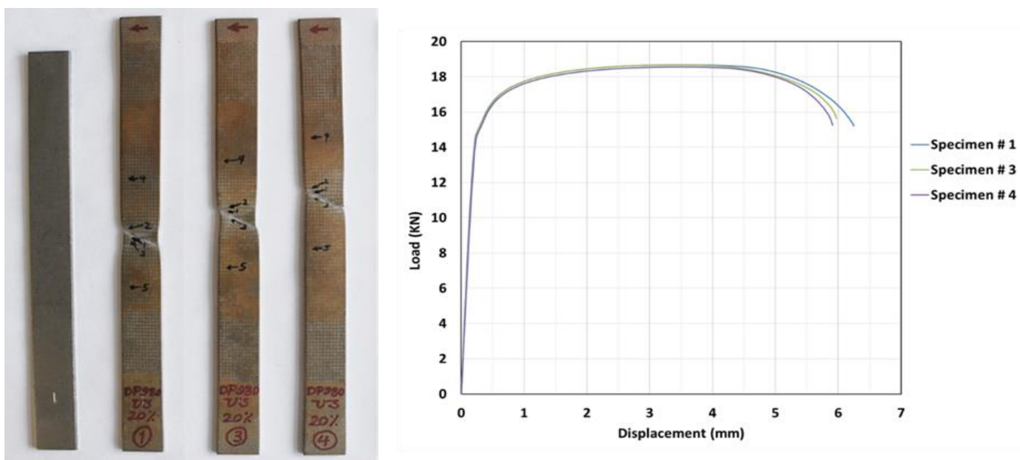

Figure 5.12. Load-displacement curve during tensile testing of DP980-1 specimens trimmed at 20%t clearance.

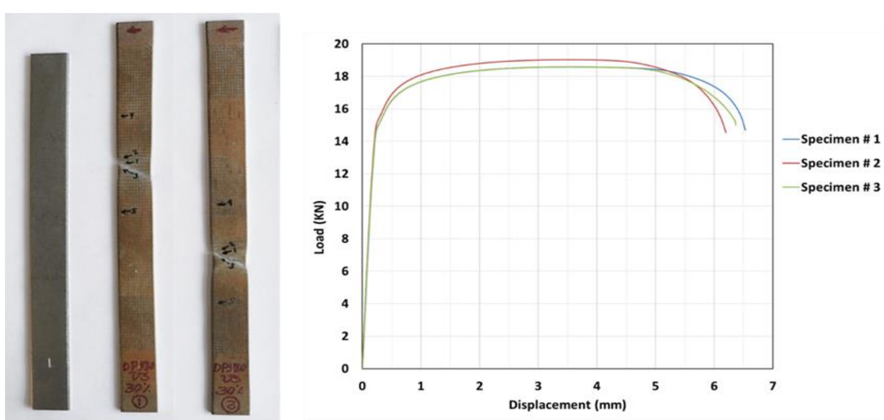

Figure 5.13. Load-displacement curve during tensile testing of DP980-1 specimens trimmed at 30%t clearance.

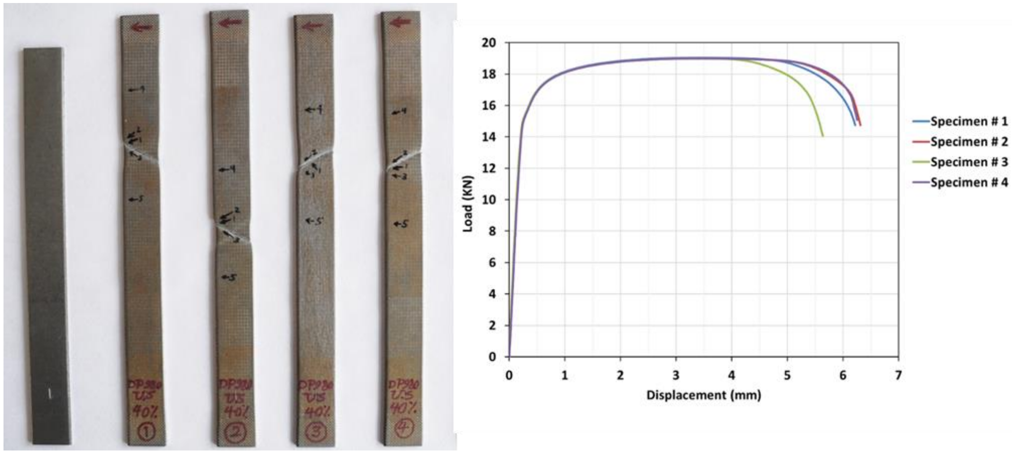

Figure 5.14. Load-displacement curve during tensile testing of DP980-1 specimens trimmed at 40%t clearance.

The fracture line in Figure 5.9 to Figure 5.14, for DP980-1, is always oblique to the edge (failure mode 1) for all ranges of clearances. As shown in the picture of the specimens, localized necking occurs across the width of the specimens, even with very large clearances.

In Figure 5.15 to Figure 5.20, load-displacement curves for DP980-2 are plotted for different clearances, along with pictures of corresponding specimens.

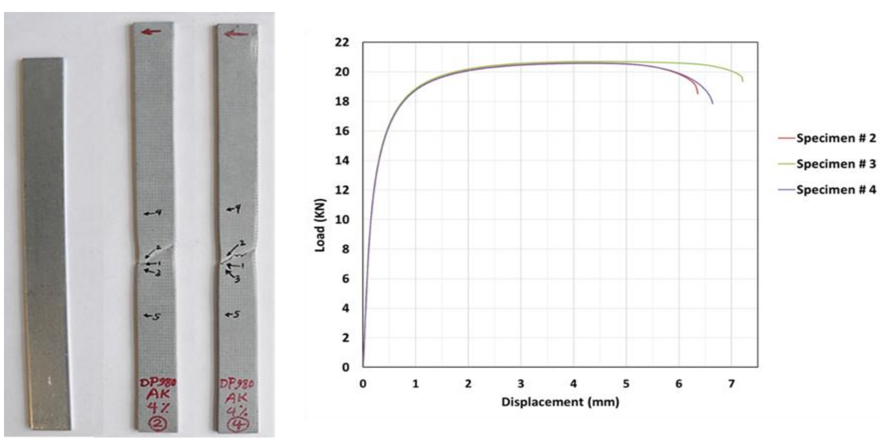

Figure 5.15. Load-displacement curve during tensile testing of DP980-2 specimens trimmed at 4%t clearance.

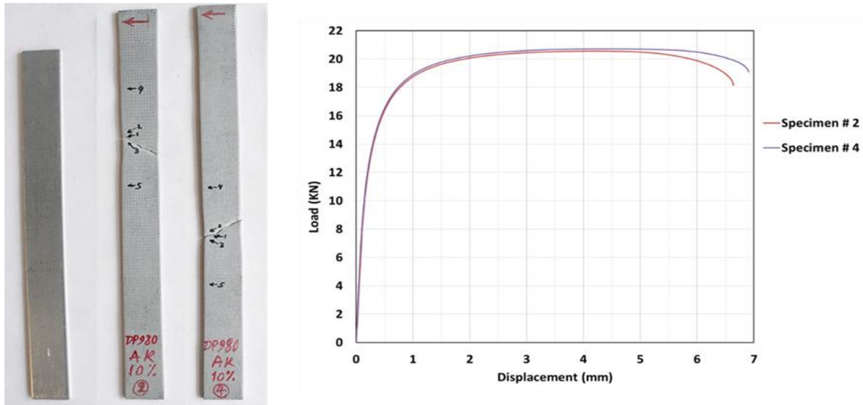

Figure 5.16. Load-displacement curve during tensile testing of DP980-2 specimens trimmed at 10%t clearance.

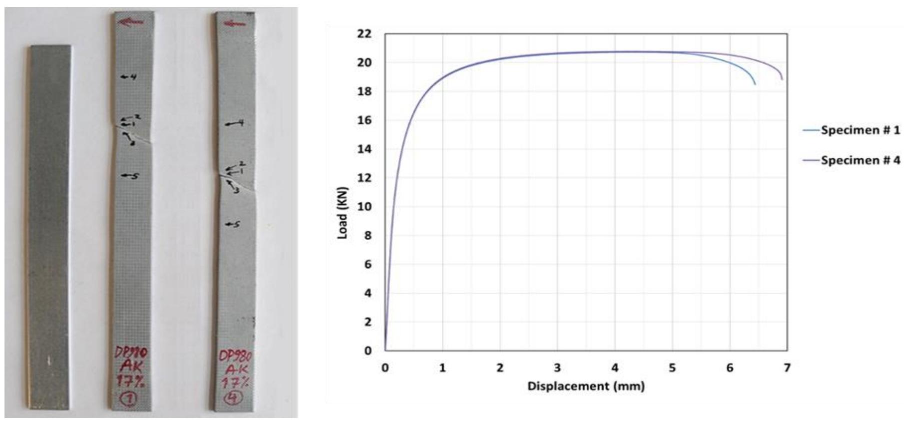

Figure 5.17. Load-displacement curve during tensile testing of DP980-2 specimens trimmed at 17%t clearance.

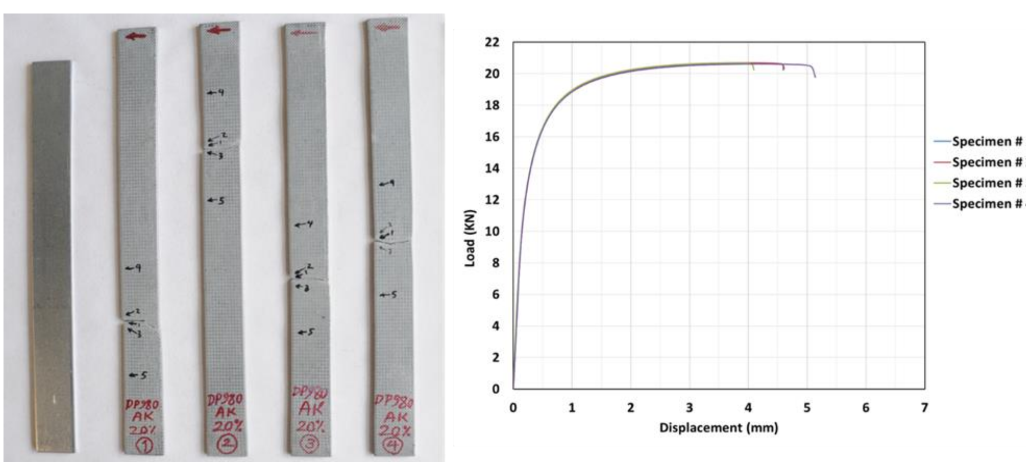

Figure 5.18. Load-displacement curve during tensile testing of DP980-2 specimens trimmed at 20%t clearance.

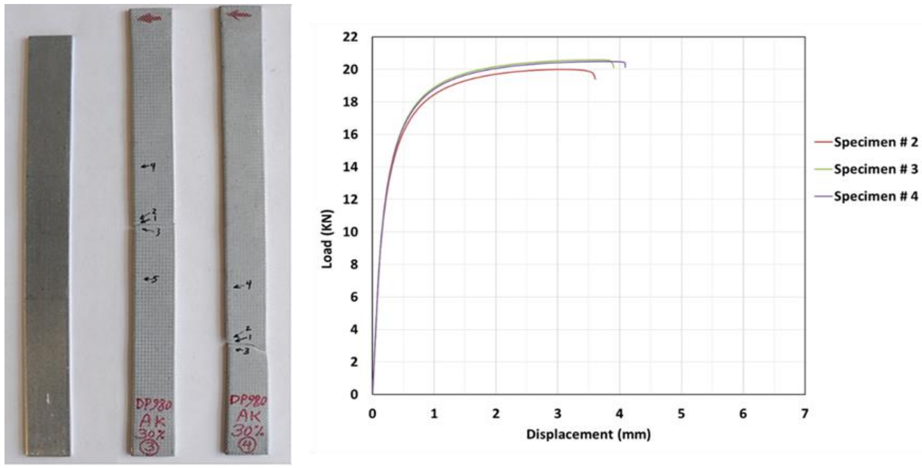

Figure 5.19. Load-displacement curve during tensile testing of DP980-2 specimens trimmed at 30%t clearance.

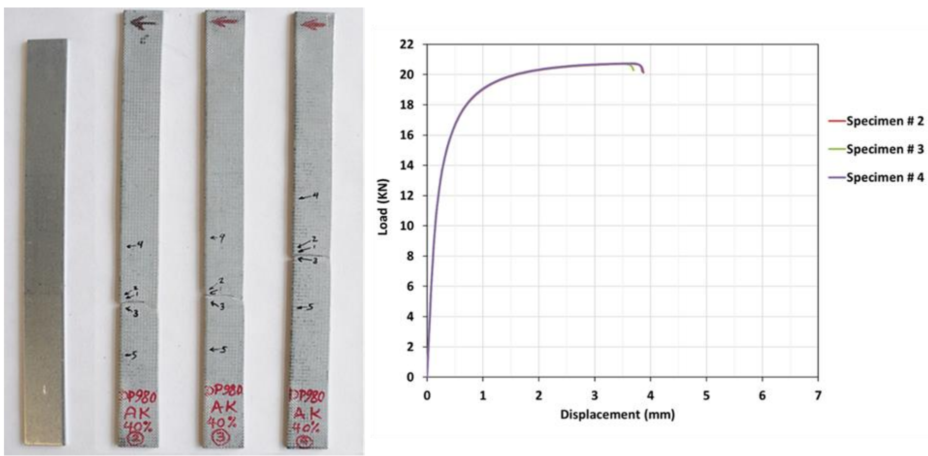

Figure 5.20. Load-displacement curve during tensile testing of DP980-2 specimens trimmed at 40%t clearance.

Looking into the images of DP980-2 specimens in Figure 5.15 to Figure 5.20, with increasing the clearance, the failure mode changes from the oblique fracture line (mode 1) to the horizontal direction (mode 2). In this case, as the clearance increases, burr and imperfections on the sheared edge increase; therefore, for the larger clearances on DP980-2, fracture always initiates from the sheared edge, leading to crack propagation perpendicular to the tensile direction and results in lower total elongation and lower fracture strains. Substantial changes in the displacement at fracture in the graphs of 4% clearance to the graphs of 40% clearance are observed due to changes in failure mode.

In conclusion, unlike DP980-1 steel, DP980-2 is very sensitive to the sheared edge and the trimming clearance.

5.1.4. Fracture Observation of Trimmed DP980 during Tensile Testing

The sheared surface of trimmed samples during the tensile test was tracked using a Canon Rebel T6i DSLR camera equipped with an EF-S 60 mm 1:2.8 macro lens, as shown in Figure 5.21.

Figure 5.21. Tracking the fracture progression using a Canon T6i camera.

The mechanism of fracture of the sheared edge of DP980-1 during the tensile test is illustrated in Figure 5.22. In this figure, in addition to as-sheared images of specimens, the sheared surface corresponding to the moments when the first visible cracks are initiated and when the predominant cracks are propagating, as well as the moment before the final separation, are shown sequentially.

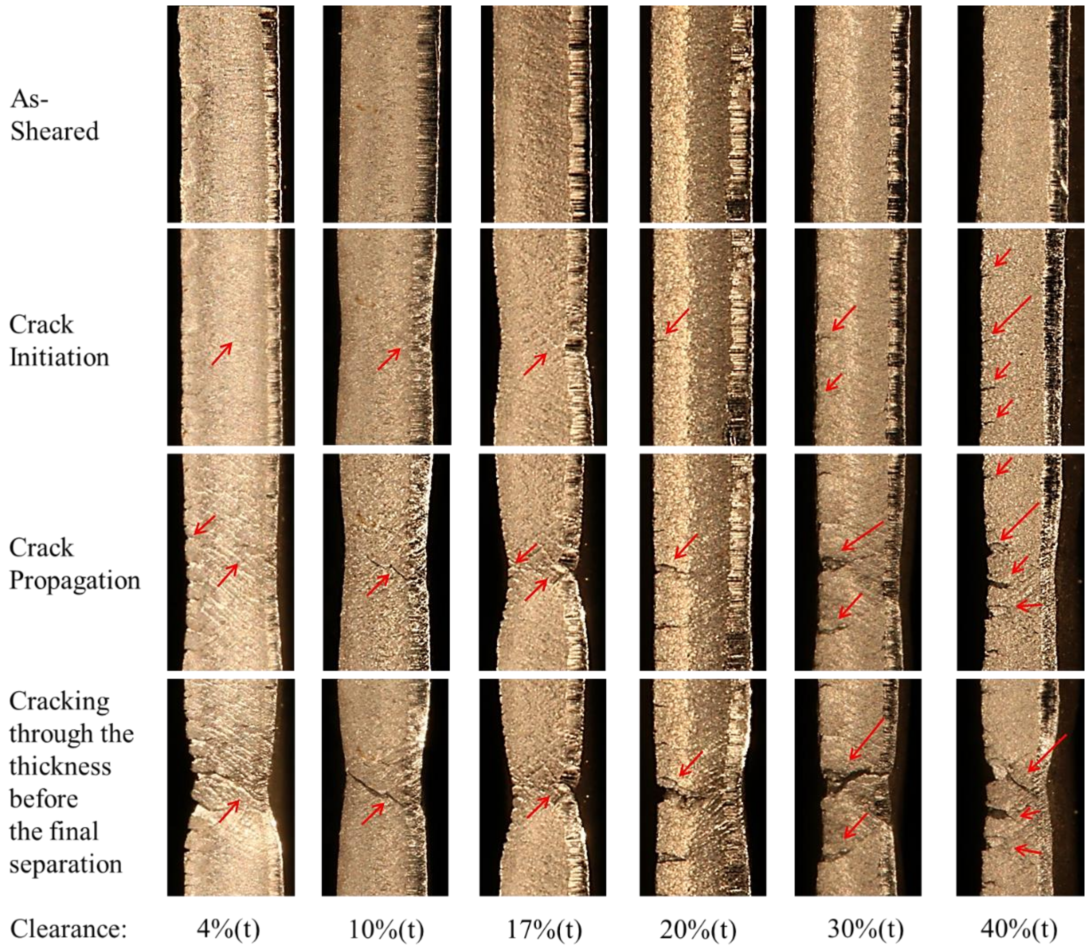

Figure 5.22. The sheared surface of DP980-1, trimmed with different clearances during the tensile test.

For DP980-1 steel, sheared surface images of clearances of 4%, 10%, and 17% show no imperfection and no visible burr at the sheared edge. In these specimens, cracks initiated from the multiple cross-hatched lines throughout the fracture surface and the bottom of the burnish zone. Then, these cracks propagated toward the burr side and, in the cases of 4% and 17%, met with cracks initiated from the burr side and caused the total separation. In the 10% specimen, a crack initiated from the bottom of the burnish zone and propagated through the thickness, causing the failure. Wu and Bahmanpour [156] demonstrated through SEM observation that numerous microcracks exist within the burnish zone of sheared DP980, where the blank material undergoes significant plastic deformation. These microcracks can grow and spread during stretching, such as in a tension test.

For other specimens sheared with 20% to 40% clearances, the crack initiation site moves to the burr side. Even though either the burr is removed or a very tiny burr is formed on the sheared edge of these specimens, the location of the crack initiation is very repeatable. In other words, at clearances higher than 20%, when the sheared edge is more heavily deformed with some small burrs, the crack grows easier from the burr tip and propagates faster. Also, more cracks initiated and propagated simultaneously, with less localized necking. Removing the burr at clearances 30% and 40% creates a dent elongated throughout the specimen length, which acts as an imperfection and nucleation site for cracking. Therefore, the sheared edge stretchability is typically smaller for larger cutting clearances.

Another quantitative parameter that can be characterized in the tensile test is the reduction of area. The final thickness after fracture was measured from Figure 5.22 at the narrowest section of each specimen. The initial thickness was determined at four to five locations along the gauge length using the captured images, and the average was used for calculations. Since the rollover region created during trimming is not visible in the tensile test images, a geometric correction was applied to account for its contribution to the effective cross-sectional area. The initial and final widths were also measured with a digital micrometer. Using the corrected initial (A_0) and final (A_f) cross-sectional areas, the reduction of area (RA) was calculated according to Equation (5.1).

$$RA = \frac{A_0 - A_f}{A_0} \times 100 \tag{5.1}$$

The percentage reduction in area at the end of the tensile tests for different clearances of DP980-1 is shown in the table. The specimens sheared with 17% clearance have the most significant reduction of area and, accordingly, the longest localized necking during the tensile test compared to the tensile tests of the samples sheared with other cutting clearances. The trend of changes in the reduction of area in the tensile test specimens is well-matched with the stretchability results.

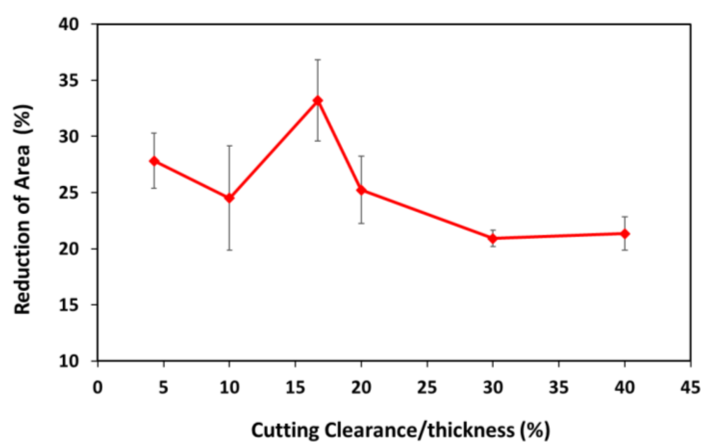

Figure 5.23. Reduction of the area after the tensile test for different cutting clearances for DP980-1.

Similarly, mechanisms of fracture initiation and progression for DP980-2 during the tensile test for different clearances are illustrated in Figure 5.24. The tensile testing of DP980-2 shows crack initiation from the burnish in the clearances of 4%t and crack initiation from both the bottom of the burnish (hatch lines) and the burr at clearances of 10 and 17%t. At larger clearances of 20 to 40%t, crack is always initiated from the burr side and propagates through the thickness. It results in substantially lower total elongation than that at small clearances. This phenomenon is observable by comparing total elongations in Figure 5.4. Additionally, the fracture mode transitions from Mode 1 to Mode 2, bypassing the localization zone.

In summary, for both trimmed DP980-1 and DP980-2, as the clearance increases, the crack initiation site moves from the burnish zone and the middle of the sample toward the sheared edge and burr tips zone.

5.1.5. Measurement of Local Strains at Fracture Initiation

In addition to the grid measurements, a manual pixilation method was used to measure the local strain at the fracture initiation [43]. The basics of this method were explained earlier in Section 1.3.2.2.

In this study, trimmed specimens were speckle-painted with very fine black dots (0.02-0.1 mm in length) and then subjected to tension. During the tensile test, specimens were imaged with a Nikon D5100 DSLR camera and a 90mm macro lens at one frame per second until fracture was detected. ImageJ [157] software was used to measure the distance between two known points before and after stretching and to calculate local strains.

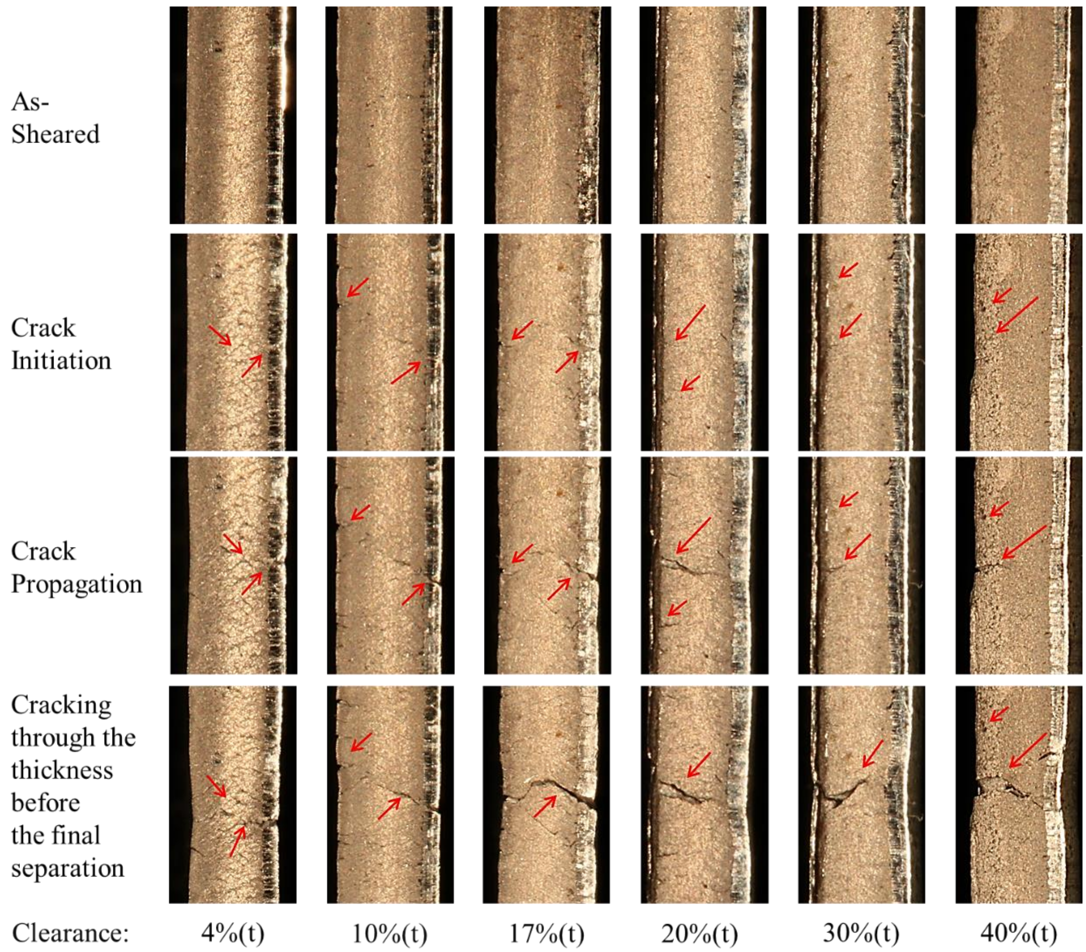

Figure 5.24. The sheared surface of DP980-2, trimmed with different clearances during the tensile test.

Two types of local strain were measured in this analysis: the fracture initiation strain and the through-thickness fracture strain. The latter was determined from the deformation of the fractured dots at the final stage of fracture. The fracture initiation strain was obtained from high-speed camera images of the same exact dots captured at the corresponding moment immediately before crack formation.

In Figure 5.25 and Figure 5.26, the fracture initiation and through-thickness fracture strains are plotted for DP980-1 and DP980-2, respectively.

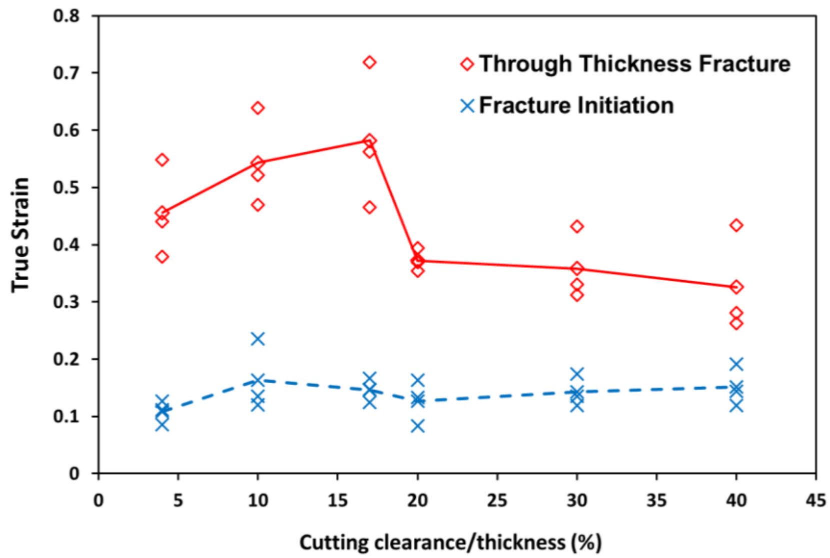

Figure 5.25. Local strains in tensile test versus the trimming clearance for DP980-1.

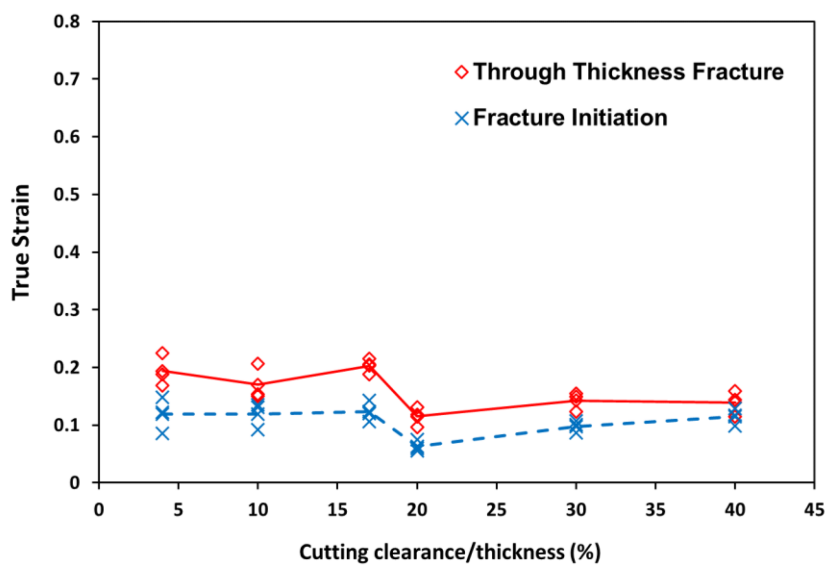

Figure 5.26. Local strains in tensile test versus the trimming clearance for DP980-2.

Comparing the graphs of Figure 5.25 and Figure 5.26, the fracture initiation strains are marginally higher for DP980-1 compared to DP980-2; however, the thickness-fracture strains in DP980-1 are significantly greater than those in DP980-2.

Also, the margin between the two strains for DP980-1 is substantially wider than that for DP980-2, indicating that DP980-1 material lasts much longer after the first crack is initiated.

When comparing the dot measurements of through-thickness fracture strain in Figure 5.25 and Figure 5.26 with the corresponding fractured strains from grid measurements plotted in Figure 5.3 and Figure 5.4, it is evident that the grid-derived strain values are consistently higher than those obtained using the dot method. This difference mainly results from the spatial resolution and measurement scale of each technique. In the dot method, the local strain is calculated over a very small, localized region, typically between two adjacent dots, providing a more precise representation of the local deformation near the fracture surface. In contrast, the grid method measures strain over a larger gauge length—in this case, grids initially spaced at 1 mm—averaging deformation across a broader area. Consequently, localized strain peaks immediately adjacent to the fracture zone are partially smoothed out, leading to higher apparent fracture strains when measured on the grid scale.

Furthermore, the accuracy of the grid analysis can be influenced by several practical factors. Variations in grid printing quality, uneven lighting, or distortion of grid lines, along with the manual grid selection process, may introduce uncertainties into measurement results. These combined effects lead to systematically higher strain values in grid-based measurements than in more localized, precise dot-based measurements.

5.2. Sheared Edge Stretchability by Side Bending

In-plane side bending of trimmed specimens is a unique method to simulate edge stretching in some stamping operations [38]. The basics of this method were explained earlier in Section 1.3.1.2, and its schematic representation is shown in Figure 1.21. In this study, as demonstrated in Figure 5.27, the specimen with the trimmed edge on the outer side was bent about the rolling pin until the first crack was detected on the edge. Two Nikon DSLR cameras captured the fracture event. After reviewing the captured images, local strains were measured using the pixelation method.

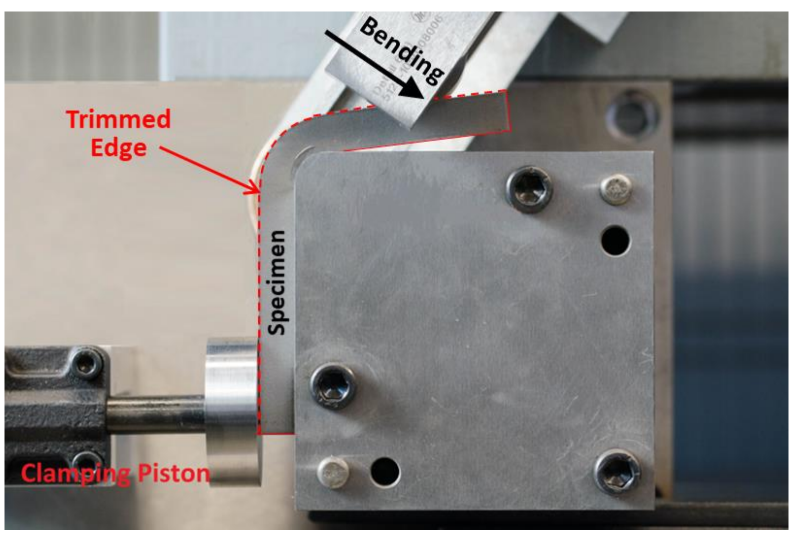

Figure 5.27. Top view of experimental apparatus for side-bending test.

Figure 5.28 shows fracture development during the side-bending test for the DP980-1 sample trimmed at 4% clearance. The top face and sheared edge view images are shown in the left and right columns, respectively. Fracture initiation and through-thickness cracking are detected from edge-view images. Similar to the local strain measurement in tensile testing, the through-thickness fracture strain was defined as the through-thickness crack detected on the edge side. The fracture initiation strain was defined as the strain at which hairline cracks were first detected on the sheared edge.

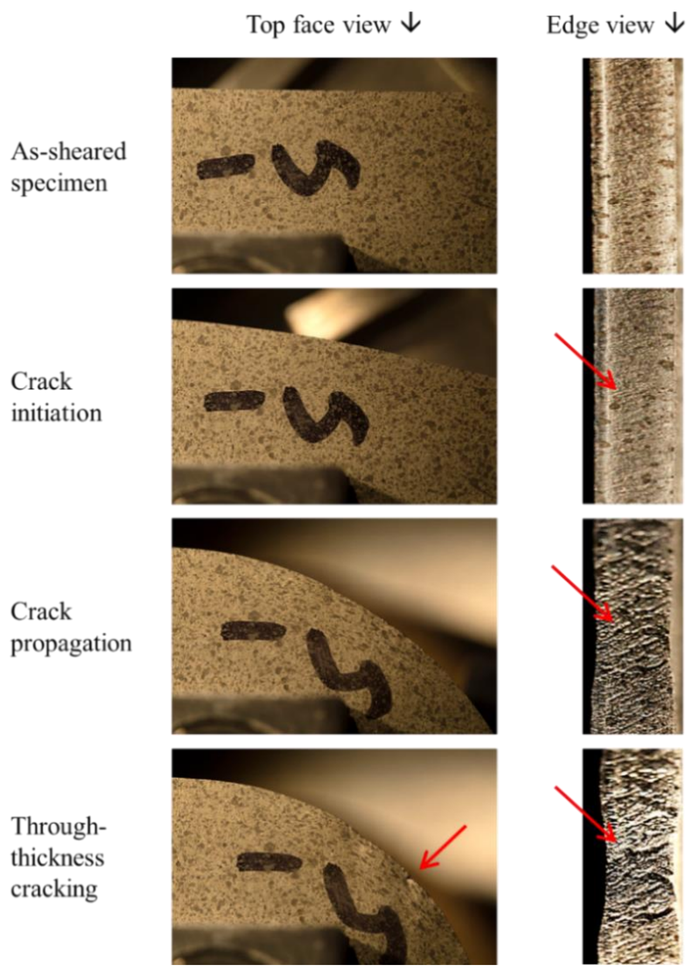

Figure 5.28. Fracture development in the side-bending test for DP980-1 trimmed at 4% clearance.

In the case of 4% clearance, as shown in Figure 5.28, fractures initiate from cross-hatched lines throughout the fracture surface and propagate through the thickness. Figure 5.28 shows how fracture events are captured in the side-bending of the DP980-1 specimen trimmed at 4% clearance. Due to similarities, images of other cases are not presented in this dissertation.

In Figure 5.29 and Figure 5.30, the results of the side-bending test as local strain measures in the close vicinity to the crack on the sheared edge at the moment of fracture initiation, as well as through-thickness fracture strains, are plotted for DP980-1 and DP980-2, respectively. Dots were tracked before and after deformation using the coordinate system, and the changes in their diameters were measured to calculate the strain.

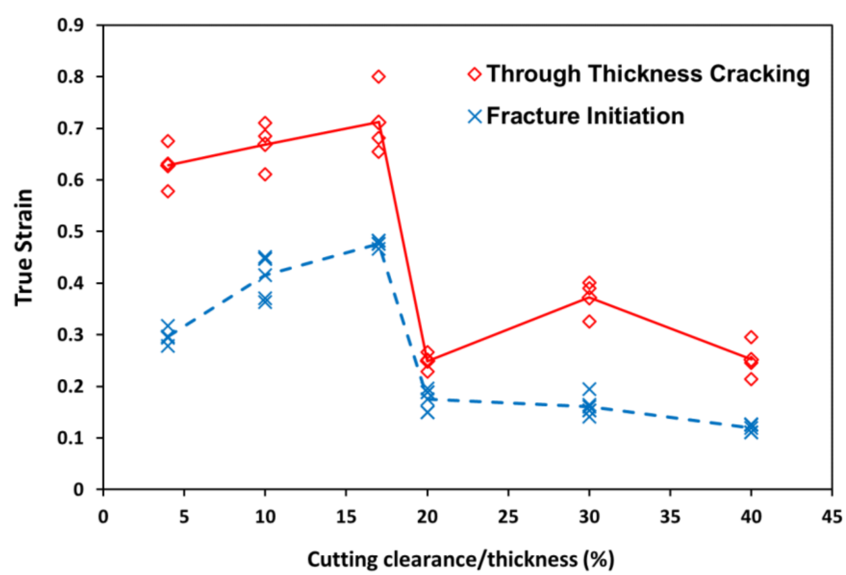

Figure 5.29. Local strains in side-bending versus the trimming clearance for DP980-1.

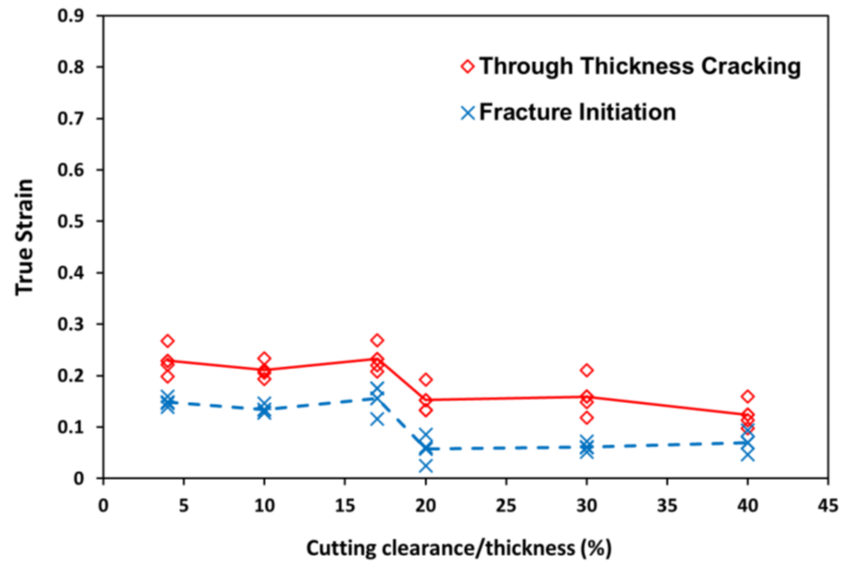

Figure 5.30. Local strains in side-bending versus the trimming clearance for DP980-2.

DP980-1's through-thickness strain follows a similar pattern as in the tensile test, but shows higher values because of reduced necking in the side bending. The fracture initiation strain is higher than the tensile test values, since the n-value limits tensile test results.

For DP980-1, 17% clearance shows the highest strain levels, indicating the best edge stretchability. In this case, the crack initiates from the bottom of the burnish area and propagates through the thickness. As the clearance increases, the stretchability limit decreases. DP980-2 shows substantially lower initiation and through-thickness strains than DP980-1. Specimens trimmed at clearances greater than 17% exhibit very low edge-stretching limits, as they crack early and fracture at low strains. The margin band between the two strain lines in DP980-1 is wider than in DP980-2, indicating that material 1 lasts longer than material 2 from fracture initiation through thickness cracking to total separation.

5.3. Sheared Edge Stretchability by Hole Expansion Test

A well-known hole expansion test was employed in this work to determine the edge stretchability limit of punched DP980 sheet material. The basics of this test were explained earlier in Section 1.3.1.3. This test was done based on the ISO 16630 Standard [40]. A 102 mm × 102 mm punched blank was fixed between the die and the blank holder, with the burr side facing up and not contacting the punch surface. The hole edge expansion was performed using a Hille-Wallace machine with a 60 ° conical punch, a 52.70 mm-diameter die, and a 51.23 mm-diameter blank holder, with a hold-down pressure of 6.89 MPa.

Hole flanging was continued until the first crack appeared through the entire thickness of the specimen. Knowing the initial and the final inner diameters (Figure 5.31) and using Equation (1.2), the hole expansion ratio (HER) was calculated as the edge formability measure.

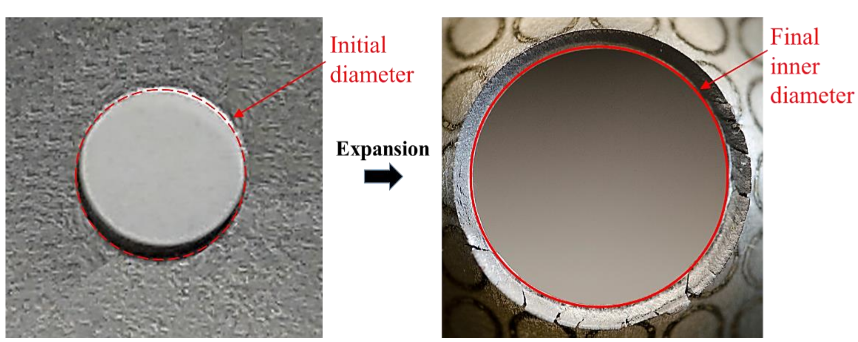

Figure 5.31. Punched hole before and after expansion.

Figure 5.32 and Figure 5.33 show the hole expansion ratio for DP980-1 and DP980-2, respectively. To gain a better understanding, the burr height profile is plotted alongside the hole expansion ratio, using the right vertical axis. The graphs show an optimum clearance where hole expansion ratios are maximum. The punched edge quality affects the hole expansion ratio, and the cutting clearance influences the edge quality.

Based on the graphs, there is an interesting correlation between the average burr profile and the hole expansion ratio. For DP980-1, at 10%, we have the highest HER; the burr height is almost zero. After this optimum clearance, as the burr grows, the hole expansion ratio declines to 34% clearance, then increases slightly to 46% clearance. The larger the clearance, the greater the bending, deformation, and material flow. Also, it creates substantially larger burrs, as shown in Figure 4.31 for DP980-1. However, the very large, thick burr for 46% clearance acts as a barrier, breaks, and deforms more than smaller burrs. Accordingly, the resulting HER for 46% clearance is relatively higher than that for 24% and 34% clearances.

Similar to the stretchability results from the tensile and side-bending tests, DP980-2 shows noticeably lower hole expansion ratios than DP980-1 across all clearances. The optimal clearance for punching 10 mm-diameter holes is about 10% for DP980-1 and 17% for DP980-2.

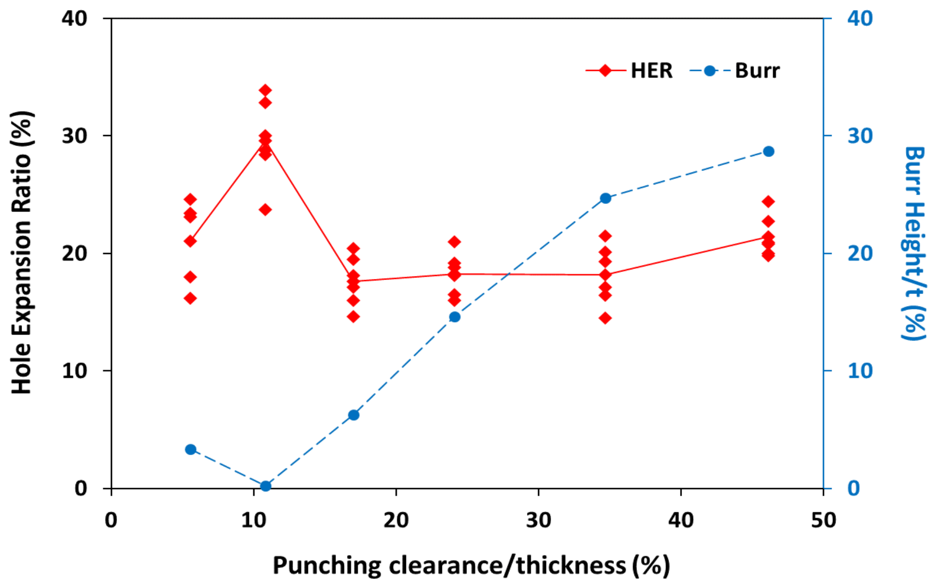

Figure 5.32. Hole expansion ratio for punched DP980-1.

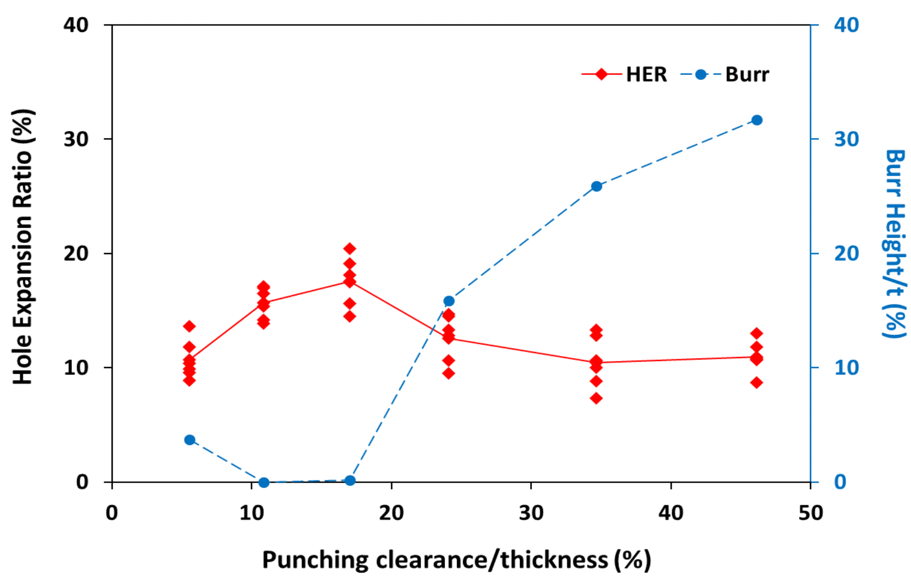

Figure 5.33. Hole expansion ratio for punched DP980-2.

5.3.1. Effect of Punch Misalignment and Punching Tolerances

For punched specimens, it is found that the burr height alters substantially along the edge of the punched hole (in the hoop direction), including some burr-free locations.

This is primarily due to variations in clearance from the intended design. Figure 5.34 and Figure 5.35 show the geographic burr height profile for eight locations along the punched hole, as well as the image of one corresponding specimen of DP980-1 for different clearances.

As shown in Figure 5.34, misalignment in 6% clearance is toward the bottom of the hole, resulting in all burrs being formed in the upper locations. 10% clearance, which is the optimum condition for DP980-1, was well aligned, and no visible burr was formed on any side of the punched hole. The 17% case was the exact opposite of the 6% case, since the punch moved toward the upper portion and left more clearance behind it in the bottom, leading to larger burrs at locations 3 to 7.

As shown in Figure 5.35, for 24% clearance, a significant misalignment was observed, with all burrs forming at locations 4 to 8. For very large clearances of 34% and 46%, there was a minor misalignment, or the misalignment effect was not significant relative to the clearance size, so large burrs formed everywhere along the punched hole. One reason for these misalignments and the uneven cutting clearance could be the use of multiple sets of punches and dies to achieve the desired clearance. Another reason might be the significantly higher cutting force required for UHSS DP980 compared to other materials, such as mild steels or aluminum alloys. Therefore, the tooling stiffness during punching and trimming of ultra-high-strength steels should be considered.

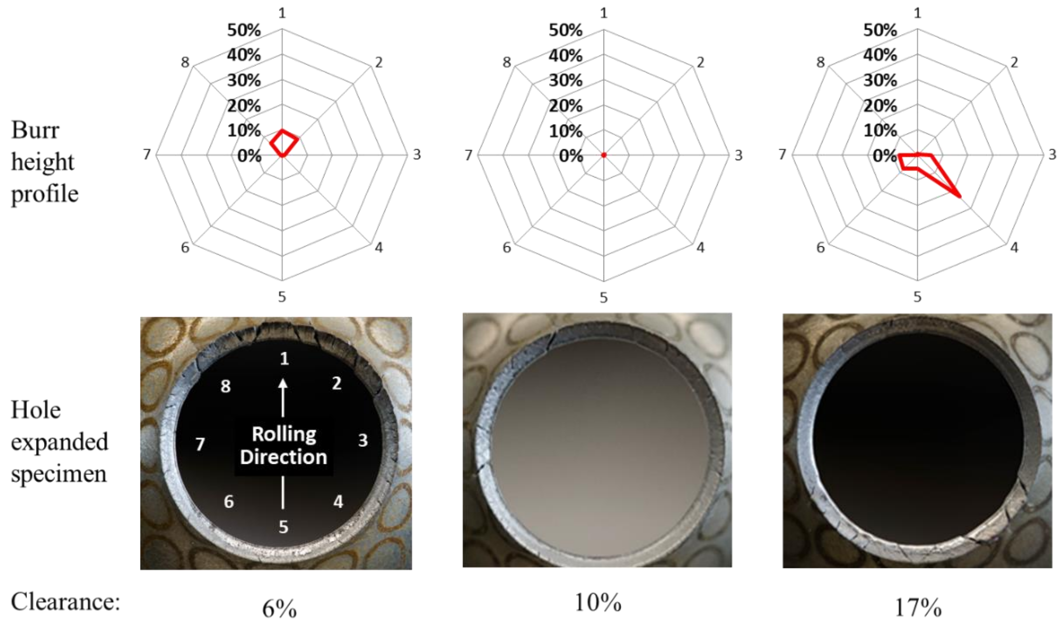

Figure 5.34. Burr height profile of punched DP980-1 specimens along the punched hole (on top) and image of the corresponding specimen after the hole expansion test (on bottom) for clearances 6%, 10% and 17% of sheet thickness.

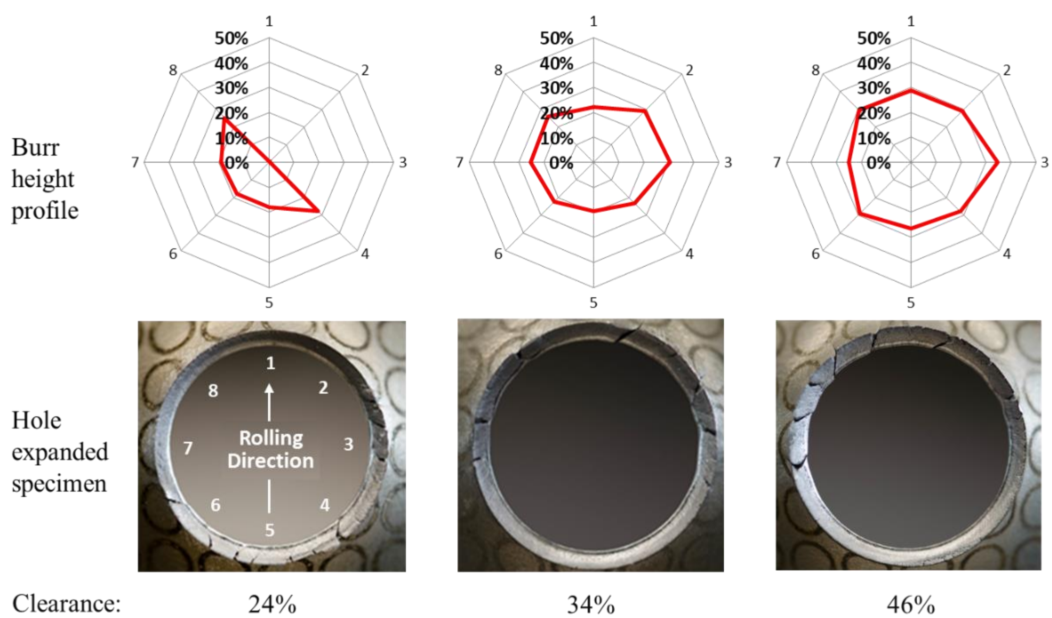

Figure 5.35. Burr height profile of punched DP980-1 specimens along the punched hole (on top) and image of the corresponding specimen after the hole expansion test (on bottom) for clearances 24%, 34%, and 46% of sheet thickness.

An exciting observation from the burr profile and images of hole-expanded specimens is the location of crack formation along the hole during the hole expansion test. For cases where the effect of clearance variation due to punch misalignment is significant —i.e., clearances of 6%, 17%, and 24% —cracks form precisely at the burr locations. This correlation is always expected since burrs, and especially inconsistent burrs, are imperfections and suitable for crack nucleation.

Similarly, Figure 5.36 and Figure 5.37 are dedicated to the DP980-2 material and present the geographic burr height profile at eight locations along the punched hole, as well as an image of one corresponding specimen for different clearances.

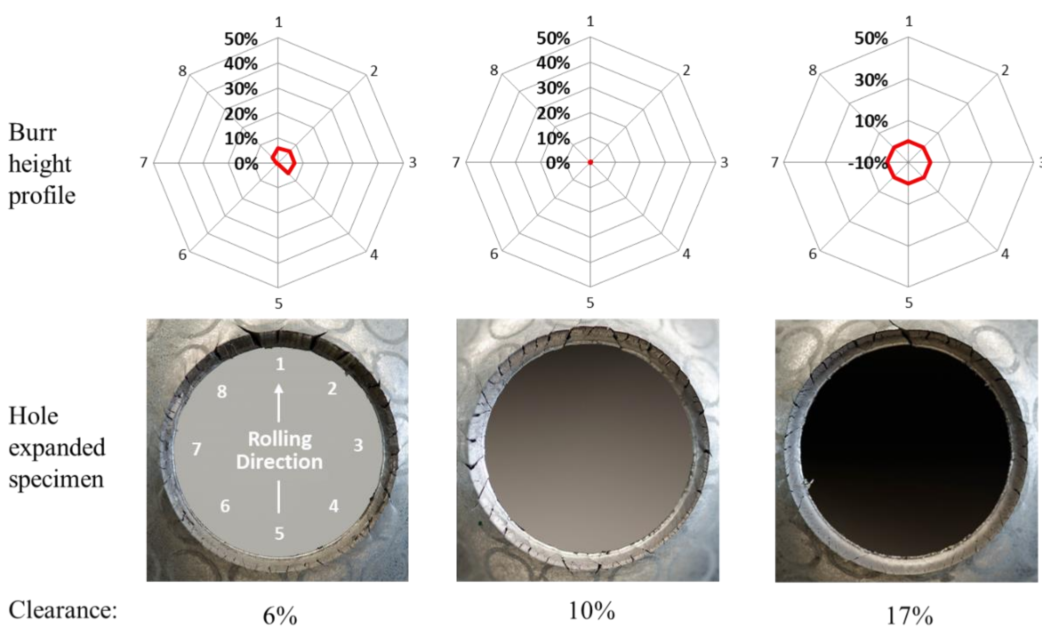

Figure 5.36. Burr height profile of punched DP980-2 specimens along the punched hole (on top) and image of the corresponding specimen after the hole expansion test (on bottom) for clearances 6%, 10% and 17% of sheet thickness.

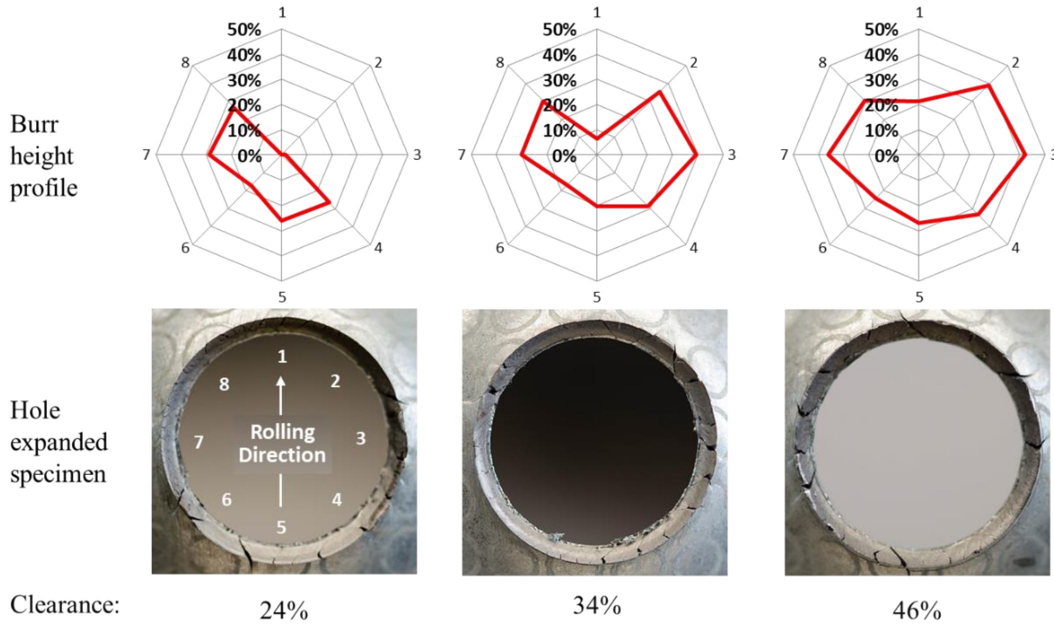

Figure 5.37. Burr height profile of punched DP980-2 specimens along the punched hole (on top) and image of the corresponding specimen after the hole expansion test (on bottom) for clearances 24%, 34% and 46% of sheet thickness.

The punch misalignment and preferential burr formation along the punched hole are observable in most clearances, particularly at smaller clearances. In a 10% clearance case, no burr forms; the edge quality and stretchability are highest, and cracks form uniformly around the punched hole.

5.4. Summary

In this chapter, the formability of two DP980 sheets, in terms of sheared edge, was examined through tensile, side-bending, and hole expansion tests. Figure 5.38 and Figure 5.39 show a comparison of these three stretchability tests for DP980-1 and DP980-2, respectively.

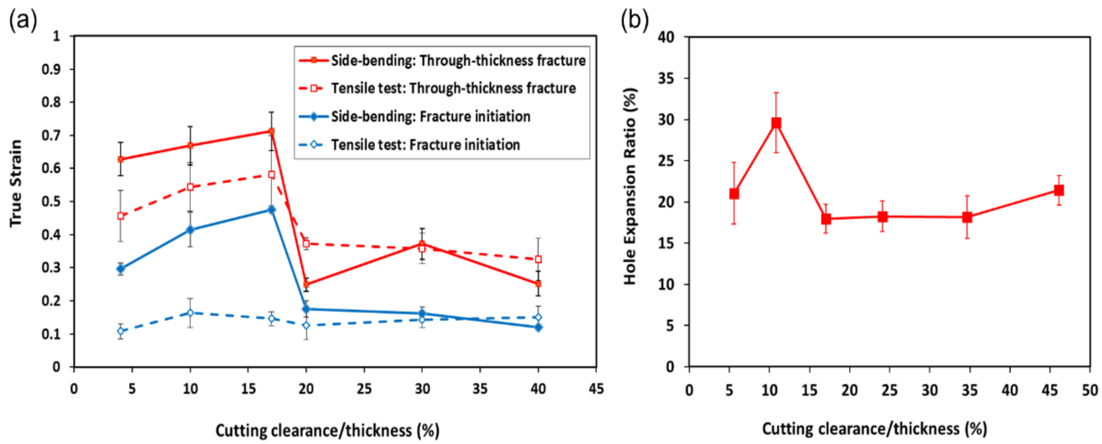

Figure 5.38. Comparison of stretchability results for DP980-1 by (a) tension and side-bending tests and (b) hole expansion test.

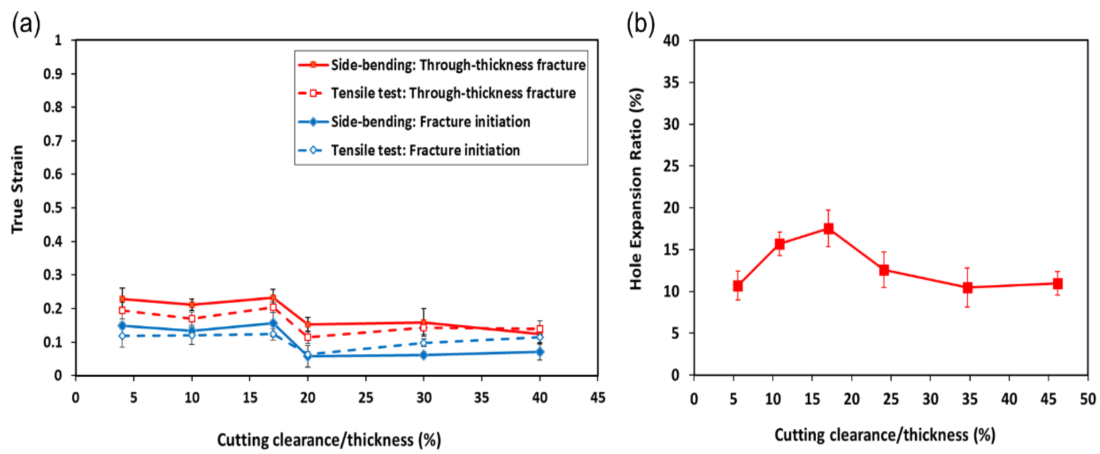

Figure 5.39. Comparison of stretchability results for DP980-2 by (a) tension and side-bending tests and (b) hole expansion test

Both the side-bending and tensile tests showed a similar range of acceptable trimming clearances when considering sheared edge stretchability. However, the local strain levels measured during side-bending were higher than those obtained from the corresponding tensile tests. This difference can be explained by the different deformation mechanisms involved in the two tests. In the tensile test, diffuse necking develops before localized fracture, which limits the maximum local strain in the gauge section. Conversely, side-bending applies a more uniform bending-induced strain along the edge, without diffuse necking, allowing the material to withstand higher local deformation before fracture begins.

Furthermore, in tensile testing, the fracture initiation strain is inherently limited by the material's strain-hardening exponent (n-value), which determines the maximum uniform elongation. Once necking begins, strain localization accelerates, and the overall deformation capacity decreases. The side-bending test, however, is not restricted by this limit, making it a more suitable and reliable method for evaluating materials whose sheared edge stretchability exceeds their uniform elongation. In such cases, side-bending provides a better reflection of the true edge formability potential of advanced high-strength steels like DP980.

In all tests, an optimal clearance was found that offered the greatest edge stretchability. Beyond this point, increasing the clearance led to a decline in stretchability. Based on tension and side-bending tests, the ideal clearance was 17% for DP980-1. Conversely, the hole expansion test yielded the best results with a 10% clearance. For DP980-2, the best outcomes across all three tests occurred at 17% clearance.

Tracking the fracture progression during stretching of trimmed DP980 specimens revealed that as clearance increased, the crack initiation site shifted from the middle of the sheared surface and the bottom of the burnish zone toward the edge and burr tips, resulting in lower total elongations and decreased stretchability measures.

Although the DP980-1 and DP980-2 sheet materials exhibited similar strength levels and overall mechanical behavior in the tensile test, they showed notably different results in trimmed-edge stretchability and hole expansion ratio of punched holes. DP980-2 experienced significantly lower strain levels during stretching and was more sensitive to changes in cutting clearance than DP980-1. DP980-1 failed in diffuse or localized necking mode, whereas DP980-2 failed before reaching the necking limit. Additionally, DP980-1 lasted considerably longer than DP980-2 after the first crack appeared, continuing until the through-thickness fracture occurred.

In summary, tensile, side-bending, and hole expansion tests provide crucial information for designing stamping dies. The stretchability observed in tensile and side-bending tests is particularly relevant for trimming along the edge of the blank. In contrast, data from the hole expansion test can be used in die design for punching holes.

CHAPTER SIX

FINITE ELEMENT SIMULATION OF THE TRIMMING PROCESS

The objective of this chapter was to develop a finite element model of the trimming process for UHSS DP980.

A commercial finite element software package, ABAQUS/Explicit [158], was used as the primary tool for numerical analysis. Two other software programs, including SIMUFACT [159] and QFORM [160], were also used in some parts of this study.

Because the trimming processes could be assumed to be plane-strain, a two-dimensional (2D) plane-strain model was employed in the study [95]–[97].

This study considered two different simulation cases. The first case aimed to evaluate the strain distribution, damage accumulation, and crack development path, especially at large clearances. In this case, the trimming tools and binder were modeled as rigid bodies, while the sheet material was modeled as deformable. The second case focused on determining the load and stress levels on the tools, followed by a fatigue analysis of the tools. Here, both the sheet metal blank and the trimming tools are modeled as deformable bodies.

6.1. Finite Element Model

The model characteristics were as follows:

6.1.1. Boundary Conditions

Figure 6.1 shows the finite element model and boundary conditions in the Abaqus model. The binder is analytically rigid, and its movement is fixed with the following parameters: U1 = 0, U2 = 0, and U3 = 0. The lower trimming tool is also fixed at the lower and left edges, with U1 = U2 = U3 = UR1 = UR2 = UR3 = 0. The upper trimming tool is moving downward with U1=0, U2=–0.3 mm, and UR3=0. Where, U1, U2, and U3 are displacements in x, y, and z directions, and UR1, UR2, and UR3 are rotations against x, y, and z axes, respectively. An upper tool velocity of 1 m/s was prescribed through a displacement boundary condition. The total simulation time was approximately 0.003 s, corresponding to the punch stroke. Also, no artificial mass scaling was applied.

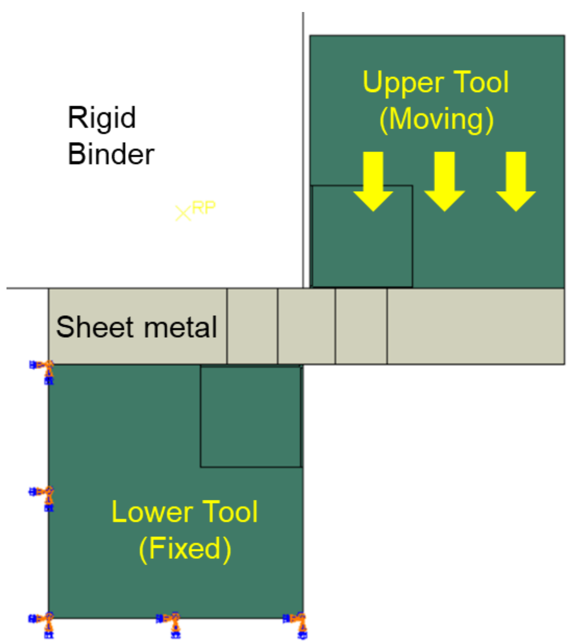

Figure 6.1. Boundary condition for Abaqus modeling of the trimming operation.

6.1.2. Contact Properties and Friction

For the rigid tool case, the selected friction formulation between surfaces is a penalty-type Coulomb friction law. The trimming process involves high contact pressure, localized deformation, and, in our case, no lubrication, which supports a relatively low but non-negligible coefficient of friction (COF).

High-strength dual-phase DP980 steel resists galling more effectively than soft steels, maintaining a moderate coefficient of friction. Daodon & Saetang [161] measured the friction between D2 tool steel and JIS SPFC 980Y (similar to DP980 in terms of strength level) sheets using a pin-on-disc setup. They found that the average coefficient of friction for the untextured surface was 0.117, while a D2 tool with a laser-textured surface showed a lower average coefficient of 0.097.

In this ABAQUS simulation, the coefficient of friction was calibrated by comparing simulated trimming forces with experimentally measured forces. Multiple simulations were conducted with varying COFs (0.05, 0.1, and 0.15), and the corresponding maximum trimming forces were analyzed. As shown in Figure 6.2, the experimental trimming force, obtained from press tonnage data for the case of 10% clearance and fresh trimming inserts, served as the reference point. Section 6.3 describes the methodology for determining the experimental force. In conclusion, a COF of 0.1 provided the best match, yielding a simulated maximum trimming force of 72.5 kN, in good agreement with the experimental value of approximately 73 kN. The coefficient of friction of 0.1 was then applied in all subsequent trimming simulations to ensure a realistic representation of the contact conditions between the DP980 sheet and the D2 trimming tools.

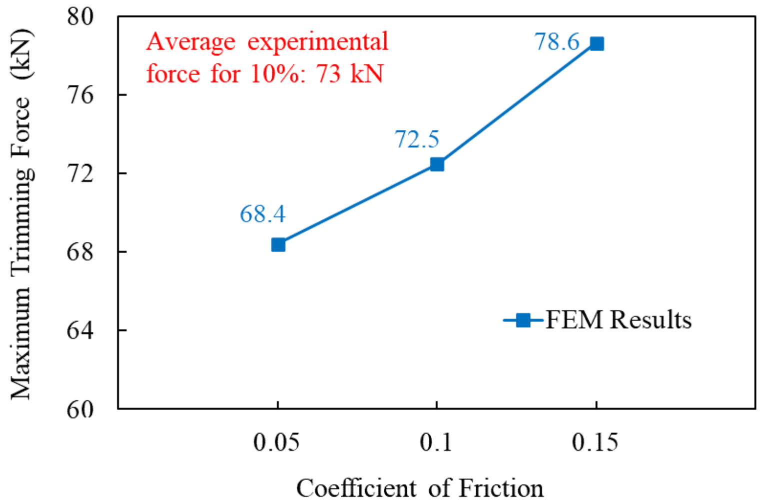

Figure 6.2. Impact of changing the coefficient of friction on simulation results.

A surface-to-surface contact is created between the tool's surface and all the internal nodes of the blank. The trimmed edges of the upper and lower tools had fillet radii of 0.02 mm, like those measured in the experimental tools, as shown in Figure 6.3.

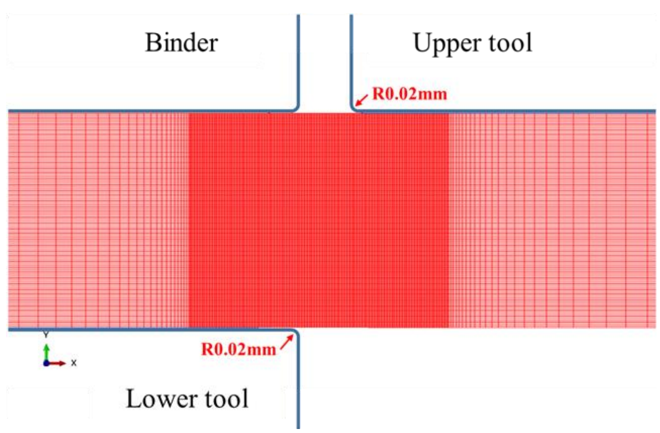

Figure 6.3. ABAQUS Finite element model of trimming with rigid tools.

6.1.3. Blank Mesh Type Selection

The isoperimetric linear quadrilateral (QUAD) plane strain elements with reduced integration (CPE4R) and hourglass control are used for meshing the blank. Since considerable plastic deformations, large displacements, and damage occur during the trimming process, the Arbitrary Lagrangian-Eulerian (ALE) and adaptive remeshing features were applied in the fine mesh shearing zone to reduce mesh distortion.

6.1.4. Arbitrary Lagrangian-Eulerian (ALE)

The ALE method was employed in these simulations to minimize excessive element distortion. ALE adaptive meshing is a technique that combines features of Lagrangian and Eulerian analysis within the same part mesh. In such a formulation, the frame of reference is not necessarily equal to the material displacement (Lagrangian formulation) or zero (Eulerian formulation). Still, it can be chosen independently of the material displacement. ALE is a tool that enables maintaining a high-quality mesh throughout an analysis, even when large deformations or material loss occur, as in the trimming operation, by allowing the mesh to move independently of the material [158].

This study employed the enhanced smoothing algorithm based on evolving geometry, utilizing three remeshing sweeps per increment for the ALE configuration.

6.1.5. Adaptive Remeshing

While having a significant tool penetration into the workpiece during the trimming results in crack initiation and propagation, the ALE method no longer suffices, and remeshing becomes necessary. In other words, when the strains become large in a geometrically nonlinear analysis, the elements often become so distorted that they no longer appropriately discretize the problem. When this occurs, it is necessary to map the solution onto a new mesh better designed to continue the analysis. When mesh distortion is so severe that a new mesh must be created, it can be generated using the mesh generation options in Abaqus/CAE. Adaptive remeshing consists of two fundamental tasks: creating a new mesh and remapping the solution variables from the old mesh to the new mesh with advection [158]. This study applied adaptive remeshing with ALE to sheet metal elements in the shear-affected zone.

6.1.6. Mesh Dependability Analysis

The number of elements used in every simulation is critical, as a large number enhances the accuracy of the result; however, it significantly increases the calculation time. Therefore, a very fine mesh is defined in the shearing zone, where deformation is concentrated, and relatively large elements are used for the rest of the blank. The mesh-size recommendation for modeling material failure and fracture path was provided by Cheng et al. [162]. They showed that if the mesh size is not optimal and is larger than the defined optimum size, the results of the sheared edge profile won't match the experimental data.

In the current ABAQUS simulation, a mesh sensitivity analysis was conducted to determine the optimal mesh size in the shear-affected zone, yielding results closest to the experimental data. The sensitivity analysis ensures that the results (e.g., trimming force, sheared edge profile, damage) are not affected by the mesh size. To achieve this, the rigid tool model with a 10% cutting clearance was selected, and different mesh sizes in the shearing zone were utilized. A mesh sensitivity analysis was then conducted. Mesh densities were selected by starting with 15 through-thickness elements, then testing with 30, 50, 75, 100, 145, and 207 elements. In Table 6.1, the sizes of the corresponding elements are shown relative to the number of elements.

Table 6.1. Element size and number selection for the mesh sensitivity analysis.

Number of through-thickness elements in the sheet	Element size in the thickness direction, mm	Element size in the width direction, mm
15	0.100	0.060
30	0.050	0.030
50	0.030	0.018
75	0.020	0.012
100	0.015	0.009
145	0.010	0.006
207	0.007	0.004

First, the influence of mesh size on the trimming force was studied, and the results are shown in Figure 6.4. As shown, the mesh density has a greater impact on the fracture behavior and the moment of total separation than the maximum force. As the mesh density and number of elements increase, localized plastic deformation increases, resulting in higher strains at the early stage of the simulation. This triggers the failure criterion, which in turn leads to the element's deletion and a load drop. Section 6.1.86.1.8 later describes the details of fracture criterion selection.

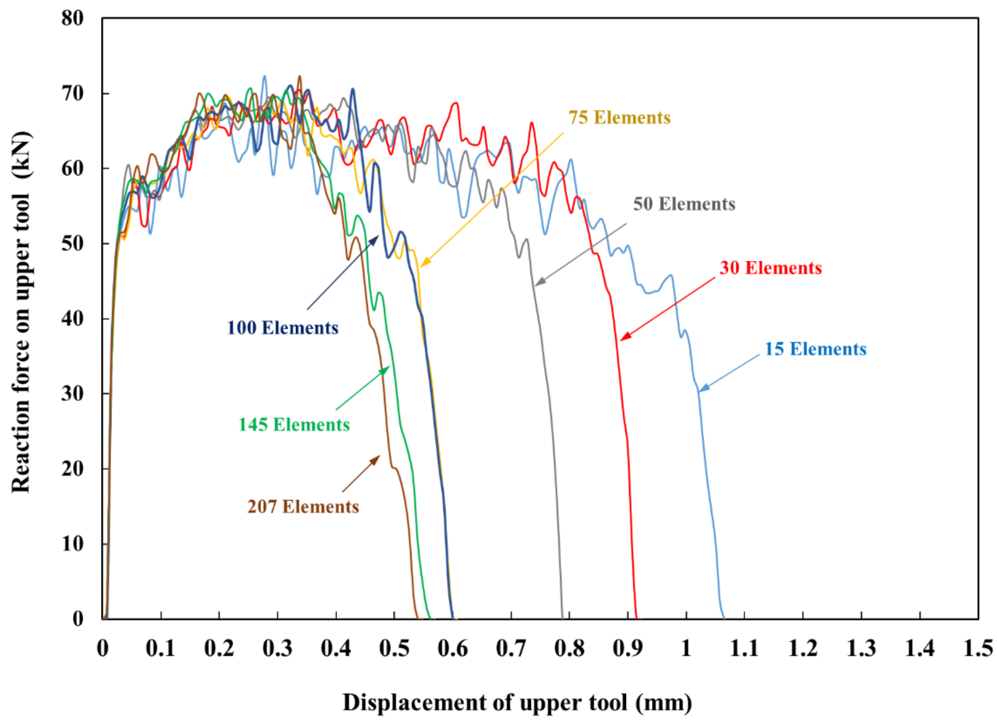

Figure 6.4. Trimming force versus upper die displacement for various numbers of through-thickness elements in the 10% clearance case.

Figure 6.5 shows how mesh refinement affects the predicted indentation depth at fracture initiation during trimming of the 1.45-mm-thick DP980 sheet. The horizontal axis indicates the number of elements through the sheet thickness, from a coarse discretization of 15 elements to a very fine discretization of 207 elements. The vertical axis represents the punch indentation depth at which the first crack begins, as predicted by the Johnson–Cook damage criterion.

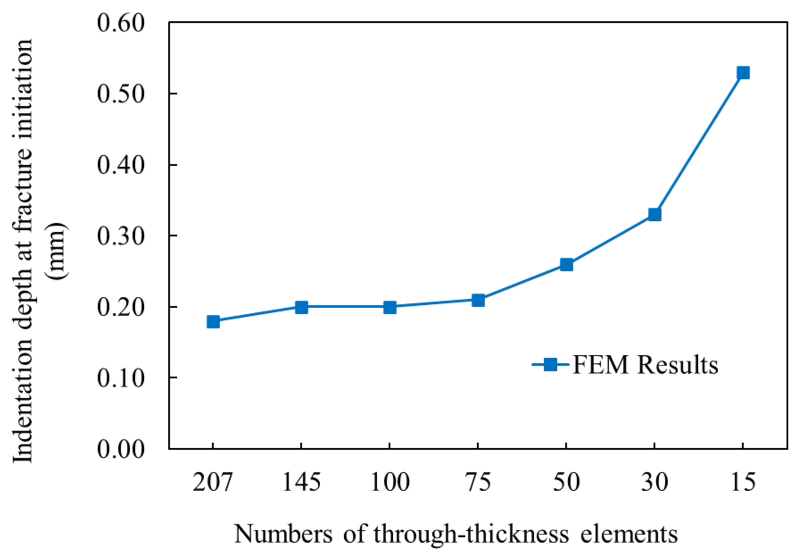

Figure 6.5. Effect of mesh density on the predicted indentation depth at fracture initiation in DP980 sheet trimming.

The results demonstrate a clear dependence of fracture initiation prediction on mesh density. For coarse meshes (fewer than 30 elements through thickness), the predicted indentation depth is significantly higher (≈0.5 mm), indicating delayed crack initiation. As the mesh is refined (more than 100 elements), the predictions stabilize around ≈0.20 mm, with minimal variation among 100, 145, and 207 elements. This trend confirms that finer discretization is necessary to accurately capture the localized strain and damage development at the shearing zone. Therefore, a mesh density of at least 100 elements through the thickness is considered sufficient for reliable trimming simulations, balancing accuracy with computational efficiency. Ultimately, a discretization of 145 through-thickness elements, with an element size of 0.010 mm in length and 0.006 mm in width in the shearing zone, was chosen for the simulations. The 0.010 mm mesh (through-thickness elements) lies within the stable convergence range and offers accurate predictions without the unnecessary computational expense of an even finer mesh. For the rigid tool case, a total of 58727 quadrilateral elements were used in the model.

The contour plots of plastic equivalent strain (PEEQ) across different mesh sizes further highlight the importance of selecting an appropriate element refinement. As shown in Figure 6.6, finer meshes, such as 207 and 145 elements, can capture the highly localized plastic strain gradients along the shear and fracture zones. These localized features are critical in trimming simulations because they directly influence crack initiation and propagation, as well as the formation of rollover, burnish, and fracture zones on the cut edge. On the other hand, coarser meshes (15 and 30 elements) fail to resolve these gradients adequately, resulting in artificially smeared strain distributions and unrealistic predictions of the deformation field.

Together with the trimming force and indentation depth results, the strain field analysis validates the choice of 145 through-thickness elements as the most suitable compromise between accuracy and efficiency for simulating the trimming of DP980 steel at 10% clearance.

In the second modeling case, to determine the load levels and stresses on the trimming tools where the deformable tool model was used, careful attention was given to optimizing the mesh size of the tools, especially at the corners and contact areas with the sheet metal blank. Pereira et al. [104] found that the ratio of the die element side length to the blank element side length at the interacting surfaces has a significant effect on the contact pressure results in sheet metal forming, particularly in the channel forming wear test. They demonstrated that a ratio of 1:2 between the die element side length and the blank element side length at the die radius interface yields the most accurate convergence of contact pressure results.

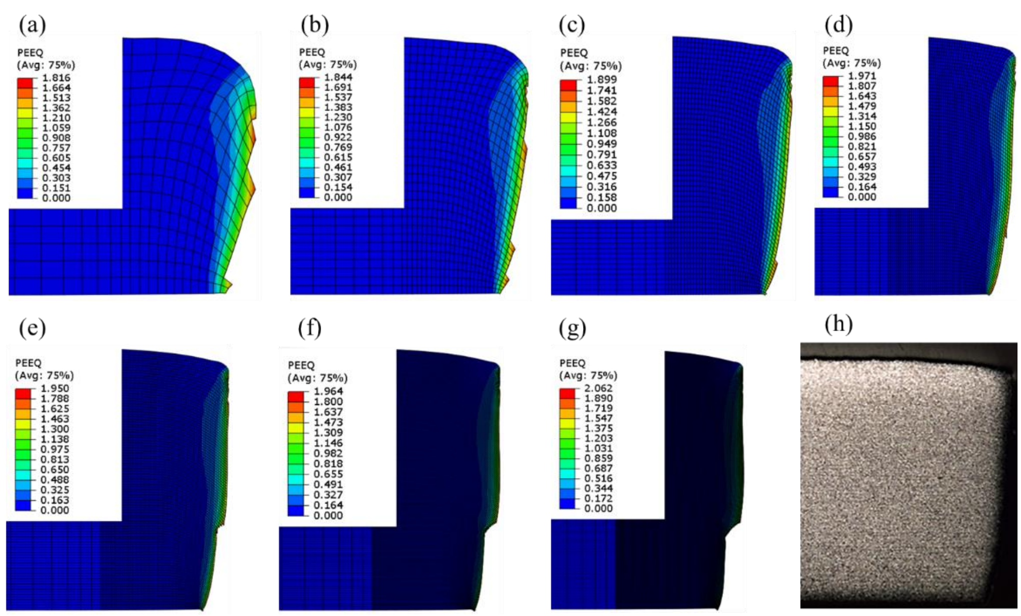

Figure 6.6. The simulated sheared edge with (a) 15 elements, (b) 30 elements, (c) 50 elements, (d) 75 elements, (e) 100 elements, (f) 145 elements, (g) 207 elements, and (h) experimental cross section of the sheared edge of DP980 trimmed at 10% clearance. The contour shows the plastic equivalent strain (PEEQ).

To investigate the effect of mesh refinement on the trimming die corner and adjacent edges, three different mesh sizes were analyzed: 0.05 mm, 0.025 mm, and 0.005 mm, as shown in Figure 6.7. The smallest mesh size at the corner radius of the die was selected to be very fine, equal to 0.005 mm, closely matching the blank mesh size, as shown in Figure 6.7 (c). The two coarser meshes (0.025 mm and 0.05 mm) were introduced for comparison, with element sizes gradually increasing away from the corner radius to reduce the overall model size.

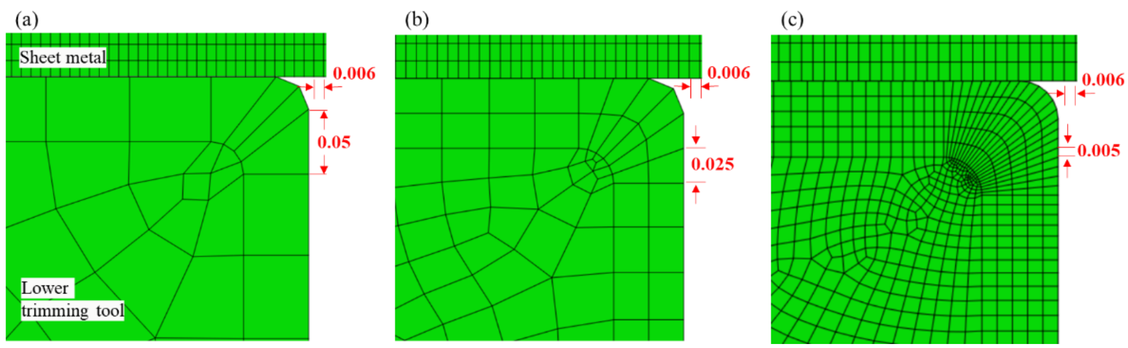

Figure 6.7. Mesh size sensitivity analysis of the deformable die corner radius using mesh sizes of (a) 0.05 mm, (b) 0.025 mm, and (c) 0.005 mm.

The results of the maximum principal stress distribution are shown in Figure 6.8. While the overall stress patterns remain qualitatively similar across the three cases, the peak stress values are sensitive to mesh size. The finest mesh (0.005 mm) captured higher localized stresses compared to the coarser meshes, indicating that mesh refinement at the die corner radius is critical for accurately evaluating stress concentrations. The red-marked elements in each subfigure highlight the peak surface elements where fatigue evaluation was performed.

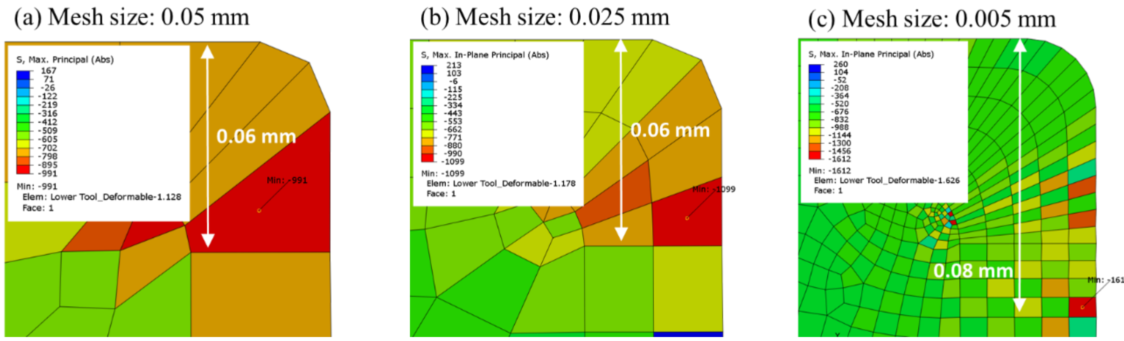

Figure 6.8. The results of the maximum principal stress for different die mesh sizes of (a) 0.05 mm, (b) 0.025 mm, and (c) 0.005 mm. The red-marked elements are the peak surface elements for each case.

Figure 6.9 presents the stress histories of these peak surface elements for the three mesh cases. The results demonstrate that the calculated mean and alternating stress values converge as the mesh is refined. The coarsest mesh (0.05 mm) underestimated the stress amplitude, while the 0.025 mm mesh provided intermediate results. The finest mesh (0.005 mm) produced the most consistent and reliable stress histories, which were subsequently used in the fatigue analysis. Note that the graphs shown in Figure 6.9 are the results as received. Later, for the fatigue analysis, the standalone peaks – which might be non-physical – are removed and curves are smoothed using a moving average formulation.

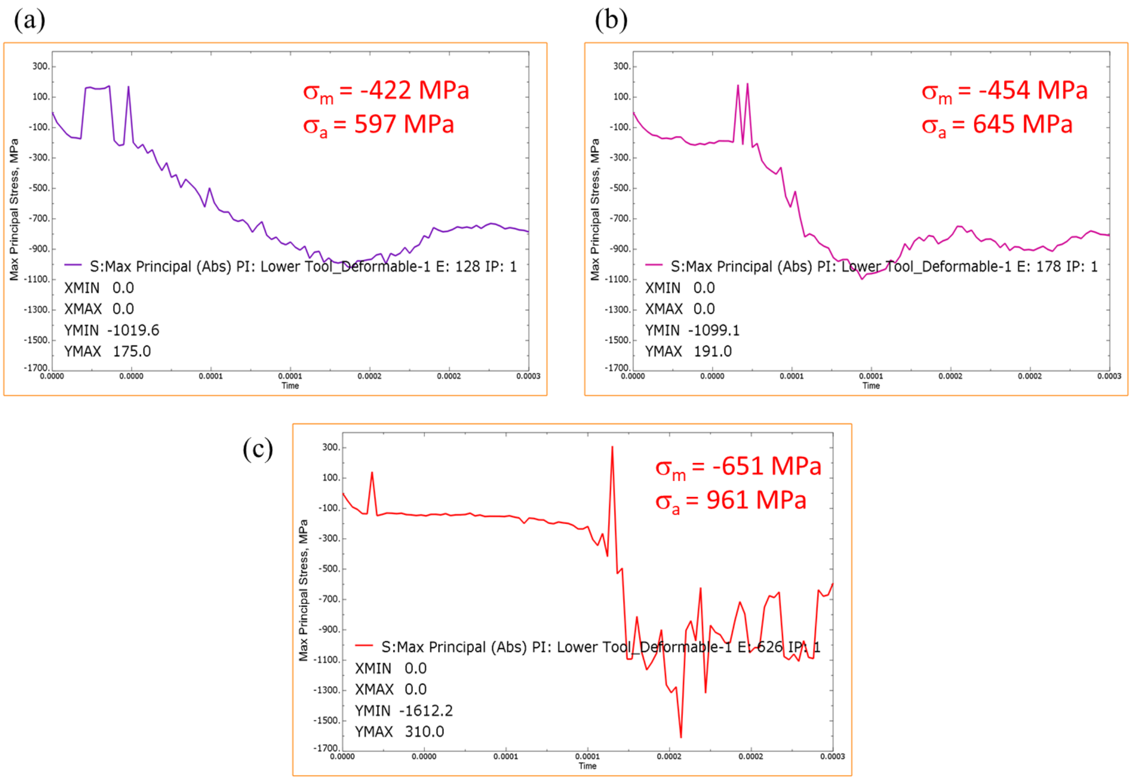

Figure 6.9. The stress history for the peak surface element, along with the mean stress and alternating stress values used in the fatigue analysis for different die mesh sizes of (a) 0.05 mm, (b) 0.025 mm, and (c) 0.005 mm.

Figure 6.10 presents the mesh sensitivity analysis, in which the maximum reaction force on the lower trimming tool is used as the finite-element estimate of the trimming force. The results show that the reaction force stabilizes for the finer meshes (0.005 mm and 0.025 mm), with only a marginal difference between them. In contrast, the coarser 0.05 mm mesh shows a larger upward deviation. Notably, the reaction force predicted with the 0.005 mm mesh (~77.6 kN) is closer to the experimentally measured trimming force of 73 kN, further supporting the validity of this refinement level.

Overall, the mesh sensitivity study confirms that sufficient refinement at the die corner radius is necessary to capture the true stress gradient and ensure acceptable stress evaluation and fatigue life prediction. By selecting a mesh size of 0.005 mm at the die corner radius, the curvature of the die geometry is also well-preserved, preventing sharp contact points that could occur with coarser discretization. Therefore, a mesh size of 0.005 mm was selected for all subsequent simulations, as further refinement would not significantly change the results.

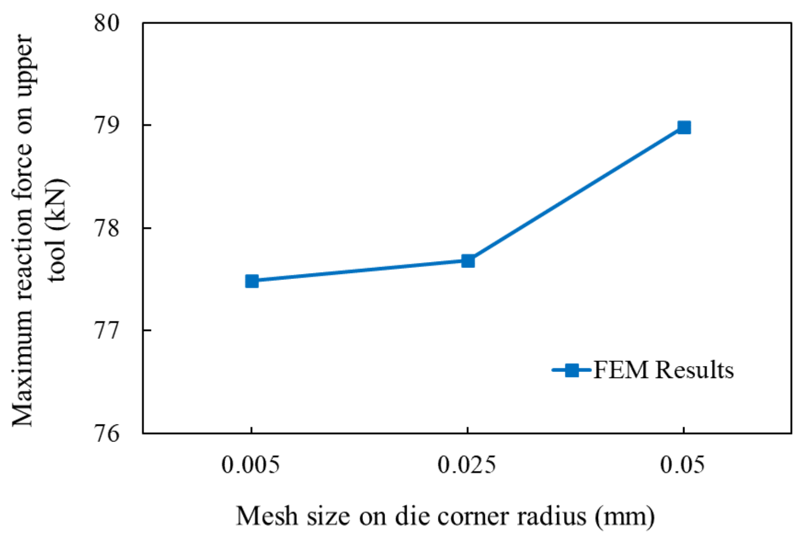

Figure 6.10. Mesh sensitivity analysis using the maximum reaction force on the lower die.

In Figure 6.11, the chosen model and mesh sizes within the shearing zone are displayed for both the sheet metal blank and the trimming tools.

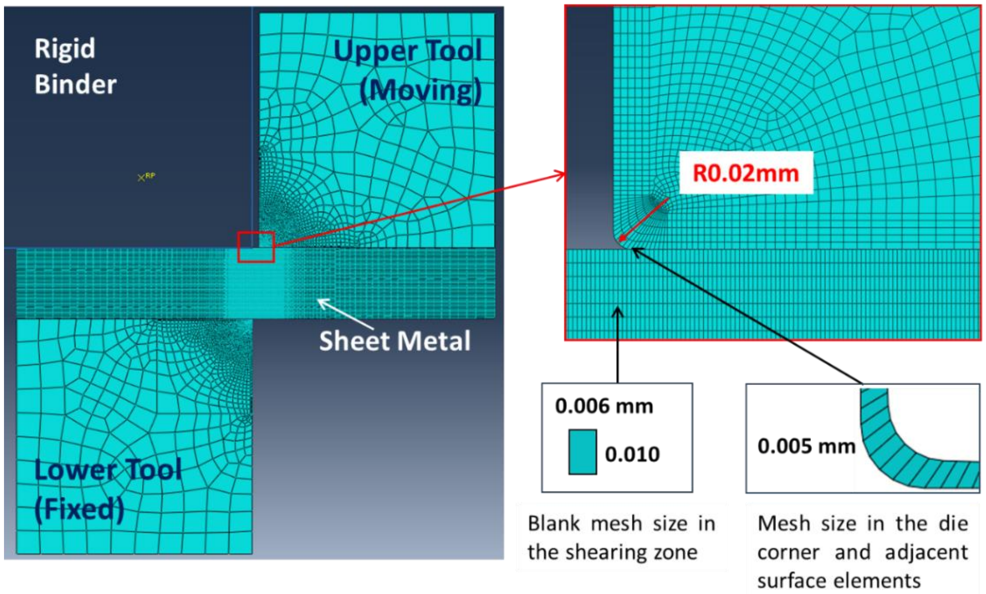

Figure 6.11. ABAQUS model with deformable trimming tools and mesh sizes in the shearing zone.

6.1.7. Sheet Material's Flow Curve

The trimming process involves substantial deformations and material damage; therefore, it is necessary to simulate an accurate flow behavior up to large strains.

Generally, sheet metal characterization through standard tensile testing provides data only up to a true strain of approximately 0.1-0.5 for most steel and aluminum grades. Plastic deformation in tensile tests and sheet metal forming is limited by dimensional (geometric) instability, such as localized necking, which does not occur in other forming processes. In most forming processes, characterized mainly by compressive or tensile-compressive stress states, the maximum attainable strain is limited only by the material's ductility. A finite element simulation of the trimming process done by Hu et al. [97] demonstrated that the equivalent plastic strain in the shearing zone in the trimming of

AA6111 can reach values as high as 3.0. This indicates that the local strain levels during trimming exceed those achievable in a typical tensile test by a factor of 10 or more. In other words, the deformation severity in the shearing zone far exceeds the strain range measurable in standard uniaxial tension, highlighting the limitations of tensile testing in fully capturing the strain conditions experienced during trimming. Extrapolation is often used, but it can lead to significant errors because of the large extrapolation domain. Therefore, an alternative approach that accounts for large strains must be considered.

A major obstacle to understanding large-strain deformation is the challenge of performing definitive experiments. Large-strain experiments are plagued by substantial changes in specimen geometry and various instabilities, which terminate experiments prematurely. Ideally, strain hardening should be calculated directly from a test run continuously (without interruption) on a uniformly loaded specimen. The stress should be calculated directly from the measured loads, and the strains should be measured directly from the deforming specimen. Table 6.2 lists several direct and indirect tests, describing their limitations [163].

6.1.7.1. Direct Tests Characterizing Flow Curve over Large Strains

Plastic instability (necking) restricts uniaxial tension to small strains. Few metals can stretch more than 50% before necking. Early attempts to remachining specimens to remove the neck have not gained popularity. That’s because the material in the diffused necking area is already work-hardened. So, machining cannot clean it.

Table 6.2. Large-strain test techniques and their limitations [163].

Test Technique	Strain Limits	Comments
Direct Tests		
Uniaxial Tension	<0.5	Limited by plastic instability
	1 to 1.5	After necking correction
Biaxial Tension	<0.8	Limited by plastic instability
Compression	<0.7	Limited by barrelling
	3 to 4	After remachining
Torsion – Round bars	2 to 5	Limited by ductility
Indirect Tests		
Wire Drawing + Tension	10	
Strip Drawing + Tension	4	
Rolling + Tension	7	
+ Plane Strain Compression	7	

Uniaxial compression is limited by barreling and end effects from the platen, as well as frictional effects. Excellent lubrication and a length/diameter ratio of ~1.6 are required to achieve a true uniaxial stress state. Significant changes in geometry require re-machining, which has been practiced much more extensively in compression testing than in tension testing. It requires starting with a relatively large specimen. The friction effect in the stress measurement also limits compression tests.

Biaxial tension tests on sheet material can generate effective strain levels roughly twice those achievable in uniaxial tension. The stress-strain data obtained are suitable only for stamping and other sheet metal forming processes involving moderate maximum effective strain (less than 0.8). They are not appropriate for more severe operations, such as trimming and blanking.

Torsional deformation offers the best hope for large-strain experiments because it involves minimal geometry changes. However, torsion also suffers from several significant restrictions. Experimentally, specimens elongate during torsion, and care must be exercised not to restrain their length. Torsion of solid rods also produces an inherently non-uniform stress state, varying from zero at the axis to a maximum at the surface [163].

6.1.7.2. Indirect Tests Characterizing Flow Curve over Large Strains

The indirect techniques are more feasible and don't need a complex specimen preparation procedure [163]. Most of the large-strain information available in the literature is obtained by one of the indirect tests listed in Table 6.2. These tests are conducted by imparting large pre-strains in a deformation mode relatively insensitive to plastic instability (such as wire drawing or sheet rolling) and then testing the pre-strained material in uniaxial tension to establish its flow stress level [164].

In 1948, Ford [165] proposed a series of rolling and tensile tests to obtain a stress-strain curve over an extended range of strains. Later, Hecker et al. [163] performed rolling and tension experiments on Aluminum 1100 and acquired true strains of approximately 5. Goijaerts et al. [95], [96] followed the same methodology to obtain large strain-stress curves for various sheet materials, including steels (X30Cr13, 316Ti, and DC04), Brass (Ms64), and Aluminum (Al51ST). More recently, Golovashchenko et al. [89] reported the large strain-stress curve for AA6111-T4 using sequential rolling and tensile testing.

6.1.7.3. DP980's Flow Curve over Large Strains

In the present work, an experimental method based on accumulated rolling and tensile tests has been developed to determine the stress-strain curve for DP980 sheets over a wide strain range. Tensile samples were fabricated using wire EDM from strips of DP980 rolled in steps with successive thickness reductions. Thirteen sequential rolling processes were conducted, each with approximately 0.1 mm thickness reduction. For DP980-1, the initial thickness, t_0, was 1.45 mm with a zero pre-strain level, and it was rolled down to the thinnest gauge of 0.24 mm. For DP980-2, the initial gauge was 1.5 mm, and the thinnest sheet had a thickness of 0.3 mm.

Tensile specimens were sub-sized miniature specimens with dimensions shown in Figure 6.12 (a). The tensile direction was parallel to the rolling direction. To obtain more reliable data (particularly for the very thin rolled strips), five specimens were tested for each thickness of rolled material, and the average was plotted.

An Instron 5982 universal testing machine was equipped with a 10 kN Static Load Cell and hydraulic grips. To apply the appropriate strain rate as outlined in ASTM E-8 [166], an extension rate of 1.27 mm/min was utilized. A fine paint marker was used to apply white dots to the specimen (Figure 6.12 (b)) for recognition by the Advanced

Video Extensometer (AVE 2.0), equipped with a 16 mm lens. This allowed for the successful testing of the specimens.

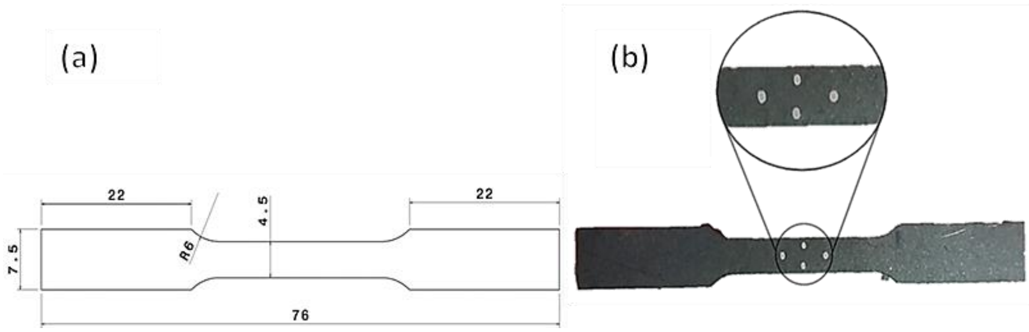

Figure 6.12. (a) Dimensions of miniature dog-bone specimens (dimensions are in mm), (b) fine white markings for video extensometer.

According to Marciniak et al. [152], an effective strain increment can be defined by Equation (6.1) assuming that direction 1 coincides with the rolling direction, direction 2 coincides with the transverse direction, and direction 3 is normal to the sheet plane.

$$d\bar{\varepsilon} = \sqrt{\frac{2}{3}\left(d{\varepsilon_1}^2 + d{\varepsilon_2}^2 + d{\varepsilon_3}^2\right)} \tag{6.1}$$

It was assumed that during the rolling process, the central portion of the strip deforms in-plane strain ($d\varepsilon_2 = 0$), and material from the thickness flows into the length of the strip ($d\varepsilon_3 = -d\varepsilon_1$) without changing its width. It was observed from the rolling experiments that very minimal transverse flow occurs near the edges of the rolled strip. These areas were excluded from the experiments by fabricating miniature tensile samples from the strip's central portion. Increments of the through-thickness strain component were calculated using Equation (6.2).

$$\Delta\varepsilon_1^{(i)} = \ln(\frac{t_i}{t_{i+1}}) \tag{6.2}$$

Where t_i and t_{i+1} are the material thickness before and after the i^{th} increment of rolling deformation, the total accumulated pre-strain value for the i^{th} step is calculated based on Equation (6.3).

$$\bar{\varepsilon} = \sum_{i=1}^{n} \frac{2}{\sqrt{3}} \Delta\varepsilon_1^{(i)} = \sum_{i=1}^{n} \frac{2}{\sqrt{3}} ln \frac{t_i}{t_{i+1}} \tag{6.3}$$

All these formulations are developed assuming that the sheet material is isotropic, as the general form of Equation (6.3) is written as Equation (6.4):

$$\bar{\varepsilon} = \sum_{i=1}^{n} \frac{1 + r_i}{\sqrt{1 + 2r_i}} \Delta\varepsilon_1^{(i)} \tag{6.4}$$

Where r_i is the r-value for the corresponding thickness.

To prove that DP980 used in this study is an isotropic material, r-values for different thicknesses were measured and presented in Table 6.3. The table shows that all r-values are approximately 1, with an average of 1.081. So, for the sake of an acceptable analysis, the r-value for whole thicknesses was considered constant, equal to 1.0.

Table 6.3. Measured r-value (L direction) for different sample thicknesses for DP980.

Thickness: (mm)	1.5	1.4	1.3	1.2	1.1	1.0	0.9	0.8	0.7	0.6	0.5	Average
r-value:	0.954	1.192	1.247	1.029	1.138	1.224	1.115	0.999	1.064	1.030	0.909	1.081

Finally, the i^{th} accumulated effective strain in the final stress-strain curves was calculated using Equation (6.5).

$$\bar{\varepsilon}_{i-th\,step} = \varepsilon_{tensile\,test} + \frac{2}{\sqrt{3}} ln(\frac{1.45}{t_i}) \tag{6.5}$$

Where the thickness for each step, t_i, was 1.45 to 0.24 mm for DP980-1 and 1.5 to 0.3 mm for DP980-2 rolled samples. Additionally, effective true stress was directly calculated from the tensile test outputs using Equation (6.6).

$$\bar{\sigma}_{i-th\,step} = \sigma_{tensile\,test} \tag{6.6}$$

The raw tensile test results, without any calculations, of all samples with various thicknesses after each rolling reduction, are shown in the Figure 6.13 for DP980-1. From the graphs, it can be seen that as the thickness decreases, the stress level increases as the material work-hardens. Additionally, the material shows less total elongation.

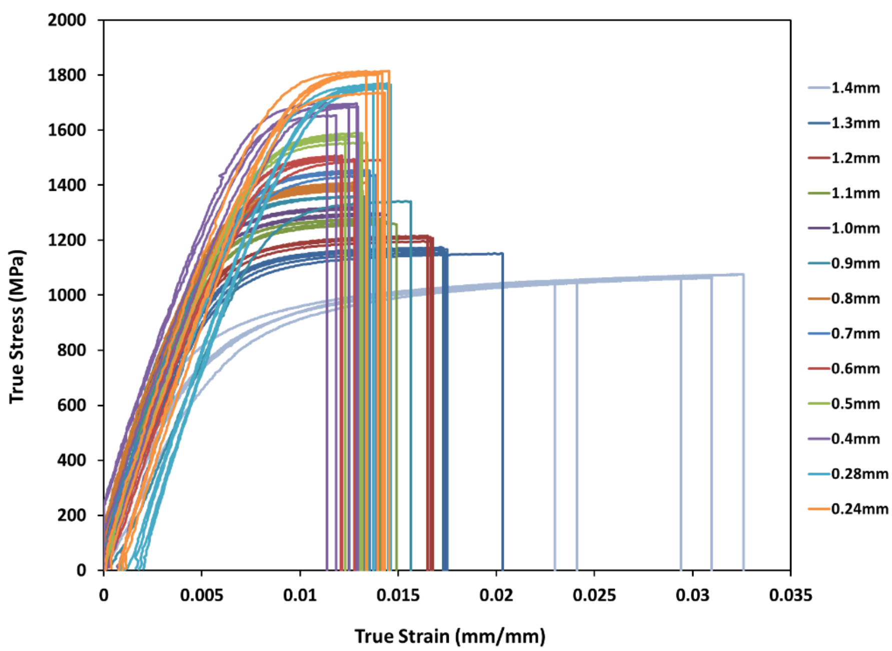

Figure 6.13. The raw tensile test results of rolled DP980-1 specimens.

Then, by using Equation (6.5), the accumulated effective pre-strain was added to the true strain values measured for each sample. The combined results of curves accounting for accumulated pre-strain values are plotted in Figure 6.14 for DP980-1. In these graphs, Triangles show the maximum point of each curve where engineering stress is equal to ultimate tensile strength (UTS), and circles represent the results of tensile testing of initial as-received material (i.e., 1.45 mm-thick DP980-1 sheet) up to its maximum point.

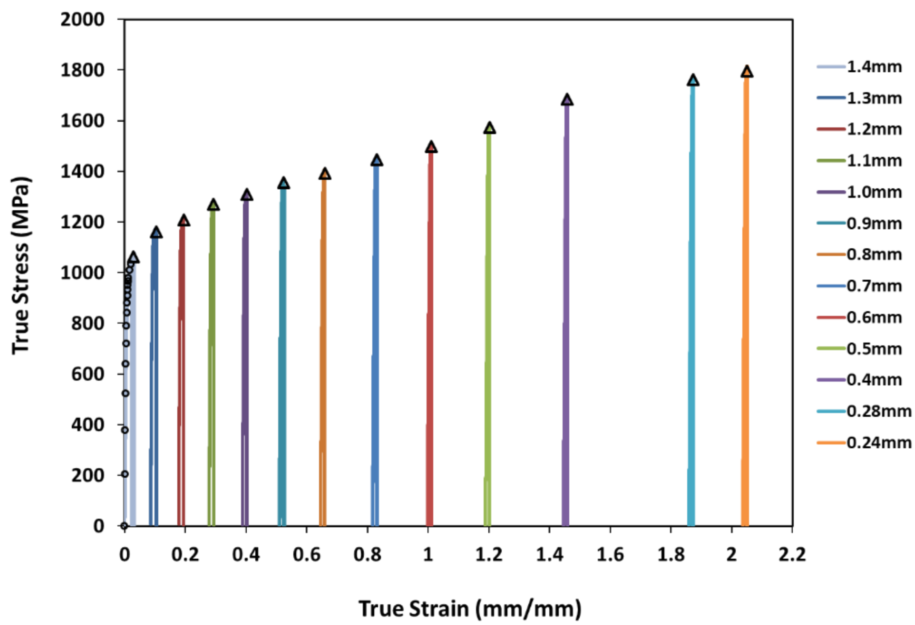

Figure 6.14. Sequential tensile testing of rolled DP980-1 specimens accounting for pre-strain values.

Looking at the curves of Figure 6.13 and Figure 6.14, the flow stress increased significantly while the strain before fracture decreased with the increase of pre-strain. In addition, the pre-strain level was gradually increased through multiple steps of cold rolling, thereby increasing the thickness reduction due to work-hardening.

Figure 6.15 plots the final flow curve of DP980-1 over a large strain range. It is the result of a curve-fitting procedure using circles, triangles, and symmetrical sigmoidal extrapolation. This curve was employed as the sheet material input for trimming simulations.

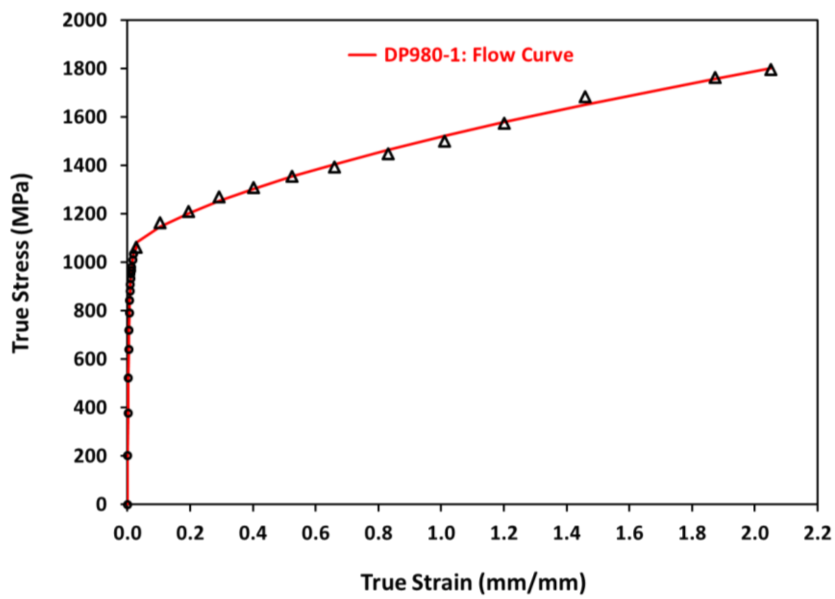

Figure 6.15. Fitted flow curve for DP980-1 over large strains.

In Figure 6.16, Figure 6.17, and Figure 6.18, the raw tensile test results, true stress-accumulated true strain curves after multiple rolling steps, and the final flow curve over large strains for DP980-2 are plotted, respectively. The methodology is the same as what was used for DP980-1.

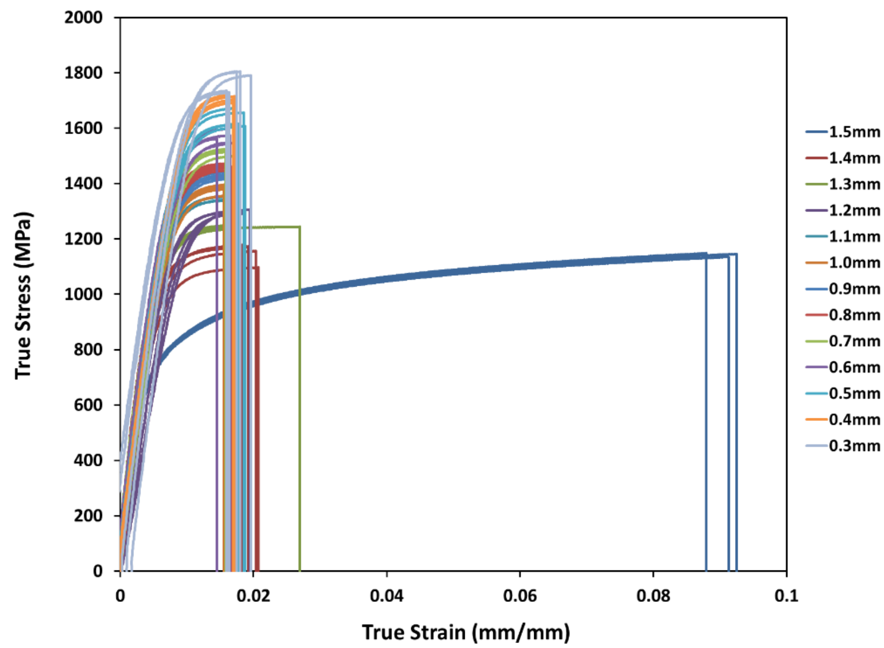

Figure 6.16. The raw tensile test results of rolled DP980-2 specimens.

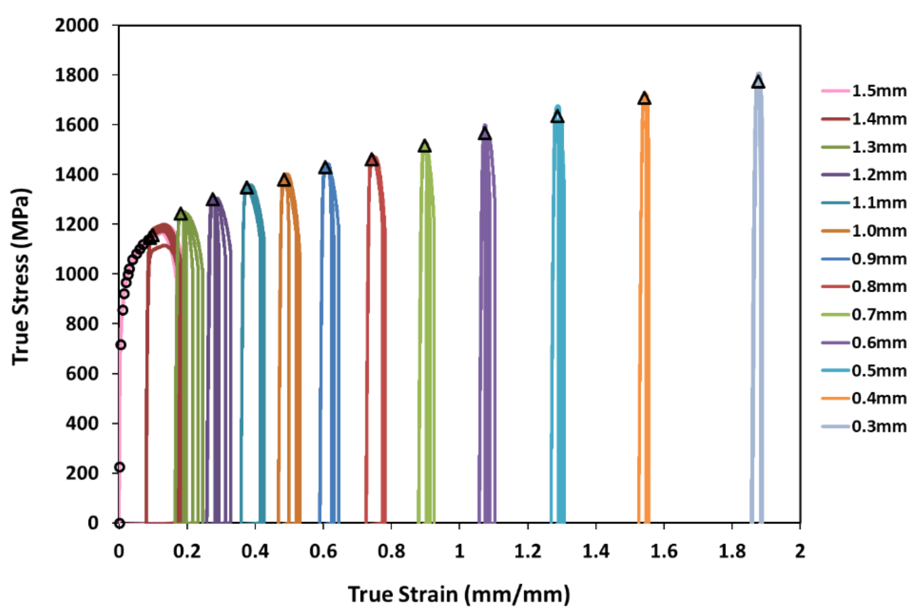

Figure 6.17. Sequential tensile testing of rolled DP980-2 specimens accounting for pre-strain values.

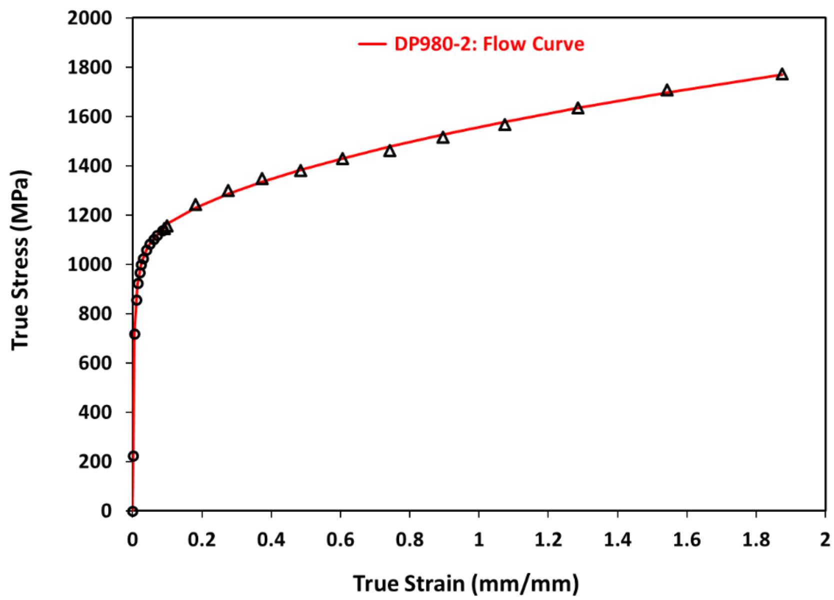

Figure 6.18. Fitted flow curve for DP980-2 over large strains.

6.1.8. Fracture Criteria Selection

The trimming process results in the complete separation of the sheet from the remaining material. Before a total fracture occurs, the material undergoes crack propagation and damage. A suitable fracture criterion is required in the model to predict the occurrence and progression of the crack.

6.1.8.1. Ductile Fracture Criteria

Ductile fracture, which differs from brittle fracture, is a failure process in which the material undergoes plastic deformation before separating into pieces under imposed stress at a temperature below its melting point [167]. Most metals, including dual-phase steels, fail due to a ductile fracture mechanism resulting from the nucleation, growth, and coalescence of microscopic voids. When sufficient stress is applied to break the interfacial bonds between the particle and matrix, voids can form around a second-phase particle or inclusion. Once the voids form, further plastic strain and hydrostatic stress cause the voids to grow and eventually coalesce. If void nucleation occurs with little difficulty, the growth and coalescence of the voids control the fracture properties. The growing voids reach a critical size relative to their spacing, and local plastic instability develops between them, resulting in failure [168].

The degradation or damage in a material is typically expressed in terms of a damage parameter, and failure occurs through the evolution of damage. In the described ductile fracture mechanism, voids around particles grow when subjected to plastic strain and hydrostatic tension. Furthermore, experimental investigations have shown that ductility depends on the triaxiality, η, of the stress state [168]. Therefore, comprehensive ductile fracture criteria should also include stress triaxiality. Stress triaxiality is the ratio between the mean stress (σ_m) and von Mises equivalent stress ($\bar{\sigma}$) as given in Equation (6.7):

$$\eta = \frac{\sigma_m}{\bar{\sigma}} \tag{6.7}$$

In the plane strain tension, the stress triaxiality would be equal to $\eta = 1/\sqrt{3} = 0.58$. Also, $\eta = 1/3$ for uniaxial tension, and $\eta = 0$ for pure shear condition [169].

Ductile fracture criteria are mostly based on an effective strain path integral, according to Johnson [170]:

$$D = \int_0^{\varepsilon_p} \frac{d\varepsilon_p}{\bar{\varepsilon}_f} = 1 \tag{6.8}$$

Where ε_p and $\bar{\varepsilon}_f$ are plastic and effective fracture strains, respectively. $\bar{\varepsilon}_f$ is a function of triaxiality and material parameters. The accumulated damage model assumes that material failure occurs when the damage indicator, *D*, reaches 1.

Multiple ductile fracture criteria have been developed to describe the damage growth and fracture processes in the forming operations [171]. In this study, several fracture criteria have been examined, including the following:

Cockcroft-Latham (C-L) Damage Criterion:

Cockcroft and Latham [172] suggested a simple fracture criterion based on plastic work per unit volume. In their formulation, the fracture criterion is constructed from some combination of stress and strain, and damage accumulates during straining until a critical value C is reached at $\bar{\varepsilon} = \varepsilon_f$. To account for hydrostatic tension, they built the criterion on the magnitude of the major principal stress, σ^*, as given by Equation (6.9):

$$C = \int_0^{\bar{\varepsilon}_f} \sigma^* \, d\bar{\varepsilon} \tag{6.9}$$

Where $\bar{\varepsilon}$ represents the effective strain and ε_f is the strain at fracture. Parameter C can be calculated in an experimental test with a known triaxiality leading to the fracture and upon strain measurement at fracture.

Rice-Tracey (R-T) Damage Criterion:

Rice and Tracey [173] evaluated the behavior of spherical voids in an incompressible, rigid-perfectly plastic solid for high triaxiality loading cases. They proposed an exponential function describing the effect of stress triaxiality (η) on the effective fracture strain ($\overline{\varepsilon_f}$), given in Equation (6.10):

$$\overline{\varepsilon_f} = A \cdot \exp\left(-B\eta\right) \tag{6.10}$$

To find material constants A and B, two experimental tests with known triaxiality are required, for instance, plane strain tension and plane strain compression tests.

Rice-Tracey fracture criterion was found to be employed by several researchers while simulating shearing processes [26], [71], [95]–[98].

Johnson-Cook (J-C) Damage Criterion:

Johnson and Cook [174] modified the Rice-Tracey fracture criterion by adding an extra term to the model, including the strain rate ($\dot{\varepsilon}$) and temperature effects. The mathematical representation of the Johnson-Cook damage model is shown in Equation (6.11):

$$\bar{\varepsilon}_f = [D_1 + D_2 \cdot \exp\left(-D_3\eta\right)]\left[1 + D_4 ln\left(\dot{\bar{\varepsilon}}_f / \dot{\varepsilon}_0\right)\right][1 + D_5 T^*] \tag{6.11}$$

Where D_1, D_2, D_3, D_4, and D_5 are material-dependent damage parameters. $\dot{\varepsilon}_0$ is the reference strain rate, and T^* is the non-dimensional temperature.

Due to the advantages of a simple equation form, small calculation quantity, and rapid calculation speed, the Johnson-Cook model has been widely used to simulate sheet metal shearing processes. Krinninger et al. [175] applied the Johnson-Cook fracture criterion to investigate the failure behavior of an aluminum alloy in a problem-oriented simulation of a shear-cutting process, achieving a good correlation with experimental results. Cheng et al. [162] employed the Johnson-Cook fracture criterion in a microstructure-based 2-D plane strain post-necking model to predict the fracture strain for a commercial DP980 material.

Oyane Damage Criterion:

Oyane [176] proposed a fracture criterion that considers a porous ductile body, assuming that, as plastic deformation increases, the hydrostatic stress history of that body affects the formation, coalescence, and growth of voids, with fracture occurring when the void density reaches a critical value. The Oyane fracture criterion is expressed as Equation (6.12):

$$\int_0^{\bar{\varepsilon}_f} (1 + a\eta)\, d\bar{\varepsilon} = C \tag{6.12}$$

Where $\bar{\varepsilon}$ is the equivalent plastic strain, $\bar{\varepsilon}_f$, is the accumulated equivalent plastic strain at fracture, and η is the stress triaxiality. Parameter a and the threshold integrated value of C are material constants that can be obtained by calibrating the fracture criterion using experimental results. When the integral value reaches the critical value of C, the ductile fracture is supposed to happen.

Lou-Huh (L-H) Fracture Criterion:

Lou et al. [177] proposed an empirical model based on the physical processes of micro-voids' nucleation, growth, and coalescence from a micro-prospective on mild fracture. The fracture model included terms representing nucleation, growth, and coalescence of voids. This formulation expresses the void nucleation based on the equivalent plastic strain. The L-H model represented the stress triaxiality normalized as von Mises equivalent stress, considering Bao and Wierzbicki's research result [178] that fracture did not occur below $\eta = -1/3$. The coalescence of the micro-void was simulated by using the maximum shear stress (τ_{max}) and normalized to von Mises equivalent stress ($\bar{\sigma}$). The accumulated damage, D in the L-H model is represented in Equation (6.13):

$$D = \begin{cases} \frac{1}{C_3}\int_0^{\bar{\varepsilon}_f} \left(\frac{2\tau_{max}}{\bar{\sigma}}\right)^{C_1} \left(\frac{1+3\eta}{2}\right)^{C_2} d\bar{\varepsilon}, & \eta > -1/3 \\ 0, & \eta \leq -1/3 \end{cases} \tag{6.13}$$

Where C_1, C_2, and C_3 are three model constants.

6.1.8.2. Calibration of Damage Parameters

Three mechanical tests were conducted in this study to calibrate the Cockroft-Latham and Johnson-Cook fracture criteria and determine material constants, including the plane-strain bending test, the equi-biaxial bulging test, and hole flanging of a reamed hole.

Plane Strain Bending

The calibration of the Cockroft-Latham fracture criterion is straightforward and requires only the identification of a single material parameter. Plane-strain bending experiments were selected to determine the damage parameter in the Cockcroft and Latham fracture criterion. To do so, a strip-bending fixture was designed and built into a two-column die set, as shown in Figure 6.19 .

In this experiment, the sheet metal strip was bent to a small radius until it fractured locally, as shown in Figure 6.20. A Dake 100-ton hydraulic press was used to lower the upper die and bend the strip. The fracture strain was measured using the pixelation method described earlier in section 1.3.2.2.

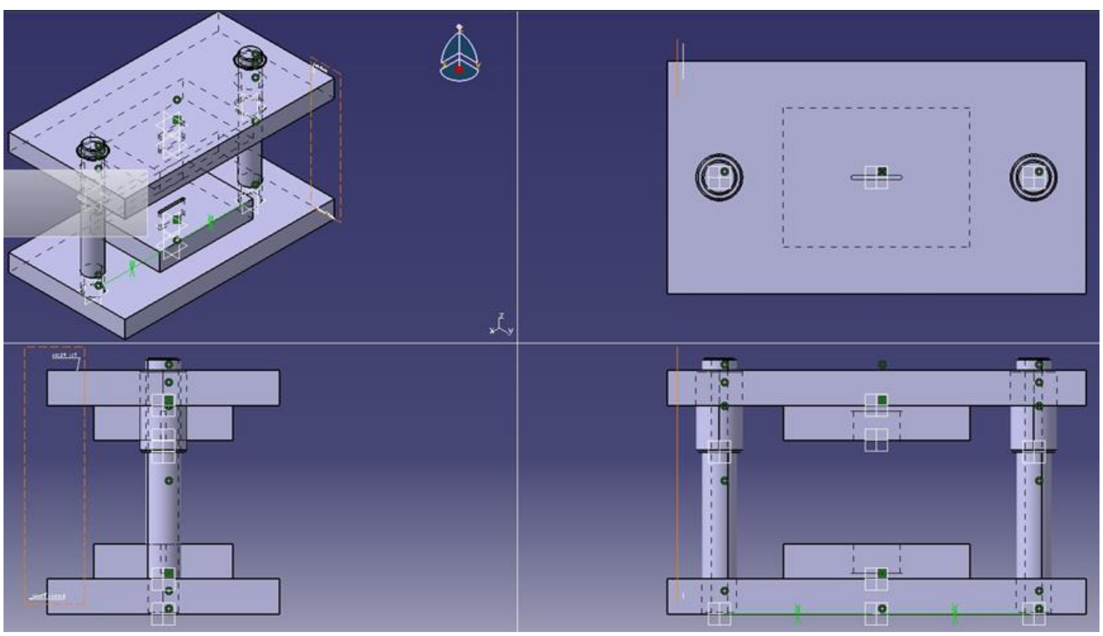

Figure 6.19. CAD drawing of strip-bending fixture.

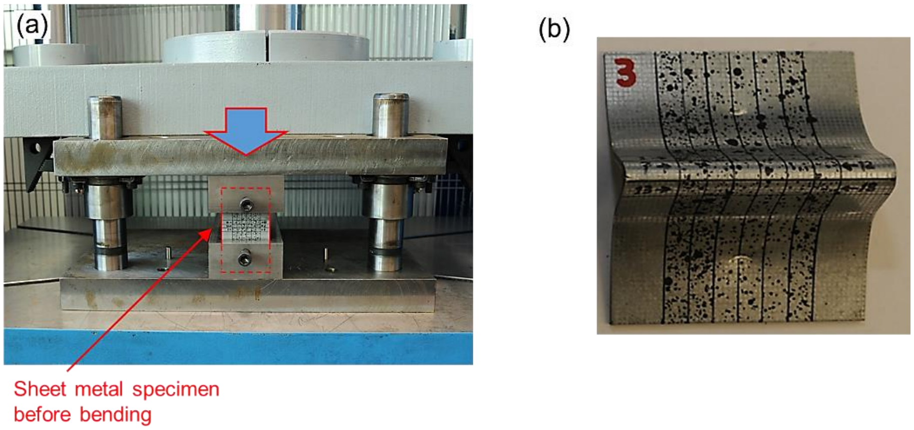

Figure 6.20. (a) Strip bending fixture with the specimen installed before the deformation, and (b) bent specimen with a crack on the outer radius.

In the plane strain bending, σ^*, represents the highest local tensile stress. In the bending of sheet metal, the highest local tensile stress is the principal stress along the direction of major deformation, so $\sigma^* = \sigma_1$. Therefore, the Cockcroft-Latham (C-L) fracture criterion can be represented by Equation (6.14):

$$C = \int_0^{\bar{\varepsilon}_f} \sigma_1 \, d\bar{\varepsilon} \tag{6.14}$$

The bending condition in this experiment can be considered a small radius bending. In small radius bending, according to Marciniak et al. [152], as plane strain is assumed, the strain and stress state is:

$$\begin{aligned} &\varepsilon_1; \quad \varepsilon_2 = 0; \quad \varepsilon_3 = -\varepsilon_1 \\ &\sigma_1; \quad \sigma_2 = \frac{(\sigma_1 + \sigma_3)}{2}; \quad \sigma_3 \end{aligned} \tag{6.15}$$

Von Mises yield criterion in principal stresses can be expressed as Equation (6.16):

$$(\sigma_1 - \sigma_2)^2 + (\sigma_2 - \sigma_3)^2 + (\sigma_3 - \sigma_1)^2 = 2{\sigma_f}^2 \tag{6.16}$$

As mentioned earlier in Equation (6.7), stress triaxiality $\eta = \frac{\sigma_m}{\bar{\sigma}} = \frac{\sigma_m}{\sigma_f}$, where the mean stress (σ_m) is given by Equation (6.17) and σ_f is the flow stress of material.

$$\sigma_m = \frac{\sigma_1 + \sigma_2 + \sigma_3}{3} \tag{6.17}$$

By combining Equation (6.15) through Equation (6.17), the major principal strain of σ_1 can be given by Equation (6.18):

$$\sigma_1 = \sigma_f(\frac{1}{\sqrt{3}} + \eta) \tag{6.18}$$

By substituting Equation (6.18) into Equation (6.14), the Cockroft-Latham model can be written as Equation (6.19):

$$C = \int_0^{\bar{\varepsilon}_f} \sigma_f \left(\frac{1}{\sqrt{3}} + \eta\right) d\bar{\varepsilon} \tag{6.19}$$

In the plane strain bending test of DP980-1, we measured the fracture strain in the principal direction (ε_{1f}) using the pixelation method for five specimens and 59 dots in total. Averaging the measurements and converting to the effective strain using the formula $\bar{\varepsilon}_f = \frac{2}{\sqrt{3}} \varepsilon_{1f}$ resulted in $\bar{\varepsilon}_f = 0.42$ with a standard deviation of 0.08.

Since a power law can express the flow stress as $\sigma_f = K\bar{\varepsilon}^n$, the Equation (6.19) can be written as:

$$C = \int_0^{\bar{\varepsilon}_f} K\bar{\varepsilon}^n \left(\frac{1}{\sqrt{3}} + \eta\right) d\bar{\varepsilon} = \left(\frac{1}{\sqrt{3}} + \eta\right) \frac{K}{n+1} {\bar{\varepsilon}_f}^{(n+1)} \tag{6.20}$$

Therefore, parameter C in the plane strain bending for DP980-1 was calculated to equal $C = \left(\frac{1}{\sqrt{3}} + 0.58\right) \frac{1228.8 \text{ MPa}}{0.08+1} 0.42^{(0.08+1)} = 514.8$ MPa.

Having the parameter C, it is possible to calculate the fracture strain for all ranges of stress triaxiality using Equation (6.20) and to plot the $\bar{\varepsilon}_f - \eta$ curve for our sheet material as an input for the finite element model.

Equi-biaxial Bulging Test

The equi-biaxial bulging test was also performed to determine the fracture loci of DP980. In this test, the sheet material was bulged using a 20-mm diameter hemispherical punch on a Louis Small ductility tester, as shown in Figure 6.21. The bulge test was stopped when the crack appeared on the top surface of the sample. The fracture strain was measured using the pixelation method described earlier in section 1.3.2.2, in which the deformation of fractured dots painted on the surface of the specimen was measured.

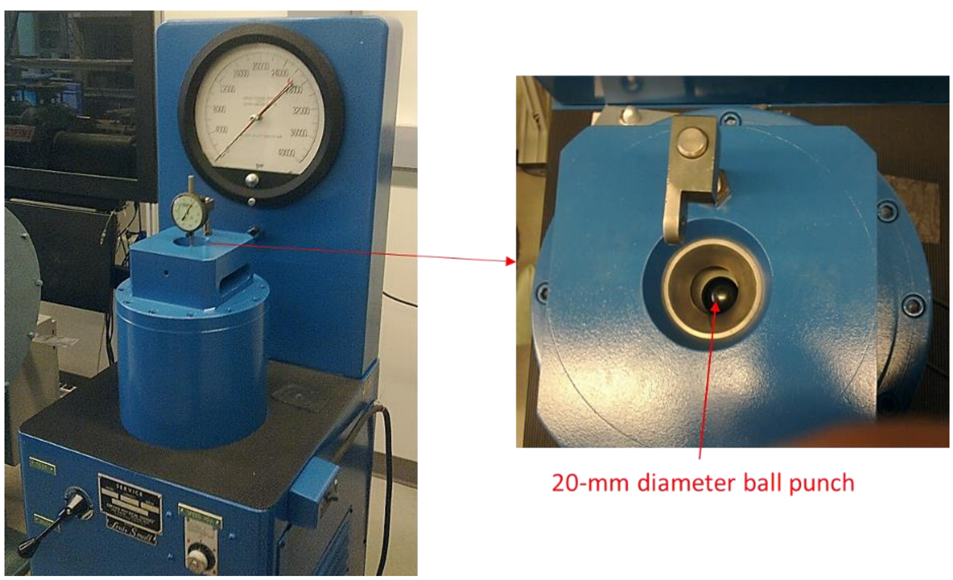

Figure 6.21. Louis Small ductility tester.

Figure 6.22 (a) shows the bulged sample of DP980. These experimental measurements for DP980-1 determined that the average effective fracture strain under this condition was 0.52 true strain with a standard deviation of 0.09. The stress state in this test is equi-biaxial tension with the stress triaxiality of $\eta = 2/3 = 0.66$.

<u>Hole-flanging of Reamed Hole</u>:

The final experimental test to determine the fracture strain of DP980 was the hole expansion of a reamed hole. In this test, a 5-mm-diameter hole was pre-drilled and later reamed in the center of a 40 × 40 mm² square blank. The hole flanging procedure was similar to the bulging test and was performed using the ductility tester with a 20-mm diameter hemispherical punch, as shown in Figure 6.21. The hole was expanded until the first crack appeared on the edge of the hole. The hole-flanged specimen of DP980 is illustrated in Figure 6.22 (b).

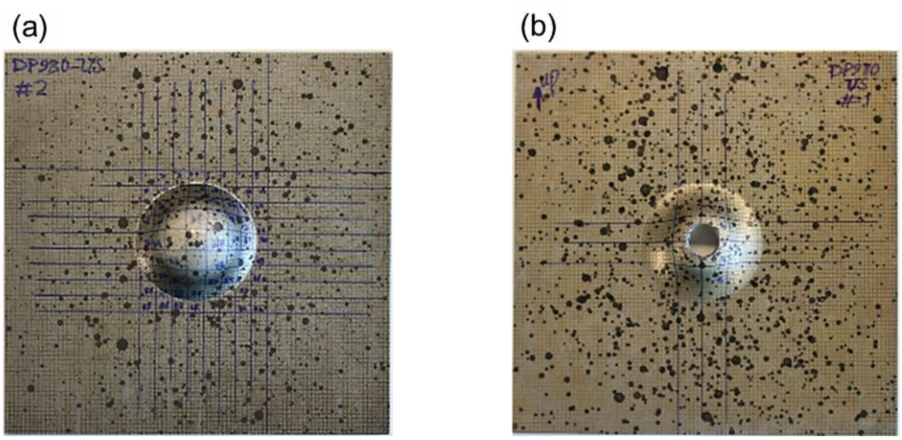

Figure 6.22. (a) Bulged specimen and (b) hole-flanged specimen of DP980.

The strain measurement was also done using the dot measurement technique in this test. The fracture strain was measured along the perimeter of the hole. This test gives a stress state similar to uniaxial tension, with the stress triaxiality of $\eta = 1/3 = 0.33$. The average effective fracture strain of DP980-1 material for this condition was equal to 0.59 with a standard deviation of 0.05.

6.1.8.3. Used Fracture Parameters in the FE Study

A comparative evaluation of several ductile fracture criteria was carried out in this study to identify the most suitable criterion for accurately predicting fracture under the given conditions.

The Cockroft-Latham (C-L) was used and calibrated by a plane strain bending test, as described in the previous section. By replacing the material parameters of K, n, and C in Equation (6.20), the C-L fracture criterion for DP980-1 is expressed as Equation (6.21):

$$(0.58 + \eta)\bar{\varepsilon}_f^{\,1.08} = 0.45 \tag{6.21}$$

In addition to the C-L criteria calibrated in this study, the C-L criteria provided by Takada et al. [179] for DP980 were also used in the finite element model for comparison purposes.

Another implied fracture criterion was the Johnson-Cook fracture criterion. According to Johnson and Cook [180], the fracture results are very dependent on the state of hydrostatic pressure and less dependent on the strain rate and temperature. For the

DP980 material model in this study, it is assumed that there is no strain rate and temperature effect, so the parameters D_4 and D_5 assumed to be zero, and the fracture strain depends only on the stress triaxiality. Accordingly, material parameters D_1, D_2, and D_3 were considered to be equal to 1.3, 0.5, and 0.5, respectively, for DP980 sheet material. Therefore, the J-C criterion for DP980 turned out to be written as Equation (6.22):

$$\bar{\varepsilon}_f = 1.3 + 0.5\exp\left(-0.5 \times \eta\right) \tag{6.22}$$

For the Oyane criterion, parameters calculated by Wang et al. [181] for DP980 were used in this study. Accordingly, the Oyane fracture criterion was expressed as the following equation [181]:

$$\int_0^{\bar{\varepsilon}_f} (1 + 1.967\eta)\, d\bar{\varepsilon} = 0.874 \tag{6.23}$$

The last fracture criterion examined in this study was the Lou-Huh (L-H) criterion. The fracture loci and material parameters were taken from the research done by Park and Hou [182] for DP980 sheet material in the rolling direction.

Figure 6.23 shows fracture loci for DP980 with respect to the stress triaxiality for all fracture criteria examined in this study. Experimental results, presented as three data points, are also included in the figure. The first three criteria listed in the figure use literature data for the damage curve for DP980 as cited. The last two criteria use the calibrated damage parameters in this study.

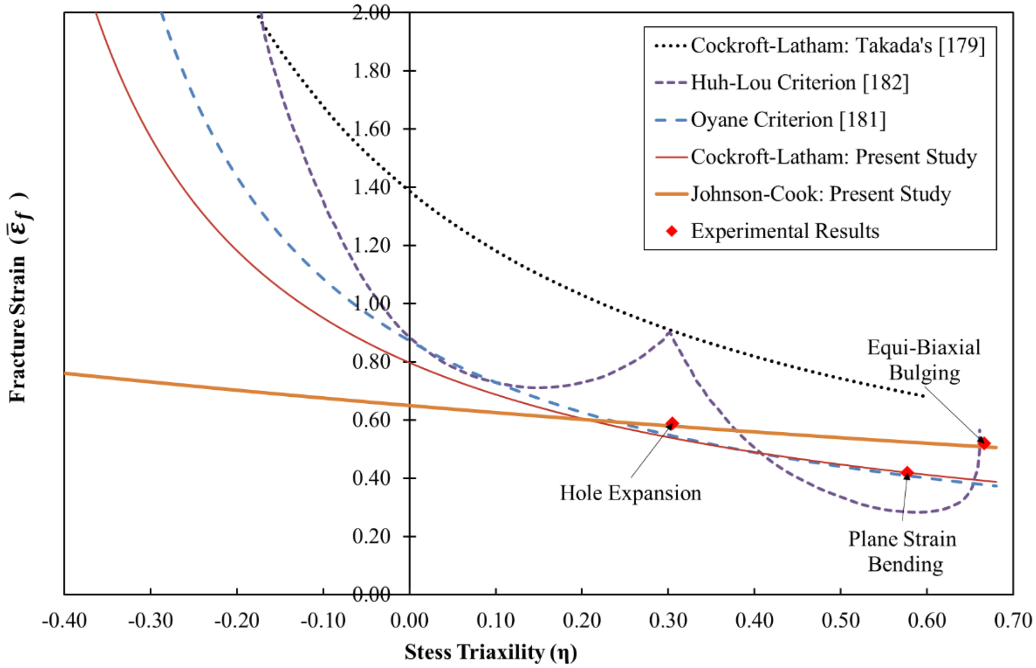

Figure 6.23. Fracture loci for all studied fracture criteria, along with experimental data points for DP980-1 sheet material.

Although none of the studied fracture criteria matched all experimental results, the Johnson–Cook (J–C) criterion was selected as the most suitable model for further analysis. The first reason for this choice is its ability to accurately describe fractures under both hole expansion and equi-biaxial bulging conditions, which represent the extremes of stress triaxiality commonly encountered in automotive forming and trimming operations. Additionally, using the calibrated Johnson–Cook (J–C) criterion, we were able to replicate the sheared edge profile observed in the trimming experiments on DP980-1 across different cutting clearances.

In addition to direct calibration of damage parameters through controlled experiments, as performed in the present study, some researchers have adopted a reverse engineering approach. Gutknecht et al. [183] calibrated the damage parameter, *D,* by correlating the experimentally measured burnish zone height of DP600 steel with the corresponding finite element simulation results.

6.1.9. Mechanical Properties of D2 Tool Steel

For the second simulation case, where the trimming tools are deformable and loads and stresses on the tools are of concern, the mechanical properties and flow curve of D2 tool steel are required. In the absence of experimental mechanical data for our D2 tool steel, the literature data have been used to estimate the mechanical properties. The existing literature data for the yield strength and tensile strength of D2 are listed and plotted against the hardness value, as shown in Figure 6.24 and Figure 6.25 [184]–[192].

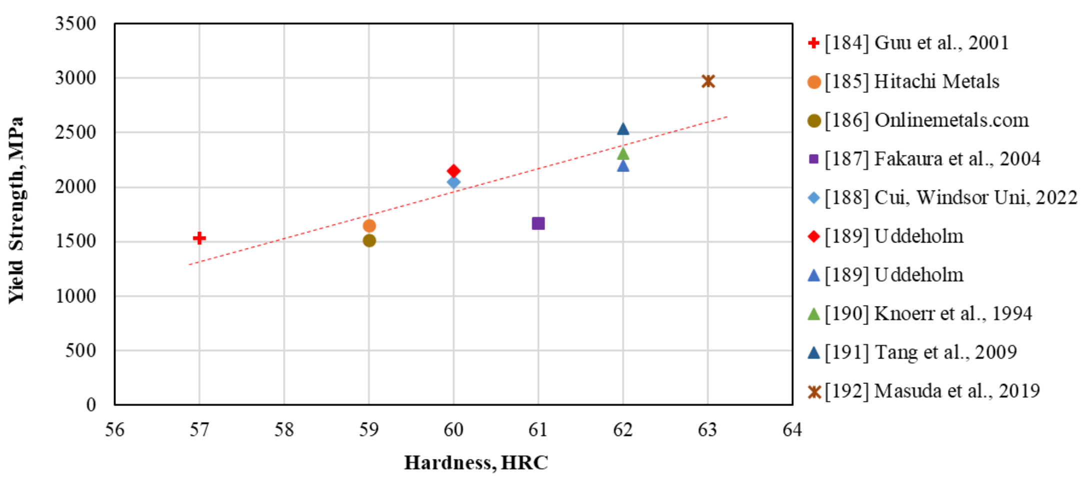

Figure 6.24. Literature data on the yield strength vs. Rockwell hardness for D2 tool steel.

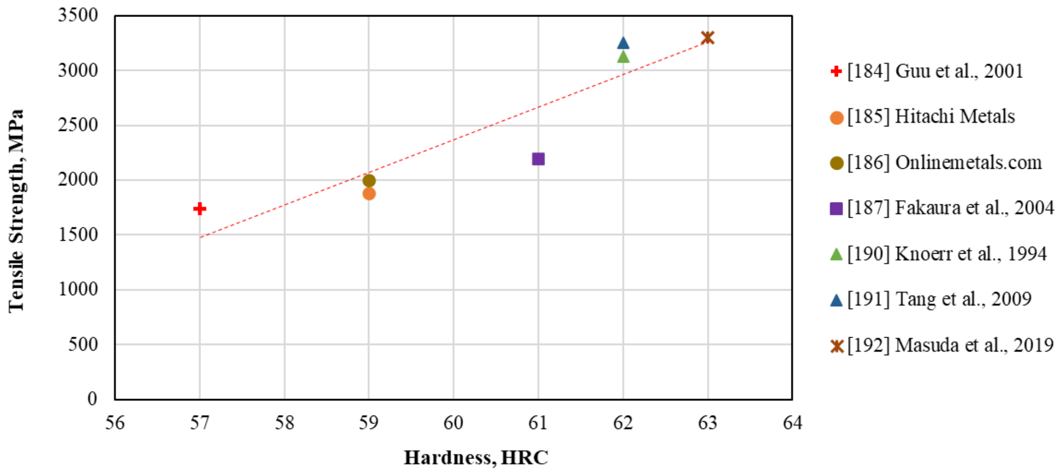

Figure 6.25. Literature data on the tensile strength vs. Rockwell hardness for D2 tool steel.

To compare with the literature data, the Rockwell hardness of our D2 trimming inserts at several locations near the trim edge was measured. In total, 30 locations were examined, 15 locations on the side wall and 15 locations on the side face, as shown in Figure 6.26, and the results are plotted in Figure 6.27.

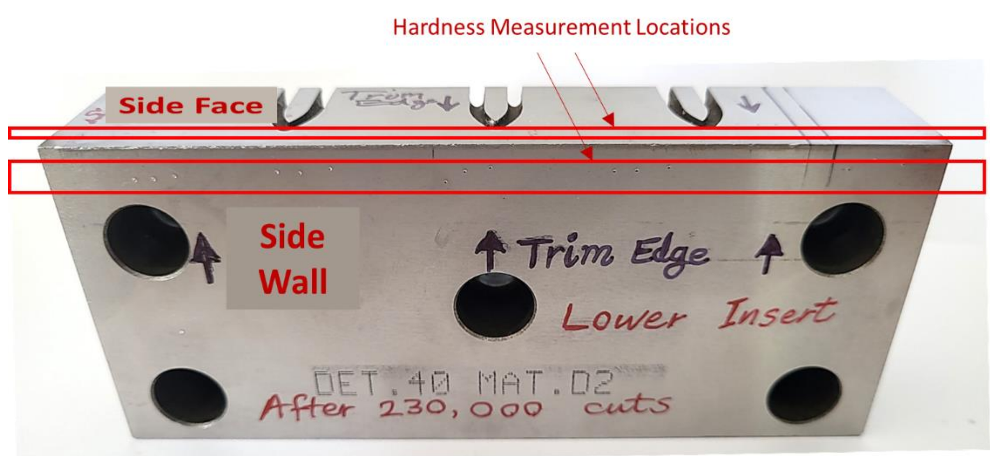

Figure 6.26. Hardness measurement locations on the side wall and side face of the lower D2 trimming insert.

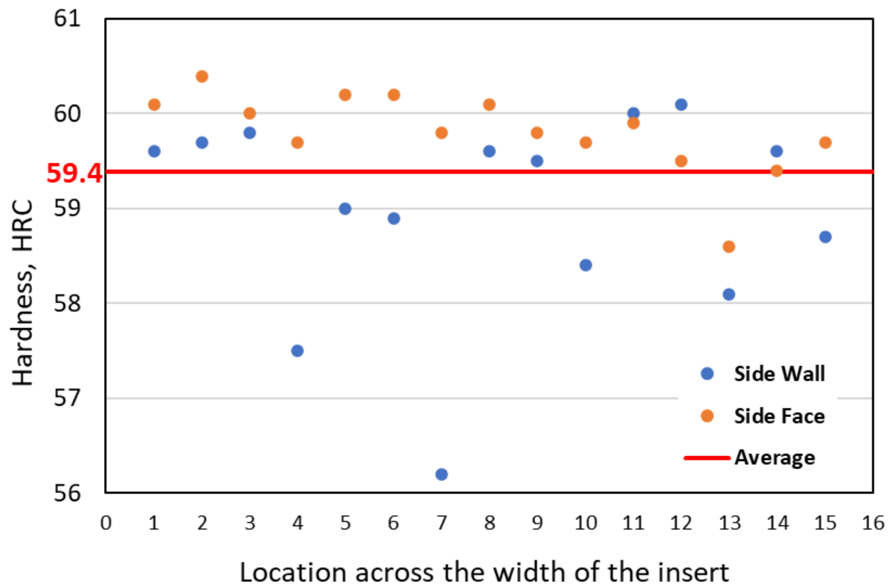

Figure 6.27. Measured Rockwell C hardness across the width of the D2 lower trimming insert in the near vicinity of the trim edge.

The average hardness of the lower D2 insert was measured at 59 HRC, equivalent to 684 HV and 645 Brinell. Using the graphs in Figure 6.24 and Figure 6.25, the mechanical properties of D2 tool steel are selected as listed in Table 6.4.

Table 6.4. Selected mechanical properties for D2 tool steel.

Mechanical property	Yield Strength σ_y (MPa)	Ultimate Tensile Stress σ_u (MPa)	True Fracture Strength σ_f (MPa)
D2 tool steel	1820	2190	2624 [193]

The flow curve for D2 steel in the plastic region, as the Abaqus input, is also illustrated in Figure 6.28.

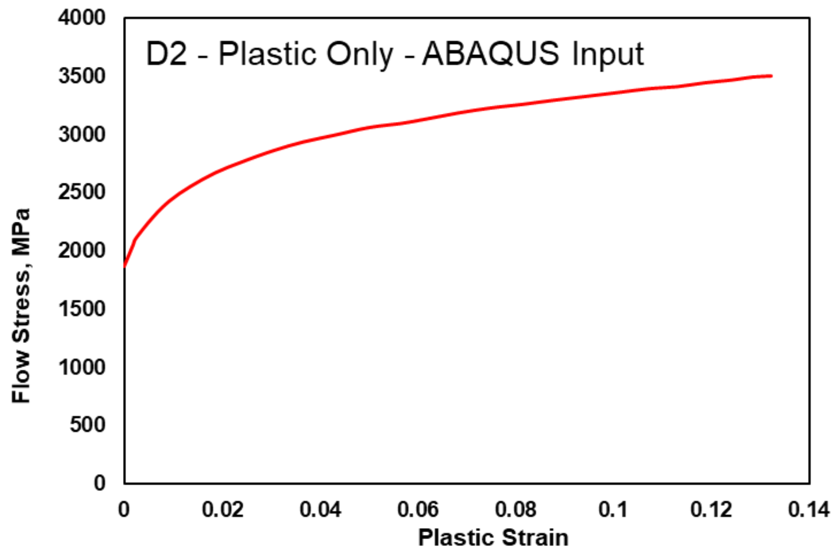

Figure 6.28. Flow curve for D2 tool steel in the plastic range for FEA.

6.2. Mesh Penetration and Contact Issues in Simulations with Deformable Tools

For the rigid tool case, the penalty contact algorithm worked well with acceptable outcomes. However, when applying the same contact properties, as described in Section 6.1.2, to the simulation case with deformable tools, mesh penetration was observed at the sheet–tool interface. Figure 6.29 and Figure 6.30 show the Abaqus results of the maximum equivalent stress on the upper and lower trimming tools during the trimming operation, respectively. The penetration of the tool meshes into the sheet is also visible in the figures. The calculated stress level indicates that both the upper and lower tools would undergo plastic deformation within the first trimming cycle, which contradicts actual experimental evidence, as no such failure occurs in practice.

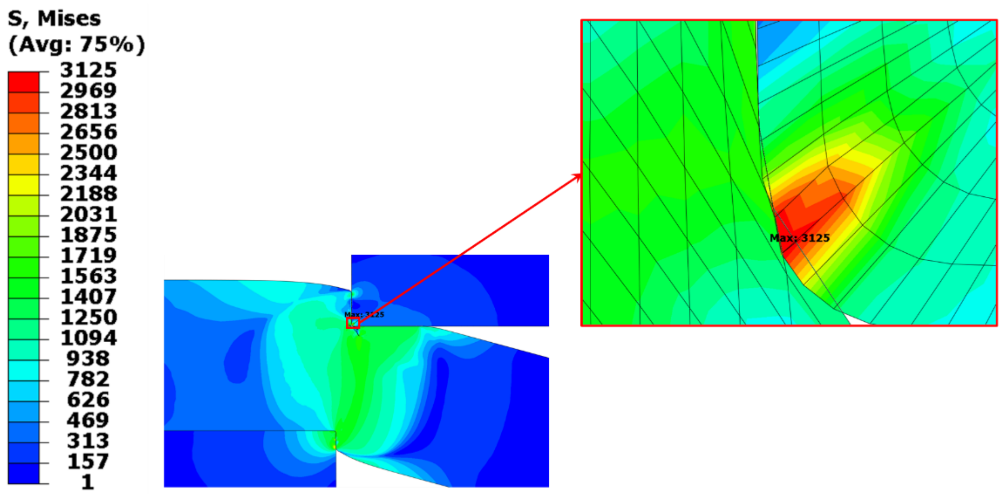

Figure 6.29. Maximum von Mises stress distribution on the upper trimming tool at a displacement of 0.43 mm.

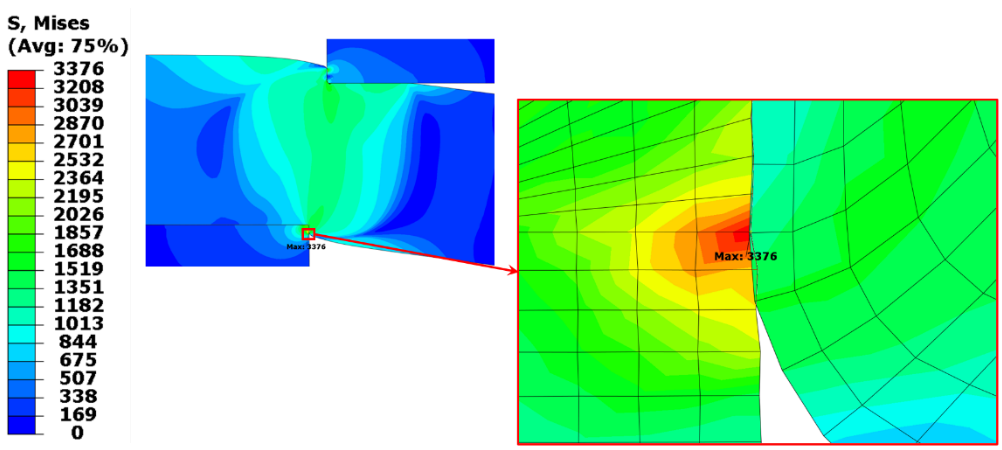

Figure 6.30. Maximum von Mises stress distribution on the lower trimming tool at a displacement of 0.25 mm.

This penetration had a profound impact on the predicted tool stresses. Specifically, the local contact stress on the trimming tool exceeded the yield strength of the D2 die material, which is not consistent with experimental evidence. In reality, the same die material withstood over 200,000 trimming strokes before local failure was observed, indicating that the predicted tool stresses were non-physical and caused by numerical issues.

Additional efforts were made to reduce penetration by refining the tool mesh, especially in the corner region of the punch and die, where contact with the sheet is most intense. By maintaining the tool mesh size in the corner similar to the sheet mesh size in the shearing zone, the penetration depth was decreased, and the severity of non-physical contact stresses was lessened; however, the problem was not completely resolved. The mesh shown in Figure 6.29 and Figure 6.30 are optimized meshes as described in Section 6.1.6.

6.2.1. Evaluation of Alternative Simulation Codes

To address the mesh penetration and non-physical tool loading encountered in Abaqus simulations, two additional commercial finite element (FE) packages were evaluated: SIMUFACT Forming [159] and QFORM [160]. Both codes are widely applied in the forming industry and were expected to offer process-specific features that might mitigate the penetration artifacts observed with the penalty contact algorithm.

6.2.1.1. SimuFact Forming

SimuFact, as a comprehensive simulation package, includes multiple modules, such as SimuFact Forming, which is specially designed for the sheet metal forming industry. In the trimming simulations performed with SimuFact, two different modeling approaches for the tools were investigated: rigid analytical tools and deformable elastic–

plastic tools. Each method has advantages and drawbacks in terms of computational efficiency, physical accuracy, and stability of the contact solution.

Case A, rigid tools – When the trimming punch and die are defined as rigid analytical surfaces, the blank is the only deformable body in the simulation. This assumption eliminates tool compliance and ensures that the tools do not deform under the applied forces. The primary advantage of this approach is its computational robustness and efficiency, as the solver is not required to account for tool material behavior.

The contact pressure distribution along the cutting edge just before fracture initiation in the sheet is shown in Figure 6.31. The close-up views reveal mesh penetration issues: the sheet elements seem to “cut through” the rigid tool surface because the penalty-based contact algorithm allows slight interpenetration to enforce contact. While the overall trimming behavior can still be captured, force prediction and fracture initiation sites may not accurately reflect physical reality.

Although rigid tools simplify calculations and prevent tool deformation artifacts, they cannot replicate the local compliance of the dies. This often results in unrealistic stress peaks and inaccuracies in force prediction, especially around sharp corners where mesh mismatch is significant.

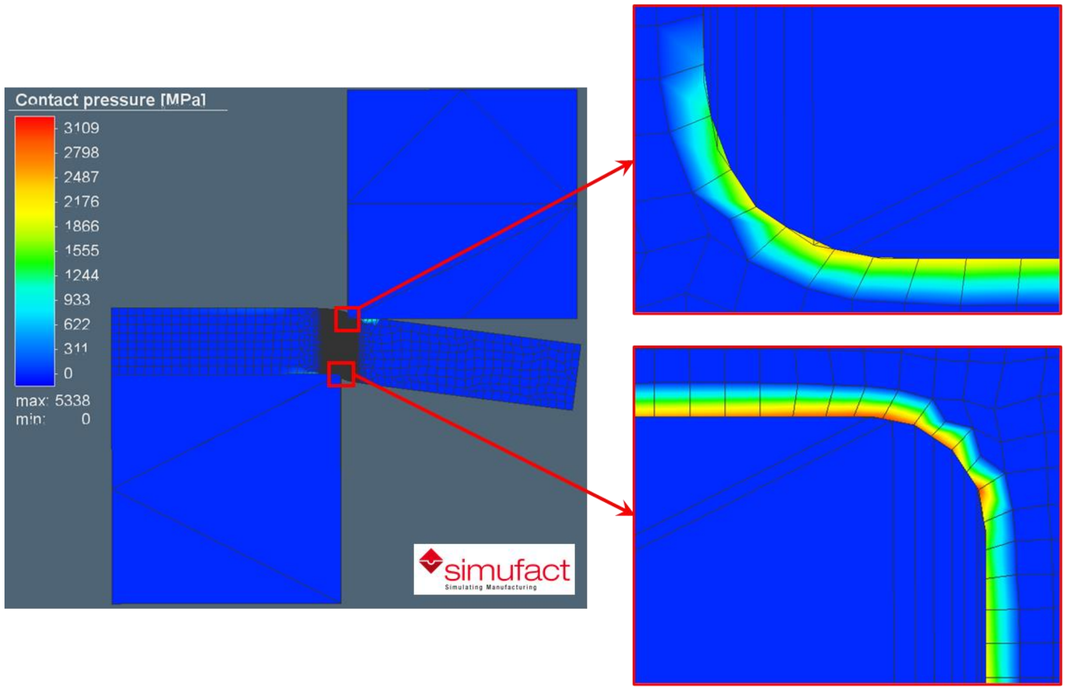

Figure 6.31. Contact pressure distribution along the cutting edge just before fracture initiation in the sheet for the rigid tools simulation case.

Case B, deformable tools – In the second approach, the trimming punch and die were modeled as deformable solids with the properties and flow curves described in Section 6.1.8. This method enables a more accurate distribution of stress transfer between the blank and the tools, thereby reducing the artificial rigidity introduced in Case A. In principle, this should allow for more precise predictions of local stress and strain conditions in the shearing zone. The contact algorithm used in this model was a penalty type with node-to-segment contact attributes.

Figure 6.32 shows the contact pressure distribution along the cutting edge just before fracture initiation in the blank sheet for case B. The results show that deformable tool modeling causes non-physical tool overloading due to ongoing penetration issues in the contact algorithm. Contact pressures reaching as high as 9,500 MPa were recorded, significantly exceeding the actual strength of D2 tool steel. As a result, the dies were predicted to deform plastically during the very first stroke, which does not happen under real trimming conditions. This reveals a major numerical artifact: the combination of penalty contact enforcement and inadequate mesh compatibility between the tool and blank encourages unrealistic stress buildup and tool yielding.

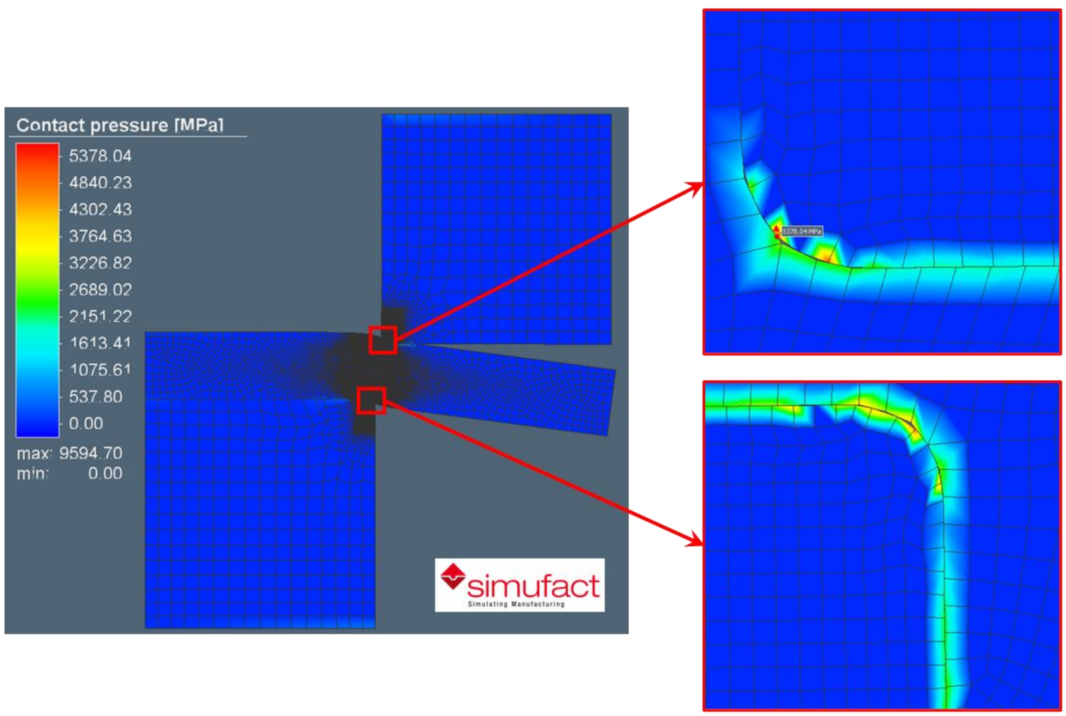

Figure 6.32. Contact pressure distribution along the cutting edge just before fracture initiation in the sheet for the deformable tools simulation case.

6.2.1.2. QForm

QForm is another commercial FE package frequently used in metal forming simulations. Similar to Abaqus, QForm is capable of utilizing both implicit and explicit integration schemes, making it suitable for quasistatic as well as high-rate contact interactions. With explicit time integration, the solver can capture transient events and sharp contact interactions without needing prohibitively small time steps. The software was developed for industrial process design, where quick turnaround is essential [160]. It also employs parallelization (multi-core CPUs) and efficient data/task partitioning to reduce solving time [194]. For these reasons, the software was selected to test smaller mesh sizes in the sheet–die contact region, especially in the shearing zone and tool corners where penetration artifacts are most severe.

In this work, multiple explicit simulation cases with different mesh sizes were tested, and the finest mesh was chosen for analysis. For this study, a 0.002 mm mesh was used for the sheet and a 0.001 mm mesh for the dies, providing high resolution at the contact interface. Contact is modeled using a penalty formulation with a coefficient of friction of 0.1, corresponding to Coulomb friction.

The equivalent stress distribution in the trimming tools during the initial steps of the trimming process is shown in Figure 6.33. The zoomed-in views reveal that there are local stress risers due to mesh penetration exceeding the yield strength of D2 steel. As shown in Figure 6.34, for the upper tool, the resulting overloading and highly exposed stresses cause plastic deformation in the tool just after the first stroke.

Although the explicit solver and fine mesh resolution offered advantages in

QForm software, mesh penetration at the sheet–tool interface remained a problem, and unrealistic stress concentrations were still predicted in the dies.

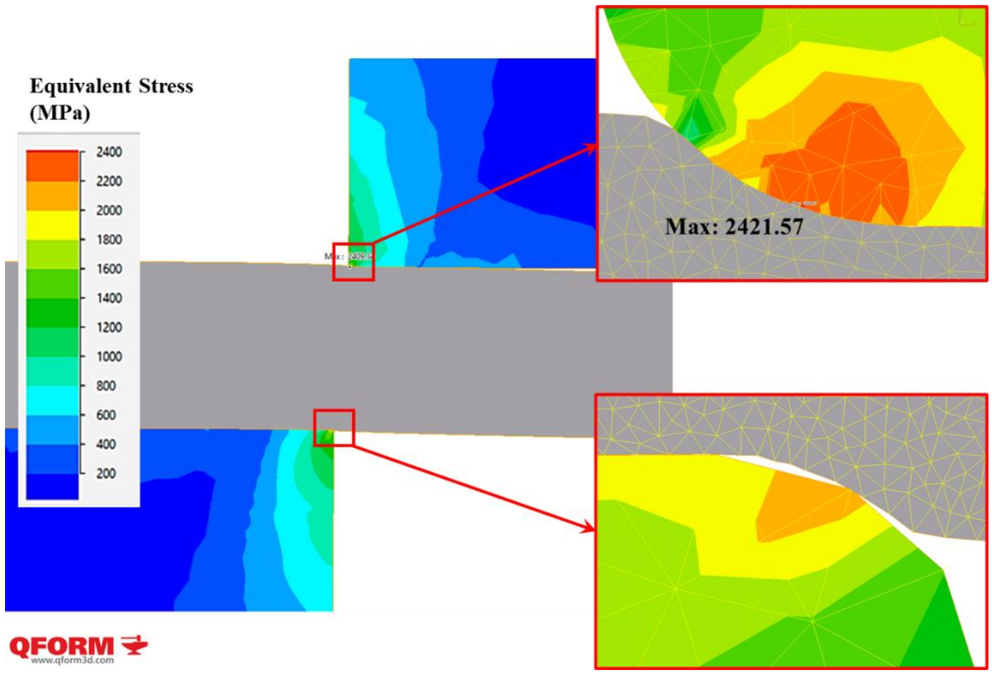

Figure 6.33. Equivalent stress distribution in the trimming tools, with zoomed-in views of the upper and lower tool corners.

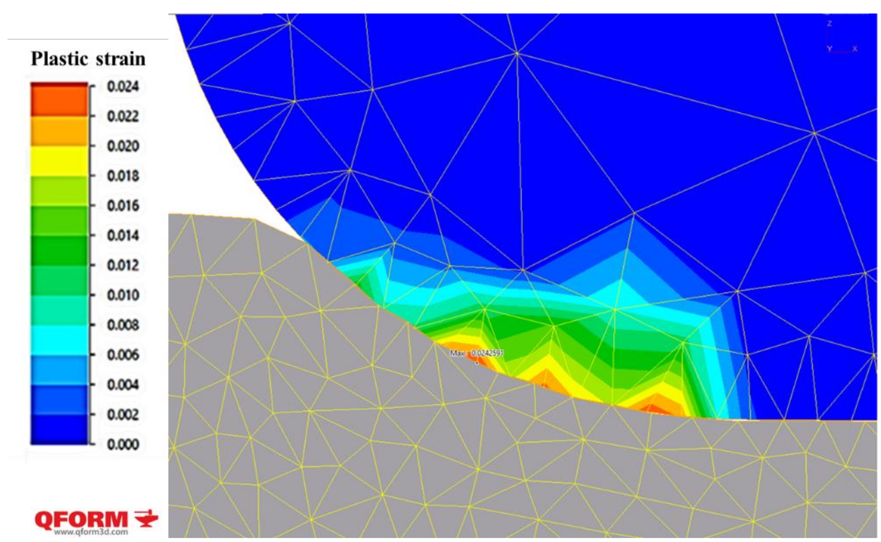

Figure 6.34. Plastic strain contour of the upper tool in contact with the sheet metal blank.

Table 6.5 summarizes the simulation efforts using various FE codes for the deformable trimming tools, confirming that mesh penetration occurs in all cases.

Table 6.5. Comparison of FE models evaluated for trimming simulations of DP980 steel with deformable tools.

Feature / Aspect	Abaqus/Explicit	SimuFact Forming	QForm
Solver type	Explicit dynamic, general-purpose FE	Explicit dynamic, forming-specialized	Explicit dynamic, forming-specialized
Tool modeling	Elastoplastic	Elastoplastic	Elastoplastic
Applied contact algorithm	Node-to-surface, Penalty	Node-to-segment, Penalty	Node-to-surface, Penalty
Mesh control	ALE remeshing, adaptive remeshing	ALE remeshing, adaptive meshing	Very fine mesh definition
Fracture/damage modeling	Johnson–Cook and others (user-calibrated)	Built-in fracture criteria (J–C)	User-defined fracture
Strengths	Flexible material models, widely validated	Tailored for forming, easier setup, ALE	Lighter explicit solver, very fine mesh control
Observed issue	Penetration, unrealistic tool stresses	Penetration persisted, with the highest stress levels	Penetration persisted, plastic strain in dies

One similarity between models in Table 6.5 is the use of a penalty-based contact algorithm between the DP980 blank and D2 tool steels. The penalty algorithm works by enforcing contact through the application of an artificial spring stiffness between the contacting surfaces. When penetration occurs, the restoring force is proportional to the depth of penetration and the chosen penalty stiffness. If the stiffness is too low, penetration is excessive, while if the stiffness is too high, the system becomes unstable.

In trimming simulations involving ultra-high-strength steels and very fine tool radii (e.g., R = 0.02 mm), the penalty algorithm seems to allow some penetration.

6.2.2. Kinematic Contact Algorithm

To observe the contact algorithm's effect, the kinematic contact algorithm was also applied in the Abaqus/Explicit model without changing material properties, loading, or boundary conditions. Unlike the penalty method, the kinematic algorithm strictly enforces the non-penetration condition by adjusting the positions of contacting nodes to prevent overlap [158].

The results show substantial improvement in minimizing the mesh penetration. Contact was satisfied without overlap of the workpiece and tool meshes, resolving the numerical artifacts caused by the penalty method. Figure 6.35 shows the von Mises equivalent stress distribution in all deformable bodies with a zoomed-in view of the lower tool at the upper tool displacement of 0.22 mm, when the stress levels are at their maximum just before fracture initiation in the sheet metal. As seen in the zoomed-in view, the mesh penetration is minimal, resulting in more realistic stress predictions. The von Mises equivalent stress is calculated using Equation (6.24):

$$\bar{\sigma} = \frac{1}{\sqrt{2}}\sqrt{[\,(\sigma_1 - \sigma_2)^2 + (\sigma_2 - \sigma_3)^2 + (\sigma_3 - \sigma_1)^2]} \tag{6.24}$$

Additionally, Figure 6.36 displays the stress history for the lower trimming tool from the start to the upper tool displacement of 0.30 mm, which corresponds to the experimental indentation depth for fracture initiation in the sheet. Maximum stresses in the D2 tools were brought within reasonable limits, potentially improving the estimated fatigue life.

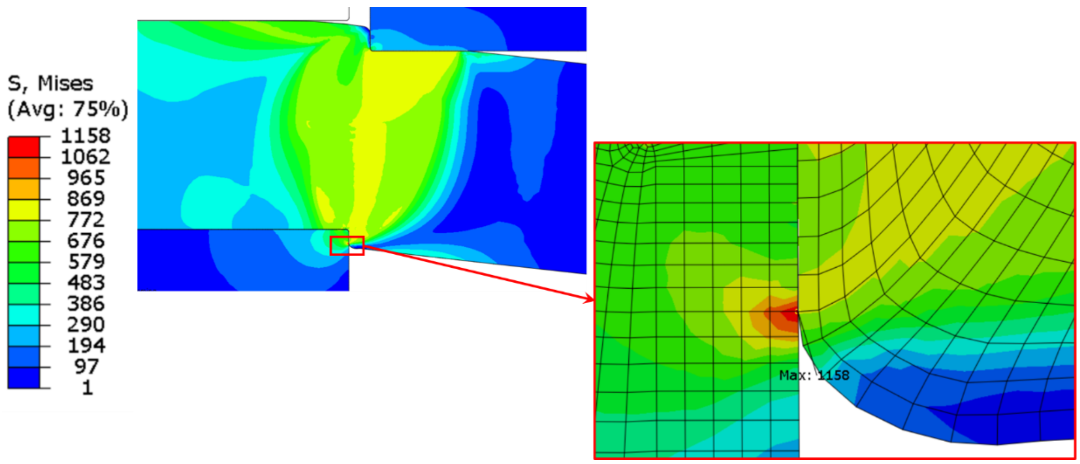

Figure 6.35. von Mises equivalent stress distribution on the sheet and trimming tools, with a zoomed-in view of the lower tool at the upper tool displacement of 0.22 mm, using the Kinematic contact algorithm.

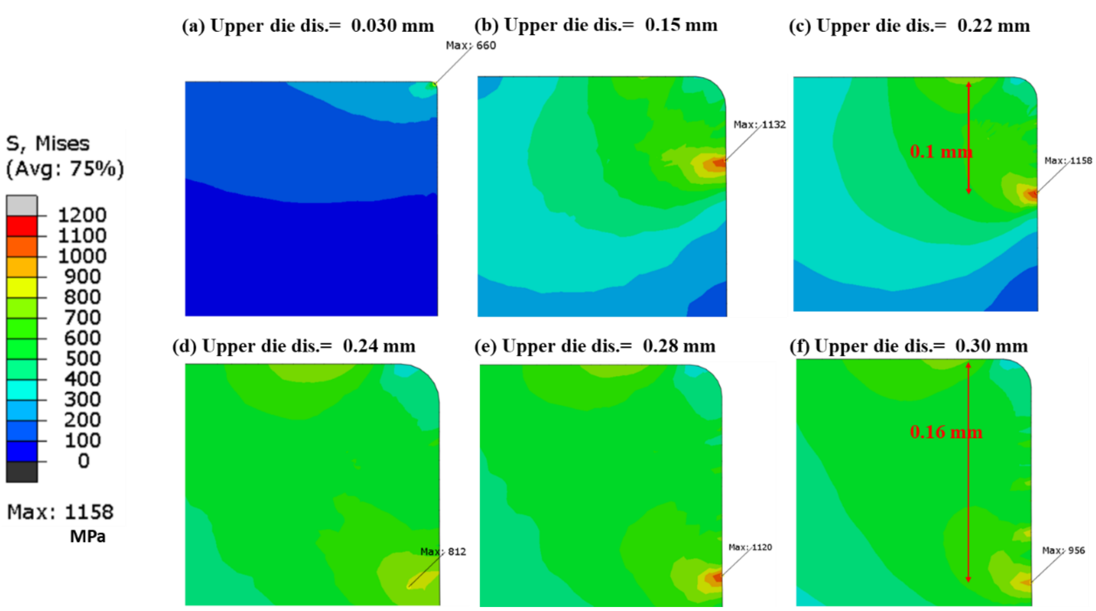

Figure 6.36. von Mises equivalent stress history on the lower trimming tools, with the maximum stress and its location identified in each step.

The findings of this study highlight the sensitivity of trimming simulations to the selection of contact algorithms. While the penalty method is widely used by other researchers [195]–[198], it failed to provide reliable results in our simulation involving high-strength DP980 steel, deformable trimming tools, and fine tool radii. However, in our case, the kinematic algorithm produced more reasonable and physically consistent results for stresses and loads on the tools, which were then used in the fatigue life prediction of the tools.

6.3. Finite Element Results

Figure 6.37 shows the simulated force–displacement curves obtained from the finite element model for different trimming clearances ranging from 4% to 40% of the sheet thickness. At smaller clearances (4% and 10%), the curves show higher peak forces, indicating increased tool loading and sharper force drops after crack initiation. As clearance increases, the peak trimming force decreases, and the curves become smoother with more gradual force declines, reflecting reduced tool–sheet interaction and lower cutting resistance. These trends highlight the significant impact of clearance on both the magnitude and development of trimming forces during the trimming process of DP980-1 steel sheets.

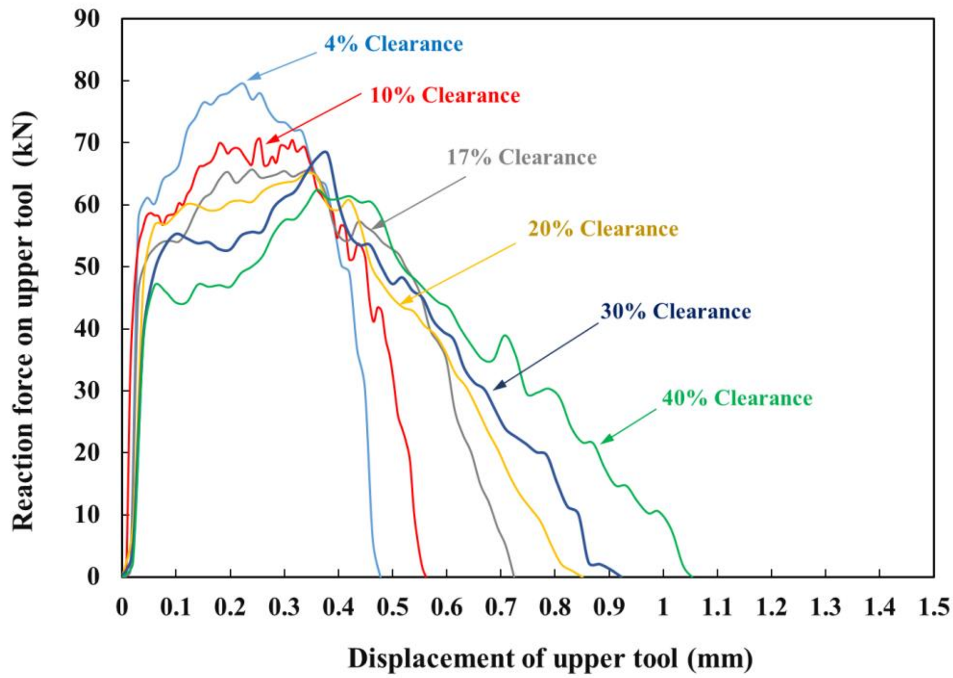

Figure 6.37. FE results of trimming force for various trimming clearances.

The experiments were carried out on a mechanical trimming press equipped with a tonnage monitor that recorded the maximum force using four sensors mounted at the corners. To determine the pure trimming force, the press was first operated without any sheet material, and the baseline load—including the blank holder, cushion, nitrogen cylinders, and frictional forces—was recorded. Then, trimming tests with sheets were performed at each clearance setting for about 30 runs, and the average force was calculated. The baseline force measured without the sheet was subtracted from these averages to find the net trimming force. These calculated trimming forces are compared with the simulated maximum forces in Figure 6.38.

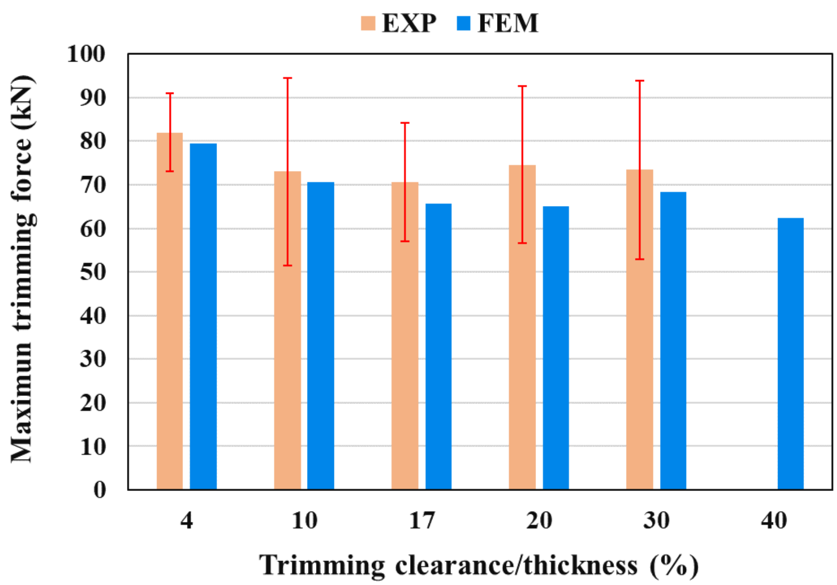

Figure 6.38. Comparison of FE and experimental results of maximum trimming force at different clearances.

The results show that the FE model reasonably captures the overall decreasing trend in the maximum trimming force as the clearance increases. At lower clearances, the simulation results closely match the experimental data. In comparison, at higher clearances, some deviations occur, but they remain within the experimental scatter range indicated by error bars. Overall, modeling results in lower maximum trimming forces than the experimental due to model simplifications, including the lack of realistic material behavior, the assumption of constant friction, and the use of perfectly rigid tool conditions. Conversely, the experiments inherently included additional resistance sources, such as variable friction, tool deflection, and press dynamics, resulting in higher measured forces. Also, in reality, the horizontal (lateral) forces are significant and can contribute to the recorded maximum trimming force.

Figure 6.39 shows a comparison of experimentally measured and FEM-predicted indentation depths as a function of cutting clearance for DP980-1 steel. The experimental data are averaged from multiple samples, with error bars indicating measurement variability. In both datasets, the indentation depth increases with larger cutting clearance, reflecting more plastic deformation and localized material displacement near the die corner as the clearance widens.

Although the simulation captures the overall trend observed experimentally, the FEM results consistently underestimate the indentation depth. Among the factors influencing this, the fracture criterion used in the numerical model has a particularly strong effect on the predicted indentation behavior. The critical strain for damage initiation and parameters governing damage evolution determine how quickly material separation occurs in the shear zone. While the Johnson–Cook fracture criterion calibrated for DP980-1 in this study shows reasonable correlation, there is still room to improve the match with the experimental indentation depth, especially at larger clearances where strain localization and triaxial stress states are more prominent. Besides the fracture and damage parameters, several other factors influence the indentation depth and its agreement with experimental results. These include the constitutive material behavior, friction coefficient at the sheet–die interfaces, mesh resolution near the contact zone, clearance ratio, and assumptions about tool rigidity. Each of these elements contributes to the predicted indentation response, though their impacts vary.

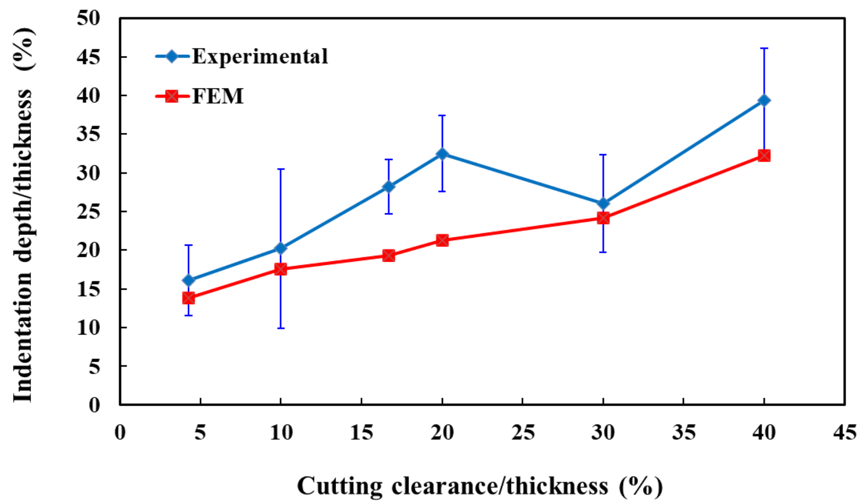

Figure 6.39. Comparison of FE and experimental results of penetration depth at different clearances for DP980-1.

6.4. Mechanism of Fracture in Trimmed DP980

An ideal separation mechanism for shearing and blanking was described earlier by Johnson and Slater [65] and addressed lately by Suchy [199], in which two cracks initiate from the cutting edges of the upper and lower dies and propagate through the sheet blank thickness. When these two cracks intersect, a relatively smooth sheared edge is created. The sheet blank should not be bent substantially during the shearing process to achieve this ideal mechanism. In automotive manufacturing, stamping of rather large body components often results in bending of scrap, which affects the fracture mechanism. Accordingly, one single crack initiates and propagates from the moving cutting edge of the tool.

Partially sheared DP980-1 sheets under 10% and 40% clearances are shown in Figure 6.40 (a) and (b), respectively. As the trimming process starts, the sharp edge of the moving tool penetrates the blank material, deforms it plastically, and applies the bending load in the direction of displacement of the moving edge. Figure 6.40 (a) for 10% clearance represents the stage right before the crack initiation. In relatively small cutting clearances, the initiated crack can propagate toward the stationary cutting edge, leaving the severely deformed material region on the scrap side of the sheet. This mechanism is desirable from the perspective of the stamped blank. However, a small increase in clearance leads to the formation of burrs, characterized by a thick, severely deformed portion. This scenario is very typical for Aluminum blanks, as described by Wang and Golovashchenko [88], as well as for other steel grades, including DP500 and DP600, reported by Golovashchenko and Ilinich [37].

However, a very different fracture mechanism was observed for DP980 steels: the burr showed the tendency to break under the bending loads during the final stage of the trimming process, which is demonstrated in Figure 6.40 (c) for DP980-1 trimmed at 40% clearance. In this regard, the heavily deformed fragment of material extruded around the lower trimming edge was mainly shifted toward the scrap side. Consequently, the burr was being removed from the trimmed edge of the part, and, therefore, increasing the trimming clearance for DP980 steels did not lead to a significant increase in burr height.

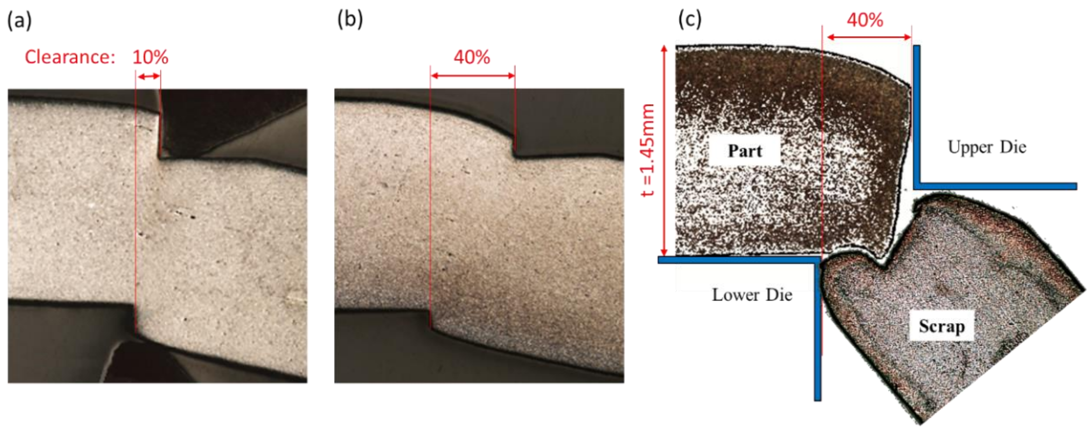

Figure 6.40. (a) Partial trimming process of DP980-1 under 10% clearance; (b) partial trimming process of DP980-1 under 40% clearance; (c) cross-section of the fully separated part and scrap of DP980-1 under 40% clearance.

At higher clearances, two factors improve burr removal during DP980 trimming. First, as the upper tool's indentation increases, the material near the lower edge experiences compressive stresses that can prevent the initiation of a second crack at the lower tool's edge. Figure 6.41 helps to illustrate the shear, tensile, and compressive stresses during the shearing process. Second, as the clearance increases, the bending of the scrap becomes more effective, helping to break the burr.

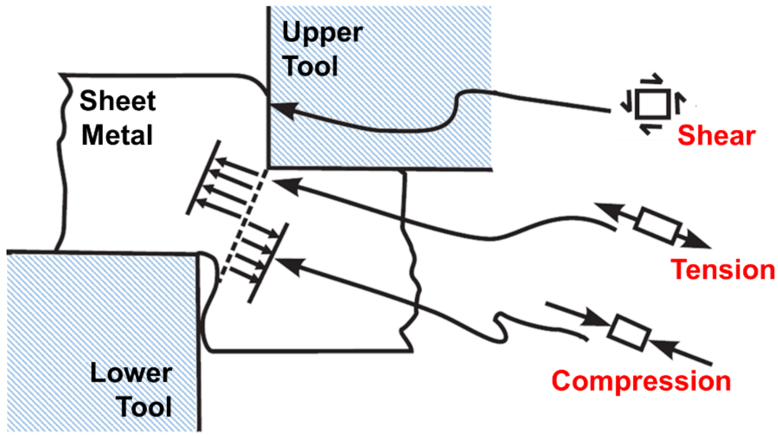

Figure 6.41. Shear, tensile, and compressive stress during the trimming process.

The predicted trimming sequence for DP980-1 trimmed under 40% clearance is summarized in Figure 6.42. The color contour indicates the accumulated damage (*D*) during the trimming process. Due to strain localization and damage concentration near the corner of the upper tool, the first crack initiates at a penetration of 0.46 mm. The crack formation site at this stage is subjected to a local tensile stress condition with positive stress triaxiality ($\eta \approx 0.57$), as occurs during a plane-strain tension test. This is illustrated in Figure 6.43 (a) for DP980-1 trimmed with 40% clearance. Notably, during trimming, as the upper fiber of the sheet is under tension, the corresponding stress triaxiality is approximately 0.57.

Further penetration of the upper tool and bending down of the scrap open up the propagated crack until penetration reaches 1.01 mm, at which point the secondary crack initiates from the corner of the lower tool, and the first propagated crack tends to turn toward it. The portion of the blank near the lower tool is under compression, as shown in

Figure 6.43 (b). Later, burr removal occurs when the secondary crack propagates along the curved path and meets the main propagated crack. As a result, the trimmed edge of DP980 is left with a broken burr, as previously shown in the experimental cross-sections.

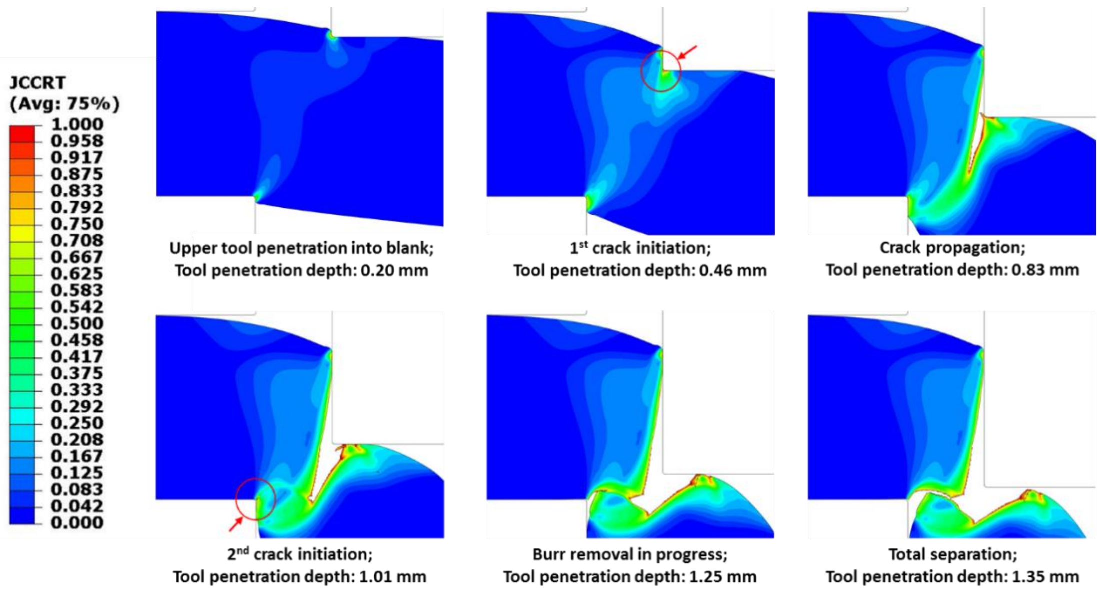

Figure 6.42. The results of FE modeling of the trimming process of the DP980-1 sheet with 40% clearance. The contour shows the accumulated damage during the trimming process.

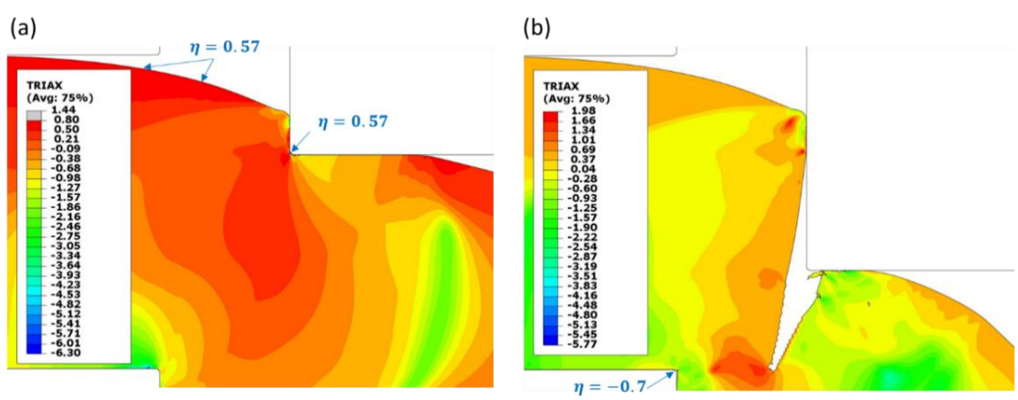

Figure 6.43. Stress triaxiality at the time of initiation of (a) the first crack from the upper edge and (b) the second crack from the lower trimming edge.

6.5. Results of Damage Accumulation

The FE results of the trimmed edge profile for clearances of 4, 10, and 40% are shown in Figure 6.44. The color contour in this figure represents the accumulated damage. Arrows in the figure show the locations where damage is more accumulated and is deeper. Interestingly, for 4% clearance, highly damaged areas are the bottom of the burnish and the burr zones, where the cracks are initiated during the stretching, as shown before in Figure 5.22. For 10% clearance, the same correlation is observed, i.e., the crack initiation site and the highly damaged zone are located in the middle of the trimmed edge, where the fracture surface and the cross-hatch lines are formed. For the largest clearance, 40%, even though the burr is broken off, the most accumulated damage happens at the burr zone, and cracks always initiate from there and propagate very fast, resulting in lower stretchability.

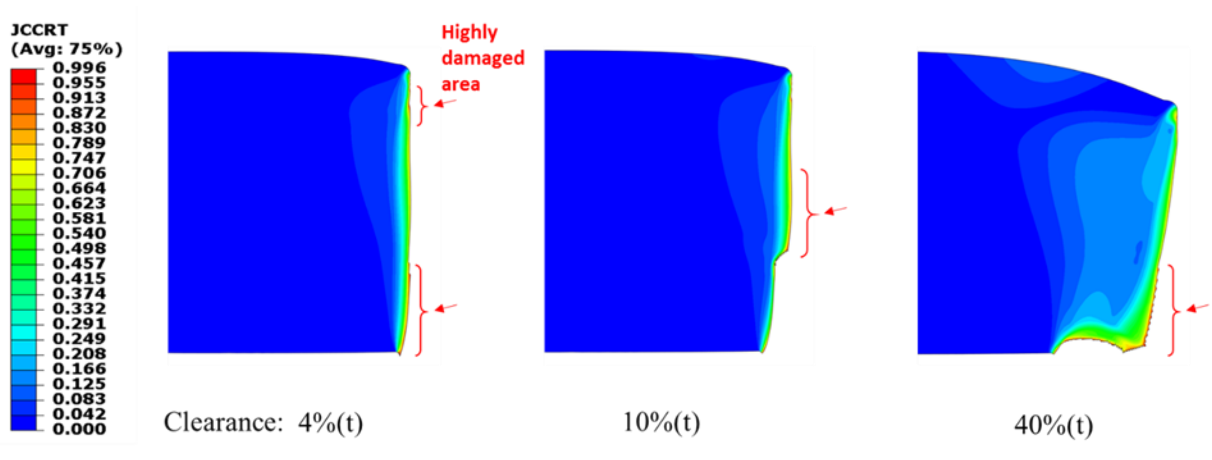

Figure 6.44. FE simulation results of accumulated damage on the trimmed edge of DP980-1 with clearances of 4%, 10%, and 40%.

6.6. Summary

This chapter describes the development of a finite-element (FE) model for trimming DP980 steel, with a focus on strain distribution, fracture behavior, and tool stresses. ABAQUS/Explicit was used as the main solver. Two modeling approaches were explored: (i) rigid tools to study strain localization, damage buildup, and crack growth, and (ii) deformable tools to assess load histories and stress conditions within the dies.

The blank was modeled using plane-strain quadrilateral elements with finer meshing in the shear zone where deformation concentrates. ALE smoothing and adaptive remeshing maintained mesh quality under high strains. A mesh sensitivity study showed that at least 100 through-thickness elements were needed for stable results. Ultimately, 145 elements were chosen as the best balance between accuracy and computational efficiency. For the deformable die case, refining the mesh at tool corners was also crucial for capturing stress gradients and providing reliable data for fatigue analysis.

Since trimming involves strains much greater than those in standard tensile tests, extended flow curves were obtained through sequential rolling followed by tensile testing, providing constitutive data across a wide strain range. Mechanical properties of the D2 trimming tools were estimated from hardness measurements and existing literature. Fracture modeling employed several ductile fracture criteria, calibrated through experimental tests.

A major challenge was mesh penetration at the sheet–tool interface in deformable tool simulations. Penalty contact algorithms caused non-physical stress peaks that exceeded the yield strength of D2 steel, which was inconsistent with experimental die life. Similar issues appeared in SIMUFACT and QFORM codes. Switching to the kinematic contact algorithm in ABAQUS reduced penetration and generated more realistic stress distributions. These corrected stress histories served as the basis for fatigue life predictions discussed later.

Damage contour maps indicated that crack initiation depends on clearance: at 4%, cracks began near burr zones; at 10%, in the mid-thickness region; and at 40%, again near the burr, where cracks grew quickly but burr height remained limited.

In conclusion, the study developed a validated framework for trimming DP980 using FEA. Key elements included refined meshing, extended flow curves, Johnson–Cook fracture criteria, and kinematic contact modeling. The model explained DP980's unique burr-breaking behavior, matched experimental force–clearance trends, and produced reliable tool stress histories for fatigue analysis—creating a solid predictive tool for UHSS trimming processes.

CHAPTER SEVEN
ANALYSIS OF TRIMMING DIE DEGRADATION

Analyzing the degradation of trimming tools is crucial for extending tool life, maintaining consistent product quality, and reducing production costs. The main types of degradation include abrasive wear, adhesive wear, fatigue cracking, and edge chipping, all of which are influenced by the properties of the die and sheet materials, process settings, and surface conditions. With the growing use of ultra-high-strength steels like DP980, these failure modes have become more pronounced due to increased cutting forces, high stress concentrations, and the presence of a hard martensitic phase in the microstructure.

In this chapter, the wear behavior of trimming tools in contact with DP980 steel is examined through optical microscopy, profilometry, and visualization techniques. The influence of tool wear on sheared edge quality and stretchability performance is then analyzed.

Next, the fatigue behavior of trimming tools is analyzed using a theoretical framework based on finite element results to estimate the tools' fatigue life. Also, the mechanisms behind fatigue failure are explored to gain a comprehensive understanding of trimming die degradation.

7.1. Characterization of Trimming Tool Wear

Trimming experiments were carried out using an experimental set-up explained in Section 4.2. Both upper and lower trimming tools were made of D2 tool steel. Two DP980 sheets were used: DP980-1 (1.45 mm) and DP980-2 (1.5 mm).

All sheets were trimmed with fresh inserts. Tool wear was simulated by trimming DP980-1 up to 230,000 cuts, with specimens collected every 50,000. The worn tools (230,000 cuts) were then used to trim DP980-2, enabling a comparison of material response under identical wear conditions. The cutting clearance was set at 10% for the wear study, as is common in industrial stamping production.

To evaluate trimming tool wear after prolonged use, both optical microscopy and 3D profilometry were employed following 230,000 cutting strokes. The worn surfaces of the upper and lower tools were examined, with particular attention to the side (vertical) walls, where contact with the sheared edge is most intense. Figure 7.1 shows a schematic of the trimming setup, with the side and face walls of the inserts labeled.

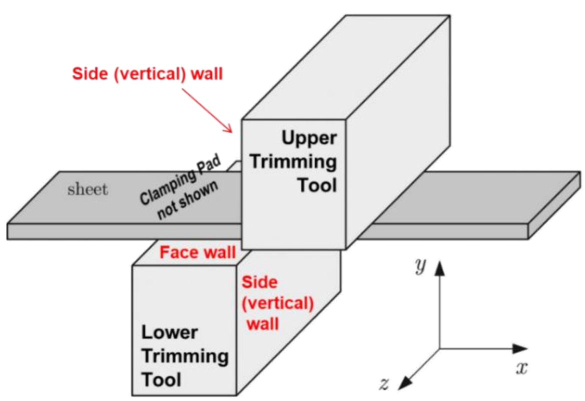

Figure 7.1. Schematic of trimming setup, with the side and face walls of the inserts labeled.

As shown in Figure 7.2, the upper tool exhibited uniform abrasive wear along the vertical wall with minor microchipping, reflecting steady material loss from repeated contact with the sheet but limited mechanical degradation. This wear pattern suggests a consistent sliding interaction between the tool and the sheet edge.

In contrast, the lower tool exhibited severe microchipping, especially along the trimming edge. The pattern and shape of the damage indicate fatigue-induced fracture mechanisms. The lower tool likely experiences higher tensile and shear stress and undergoes more intense cyclic loading while supporting the sheet during trimming. These conditions promote crack initiation and propagation in localized areas. The irregular chip patterns and deeper surface flaws further confirm the brittle nature of fatigue failure and microstructural inhomogeneities.

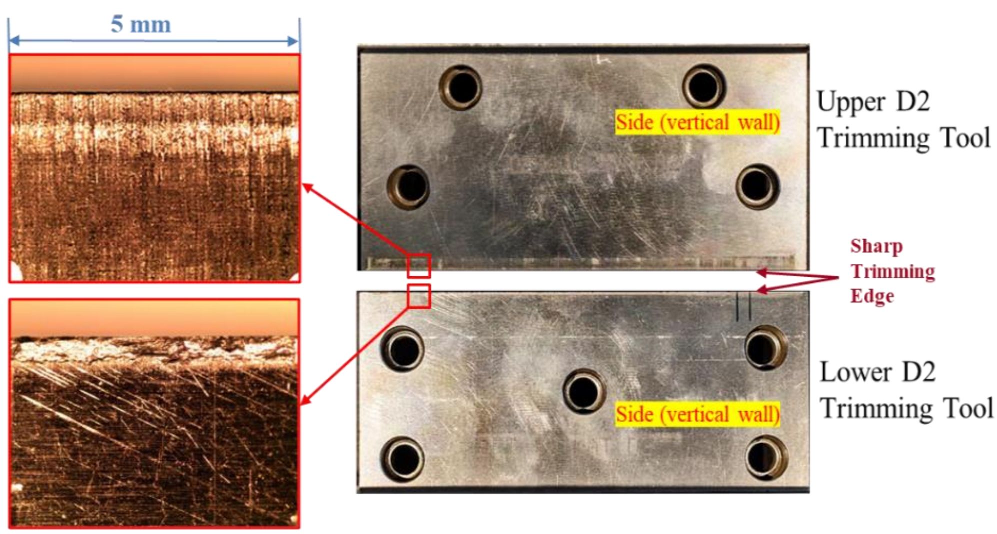

Figure 7.2. Lower and upper D2 trimming inserts after 230,000 trimming cycles, with zoomed-in views of the edge.

To quantify this degradation, surface roughness (Ra) was measured using a Keyence VR-3000 profilometer (Figure 7.3), and the results are presented in Table 7.1. The lower tool exhibited an average surface roughness of Ra = 17.4 μm and peak-to-valley height Rz = 134 μm, indicating significant wear and surface damage. In comparison, the upper tool maintained a noticeably smoother profile. These findings quantitatively confirm the greater severity of tool wear on the lower insert, supporting visual observations of microchipping and abrasive patterns.

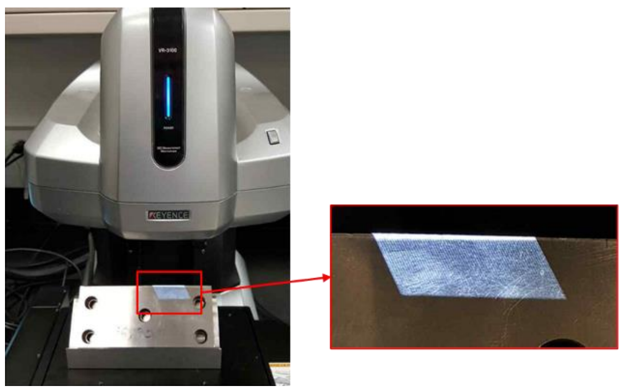

Figure 7.3. Keyence VR-3000 profilometer used in this study.

Table 7.1. Results of profilometry of inserts during high-cycle trimming.

Number of cutting cycles	Average surface roughness (Ra), μm	
	Upper tool	Lower tool
0	0.28	0.28
40,000	1.60	1.39
80,000	2.04	7.86
230,000	5.83	17.4

To complement the visual and roughness-based wear assessment, 3D profilometry was performed to obtain high-resolution surface topography of the tool walls and trimming edges after 230,000 strokes.

Figure 7.4 shows the three-dimensional surface topography of the upper and lower trimming tool side walls and cutting edges. The upper tool displays a relatively smooth and uniform wear pattern, characterized by gradual material removal along the vertical wall and minimal edge irregularities. This type of wear indicates stable contact conditions and primarily mild abrasive wear mechanisms. In contrast, the lower tool surface appears noticeably rougher near the cutting edge, with multiple localized pits, grooves, and valleys suggesting microchipping and fatigue-induced surface degradation. These wear marks are distributed along the entire active cutting edge rather than being confined to isolated areas or points.

Upper trimming tool:

Lower trimming tool:

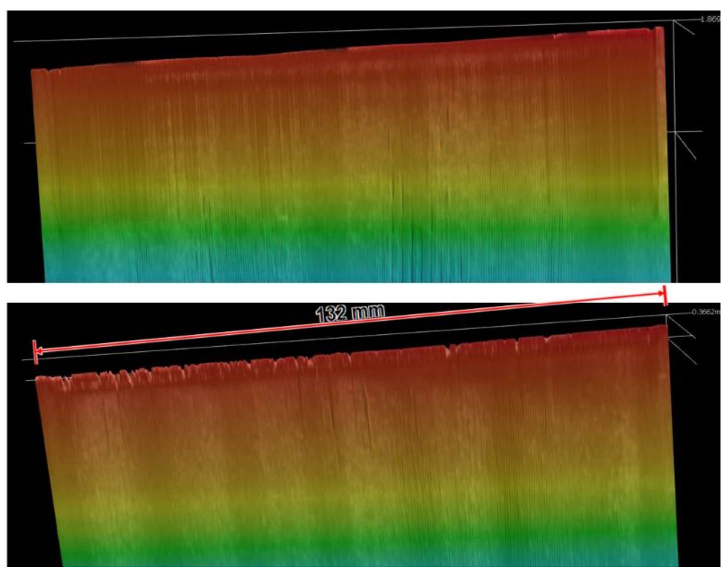

Figure 7.4. 3D wear profile of the side walls and edges of trimming tools after 230,000 trimming cycles.

These topographical observations support earlier findings that the lower tool faces experience more intense mechanical and fatigue stresses, leading to faster wear and surface fatigue.

Figure 7.5 presents the measured fillet radius of the trimming tools after 230,000 cuts, based on 3D profilometry analysis. In Figure 7.5 (a), the upper tool has a worn fillet radius of 0.077 mm, which is increased from the original 0.02 mm due to gradual abrasive wear. This increase indicates edge rounding from consistent tool–sheet interaction, despite no visible chipping. Figure 7.5 (b) features an unchipped region of the lower tool, where the fillet radius has grown to 0.087 mm—slightly larger than that of the upper tool—suggesting more significant wear, likely caused by the higher mechanical load on the lower insert during trimming. In contrast, Figure 7.5 (c) shows a chipped region of the lower tool, where the effective fillet radius has increased dramatically to 0.192 mm. This significant increase results from localized material loss due to fatigue-induced microchipping, which substantially alters the cutting-edge geometry.

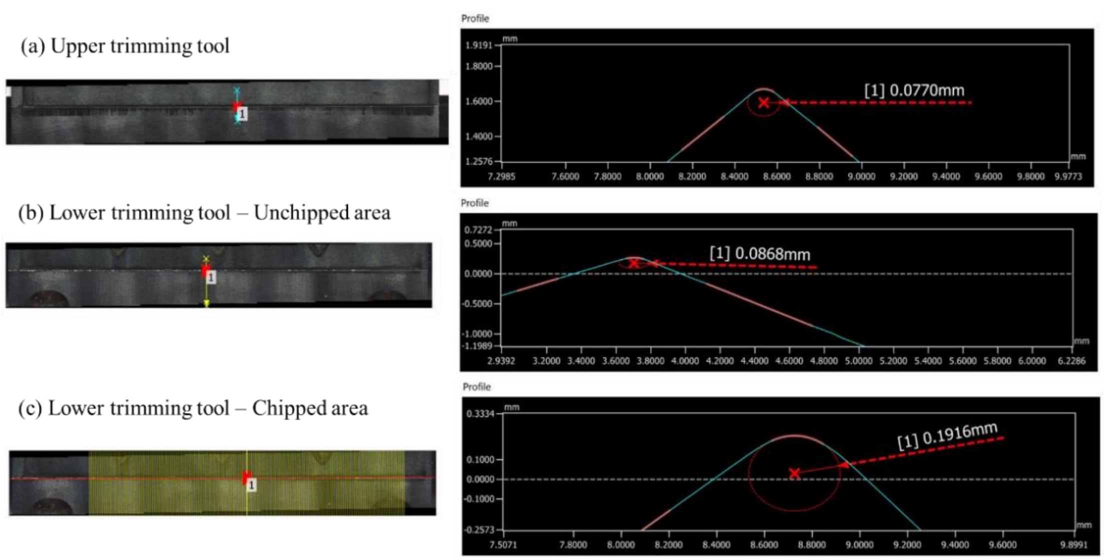

Figure 7.5. Measured fillet radius after 230,000 cuts for (a) upper trimming tool, (b) lower trimming tool – unchipped area, and (c) lower trimming tool – chipped area.

These measurements provide quantitative evidence of edge deterioration caused by both gradual abrasive wear and localized fracture. Importantly, the difference between chipped and unchipped areas emphasizes the uneven progression of wear, supporting the need for targeted tool inspection and potential reconditioning during maintenance intervals.

7.2. Influence of Tool Wear on Shear Edge Quality of DP980

Burr height and burnish depth were measured using an SFB micrometer and a Nikon SMZ745T microscope, respectively, employing the pixelation method. Ten tests were conducted for each condition. Burnish depth was measured at ten locations per sample, while burr height was measured at thirteen locations along the sheared edge. These thirteen points (Figure 7.6 (a)) were selected based on the burr profile of the 230K specimens at 10% clearance, as burrs consistently formed only at these locations. The point locations were highly reproducible across all specimens under the same conditions.

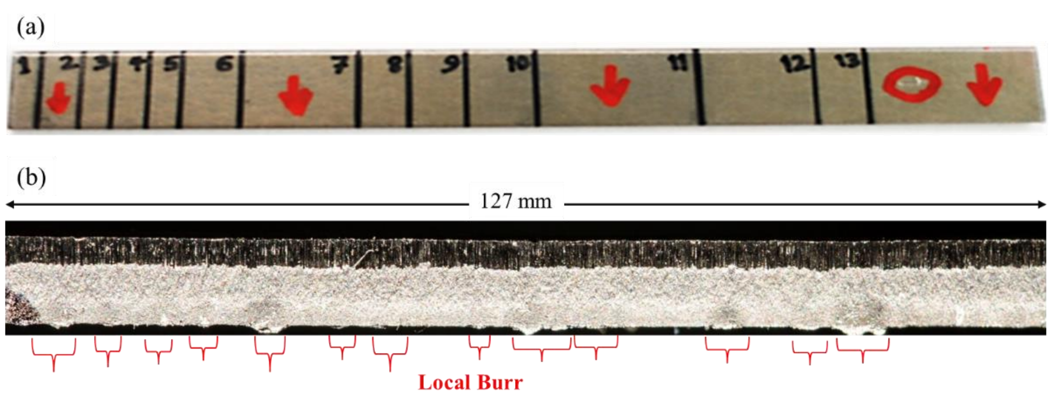

Figure 7.6. (a) Selected locations for local burr measurements on the sheared sample; (b) local burrs on the sheared edge of DP980-1 trimmed with worn inserts after 230,000 cuts.

Figure 7.7 shows how the average burr height and burnish depth change with increasing cutting cycles—used here as an indicator of tool wear. The graph clearly reveals that burr height rises steadily as the number of cuts increases. This trend indicates the gradual dulling of the tool edge due to wear and microchipping. A dull or chipped edge causes more plastic flow instead of sharp, localized shearing and fracture. As a result, material is pushed rather than cut cleanly, leading to a more curved strain localization zone near the edge and an increase in burr formation.

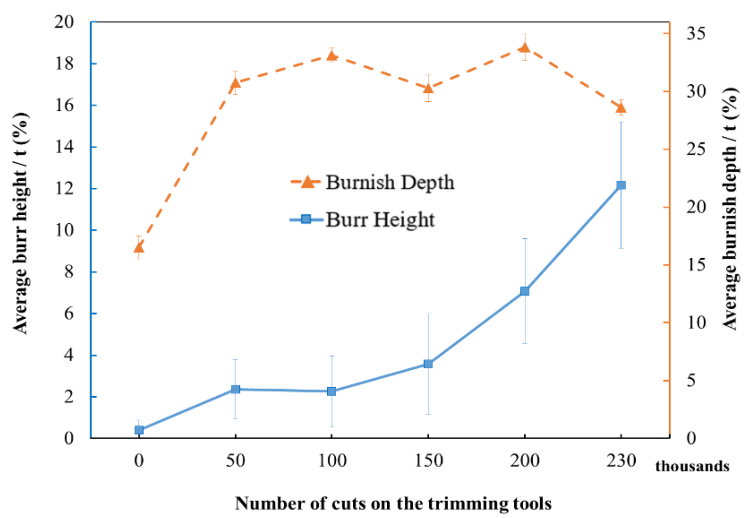

Figure 7.7. Sheared edge features as a function of cutting cycle on the trimming tools for DP980-1 sheet at trimming clearance of 10%.

Likewise, the burnish depth increases over time, although it varies somewhat during intermediate stages. The burnish zone, along with the rollover region, shows the depth of tool penetration before fracture happens. For DP980, this depth grows as the tool wears down. As the edge dulls, more penetration is needed to reach the critical damage point, which causes the burnish region to expand.

The error bars (standard deviation) in Figure 7.7, also highlight an important effect that worn tools lead to greater variation in burr height. This variability likely results from localized damage, such as microchipping or uneven wear on the trimming edges, especially at the lower die. This causes unstable edge formation and can produce excessively high burrs in specific regions of the trimmed edge. These findings confirm that tool wear not only worsens overall edge quality but also introduces instability and inconsistency in sheared edge geometry, which could impact downstream formability and dimensional accuracy.

7.2.1. Formation of Local Burrs and Their Correlation with the Trimming Tools

After carefully examining the trimmed samples, it was observed that burrs consistently formed only at specific locations along the sheared edge of the blank. These locations were highly reproducible across all test conditions, regardless of tool wear or material type. Therefore, the 13-point coordinate system introduced in Figure 7.6 was adopted as a consistent reference framework for burr height measurement in all specimens, including those trimmed with new tools, where burrs were barely visible at certain locations.

Figure 7.8 shows the local burr height profiles along the trimmed edge of DP980-1 at different stages of tool life: new, 100K, 200K, and 230K cuts. The data clearly indicate that burr height gradually increases at nearly all points as the tool wears down. However, this growth is uneven, and no consistent pattern appears across different locations. Some points (e.g., locations 2–5 and 10–12) exhibit much sharper burr growth, likely indicating localized tool damage, such as edge chipping or surface fatigue, at those specific areas on the trimming die.

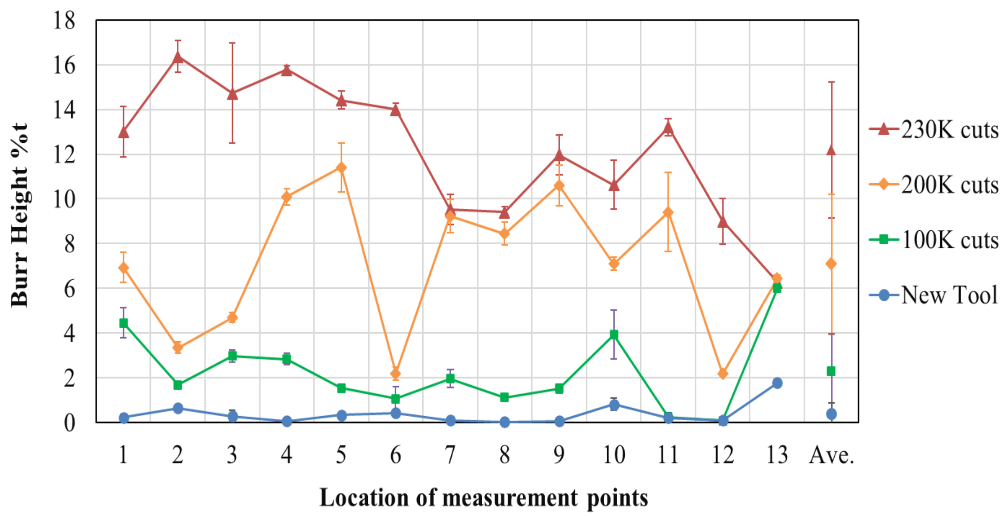

Figure 7.8. Local burr height distribution at 13 measurement points along the sheared edge of DP980-1 sheet trimmed with new, 100K, 200K, and 230K-cut tools.

To further assess material sensitivity, Figure 7.9 compares the local burr profiles of DP980-1 and DP980-2 trimmed with worn 230K-cut tools. These two DP980 steels follow a very similar pattern, with DP980-1 exhibiting higher burr height than DP980-2 in all measurement locations.

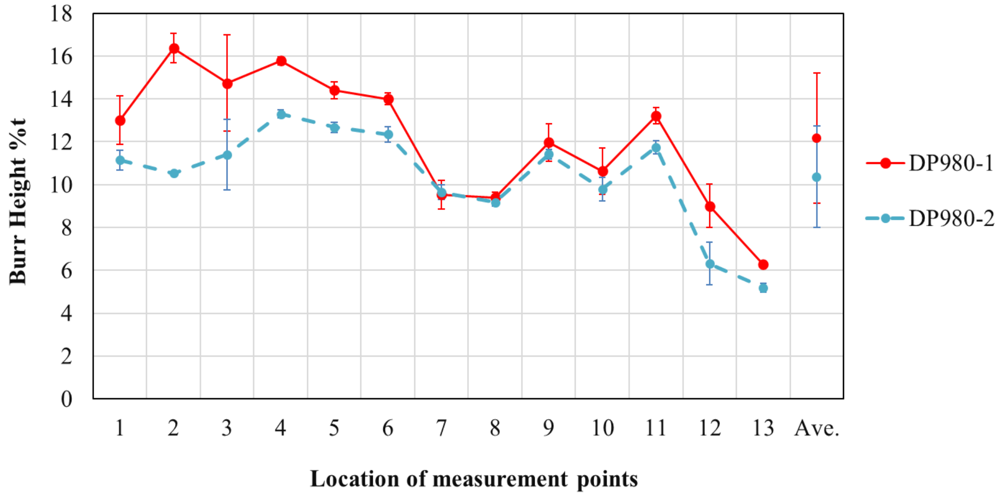

Figure 7.9. Comparison of local burr height distributions for DP980-1 and DP980-2 trimmed with 230K-cut tools.

Figure 7.10 illustrates the coordinate system on the lower trimming die, aligning each of the 13 burr measurement points on the blank with their corresponding areas on the die. Then, in Figure 7.11 and Figure 7.12, optical images of each local region of the lower trimming tool after 230,000 strokes are presented, with the matching DP980-1 blank (trimmed with these worn tools) placed on top for visual alignment. These high-magnification images clearly reveal signs of localized microchipping and abrasive wear, especially in regions that correspond to high burr formation on the blank (as seen in Figure 7.8).

This one-to-one mapping confirms that each local burr is directly affected by localized microchipping on the lower trimming tool. Deeper chips lead to increased burr formation. Each local chip on the die allows material to flow rather than causing significant shearing deformation or blank fracture. Therefore, these chips create a highly curved localization zone, resulting in a larger local burr.

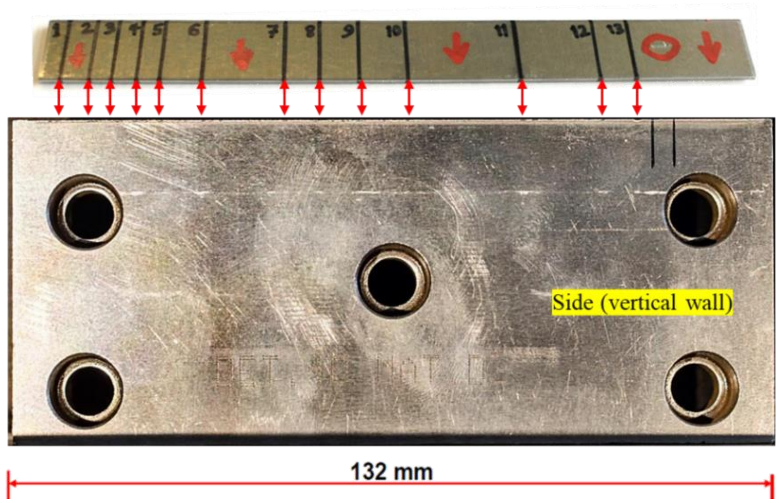

Figure 7.10. The coordinate system used to map burr measurement locations (1–13) on the trimmed blank to the corresponding zones on the lower trimming tool.

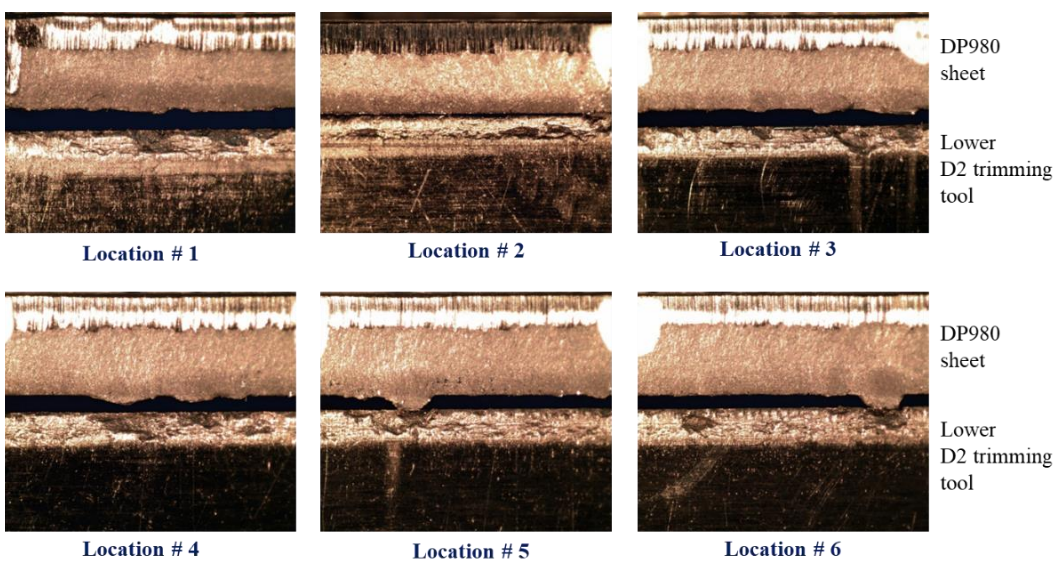

Figure 7.11. Optical views of the lower trimming tool after 230,000 cuts at designated locations 1 to 6. The trimmed DP980-1 blank is aligned above the die to visualize the correlation between local tool wear and burr formation.

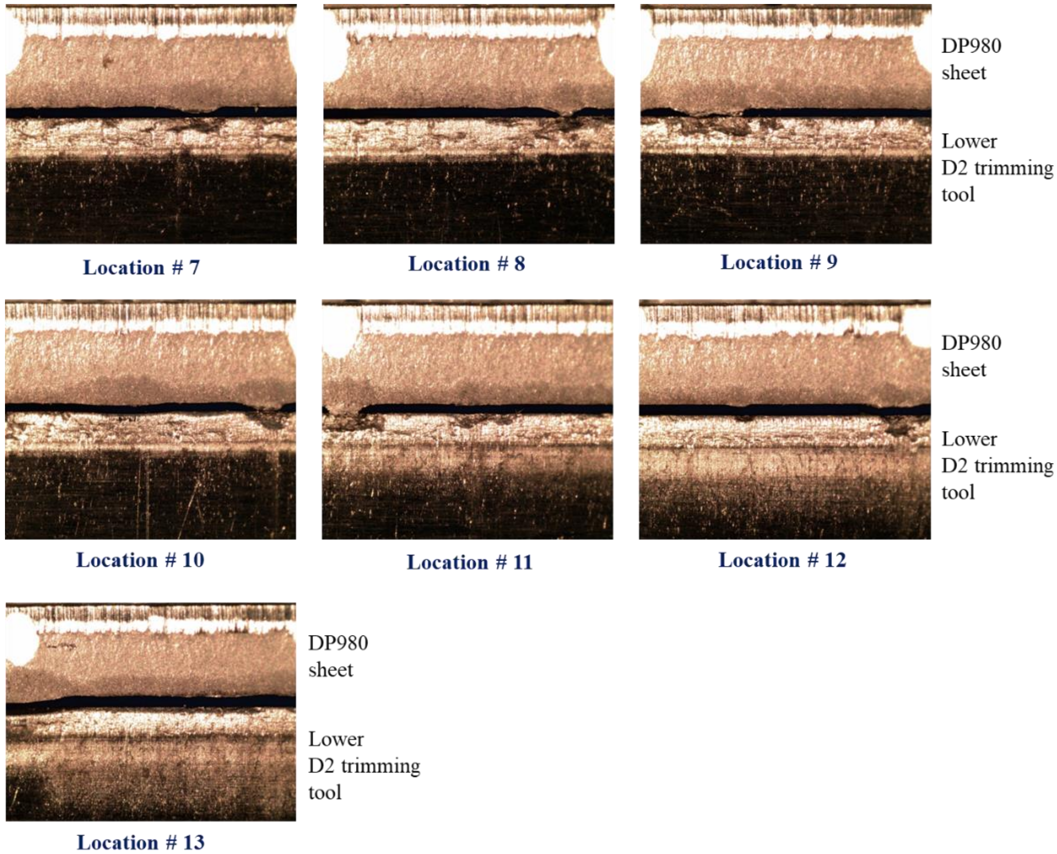

Figure 7.12. Optical views of the lower trimming tool after 230,000 cuts at designated locations 7 to 13. The trimmed DP980-1 blank is aligned above the die to visualize the correlation between local tool wear and burr formation

This interesting correlation between the local burrs on the blank and the local chippings on the die can serve as a guideline in practical stamping applications, where wear of the cutting edges of the trim die can be monitored offline by observing the shape of the trimmed edges.

7.3. Influence of Tool Wear on Shear Edge Stretchability of DP980

The stretchability of trimmed specimens with fresh inserts as well as worn inserts up to 230k cuts was evaluated by tensile testing, using the methodology described earlier in Section 5.1. The results, shown as major local strains, are plotted against the number of cutting cycles, as an indication of tool wear, for DP980-1 in Figure 7.13. In these graphs, the lowest boundary of all fractured data points indicates the fracture limit (dotted red line), while the highest boundary of all safe data points shows the safe forming limit (solid green line). Additionally, a trend line representing strains outside the necking area, crossing the averages, is included for further discussion. Besides local strain measurements, the extensometer data on total elongation are also plotted as a potential parameter for assessing the sheared edge stretching performance, using an initial gauge length of 50 mm.

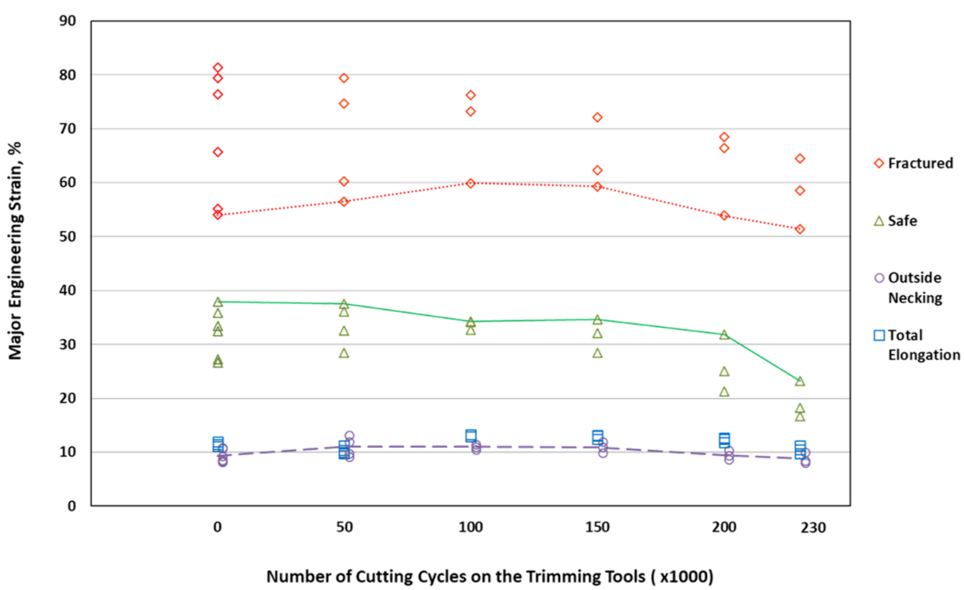

Figure 7.13. Results of the sheared edge stretchability of DP980-1 as a function of cutting cycles on the trimming tools.

The plot clearly shows that tool wear negatively affects edge stretchability, particularly at safe strain levels. As the number of cutting cycles increases to 230,000, the maximum safe strain consistently drops from about 37% to around 20%, showing that the sheared edge becomes more prone to premature fracture under tensile load. However, the total elongation and strain outside the necking region remain relatively constant, with a slight reduction at higher cycles, indicating that the material's global formability is less affected while its local formability is compromised.

This behavior confirms that the quality of the trim edge significantly influences local stretchability, especially in high-strength steels like DP980, where fractures often originate from small defects. Worn tools produce rougher, more damaged sheared edges with larger burrs —conditions that increase stress concentration during subsequent deformation and accelerate failure.

7.4. Fatigue Analysis of Trimming Tools

Metal fatigue refers to the gradual damage and eventual failure of a metallic component, specimen, or structure caused by repeated loading at levels below its static strength. Static strength is defined as the load needed to cause failure in a single application. In contrast, fatigue loads—usually cyclic—do not cause immediate failure but lead to the slow initiation and growth of cracks over time. Fatigue failure has been identified as the main cause of microchipping observed along the trim edge of trimming tools. This section presents a theoretical analysis to predict the fatigue life of D2 tool steel used in trimming operations and to explain the mechanisms underlying fatigue failure. The focus will be on the lower trimming tool, which experienced the most severe microchipping due to fatigue failure.

7.4.1. Stress-Based Fatigue Analysis

A widely used strain-based method for fatigue analysis is the Coffin–Manson–Basquin relation, which has been shown to effectively model the long-life fatigue behavior of metals under cyclic loading, as given in Equation (7.1). Basquin [200] introduced the original version to describe stress-based fatigue analysis. Later, Manson [201] and Coffin [202] expanded the formulation and linked the number of cycles to crack initiation with the amplitude of plastic strain. This combined approach accounts for both elastic and plastic responses of materials under cyclic loading.

$$\frac{\Delta\varepsilon}{2} = \varepsilon_f'\left(2N_f\right)^c + \frac{\sigma_f'}{E}\left(2N_f\right)^b \tag{7.1}$$

The first term on the right side indicates plastic deformation measured by strain, while the second represents the elastic deformation component. For fully hardened tool steel, such as the D2 trim tools examined here, bulk plastic deformation is almost negligible, meaning the first term does not significantly affect overall life.

Additionally, in long-life applications, such as those used in series production, plastic strains are minimal. In this case, the plastic strain term in Equation (7.1) is negligible, and the total strain-life Equation reduces to Basquin's Equation (7.2), which is used for the stress-life (S-N) approach [203].

$$\sigma_a = \sigma_f'\left(2N_f\right)^b \tag{7.2}$$

Where σ_a and N_f are the applied stress amplitude and number of cycles to failure, respectively. σ_f' and b are material-specific parameters of the fatigue strength coefficient and fatigue strength exponent, respectively.

7.4.2. Fatigue Parameters for D2 Tool Steel

As described in Section 6.1.9, the general mechanical properties and flow curve of the D2 trimming tools were estimated from hardness measurements and existing literature. Since there is no experimental fatigue test for D2 tool steel in this study, the fatigue strength coefficient and exponent for D2 are calculated using the methodology described as follows.

7.4.2.1. Fatigue Strength Coefficient (σ'_f) Estimation

Roessle and Fatemi [204] showed the trend that the fatigue strength coefficient (σ_f') depends more on the steel's Brinell hardness or ultimate tensile strength, as shown in Figure 7.14.

By using the above empirical Equation and Brinell hardness of 645 for the D2 inserts used in the experiments, the fatigue strength coefficient is:

$$\sigma_f' = 4.25HB + 225 = 4.25 \times 645 + 225 = 2966 \text{ MPa} \tag{7.3}$$

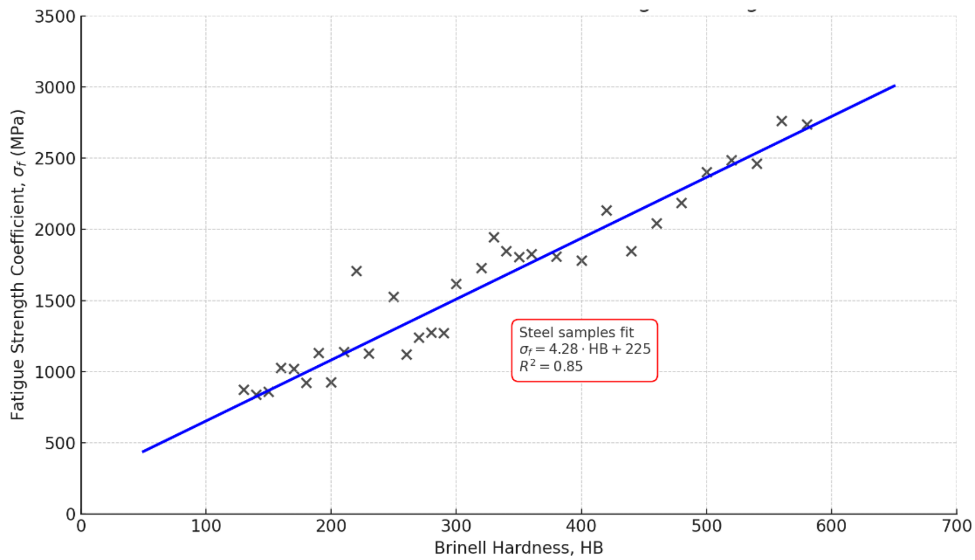

Figure 7.14. Fatigue strength coefficient vs. Brinell hardness, adopted after Roessle and Fatemi [204].

7.4.2.2. Fatigue Strength Exponent (*b*) calculation

Basquin's equation [200] describes high-cycle, low-strain behavior in an elastic nature as Equation (7.2). At the endurance limit – the limit beneath which many steels tend not to fail under constant amplitude fatigue, $\sigma_a = S_f^*$, where S_f^* is the tensile fatigue limit. For D2 tool steel, it is 550 MPa [185]. Also, $2N_f = 2N_f^*$, where N_f^* is the number of cycles corresponding to the endurance limit. Generally, for ferrous materials, 10^6 cycles can be considered to be the start of the infinite life region [205]. Therefore, the fatigue strength exponent, *b*, is given by

$$b = -\frac{\left[\log\left(\frac{\sigma_f'}{S_f^*}\right)\right]}{\left[\log\left(2N_f^*\right)\right]} = -\frac{\left[\log\left(\frac{2966}{550}\right)\right]}{[\log(2\times10^6)]} = -0.116 \tag{7.4}$$

7.4.2.3. Constructing the S-N curve for the D2 tool

Replacing the determined values of σ_f' and b in Equation (7.2), resulted in Equation (7.5), as follows, and the S-N curve plotted in Figure 7.15 for D2 tool steel.

$$\sigma_a = 2966\,(2N_f)^{-0.116} \text{ MPa} \tag{7.5}$$

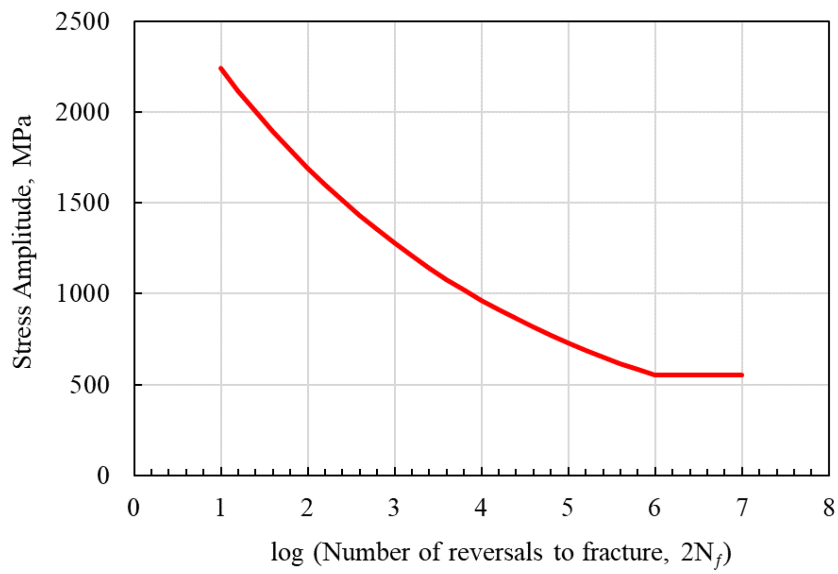

Figure 7.15. The theoretical S-N curve for D2 tool steel.

7.4.3. Fatigue Model Selection Incorporating Mean Stress Effects

Several models have been proposed to explain how mean stress affects fatigue behavior. Some of the most cited stress-based mean stress equations in the literature include the modified Goodman, Morrow, Soderberg, Smith-Watson-Topper (SWT), Gerber, and Walker equations. Section 2.5 is dedicated to a literature review of these fatigue models.

In this study, only the modified Goodman and Morrow models are used. Some limitations with other models prevent us from using them in this case:

The Gerber equation is restricted to tensile mean stresses because it incorrectly predicts a harmful effect of compressive mean stresses [121], [125]. The Soderberg equation is primarily intended for tensile mean stresses and provides a conservative estimate of fatigue life, primarily for safe design purposes. SWT cannot fully address compressive loading ($R = -\infty$) and thus is not suitable for our fully compressive loading scenario ($\sigma_{max} = 0$). The Walker equation has not been used in this study because the material exponent (γ) is not available for D2 material.

As described earlier in Section 2.5.1, the Modified Goodman and Morrow equations are given by Equation (7.6) and (7.7), respectively.

$$\frac{\sigma_a}{\sigma_{ar}} + \frac{\sigma_m}{\sigma_u} = 1 \tag{7.6}$$

$$\frac{\sigma_a}{\sigma_{ar}} + \frac{\sigma_m}{\sigma_f} = 1 \tag{7.7}$$

7.4.4. Results of the Goodman and Morrow models

To analyze the fatigue behavior of trimming tools during the shearing of DP980-1, detailed stress distributions and loading history for the tools were obtained through finite element analysis. Figure 7.16 shows the von Mises equivalent stress contours at upper tool displacements of 0.20 mm and 0.30 mm, along with high-magnification micrographs of partially sheared DP980-1 blanks. The experimental observations identified the point where the fracture begins in the sheet metal blank when the upper tool displacement reaches 0.30 mm and the lower die contacts the sheet edge by about 0.16 mm. This critical moment coincides with a localized stress peak along the tool edge, as shown in the contour plots.

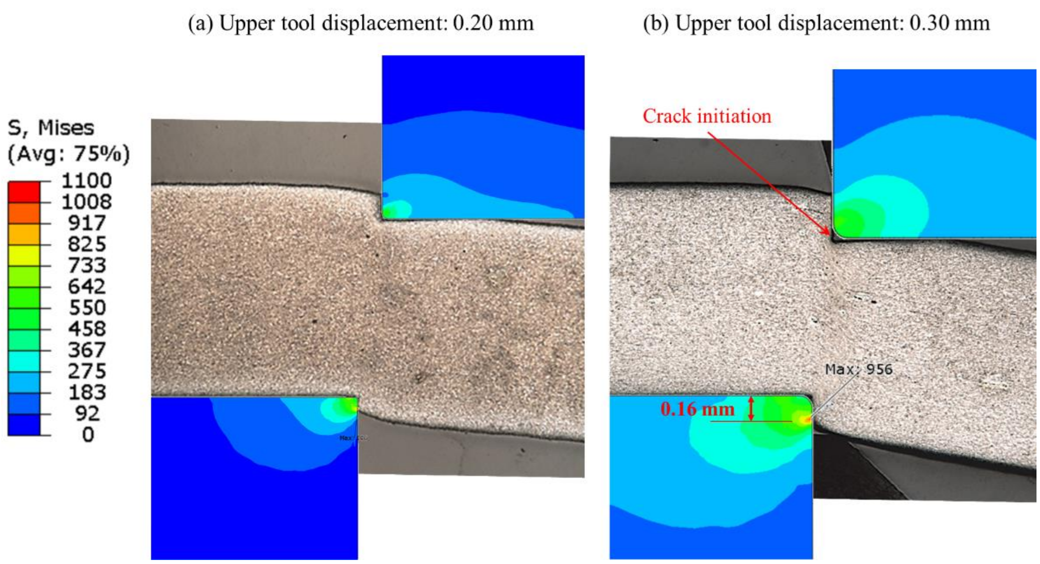

Figure 7.16. von Mises equivalent stress distribution on the trimming tools at the upper tool displacement of (a) 0.20 mm and (b) 0.30 mm. Corresponding partially sheared DP980-1 microscopic images are also included.

To capture the stress history relevant for fatigue life estimation of the lower tool, a specific selection of surface elements was made. As shown in Figure 7.17, the selection covers a width of 0.08 mm along the contact edge and a depth of 0.17 mm into the tool, slightly exceeding the experimental contact depth to ensure full coverage of the highly stressed region. This area includes the elements that best represent the cyclic loading experienced by the trimming tool due to repeated high-contact pressures and stress concentrations during the shearing process, thereby increasing their susceptibility to failure.

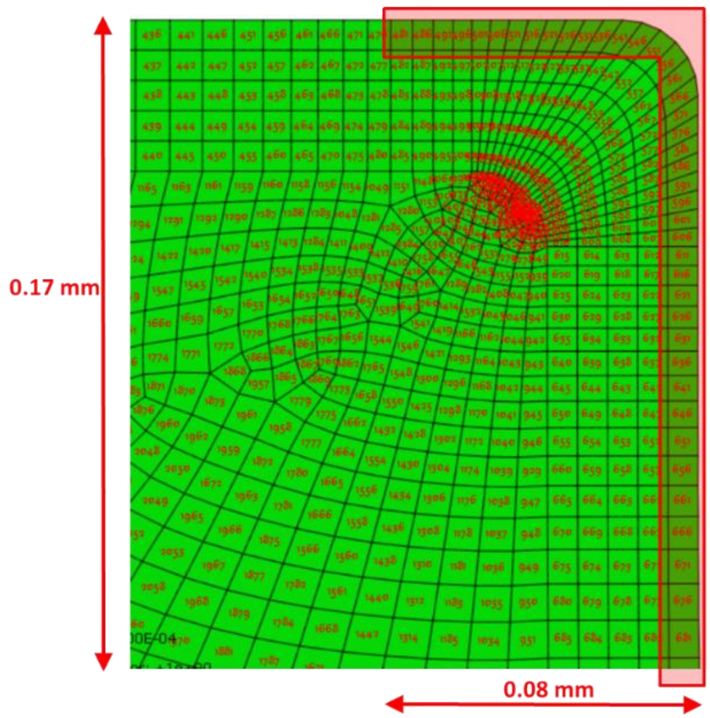

Figure 7.17. Surface elements of the lower trimming tool used in the fatigue analysis.

To assess the fatigue vulnerability of the trimming tool, stress histories were extracted from surface elements located along the lower die radius. Figure 7.18 to Figure 7.21 show the principal stress history for some of these surface elements as a typical trend for each region. The time-dependent maximum principal stresses fluctuate significantly as the sheet undergoes plastic deformation and crack initiation. These fluctuations lead to alternating stress components superimposed on high mean compressive stress levels, characteristic of contact-driven loading.

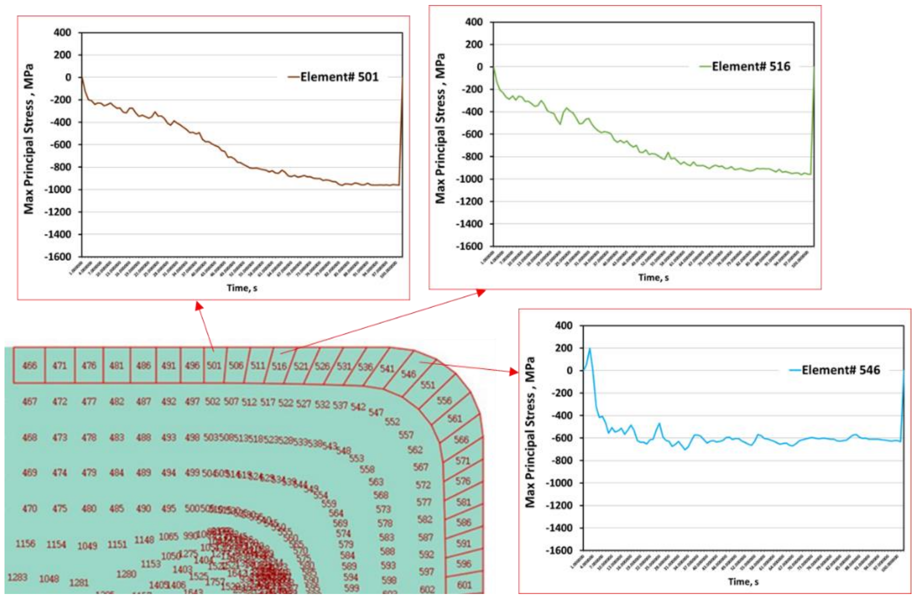

Figure 7.18. Principal stress (σ_1) history for surface elements number 501, 516, and 546.

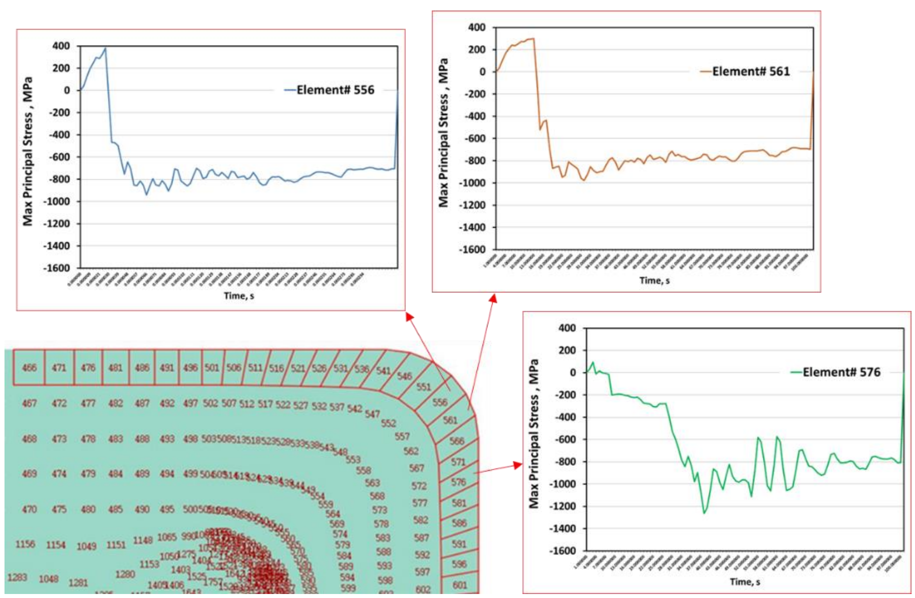

Figure 7.19. Principal stress (σ_1) history for surface elements number 556, 561, and 576.

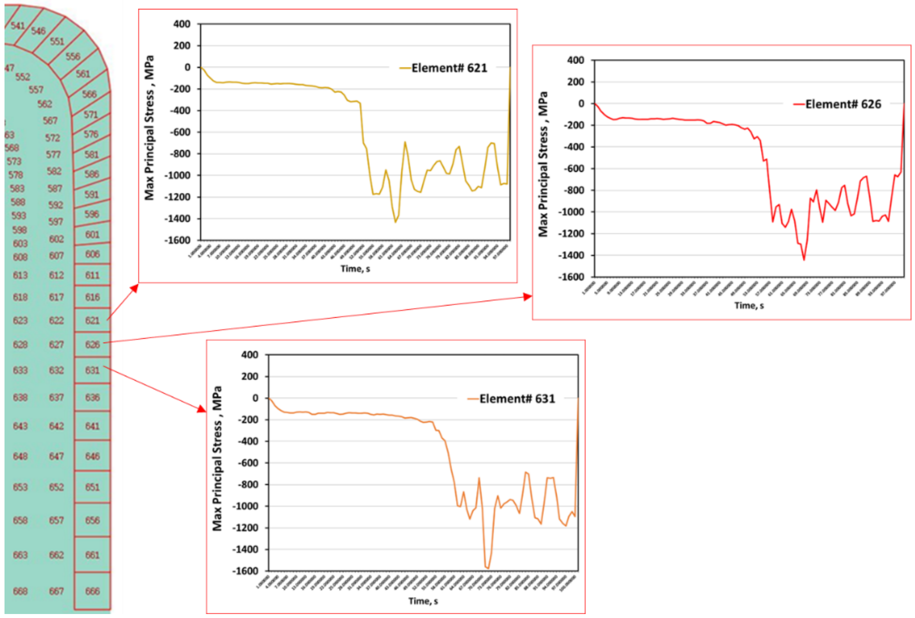

Figure 7.20. Principal stress (σ_1) history for surface elements number 621, 626, and 631.

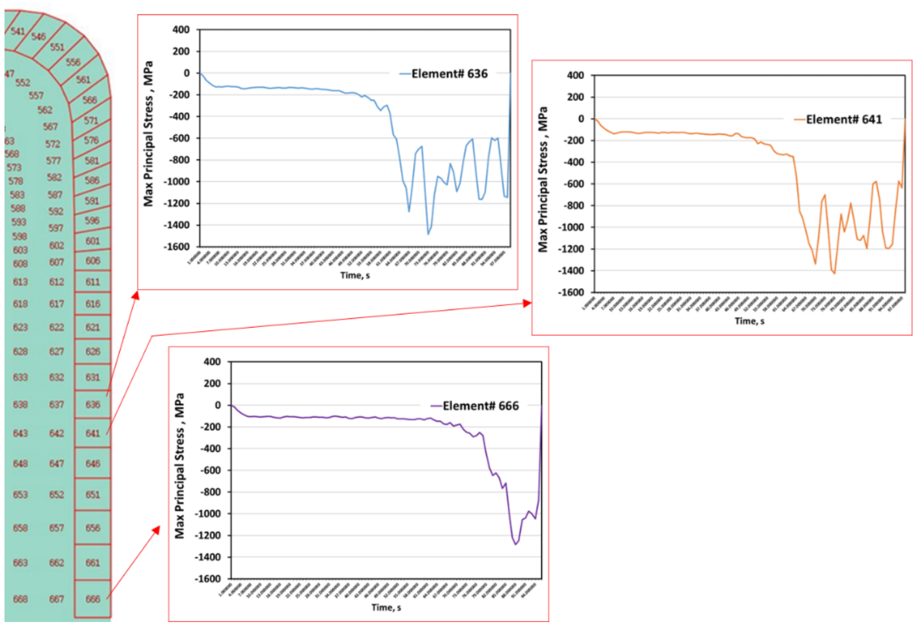

Figure 7.21. Principal stress (σ_1) history for surface elements number 636, 641, and 666.

From stress histories, the mean and alternating stresses were calculated and evaluated against fatigue failure criteria. Table 7.2 presents the results obtained using both the Modified Goodman and Morrow models. A factor of safety less than unity was interpreted as finite fatigue life ($N_f < 10^6$ cycles). Elements #556 and #561 consistently failed under both models, indicating a high-risk location. Similarly, elements #631 and #636 showed finite life predictions under both criteria. In contrast, elements #576, #621, #626, and #641 were predicted to fail only by the Morrow model, highlighting its greater sensitivity to mean stress effects.

Table 7.2. Fatigue life prediction using Goodman and Morrow models.

Element #	σ_{max}, MPa	σ_{min}, MPa	Mean Stress, σ_m, MPa	Stress Amplitude, σ_a, MPa	Goodman σ_{ar}	Goodman N_f	Goodman Factor of Safety	Morrow σ_{ar}	Morrow N_f	Morrow Factor of Safety
471	0	-835	-417.5	417.5	351	48,205,472	1.76	360	38,259,460	1.67
476	0	-864	-432	432	361	37,685,327	1.70	371	29,707,287	1.61
481	0	-885	-442.5	442.5	368	31,719,053	1.66	379	24,882,401	1.57
486	0	-908	-454	454	376	26,404,864	1.62	387	20,604,094	1.53
491	0	-942	-471	471	388	20,332,599	1.56	399	15,743,191	1.48
496	0	-964	-482	482	395	17,270,112	1.52	407	13,305,642	1.44
501	0	-963	-481.5	481.5	395	17,397,075	1.53	407	13,406,478	1.45
506	0	-967	-483.5	483.5	396	16,895,664	1.52	408	13,008,368	1.44
511	0	-967	-483.5	483.5	396	16,895,664	1.52	408	13,008,368	1.44
516	0	-959	-479.5	479.5	393	17,915,941	1.53	405	13,818,775	1.45
521	0	-935	-467.5	467.5	385	21,436,859	1.57	397	16,624,611	1.49
526	0	-907	-453.5	453.5	376	26,613,198	1.62	387	20,771,430	1.53
531	0	-801	-400.5	400.5	339	65,174,707	1.83	347	52,146,043	1.74
536	0	-682	-341	341	295	213,094,112	2.15	302	175,511,694	2.04
541	0	-616	-308	308	270	457,174,779	2.38	276	382,860,275	2.26
546	199	-703	-252	451	404	14,102,645	1.42	411	12,159,888	1.38
551	331	-804	-236.5	567.5	512	1,846,403	1.08	521	1,605,307	1.06
556	382	-941	-279.5	661.5	587	573,993	0.93	598	487,806	0.91
561	298	-977	-339.5	637.5	552	970,183	1.00	564	799,673	0.97
566	229	-990	-380.5	609.5	519	1,640,294	1.07	532	1,325,062	1.04
571	171	-1107	-468	639	526	1,456,635	1.05	542	1,129,386	1.02
576	95	-1262	-583.5	678.5	536	1,253,501	1.03	555	924,051	0.99
581	91	-1207	-558	649	517	1,697,463	1.08	535	1,264,921	1.03
586	30	-1324	-647	677	523	1,552,547	1.07	543	1,114,998	1.02
591	-29	-1306	-667.5	638.5	489	2,734,603	1.17	509	1,947,883	1.10
596	0	-1245	-622.5	622.5	485	2,967,796	1.18	503	2,152,696	1.12
601	0	-1309	-654.5	654.5	504	2,124,711	1.12	524	1,521,321	1.06
606	0	-1355	-677.5	677.5	517	1,691,487	1.08	538	1,200,100	1.03
611	0	-1293	-646.5	646.5	499	2,305,445	1.14	519	1,656,043	1.08
616	0	-1284	-642	642	496	2,415,103	1.14	516	1,737,965	1.08
621	0	-1434	-717	717	540	1,168,259	1.02	563	816,212	0.97
626	0	-1444	-722	722	543	1,116,812	1.02	566	778,771	0.96
631	0	-1576	-788	788	579	637,830	0.93	606	433,880	0.88
636	0	-1486	-743	743	555	928,203	0.99	579	642,094	0.94
641	0	-1426	-713	713	538	1,211,460	1.03	561	847,700	0.98
646	0	-1341	-670.5	670.5	513	1,811,191	1.10	534	1,288,593	1.04
651	0	-1340	-670	670	513	1,820,120	1.10	534	1,295,202	1.04
656	0	-1330	-665	665	510	1,912,345	1.10	531	1,363,535	1.05
661	0	-1264	-632	632	490	2,681,700	1.16	509	1,937,652	1.10
666	0	-1283	-641.5	641.5	496	2,427,665	1.14	515	1,747,357	1.08

The spatial distribution of critical elements in Figure 7.22 shows that fatigue-prone areas tend to cluster near the die corner radius, where contact pressures and stress gradients are most intense. Notably, the effect of compressive mean stresses shifts most elements into the safe zone, but some elements still experience alternating stresses high enough to initiate fatigue cracks.

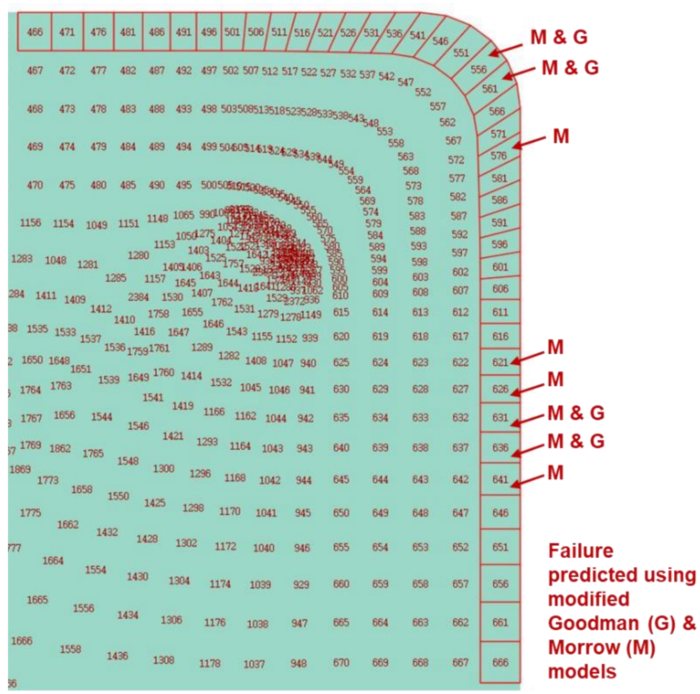

Figure 7.22. The indicated elements are predicted to have finite fatigue life using the Goodman and Morrow models.

This analysis reveals that only specific surface elements are critically loaded during trimming cycles, and their finite fatigue life is significantly influenced by local stress concentrations and mean stress sensitivity. This insight is key for identifying high-risk die areas, improving tool design, and choosing appropriate fatigue models for an acceptable life prediction.

7.4.5. The Proposed Method by Topper and Liang

Another model used for fatigue analysis of our D2 tool steel is one proposed by Liang et al. [206], [207], developed primarily to examine the effect of mean stress on the fatigue behavior of very hard carburized steels.

In this model, the positive mean stress region follows Morrow's Equation (Modified Goodman, where UTS plays a role.)

The negative mean stress region is the flat line at 90% of the fully reversed fatigue limit of the material. For our D2 tool steel with a fatigue limit (endurance limit) of 550 MPa, this 90% line intersects at 495 MPa.

Applying this model to the lower die surface elements results in the green crossed points shown in Figure 7.23. As shown in the graph, this criterion indicates an infinite life for all surface elements, meaning that compressive mean stresses have no effect as long as the maximum stress remains below the threshold flat line. Comparing these findings with experimental data shows that this model underestimates real-life results, predicting that no fatigue failure occurs on the selected surface elements of the lower trimming tool in our case.

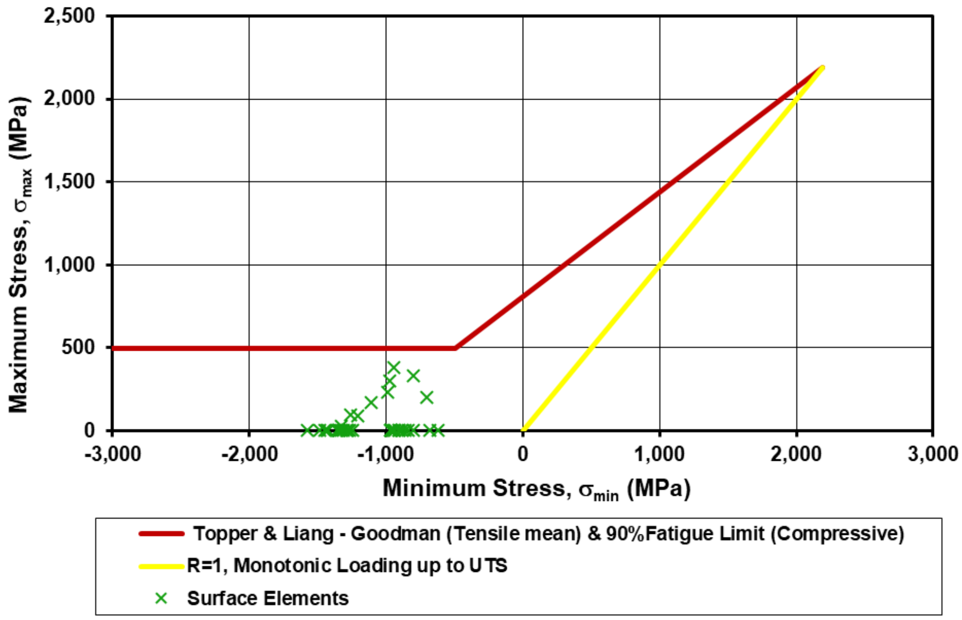

Figure 7.23. The Topper and Liang fatigue model for the selected surface elements of the lower trimming tool.

7.5. Fatigue Analysis Accounting for Shear Stress

While mapping the principal stress tensors on the lower tool in the finite element model, shear stress components around 45 degrees to the surface were observed during the trimming process. The shear stresses are shown as red arrows in Figure 7.24, applied on the upper surface, moving toward the die radius and side wall as trimming continues.

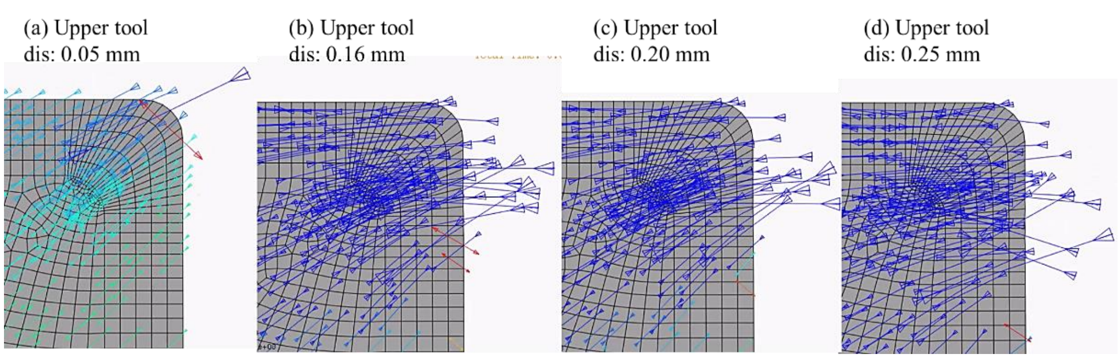

Figure 7.24. Principal stress and shear stress tensors during the trimming process at the upper tool displacement of (a) 0.05, (b) 0.16, (c) 0.20, and (d) 0.25 mm.

The principal stresses on the vertical wall of the inserts are mainly tensile or compressive and are not evenly distributed. The interaction of these stresses can produce diagonal shear stresses on planes oriented at 45 degrees to the principal stresses. An arbitrary block under uneven compressive stresses has been illustrated in Figure 7.25 to visualize how shear stress develops. Unbalanced forces generate some compressive stresses that cause materials to slide past each other, creating shear stress inside the plates. Shear stress reaches its peak when the plate angle is at 45 degrees.

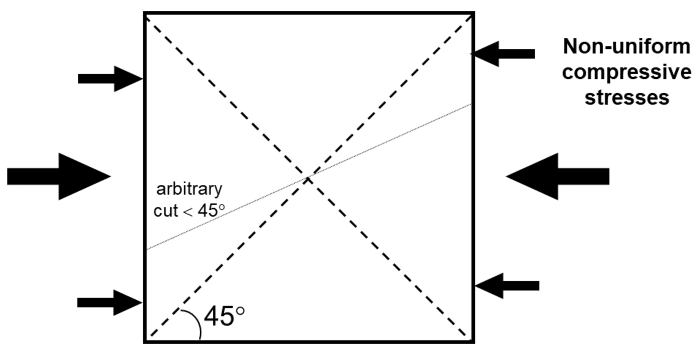

Figure 7.25. Formation of shear stress on the vertical wall of the insert during trimming.

To accurately predict fatigue failure and subsequent chipping of trimming tools, it is essential to use fatigue models that account for multiaxial stress conditions and the common shear-driven crack initiation seen in hard, brittle tool steels.

In this study, the Findley [136] critical plane model was used to evaluate the fatigue life of the D2 trimming tool by capturing the combined effects of shear and normal stresses. The model provides a useful framework for multiaxial fatigue assessment by calculating stress components on material planes and considering how normal stress influences potential crack initiation sites. Its directional nature makes it particularly effective for predicting fatigue life in critical areas such as cutting edges, where interacting tensile and shear stresses cause localized damage. Section 2.5.2 provided a detailed explanation of the Findley model and several other critical-plane multiaxial fatigue models.

Findley fatigue life is calculated using the following Equation [208]:

$$\frac{\Delta\tau}{2} + k\sigma_{n,max} = \tau_f^*\left(2N_f\right)^b \tag{7.8}$$

Where $\frac{\Delta\tau}{2}$ is shear stress amplitude, k is a material constant for the Findley equation, which describes the material's sensitivity to the impact of normal stress on fatigue life. $\sigma_{n,max}$ is the maximum normal stress, and τ_f^* is the fatigue shear strength coefficient [208].

Material Constants k and τ_f^* need to be determined experimentally for each material; however, in the absence of experimental values for our D2 tool steel, some formulations are available to estimate these values.

The Findley model was selected over other multiaxial fatigue models for several strong reasons. One main advantage is that it directly measures the shear stress amplitude (τ_a) across multiple planes while also considering the effect of the maximum normal stress ($\sigma_{n,max}$,). This dual emphasis is important because crack initiation is often driven by shear stress, while local tensile stresses influence crack growth. For D2 tool steel, which typically develops cracks that start as shear cracks and later expand under tension, the Findley model provides a particularly reasonable representation of the underlying fatigue mechanisms.

Another benefit of the Findley model is its effectiveness for applications involving cyclic contact loading. Trimming tools experience repetitive contact stress along their free edges and contact shoulders, areas where fatigue cracks are most likely to develop. The model's capacity to capture this interaction between shear-driven crack initiation and tensile-driven crack growth makes it highly useful for analyzing trimming die wear under real-world service conditions [209].

Finally, the Findley model provides practical benefits in calibration and application. It only requires two material fatigue parameters, k and τ_f^*, to describe fatigue behavior. This simplicity contrasts with other well-known multiaxial fatigue models, such as those of Dang Van [137], Fatemi-Socie [138], Brown-Miller [210], or Crossland [211], which often require more material parameters and more experimental effort to determine. Therefore, the Findley model balances prediction accuracy with ease of use, making it a suitable choice for this study.

7.5.1. Estimation of the Fatigue Shear Strength Coefficient for D2

When testing under pure torsion (so $\sigma_{n,max} = 0$), which simplifies Equation (7.8) into Equation (7.9):

$$\frac{\Delta\tau}{2} = \tau_f^*\left(2N_f\right)^b \tag{7.9}$$

So, at the endurance limit ($\frac{\Delta\tau}{2} = \tau_f'$ and $N_f = 10^6$), we have

$$\tau_f^* = \frac{\tau_f'}{(2 \times 10^6)^{\ b}} \tag{7.10}$$

Where τ_f' is the shear fatigue limit of the material.

The commonly cited approximation that the shear fatigue limit, τ_f', is equal to the normal (tensile) fatigue limit divided by $\sqrt{3}$ as follows [212]

$$\tau_f' = \frac{S_f^*}{\sqrt{3}} \tag{7.11}$$

It comes from applying the von Mises yield criterion to fatigue stress limits under multiaxial loading conditions.

For our D2 tool steel with $S_f^* = 550$ MPa, the shear fatigue limit is

$$\tau_f' = \frac{550}{\sqrt{3}} = 318 \text{ MPa} \tag{7.12}$$

And as determined earlier for our D2 tool steel using Equation (7.4),

$b = -0.116$, therefore

$$\tau_f^* = \frac{\tau_f'}{(2 \times 10^6)^{\ -0.116}} = 1713 \text{ MPa} \tag{7.13}$$

7.5.2. Estimation of the parameter *k* for D2

The material constant *k* is related to the materials' sensitivity to normal stress. For most materials, *k* typically ranges from 0.1 to 0.3. Findley assumed that the principal directions remain constant. The *k* parameter is determined by the shear fatigue limit and tensile fatigue limit by solving the following Equation [134].

$$\frac{S_f^*}{\tau_f'} = \frac{2\sqrt{1+k^2}}{\sqrt{1+k^2}+k} \tag{7.14}$$

For our D2 tool steel with $S_f^* = 550$ MPa and $\tau_f' = 318$ MP, by solving Equation (7.14), the result is

$$k = 0.162 \tag{7.15}$$

Therefore, Equation (7.8) turns into the following Equation for the fatigue life estimation of each element:

$$\frac{\Delta\tau}{2} + 0.162 \times \sigma_{n,max} = 318\left(2N_f\right)^{-0.116} \tag{7.16}$$

7.5.3. Critical Plane Search Procedure

The normal and shear stresses of an element in plane stress, which has an angle θ relative to the *x* principal axis, can be determined using Mohr's circle.

Figure 7.26 shows the stress components of Mohr's circle, and the equations are as follows [213], [214]:

$$\sigma(\theta) = \sigma_x cos^2\theta + \sigma_y sin^2\theta + 2\tau_{xy} sin\theta cos\theta \tag{7.17}$$

$$\tau(\theta) = \frac{\sigma_y - \sigma_x}{2}\sin(2\theta) + \tau_{xy}\cos(2\theta) \tag{7.18}$$

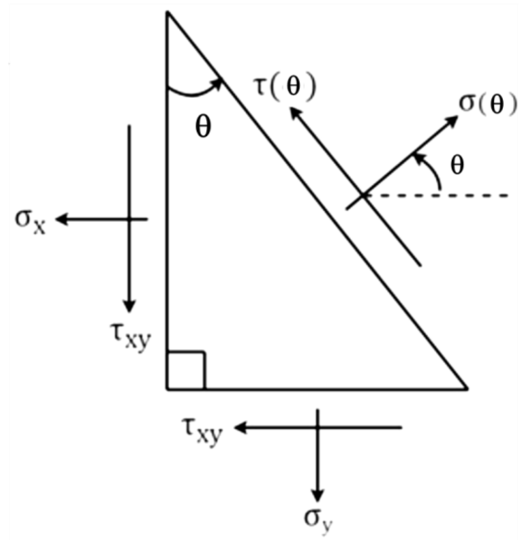

Figure 7.26. Stress components of Mohr's circle.

To find the critical plane in each surface element and to calculate the Findley fatigue life for that element, the following steps were taken:

1- The stress histories for each selected surface element, including $\sigma_x(t)$, $\sigma_y(t)$, and $\tau_{xy}(t)$, were taken from the FE analysis.

2- For each element, all possible angles in the interval 0° – 180° using steps of 5° were searched, and $\sigma(\theta)$ and $\tau(\theta)$ were calculated using Equations (7.17) and (7.18), respectively.

3- For each plane, and using the maximum and minimum calculated shear stresses, the shear stress amplitude, $\frac{\Delta\tau}{2}$, was calculated:

$$\frac{\Delta\tau}{2} = \frac{\max(\tau_\theta) - \min(\tau_\theta)}{2} \tag{7.19}$$

4- For each plane, the maximum calculated $\sigma(\theta)$ was selected as $\sigma_{n,max}$.

5- For each plane, the Findley damage parameter was calculated using

$$f = \frac{\Delta\tau}{2} + k\sigma_{n,max} \tag{7.20}$$

6- After the last plane was searched within each element, the plane with the maximum damage parameter, f, was selected as the critical plane.

7- Fatigue life, N_f, for the critical plane of each element was calculated using Equation (7.16).

The flowchart for the numerical implementation of the Findley model and estimation of fatigue life for each element is presented in Appendix B.

7.5.4. Results of the Findley Model for Tool Life Estimation

The Findley fatigue model was applied to the same surface elements of the lower tool, which were identified in Section 7.5.4 and shown in Figure 7.17. The principal stress and shear stress histories for each element were extracted, and the fatigue life was calculated following the sequence described in Section 7.5.3.

Figure 7.27 show the principal stress history for three surface elements as examples of the typical trend for each region.

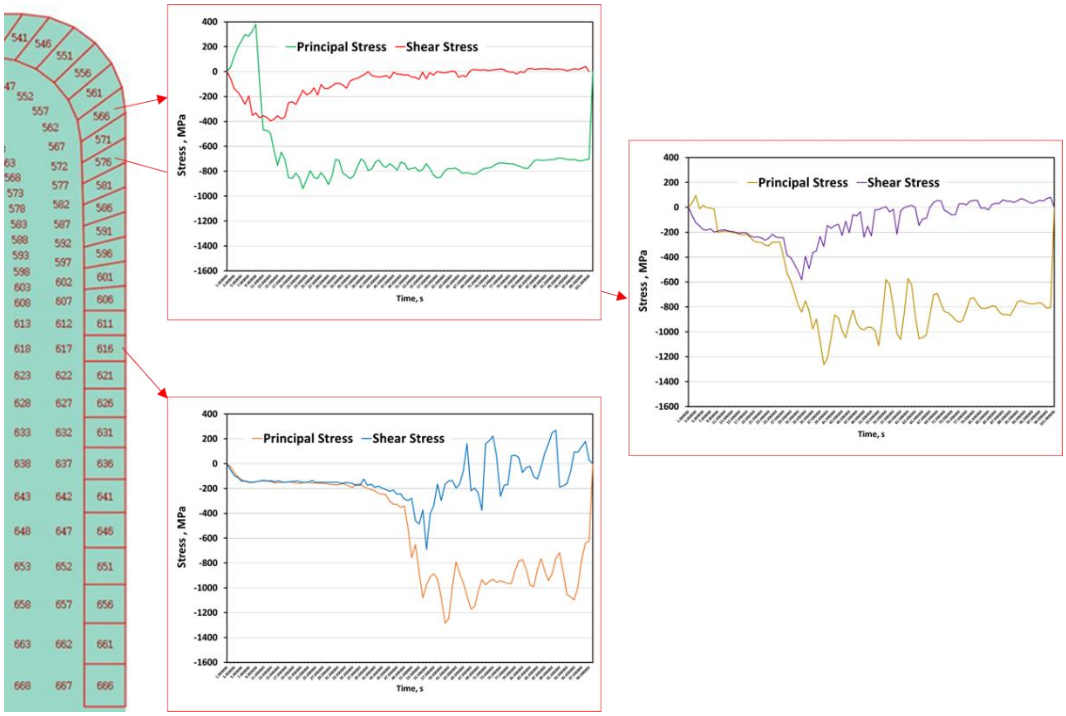

Figure 7.27. Principal stress and shear stress histories for surface elements number 556, 576, and 616 during the trimming operation.

Finally, the fatigue analysis results using the Findley model are summarized in Table 7.3. The results indicate that elements located near the die edge shoulder experience the most severe fatigue conditions and have a finite fatigue life, with the shortest being element #616, which reaches 28,098 trimming cycles. These failed elements with a finite fatigue life ($N_f < 10^6$) are highlighted in red, and the corresponding fatigue lives are substantially lower than those of the surrounding regions.

Table 7.3. Fatigue life prediction using the Findley model.

Element #	Max Shear, τ_{max}, MPa	Min Shear, τ_{min}, MPa	Shear Amplitude, τ_a, MPa	$\tau_a + k \cdot \sigma_{n,max}$	Findley Criteria	Findley N_f
471	157	-192	175	174.6	PASS	172,268,440
476	149	-189	169	168.8	PASS	230,967,238
481	147	-189	168	168.3	PASS	236,732,089
486	145	-198	172	171.9	PASS	197,109,989
491	133	-205	169	169.3	PASS	225,210,227
496	107	-197	152	152.0	PASS	569,927,887
501	90	-197	143	143.3	PASS	944,941,558
506	69	-199	134	133.9	PASS	1,694,227,722
511	46	-202	124	123.8	PASS	3,337,450,787
516	19	-218	118	118.4	PASS	4,897,022,821
521	-11	-215	102	102.0	PASS	17,652,670,593
526	-50	-203	77	76.8	PASS	203,552,168,977
531	-70	-203	67	66.6	PASS	688,183,709,640
536	-46	-233	94	93.5	PASS	37,195,215,528
541	-1	-300	149	149.5	PASS	656,843,408
546	59	-356	208	240.0	PASS	11,120,924
551	66	-411	238	292.1	PASS	2,051,620
556	41	-395	218	279.8	PASS	2,975,138
561	61	-446	254	301.9	PASS	1,544,604
566	64	-441	253	289.8	PASS	2,194,001
571	67	-445	256	284.1	PASS	2,607,037
576	82	-581	331	346.8	FAIL	467,736
581	77	-618	347	362.1	FAIL	323,141
586	117	-607	362	367.0	FAIL	287,665
591	148	-510	329	324.6	PASS	828,123
596	168	-681	424	424.3	FAIL	82,439
601	286	-583	434	434.5	FAIL	67,248
606	281	-592	436	436.5	FAIL	64,620
611	265	-492	378	378.5	FAIL	220,525
616	271	-691	481	480.8	FAIL	28,098
621	278	-512	395	394.9	FAIL	153,119
626	265	-658	461	461.5	FAIL	40,023
631	240	-663	451	451.2	FAIL	48,560
636	129	-620	374	374.3	FAIL	242,630
641	220	-607	413	413.3	FAIL	103,365
646	129	-713	421	420.6	FAIL	89,009
651	148	-526	337	336.6	PASS	605,588
656	220	-689	454	454.5	FAIL	45,636
661	109	-579	344	344.0	PASS	502,614
666	-32	-577	272	272.1	PASS	3,775,360

The predicted failures are not randomly distributed; instead, they are concentrated along the face wall and the die radius transition, as shown in Figure 7.28. The die radius transition acts as a stress riser. When the trimming tool contacts the sheet, the force is not evenly spread out and concentrates around the tool edge. The localized force creates a high-shear stress area before the material fully shears. Ultra-high strength DP980 requires greater cutting forces, which increases shear stress at the tool edge.

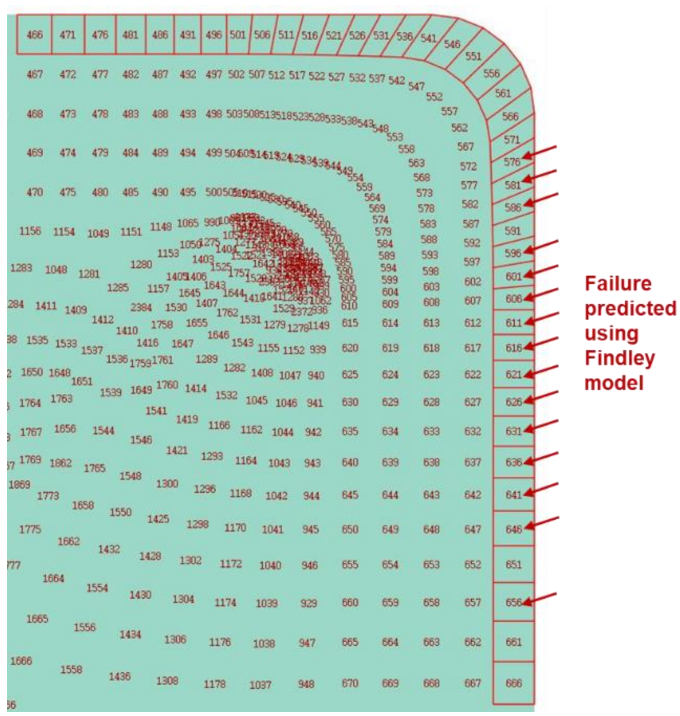

Figure 7.28. The Findley model predicts marked elements with a finite fatigue life.

7.6. Validation with Experimental Results

Figure 7.29 shows the spatial distribution of failed elements on the lower insert, including their distances from the trim edge. Each element has a different fatigue life due to local variations in shear and normal stress levels. The shortest predicted life was in element #616, which failed after only 28,098 cycles and was located 0.07 mm from the trim edge—an area that experiences concentrated loading from repeated contact with the sheet material.

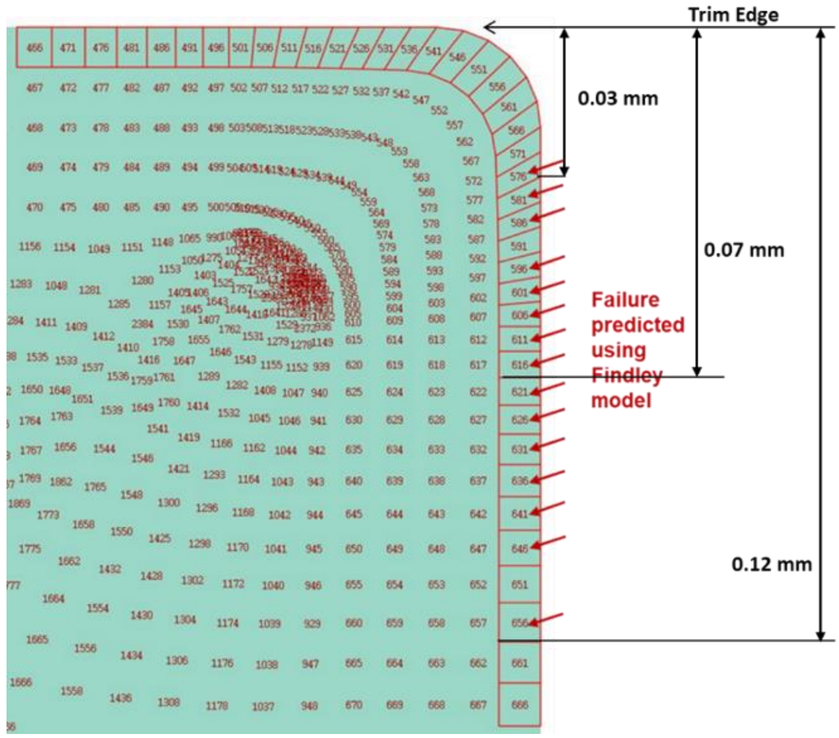

Figure 7.29. The distance of elements with a finite fatigue life from the trim edge.

Experimental validation of the fatigue analysis was conducted through surface characterization of the trimming edge at various stages of wear. Figure 7.30 shows optical profilometry images of the lower trimming insert in its initial condition and after 20,000, 40,000, 60,000, and 80,000 trimming cycles. The images reveal progressive microchipping along the cutting edge, with increasing size and frequency of material loss as the number of cycles grows. Notably, the location and depth of the chipping areas demonstrate a clear spatial correlation with the simulation results in Figure 7.29, confirming the predictive accuracy of the Findley fatigue model.

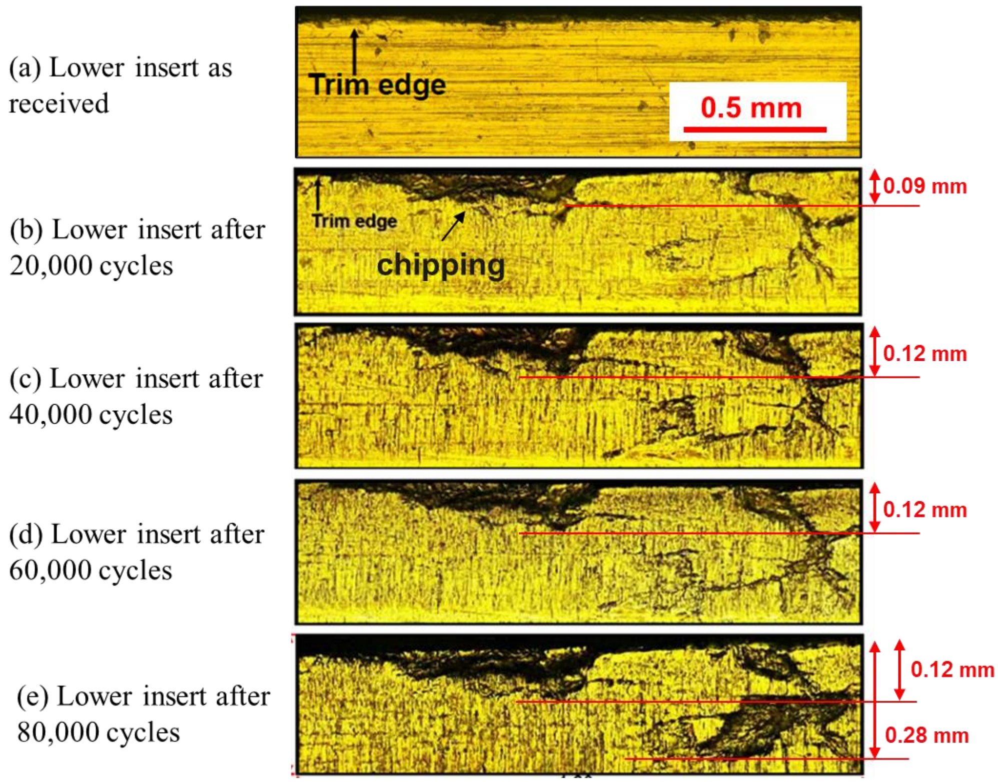

Figure 7.30. Optical profilometry images of the lower trimming insert with scales (a) as received and after (b) 20,000, (c) 40,000, (d) 60,000, and (e) 80,000 trimming cycles.

Further confirmation of the observed damage progression is shown in Figure 7.31. The 3D profilometry image captured with a Keyence microscope after 96,900 trimming cycles reveals a detailed surface topography of the lower insert. The depth of the largest measured chip was approximately 0.112 mm from the trim edge, closely matching the earlier optical profilometry measurement of 0.12 mm at the same stage of tool life. This consistency supports the reliability of both the experimental measurements and the numerical fatigue model.

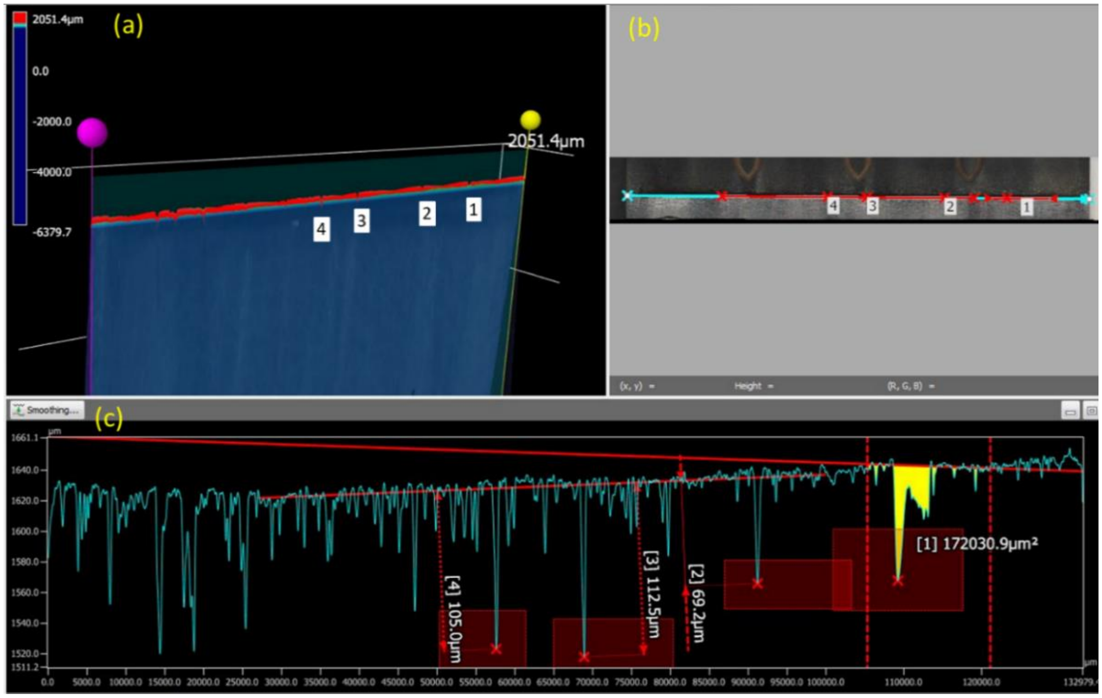

Figure 7.31. (a) Keyence 3D image of the entire trim edge of the lower tool after 96,900 trimming cycles, (b) Optical image of the lower tool trim edge with four locations marked for further measurements, and (c) Results of the profilometry of the lower trimming tool with the measured depth of microchipping for locations 1 to 4.

At the end of the trimming campaign, after 230,000 cycles, the lower trimming tool exhibited multiple irregular microchipping along the trimming edge. Figure 7.32 provides an overview of the lower trimming insert after 230k cuts. Selected regions of interest, marked with red squares and labeled 1 to 12, were then examined in greater detail using high-magnification microscopy, with the corresponding microstructural features documented in Figure 7.33 through Figure 7.36.

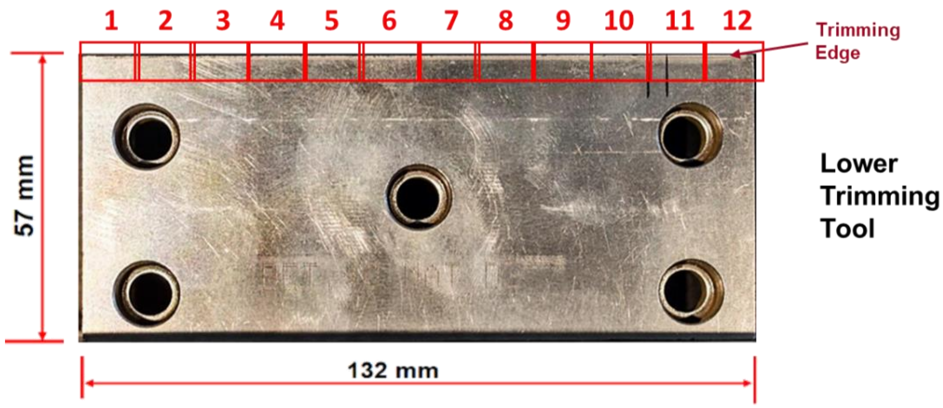

Figure 7.32. Lower trimming insert illustrating the 12 zones for higher magnification microscopy.

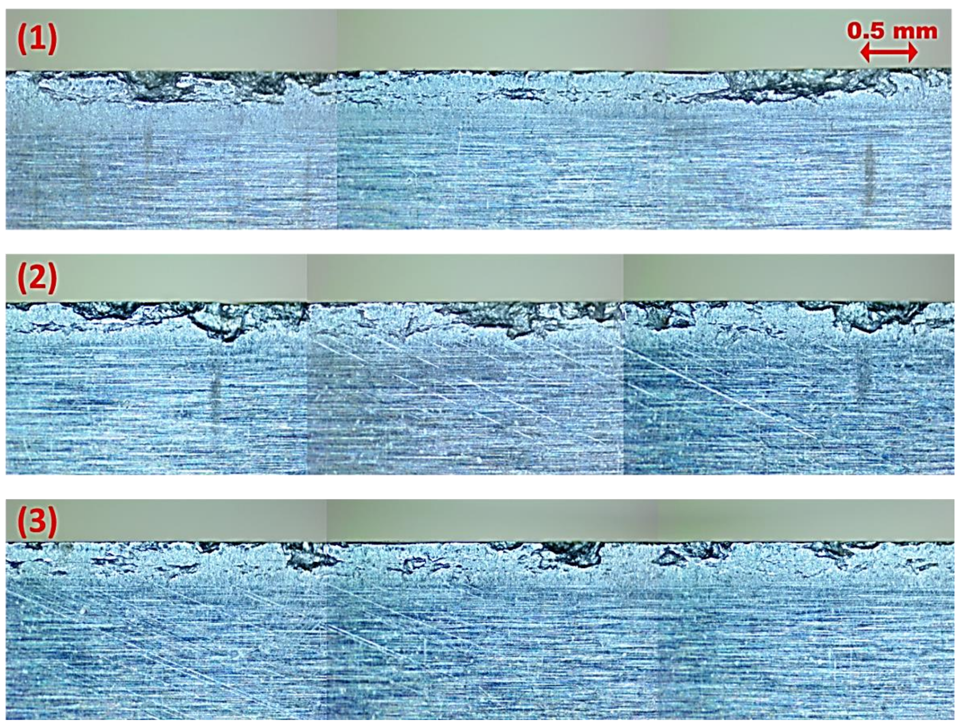

Figure 7.33. High-resolution microscopic (40x) images taken sequentially along the edge of the D2 tool after 230,000 cuts for zones 1 to 3.

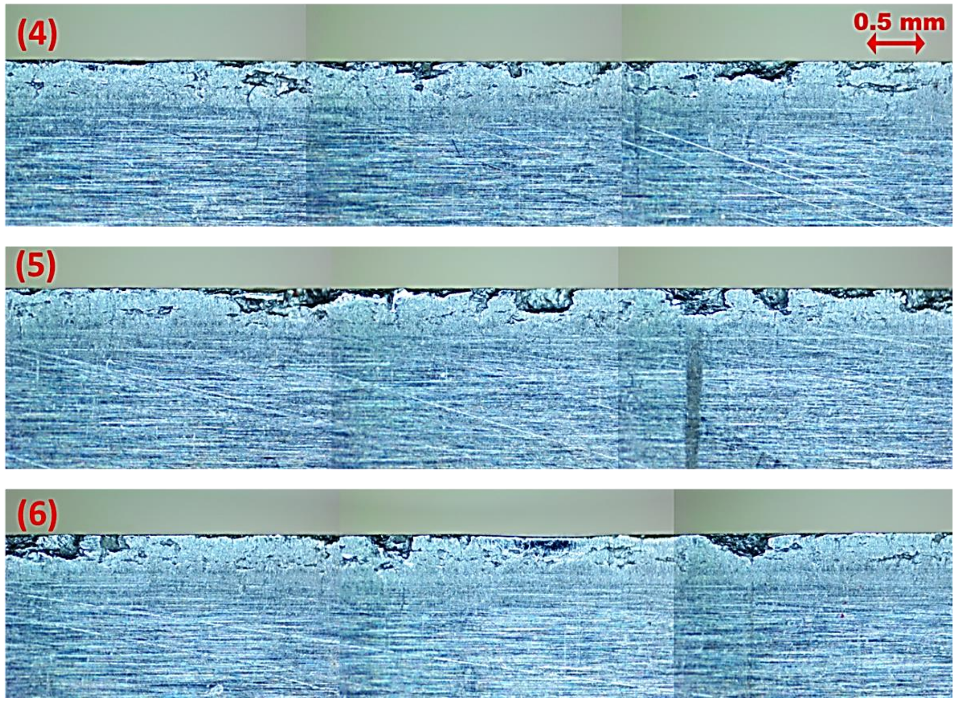

Figure 7.34. High-resolution microscopic (40x) images taken sequentially along the edge of the D2 tool after 230,000 cuts for zones 4 to 6.

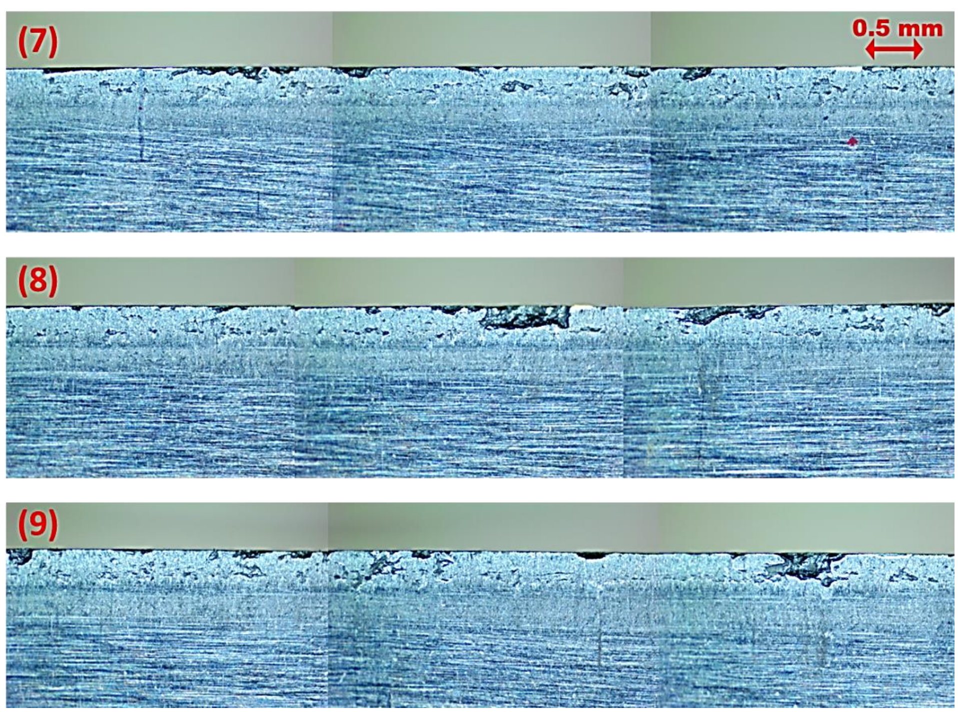

Figure 7.35. High-resolution microscopic (40x) images taken sequentially along the edge of the D2 tool after 230,000 cuts for zones 7 to 9.

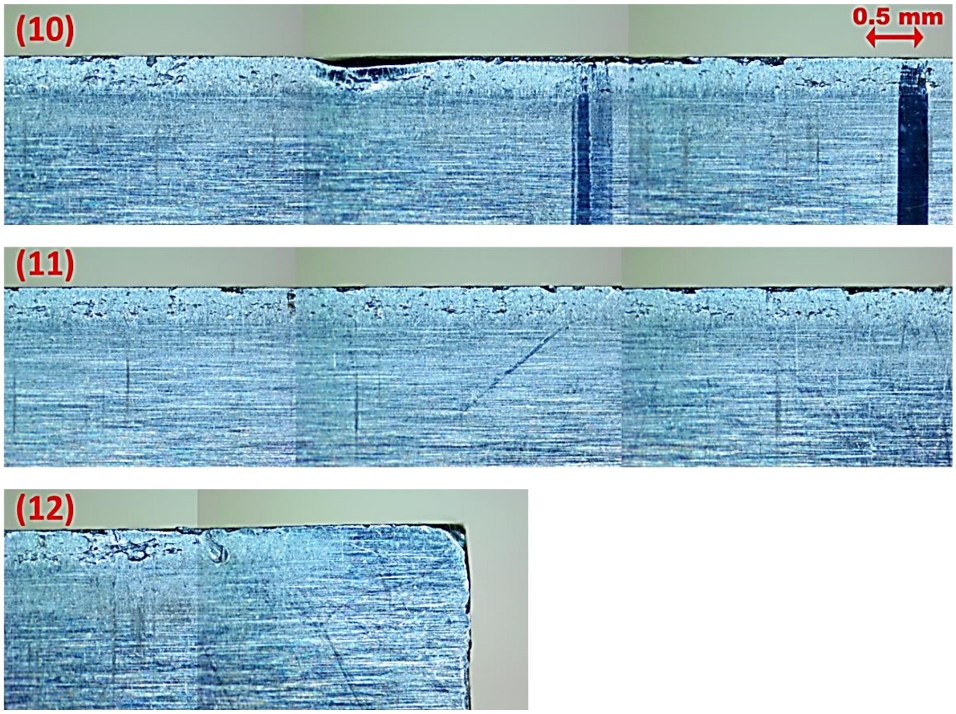

Figure 7.36. High-resolution microscopic (40x) images taken sequentially along the edge of the D2 tool after 230,000 cuts for zones 10 to 12.

As observed in the above figures, the primary failure mechanism identified in the D2 trimming tools is fracture caused by microchipping at the trimming edge. Several cracks form parallel to the edge, and the progression of these cracks results in material removal and a chipped edge. These are caused by sliding and high frictional forces along the surface of the insert in contact with the sheet material.

In summary, the simulation results, profilometry measurements, and tool inspections all show consistent trends. Fatigue-induced microchipping begins near the trim edge due to high local stress and worsens with additional trimming cycles. The spatial alignment of numerical and experimental damage confirms the validity of the fatigue analysis approach and underscores its usefulness for predicting wear in industrial trimming operations.

7.7. Influence of Carbide Orientation in D2 Tool Steel

D2 tool steel's excellent wear resistance comes from a high volume of carbides. These carbides are not evenly distributed; instead, wrought tool steels often exhibit a distinct “carbide band” microstructure. This banding results from hot forging and rolling during manufacturing, creating directional properties similar to fiber-reinforced composites. As a result, the mechanical response of D2 steel can differ greatly depending on its orientation relative to the rolling direction.

Edge chipping is closely related to the fatigue toughness of tool steels under repeated impacts and cyclic loading. While conventional fracture toughness is usually measured by a single-impact test, such as the Izod test [215], these results offer useful but limited insight into fatigue performance. Figure 7.37 shows a bar graph comparing the longitudinal and transverse unnotched Izod impact strengths of several tool steel grades, including D2 [148]. The data show that longitudinal impact strength is consistently higher than transverse impact strength across all studied steels. This trend is expected, as fractures in longitudinal specimens occur across the elongated grain and carbide structure, making crack propagation more difficult.

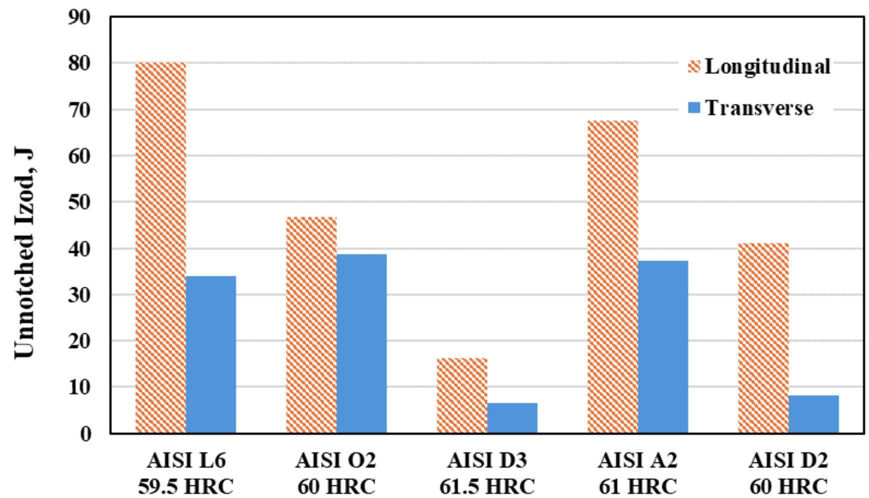

Figure 7.37. Bar graph comparing longitudinal and transverse unnotched Izod impact strengths of grades tested at working hardness level, based on data from [148].

Among the steels reported, D2 shows the greatest anisotropy, with its transverse impact strength about 80% lower than its longitudinal strength. This notable decrease highlights the strong influence of carbide band orientation. Under transverse loading, cracks can nucleate and propagate more easily along elongated carbides and inclusions, leading to decreased fracture resistance. Although Izod impact results do not directly indicate fatigue crack initiation and growth, they underscore that rolling direction significantly affects durability under cyclic conditions. The lower transverse toughness suggests that once cracks start, they can grow more quickly, lowering the fatigue limit in that orientation.

7.8. Mechanism of fatigue in trimming tools

In the current study, the primary set of worn inserts with 230,000 cuts were not salvaged for microstructural examination. However, as part of a preliminary side study, another pair of D2 inserts, manufactured with a similar hardness level and by the same tool manufacturer, was run for 35,000 cuts during the earliest phase of this research. These inserts were sectioned and characterized using scanning electron microscopy (SEM) and backscattered electron (BSE) imaging.

Although the results from the 35,000-cut inserts cannot be directly extrapolated to the long-run 230,000-cut tools, they provide valuable insight into carbide orientation within the microstructure and their role in fatigue crack behavior.

As shown in Figure 7.38, the microstructure of D2 tool steel consists of elongated bands of primary carbides, M_7C_3, aligned with the rolling direction during tool production. In the carbide notation, C is carbon, and M represents the metal elements, primarily chromium (Cr) and iron (Fe). Aligning the rolling direction relative to the trimming edge has not been considered during the production process of inserts; however, in this particular case, for the 35000-cut lower trimming insert, the rolling direction is parallel to the side wall.

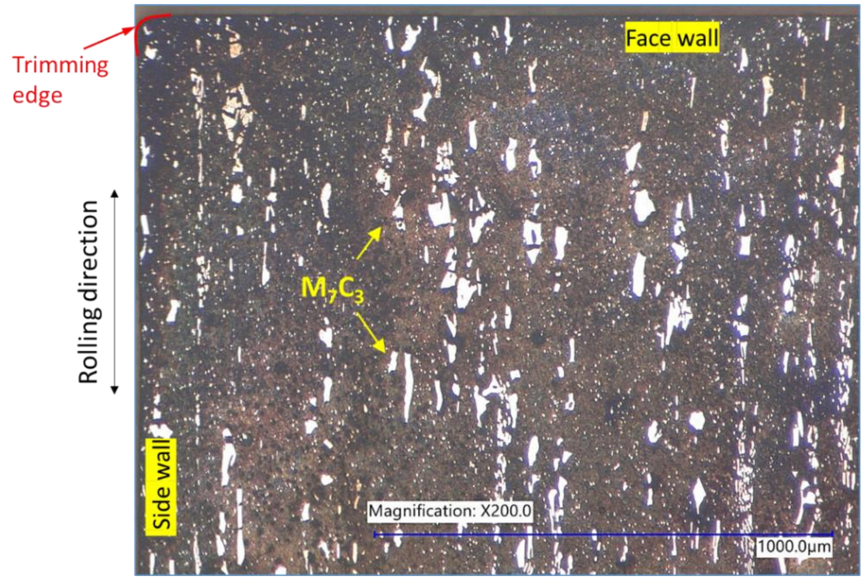

Figure 7.38. SEM Backscatter electron image of the 35,000-cut lower D2 tool, showing the carbide bands identified in the microstructure.

For the SEM analysis of the trimming edge, two different cross-sectional samples along the edge have been extracted from the lower trimming D2 insert, as shown in Figure 7.39.

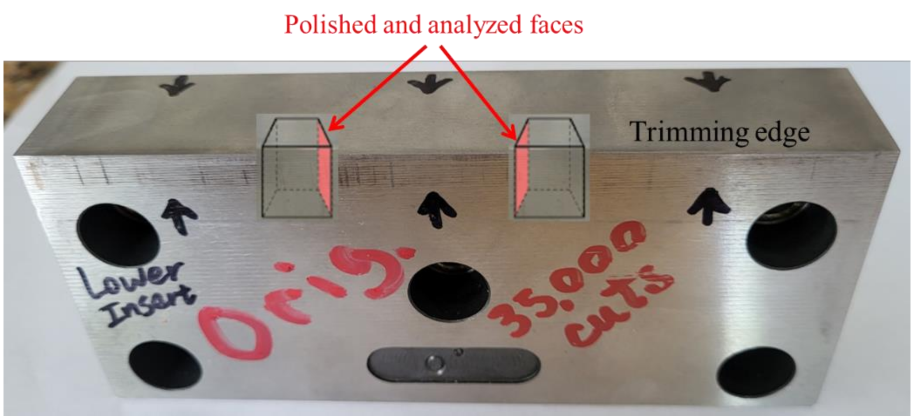

Figure 7.39. Identification of two different cross sections along the trimming edge of the 35,000-cut lower D2 tool, with the polished faces marked in red.

Figure 7.40 (a–d) shows a progressive magnification of the trimming edge, where localized microchipping is observed beneath the cutting surface after 35,000 trimming cycles. Red arrows in the pictures indicate some of the initiated cracks. Higher magnifications reveal fractured carbides and small cracks propagating outward toward the tool surface. These observations confirm that carbide breakage acts as an effective stress concentrator, serving as a preferential site for crack nucleation. Once initiated, these cracks extend toward the free surface, mainly in the vertical direction of tool movement, producing small-scale chipping along the edge.

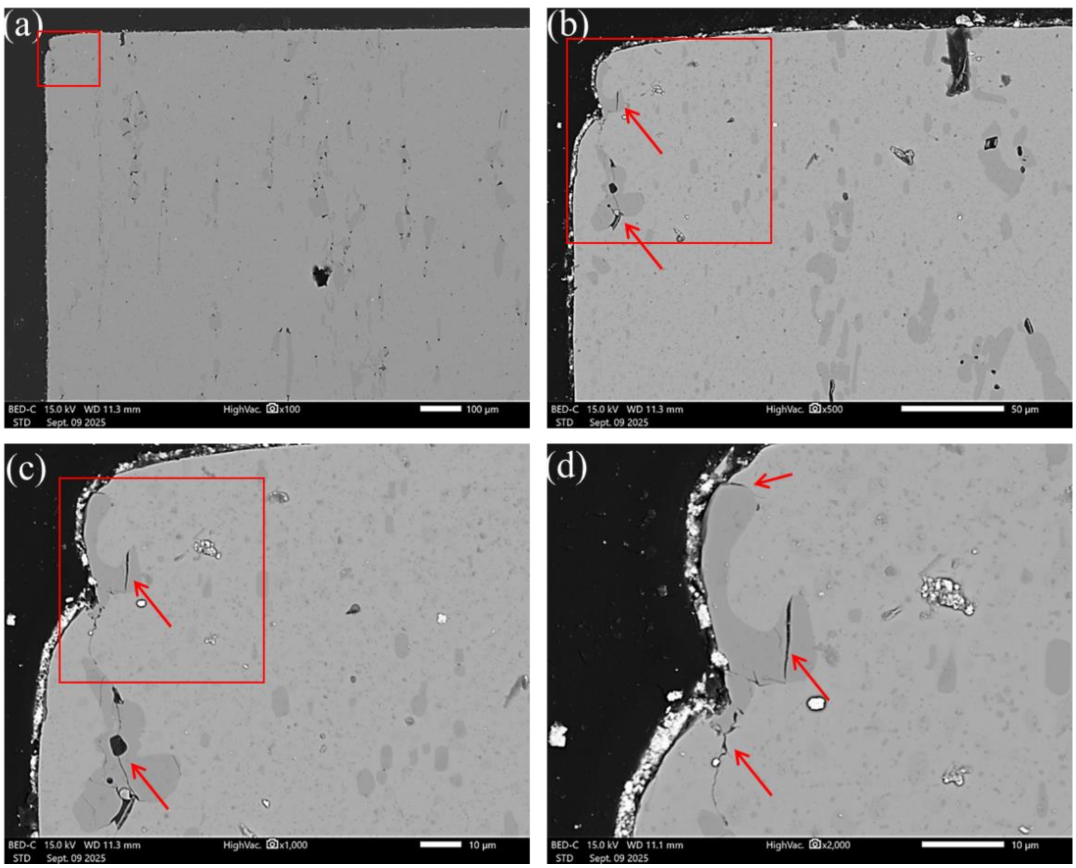

Figure 7.40. SEM cross-sectional images of the lower tool edge capturing a small microchipping at different magnifications of (a) 100x, (b) 500x, (c) 1000x, and (d) 2000x.

Further evidence of this mechanism is shown in Figure 7.41 (a–d) for the second cross-section along the edge of the 35,000-cut insert. At lower magnifications, the edge looks mostly intact; however, at higher magnifications, multiple cracks are visible near the trimming edge. The cracks have two different origins: (i) shallow cracks starting directly at the tool surface, either at the sidewall or face of the trimming edge, both of which are marked with red arrows in Figure 7.41 (b), and (ii) subsurface cracks forming from broken carbides within the microstructure. In the second case, the elongated carbide bands act as natural pathways for crack growth, allowing cracks to expand and eventually merge with surface defects. This behavior illustrates the direct connection between carbide orientation and fatigue-related fracture mechanisms in D2 tool steel.

Although the current SEM study was conducted on 35,000-cut inserts rather than the long-run 230,000-cut tools, the results strongly suggest that carbide presence and orientation are crucial in influencing tool life by affecting both the sites of crack nucleation and the preferred paths of crack propagation.

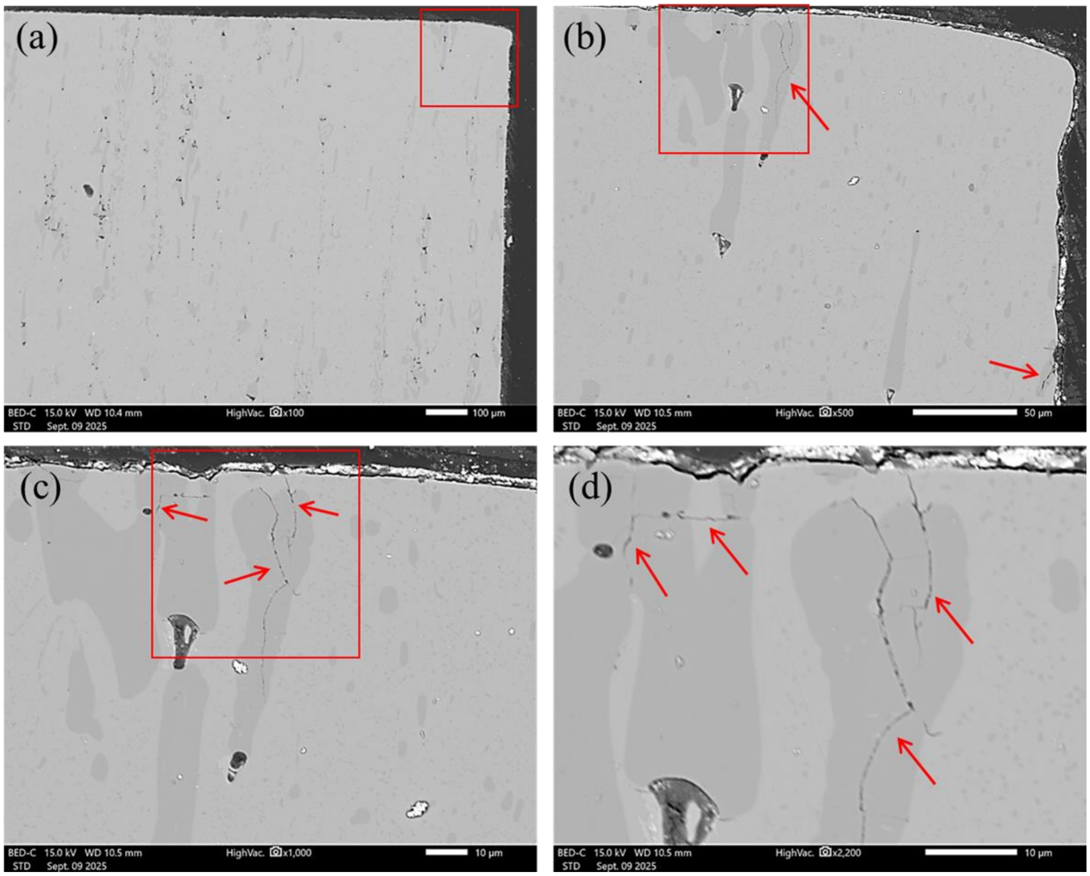

Figure 7.41. SEM cross-sectional images of the lower tool edge capturing several crack formations at different magnifications of (a) 100x, (b) 500x, (c) 1000x, and (d) 2000x

For the 230,000-cut insert, damage and microchipping are severe on the trimming edge, as shown in Figure 7.42. The maximum depth for chipping from the trim edge was found to be 0.34 mm, along with several subsurface cracks extending below the cutting edge. These cracks are likely early signs of future chipping events, indicating that fatigue-driven damage not only accumulates but also propagates in depth as the tool wears. The presence of these cracks also suggests that catastrophic edge failure could occur if the tool is used beyond its intended lifespan.

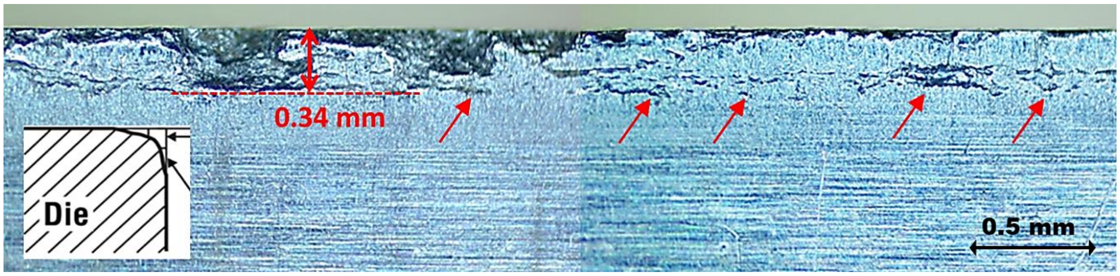

Figure 7.42. Optical microscopic image of the vertical wall of the lower tool after 230,000 trimming cycles, showing developed chipping as well as cracks below the cutting edge.

Stachowiak and Batchelor [216] discussed how cracks and fissures often appear in micrographs of worn surfaces, illustrating the mechanism of fatigue wear initiated by cracking from the contact surface, as shown in Figure 7.43. As shown in the figure, primary cracks can initiate at the surface due to weak points (such as a broken hard particle, an asperity, a crater, or an imperfection). They may spread along weak planes like slip planes or dislocation cell boundaries. This spread can happen either when a secondary crack forms from the primary one or when the primary crack merges with an existing subsurface crack. When the developing crack reaches the surface again, a piece of material breaks off. An example of cracking from the side wall surface for the 35,000-cut insert is shown in Figure 7.41 (b).

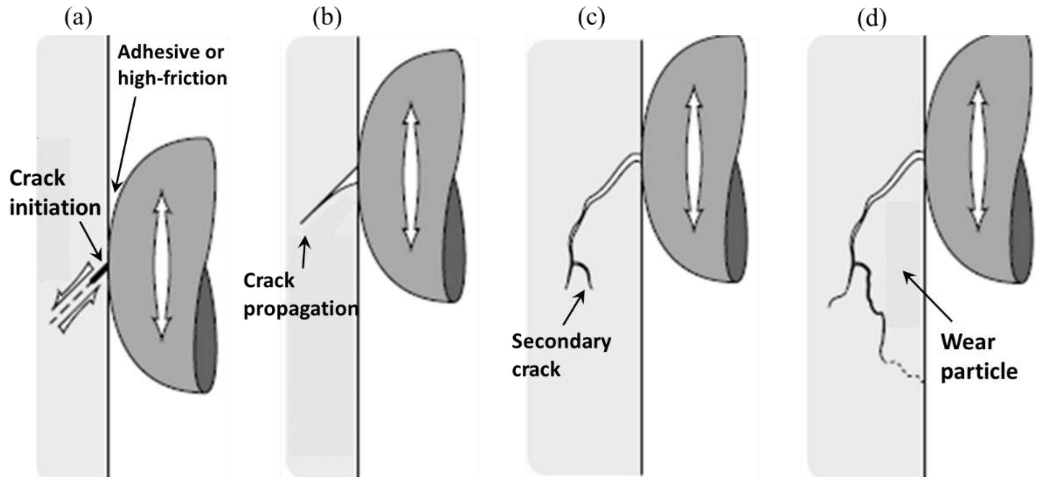

Figure 7.43. Schematic illustration of the process of surface crack initiation and propagation, including (a) crack initiation from the side wall, (b) primary crack propagation, (c) secondary crack initiation, and (d) secondary crack propagation and formation of a wear particle, adopted after [216].

One of the main questions is understanding how cracks begin under the high compressive stresses during a trimming cycle. A theory proposed by several researchers is that surface imperfections, such as craters or asperities or hard and brittle particles, can generate stress fields similar to those at a notch tip under purely compressive cyclic loading [147], [216]. As Hsu and Wang [217] observed, such discontinuities cause uneven stress distributions in the surrounding material, which can lead to residual tensile stresses even when the overall load is compressive. Fleck et al. [218] showed that the size and extent of this tensile field are closely linked to the amount of plastic deformation or strain gradients. Crack formation may then occur during the unloading phase of the cyclic process if the residual tensile stress exceeds the local fracture strength ahead of the notch.

The further propagation of these cracks can only be explained if the applied compressive stresses are high enough to generate residual tensile stresses through plastic deformation near the crack tip after complete unloading. Cracks that start from craters or other surface defects, such as asperities, tend to grow in a direction perpendicular to the surface.

In our case, for the D2 lower trimming insert up to 230,000 cuts, surface cracks developed beneath the trim edge and are marked by the red arrows in Figure 7.42. These cracks spread along planes parallel to the cutting edge, and when they reach the surface, they cause larger fragments of material to detach. This process directly contributes to microchipping and speeds up fatigue-induced edge degradation, as shown schematically in Figure 7.44.

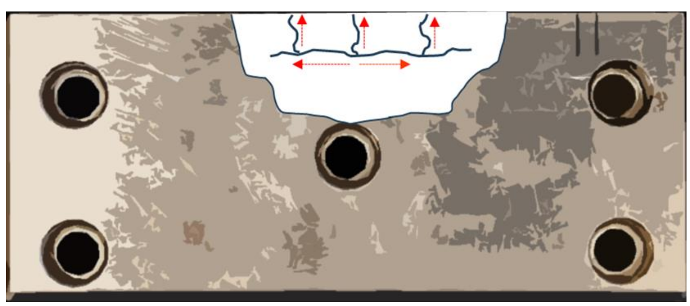

Figure 7.44. Schematic illustration of the progression of sub-superficial cracks. The arrows indicate the direction of fatigue propagation.

Crack formation may also arise from inclusions or secondary phases located in the subsurface, which act as initiation sites for voids during plastic deformation and subsequently promote the growth of cracks. Stachowiak and Batchelor [216] described the process of subsurface crack formation through the growth and connection of these voids, as illustrated schematically in Figure 7.45.

In D2 tool steel, hard carbide particles mainly initiate cracks, as shown in Figure 7.40 and Figure 7.41 for the 35,000-cut insert. These figures clearly show multiple crack formations within the carbide particles or at the interface between the carbides and the substrate. One possible explanation is that during trimming, contact pressure and frictional forces create dislocation pile-up at the carbide particles, resulting in localized stress concentrations that form voids. As deformation continues, these voids grow by trapping more dislocations and eventually merge into microcracks. The crack then turns toward the surface, releasing a thin, laminar fragment. This change in the crack's direction can be attributed to a shift in the stress state at the crack tip.

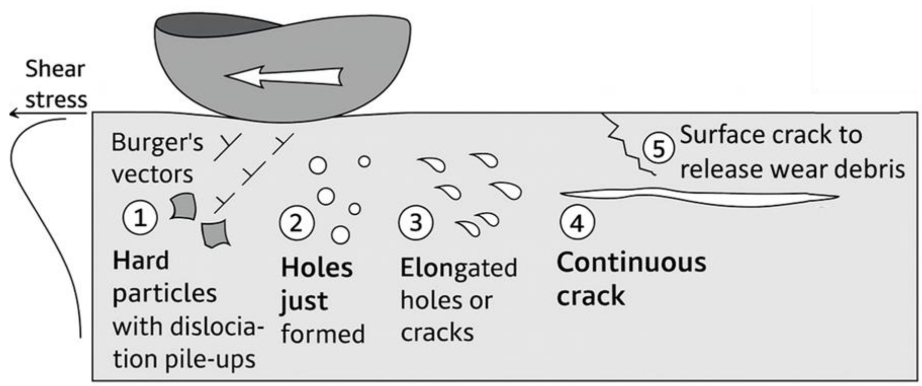

Figure 7.45. Illustration of a process of subsurface crack formation by the growth and linking up of voids, adopted after [216].

If the crack initiates from the face (horizontal) wall, as it was observed in Figure 7.41 (d) for our 35,000-cut D2 insert, it might propagate curvilinearly toward the side (vertical) wall. Picas [147] schematically demonstrated how the stress state changes following crack propagation during hole punching, as shown in Figure 7.46. Without a crack, the region where crack nucleation occurs (the face wall) experiences higher compressive stresses radially than axially. Consequently, residual tensile stresses are also stronger in the radial direction, leading the crack to grow vertically, initially perpendicular to the main stress. As the crack penetrates deeper, the stress pattern shifts, and axial compressive stresses eventually become dominant over radial ones. This shift in stress distribution causes the crack to change direction, leading it to grow horizontally toward the side wall.

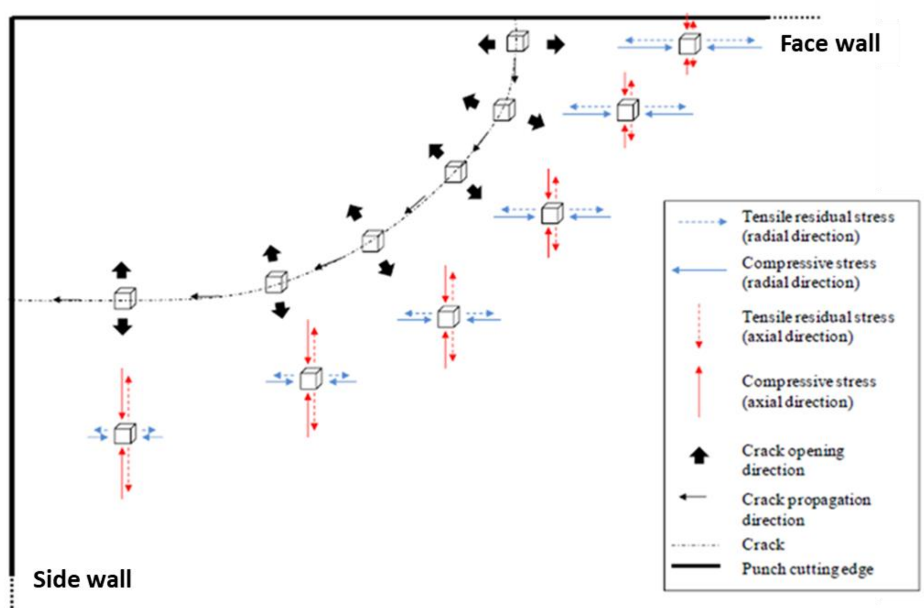

Figure 7.46. Schematic description of the different stress states acting at the cutting edge of a piercing punch, adopted after Picas [147].

In conclusion, microchipping in D2 trimming tools during high-cycle trimming of AHSS is primarily driven by fatigue crack initiation and propagation. The anisotropic microstructure of wrought D2 steel significantly affects tool durability, as elongated carbides act as preferred sites for crack initiation under cyclic loads. SEM analysis of a 35,000-cut trimming insert showed multiple crack initiation mechanisms. First, cracks can initiate within carbide particles in the microstructure and grow in the stroke direction until they reach the surface. Second, cracks may originate from the side wall beneath the trimming edge, spreading parallel to the edge, merging with other cracks, or diverting toward the face wall. Third, cracks might initiate from the face wall itself and grow along curved paths. These mechanisms highlight the complex interactions among carbide orientation, crack initiation sites, and propagation routes that ultimately lead to edge degradation and microchipping.

7.9. Summary

This chapter investigated the trimming performance and durability of D2 tool steel when trimming dual-phase DP980, focusing on tool wear, sheared edge quality, and fatigue-driven microchipping under high-cycle loading. Experiments with up to 230,000 cycles, along with fatigue modeling and microstructural analysis, provided new insights into the relationships between die wear, edge quality, and fatigue performance.

The results confirmed that tool wear directly affects sheared edge quality by increasing burr height and burnished depth. DP980-1 and DP980-2 showed the same trend, although DP980-1 consistently produced the largest burrs, and DP980-2 was less sensitive to wear compared to DP980-1. A strong link was found between localized die chipping and burr growth on trimmed blanks, indicating that monitoring edge condition is a useful way to track die wear. The quality of the trim edge was also shown to be essential for stretchability: worn tools created rougher, more damaged edges with larger burrs, which increased stress concentration during stretchability tests and led to faster failure at lower strains.

A fatigue analysis framework was developed for the D2 trimming tool by combining simulation data with existing fatigue models that account for mean stress and shear stress effects. Morrow and Goodman's methods predicted finite lives (400,000 – 900,000 cycles) for parts under high tensile or compressive stresses. The Findley model, which accounts for combined tensile and shear stresses, provided the best match to experimental results, reasonably predicting finite-life locations that aligned with observed chipping.

Experimentally, microchipping was first observed after 20,000 cycles. Although 230,000 cycles were achieved, undamaged regions remained along the trimming edge, confirming that chipping is highly localized. This could be due to inhomogeneity in microstructure and carbide distribution. Chipping most frequently occurred below the die edge radius near the punch entrance side, in areas where numerical analysis identified high normal and shear stress amplitudes. SEM examination of a 35,000-cut tool revealed three distinct crack initiation modes: cracks starting within carbide particles and propagating in the stroke direction, cracks originating from the side wall beneath the trimming edge and spreading parallel to it, and cracks initiating from the face wall and growing along curvilinear paths. These mechanisms reflect the influence of carbide banding and anisotropy in wrought D2 tool steel, which strongly influence crack nucleation and growth.

7.9.1. Practical Implications

These findings underscore the importance of closely monitoring sheared edge conditions to assess die wear in production settings indirectly. Employing fatigue-based life prediction tools in die design and maintenance can help prevent unexpected tool failures, extend service intervals, and improve process reliability. For automotive stamping, where DP980 and other ultra-high-strength steel (UHSS) grades are commonly used, maintaining edge quality throughout long production runs directly results in better formability, fewer rejected parts, and reduced manufacturing costs.

Furthermore, UHSS creates tooling demands that challenge the mechanical properties of conventional tool steels. Existing die standards and conventional tool steels, such as D2, might not be sufficient for consistently and reliably trimming and piercing UHSS with optimal performance. Selecting the right tool steel grade or using advanced die coatings helps ensure consistent, reliable tooling performance in UHSS applications.

CHAPTER EIGHT
CONCLUSIONS

This chapter offers conclusions and recommendations for future research on the durability of trimming dies and the formability of sheared edges in advanced high-strength steels, with a focus on DP980. The study combined long-term experimental trimming tests, detailed analyses of edge quality and stretchability, finite-element simulations of the trimming process, and fatigue modeling of D2 tool steel inserts. The chapter is divided into three sections: (1) a summary of the key findings from experimental, numerical, and analytical studies; (2) the scientific and practical contributions of this work; and (3) suggestions for future research and industrial implementation.

8.1. Research summary

This dissertation examined the trimming and punching behavior of dual-phase 980 (DP980) ultra-high-strength steel, focusing on how clearance, trimming line orientation, and microstructure influence sheared edge quality and stretchability. Trimming experiments on IF, BH210, and HSLA340 steels supported experiments with two commercial DP980 grades from different suppliers, using D2 trimming inserts with clearances ranging from 4% to 40% of the sheet thickness. Measurements of burr height, burnish depth, rollover, and fracture zones provided detailed insights into edge morphology, while microhardness mapping showed how clearance affects subsurface deformation. Among the DP980 steels, DP980-2 showed better edge quality and was less prone to burr formation, likely due to its finer microstructure and greater isotropy. In contrast, DP980-1 experienced more burr growth, increased anisotropy, and more variable rollover. Comparisons with more ductile grades confirmed that higher ductility generally results in larger burrs, even at small clearances. Microhardness data also indicated that intermediate clearances (~17%) create the most balanced hardness profiles, offering a good compromise between edge integrity and material work hardening.

Edge stretchability was assessed through tensile, side-bending, and hole expansion tests, revealing that optimal clearance varies depending on both test type and material. DP980-1 performed best at 17% clearance in tensile and side-bending tests but favored 10% in hole expansion, while DP980-2 consistently achieved maximum stretchability at 17% across all tests. Although the DP980-1 and DP980-2 sheets had similar tensile strengths and overall mechanical behavior, they showed notably different results in trimmed-edge stretchability. DP980-2 experienced significantly lower strain during stretching and was more influenced by changes in cutting clearance than DP980-1. Additionally, DP980-1 endured significantly longer than DP980-2 after the initial crack, continuing until a through-thickness fracture occurred. Fracture mechanism analysis during tensile testing of trimmed specimens indicated that crack initiation shifted with increasing clearance from the burnished region toward burr tips, reducing elongation, and confirming that edge formability strongly depends on clearance.

A unique fracture mechanism was observed during the trimming of DP980 steel at larger clearances, resulting in burr removal during the final trimming stage. Finite element analysis of DP980-1 showed that, at a very large clearance of 40%, a secondary crack begins at the edge of the lower tool while the primary crack propagates toward it simultaneously. The intersection of these two cracks causes complete separation, leaving the edge of the trimmed part with a broken burr.

To support the experiments, a finite element model of trimming was developed using ABAQUS/Explicit. Rigid-tool simulations captured strain localization and fracture progression, while deformable-tool models measured die stresses for fatigue analysis. A mesh sensitivity study determined that at least 100 through-thickness elements were necessary for stable results, leading to the selection of a 145-element mesh. Extended flow curves from sequential rolling and tensile testing provided constitutive data beyond uniform elongation. Fracture criteria were calibrated, with the Johnson–Cook model chosen for its ability to replicate bending, bulge, and hole-flanging test outcomes. A significant improvement was the implementation of kinematic contact, which eliminated non-physical stress peaks and produced stress states consistent with experimental trends.

The validated model reasonably reproduced force–clearance behavior and clarified how clearance influences crack initiation, providing stress histories for future fatigue life predictions.

To study the durability of D2 trimming tool steels, a high-cycle trimming test on DP980 was conducted, up to 230,000 cycles. Tool wear was shown to decrease edge quality and stretchability. Localized microchipping occurs as early as 20,000 cycles and persists through up to 230,000 cycles. SEM analysis identified three crack initiation mechanisms: cracks forming within carbides, cracks originating from side walls below the edge, and cracks initiating on the die face. These mechanisms reflect the anisotropic carbide-banded structure of wrought D2 tool steel. Fatigue analysis showed that the Findley critical plane model provided a reasonable prediction of tool failure, outperforming the Morrow and Goodman models. The combined experimental and numerical results confirm that fatigue-driven microchipping is the primary wear mechanism in trimming UHSS with D2 dies and demonstrate that part edge quality is directly related to tool durability.

8.2. Contributions

This work makes several key contributions to the field of sheet metal forming and die design for ultra-high-strength steels (UHSS).

First, it provides a systematic experimental basis for understanding how clearance and microstructure affect edge quality and formability in DP980 steel. It also introduces a new microhardness-based method for estimating local stress and strain levels along the sheared edge, enabling quantitative mapping of deformation gradients in trimmed parts.

Second, it shows that two AHSS grades with similar strength and overall mechanical behavior can exhibit very different local formability and sheared edge performance, highlighting the importance of careful consideration during part design and material selection.

Third, the findings show that the burr-breaking mechanism causing a burr-free edge challenges the traditional criterion linking burr height to edge-splitting susceptibility.

Fourth, this study provides one of the few available long-range stress–strain curves for DP980 sheet steel, offering valuable reference data for future material modeling and simulation.

Fifth, it develops a validated finite element framework for trimming DP980, incorporating refined meshing, extended flow curves, Johnson–Cook fracture calibration, and kinematic contact modeling. This framework effectively reproduces experimental force–clearance trends, fracture initiation sites, and burr-breaking behavior, and provides reliable tool stress histories for fatigue assessment.

Sixth, it establishes a direct correlation between burr formation on the part edge and microchipping on the tool edge, providing a practical way to monitor trim-die wear offline without interrupting production.

Seventh, it developed and validated a fatigue life prediction method for trimming tools that simultaneously accounts for both normal and shear stress histories—an area rarely addressed in prior studies.

Together, these contributions provide a comprehensive framework for understanding and improving both edge quality and die life in UHSS trimming operations.

8.3. Future work

Although this dissertation makes significant progress, several avenues for future research remain. From a tooling perspective, further investigation is needed into alternative tool steels and coatings that offer improved resistance to fatigue chipping and wear during UHSS trimming. Powder metallurgy and advanced alloying strategies may reduce carbide banding and improve isotropy in tool steels. Similarly, evaluating next-generation die coatings could lead to enhanced wear resistance and improved friction control during high-strength trimming. On the material side, expanding the study to include other UHSS grades, such as martensitic and press-hardened steels, would increase the applicability of the findings.

From a modeling perspective, future research could improve fracture criteria and constitutive models by including microstructural effects, such as grain orientation and phase distribution for multi-phase AHSS materials. Extending FE models to fully three-dimensional forms would also allow simulation of anisotropic effects and complex tool geometries. Additionally, experimentally determined mechanical and fatigue properties of the tool material could improve the accuracy of results.

For fatigue life analysis, future research could benefit from applying different multiaxial fatigue models and incorporating the micro-mechanical damage features of tool steels. Adding these advanced criteria might improve prediction accuracy, especially when combined with experimental fatigue data of tool steels.

From an industrial implementation perspective, integrating burr height monitoring into closed-loop production systems would enable real-time assessment of both die wear and sheared edge quality. Additional methods, such as incorporating acoustic emission, vibration, or strain sensors within the die, could further improve process control by allowing early detection of deviations in trimming performance.

APPENDICE

A. Microhardness Data for Sheared Edge Profiles

Table A.1. Vickers microhardness data for sheared edge profile trimmed at 4% clearance.

Location	HV Microhardness
1	293
2	297
3	315
4	313
5	324
6	303
7	312
8	314
9	315
10	314
11	337
12	323
13	296
14	318
15	304
16	311
17	317
18	328
19	315
20	290
21	314
22	309
23	296
24	315
25	316
26	295
27	311
28	316
29	327
30	305

Location	HV Microhardness
31	300
32	291
33	299
34	308
35	287
36	313
37	307
38	314
39	310
40	300
41	304
42	304
43	311
44	300
45	330
46	311
47	307
48	315
49	303
50	313
51	308
52	310
53	293
54	321
55	304
56	325
57	319
58	314
59	325
60	320

Location	HV Microhardness
61	319
62	328
63	318
64	309
65	315
66	306

Table A.2. Vickers microhardness data for sheared edge profile trimmed at 10% clearance.

Location	HV Microhardness
1	335
2	335
3	327
4	325
5	319
6	319
7	322
8	344
9	336
10	321
11	337
12	335
13	332
14	333
15	315
16	323
17	318
18	320
19	335
20	323
21	319
22	321
23	323
24	316
25	322
26	305
27	316
28	322
29	324
30	318

Location	HV Microhardness
31	332
32	313
33	317
34	324
35	327
36	310
37	322
38	321
39	327
40	324
41	323
42	333
43	303
44	315
45	311
46	323
47	313
48	338
49	329
50	328
51	326
52	335
53	333
54	331
55	337
56	337
57	354
58	331
59	334
60	338

Location	HV Microhardness
61	335
62	340
63	336
64	354
65	345
66	336
67	327
68	326
69	327
70	317
71	340
72	323
73	341

Table A.3. Vickers microhardness data for sheared edge profile trimmed at 17% clearance.

Location	HV Microhardness
1	308
2	307
3	303
4	316
5	310
6	299
7	311
8	313
9	302
10	325
11	334
12	322
13	321
14	326
15	317
16	324
17	317
18	322
19	317
20	335
21	328
22	319
23	326
24	316
25	336
26	318
27	338
28	319
29	317
30	332

Location	HV Microhardness
31	312
32	334
33	328
34	337
35	324
36	323
37	332
38	319
39	335
40	338
41	336
42	309
43	313
44	319
45	308
46	317
47	333
48	347
49	308
50	312
51	330
52	316
53	313
54	317
55	338
56	348
57	323
58	324
59	329
60	329

Location	HV Microhardness
61	326
62	343
63	356
64	359
65	319
66	318
67	312
68	308
69	311
70	322
71	341
72	337
73	308
74	315
75	319

Table A.4. Vickers microhardness data for sheared edge profile trimmed at 20% clearance.

Location	HV Microhardness
1	321
2	318
3	330
4	328
5	332
6	329
7	333
8	377
9	327
10	322
11	315
12	305
13	326
14	320
15	338
16	373
17	326
18	322
19	327
20	321
21	326
22	331
23	326
24	374
25	319
26	323
27	322
28	322
29	324
30	327

Location	HV Microhardness
31	349
32	364
33	305
34	307
35	328
36	323
37	331
38	336
39	348
40	366
41	308
42	317
43	324
44	324
45	336
46	318
47	363
48	365
49	307
50	317
51	318
52	314
53	341
54	327
55	348
56	374
57	338
58	343
59	337
60	330

Location	HV Microhardness
61	340
62	345
63	351
64	365
65	336
66	328
67	324
68	339
69	336
70	335
71	352
72	364
73	318
74	316
75	326
76	324
77	328
78	336
79	331
80	344

Table A.5. Vickers microhardness data for sheared edge profile trimmed at 30% clearance.

Location	HV Microhardness
1	319
2	328
3	313
4	309
5	302
6	340
7	383
8	398
9	322
10	326
11	314
12	320
13	332
14	354
15	368
16	363
17	301
18	318
19	308
20	302
21	299
22	335
23	382
24	388
25	324
26	329
27	333
28	327
29	335
30	343

Location	HV Microhardness
31	374
32	384
33	313
34	315
35	322
36	323
37	332
38	356
39	344
40	359
41	307
42	326
43	329
44	340
45	335
46	348
47	365
48	371
49	322
50	310
51	324
52	323
53	345
54	359
55	358
56	374
57	298
58	307
59	331
60	344

Location	HV Microhardness
61	361
62	358
63	365
64	379
65	319
66	311
67	321
68	342
69	352
70	355
71	348
72	368
73	327
74	324
75	326
76	324
77	327
78	328
79	330
80	315
81	310
82	324
83	340

Table A.6. Vickers microhardness data for sheared edge profile trimmed at 40% clearance.

Location	HV Microhardness
1	313
2	318
3	310
4	324
5	325
6	350
7	365
8	374
9	299
10	315
11	315
12	316
13	319
14	347
15	385
16	398
17	316
18	316
19	312
20	310
21	332
22	352
23	377
24	393
25	315
26	316
27	311
28	321
29	344
30	340

Location	HV Microhardness
31	375
32	382
33	309
34	326
35	321
36	337
37	352
38	361
39	374
40	372
41	548
42	- - -
43	326
44	345
45	363
46	392
47	382
48	384
49	327
50	336
51	311
52	345
53	355
54	352
55	361
56	367
57	319
58	335
59	327
60	333

Location	HV Microhardness
61	368
62	347
63	369
64	368
65	373
66	304
67	327
68	327
69	338
70	326
71	334
72	348
73	353
74	329
75	336
76	348
77	345
78	348
79	341
80	345

B. Flowchart for the Fatigue Life Estimation using the Findley Model

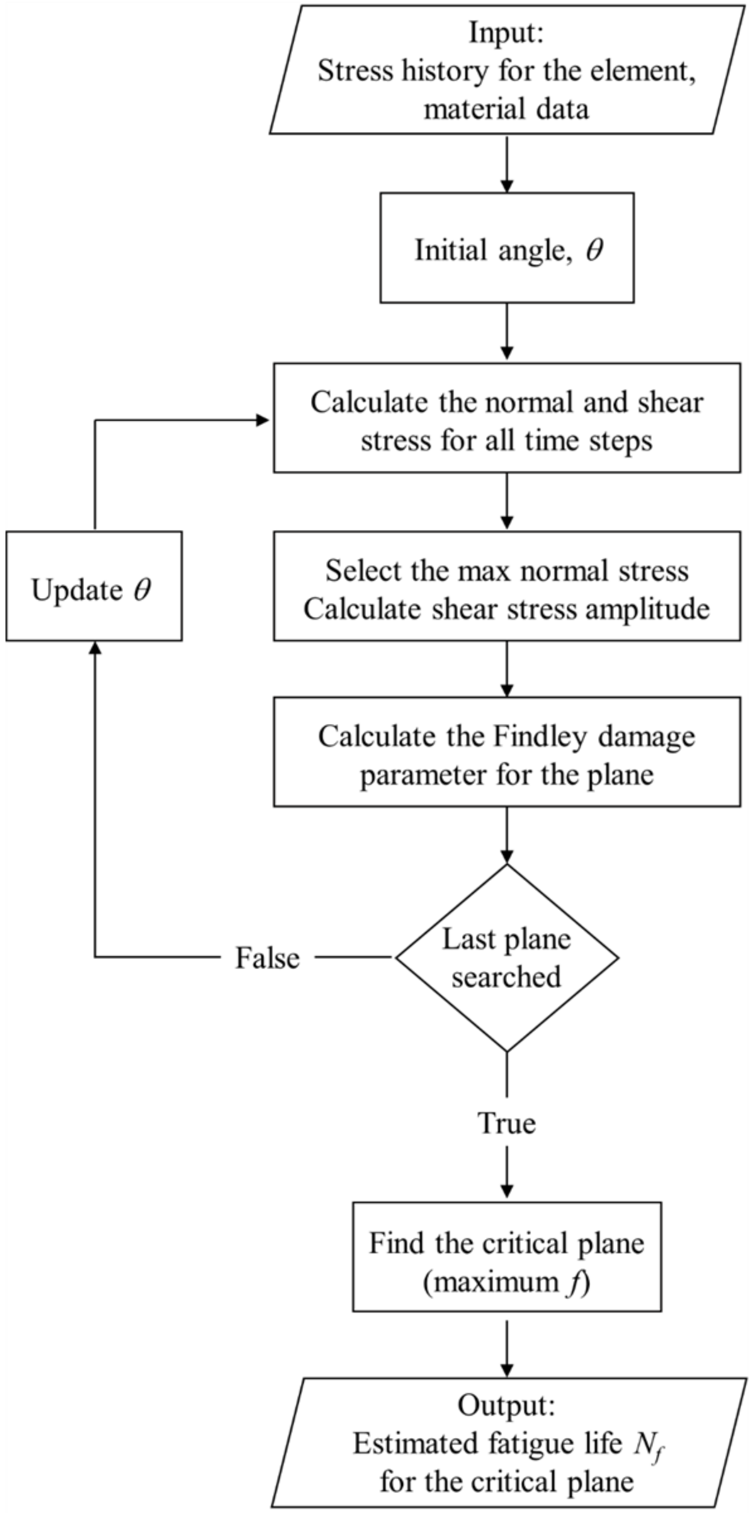

Figure B.1. Flowchart for the numerical implementation of the Findley fatigue model.

REFERENCES

[1] S. Kalpakjian, S. R. Schmid, and H. Musa, *Manufacturing Engineering and Technology*, 6th ed. Singapore: Pearson Education, 2010.

[2] V. Boljanovic, *Metal Shaping Processes: Casting and Molding; Particulate Processing; Deformation Processes; and Metal Removal*. New York, USA: Industrial Press, Inc., 2009.

[3] C. M. Tamarelli, "AHSS 101: Evolving Use Of Advanced High-Strength Steels For Automotive Applications," 2011.

[4] S. Keeler, M. Kimchi, and P. J. Mconey, *Advanced High-Strength Steels Application Guidelines: Version 6.0*. Middletown, OH. USA: World Auto Steel Association, 2017.

[5] R. Rana and S. B. Singh, *Automotive Steels: Design, Metallurgy, Processing and Applications*. Woodhead Publishing, 2017.

[6] N. Fonstein, *Advanced high strength sheet steels: Physical metallurgy, design, processing, and properties*. Switzerland: Springer International Publishing AG, 2015.

[7] M. Y. Demeri, "Forming of Advanced High Strength Steels," in *ASM Handbook, Volume 14B - Metalworking: Sheet Forming*, S. L. Semiatin, Ed. Materials Park, OH. USA: ASM International, 2006, pp. 530–538.

[8] M. Y. Demeri, *Advanced High-Strength Steels: Science, Technology, and Applications*, 1st ed. Materials Park, OH. USA: ASM International, 2013.

[9] The International UltraLight Steel Auto Body (ULSAB) Consortium, "Advanced Vehicle Concepts Overview Report," *UltraLight Steel Auto Body (ULSAB) consortium*, p. 52, 2002.

[10] D. J. Schaeffler, "Introduction to Advanced High Strength Steels - Part I: Grade Overview," *Stamping Journal*, vol. Nov., 2004.

[11] S. Sriram, B. Yan, and M. Huang, "Characterization of press formability of advanced high strength steels using laboratory tests," *SAE Technical Paper*, no. 724, 2004.

[12] J. Sulik and J. Geeraerts, "2019 Chevrolet Silverado Structure Review," *Great Design in Steel, Livonia, MI*, 2018.

[13] E. Billur and T. Altan, "Challenges in Forming Advanced High Strength Steels," *Engineering Research Center for Net Shape Manufacturing (ERC/NSM)*, 2010.

[14] K. S. Choi, W. N. Liu, X. Sun, M. A. Khaleel, and J. R. Fekete, "Influence of manufacturing processes and microstructures on the performance and manufacturability of advanced high strength steels," *J. Eng. Mater. Technol. Trans. ASME*, vol. 131, no. 4, pp. 0412051–0412059, 2009.

[15] D. A. Smith, *Die Design Handbook*, 3rd ed. Dearborn, MI. USA: Society of Manufacturing Engineers (SME), 1990.

[16] M. Chen and D. J. Zhou, "AHSS Forming Simulation for Shear Fracture and Edge Cracking," *Great Design in Steel, Livonia, MI*, 2008.

[17] P. Larour, H. Schauer, J. Lackner, and E. T. Till, "Edge crack Simulation with the modular 'smiley' forming tool," in *International Deep Drawing Research Group Conference*, 2016.

[18] Uddeholm Tooling & SSAB Swedish Steel, "Tooling Solutions for Advanced High Strength Steels," 2015.

[19] D. Zhou, C. Du, J. Siekirk, J. McGuire, X. Chen, and B. S. Levy, "A practical failure limit for sheared edge stretching of automotive body panels," *SAE Technical Paper*, no. 2010-01–0986, 2010.

[20] V. Boljanovic, *Sheet Metal Forming Processes and Die Design*. New York, USA: Industrial Press, Inc., 2004.

[21] F. Klocke, *Manufacturing Processes 4 - Forming*. Berlin, Heidelberg: Springer Berlin Heidelberg, 2013.

[22] J. Beddoes and M. J. Bibby, *Principles of Metal Manufacturing Processes*. Burlington, MA, USA: Elsevier Butterworth-Heinemann, 1999.

[23] Q. B. Le, J. A. DeVries, S. F. Golovashchenko, and J. J. F. Bonnen, "Analysis of sheared edge formability of aluminum," *J. Mater. Process. Technol.*, vol. 214, no. 4, pp. 876–891, Apr. 2014.

[24] T. Altan and A. E. Tekkaya, *Sheet Metal Forming; Processes and Applications*. USA: ASM international, 2012.

[25] X. Wu, H. Bahmanpour, and K. Schmid, "Characterization of mechanically sheared edges of dual phase steels," *J. Mater. Process. Tech*, vol. 212, no. 6, pp. 1209–1224, Jun. 2012.

[26] P. Sartkulvanich, B. Kroenauer, R. Golle, A. Konieczny, and T. Altan, "Finite

element analysis of the effect of blanked edge quality upon stretch flanging of AHSS," *CIRP Ann. Manuf. Technol.*, vol. 59, no. 1, pp. 279–282, 2010.

[27] T. B. Hilditch and P. D. Hodgson, "Development of the sheared edge in the trimming of steel and light metal sheet, Part 1—Experimental observations," *J. Mater. Process. Tech*, vol. 169, no. 2, pp. 184–191, 2005.

[28] D. Spitler, J. Lantrip, J. Nee, and D. A. Smith, *Fundamentals of Tool Design*, 5th ed. Society of Manufacturing Engineers (SMS), 2003.

[29] H. P. Weaver and K. J. Weinmann, "A study of edge characteristics of sheared and bent steel plate," *J. Appl. Metalwork.*, vol. 3, no. 4, pp. 381–390, Jan. 1985.

[30] B. Högman, "Punching tests of EHS- and UHS steel sheet," in *proceedings of Recent Advances in Manufacture & Use of Tools & Dies in Stamping of Steel Sheets*, 2004.

[31] T. Kopp *et al.*, "Experimental investigation of the lateral forces during shear cutting with an open cutting line," *J. Mater. Process. Technol.*, vol. 238, pp. 49–54, Dec. 2016.

[32] H. C. Shih and M. F. Shi, "Robust shearing process for improving AHSS sheared edge stretchability," *ASME 2012 Int. Manuf. Sci. Eng. Conf. Collocated with 40th North Am. Manuf. Res. Conf. Particip. with Int. Conf., MSEC 2012*, pp. 363–369, 2012.

[33] H. C. Shih, C. K. Hsiung, and B. Wendt, "Optimal Production Trimming Process for AHSS Sheared Edge Stretchability Improvement," in *SAE World Congress*, 2014.

[34] H. C. Shih and M. F. Shi, "An Innovative Shearing Process for AHSS Edge Stretchability Improvements," *J. Manuf. Sci. Eng.*, vol. 133, no. 6, 2011.

[35] T. Altan (Editor); Schuler GmbH, *Metal Forming Handbook*. Berlin, Germany: Springer-Verlag Berlin Heidelberg, 1998.

[36] S. Nasheralahkami, W. Zhou, and S. F. Golovashchenko, "Study of Sheared Edge Formability of Ultra High Strength DP980 Sheet Metal Blanks," *J. Manuf. Sci. Eng.*, vol. 141, no. 9, p. 091009 (15), 2019.

[37] S. F. Golovashchenko and A. M. Ilinich, "Trimming of Advanced High Strength Steels," in *ASME International Mechanical Engineering Congress*, 2005.

[38] S. F. Golovashchenko, "Screening Test for Stretch Flanging a Trimmed Metal Surface," United States Patent No. US 8,511,178 B2, 2013.

[39] S. F. Golovashchenko and S. Nasheralahkami, “Determining Sheared Edge Formability of AHSS,” *Stamping Journal*, vol. 32, no. 2, pp. 20–24, 2020.

[40] ISO 16630:2017, “Metallic Materials - Sheet and Strip - Hole Expanding Test,” Geneva, Switzerland, 2017.

[41] A. Konieczny and T. Henderson, “On Formability Limitations in Stamping Involving Sheared Edge Stretching,” in *SAE World Congress*, 2007.

[42] W. C. Emmens, *Formability: A Review of Parameters and Processes that Control, Limit or Enhance the Formability of Sheet Metal*. The Netherlands: Springer-Verlag Berlin Heidelberg, 2011.

[43] S. F. Golovashchenko, “Method of Measuring Localized Strains in Sheet Metal Stampings,” United States Patent No. US 10,907,957 B2, 2021.

[44] ISO 4957, “BS EN ISO 4957:2018 - Tool Steels,” *British Standard / European Standard / International Organization for Standardization*. 2018.

[45] K. Nothhaft, “Shear cutting of high-strength sheet materials in an open cut (in German),” Technischen Universität München, 2013.

[46] G. Roberts, G. Krauss, and R. Kennedy, *Tool Steels*, 5th Ed. Materials Park, OH. USA: ASM International, 1998.

[47] O. Sandberg and B. Johansson, “Tool Steels for Blanking and Forming - New Developments,” in *proceedings of Recent Advances in Manufacture & Use of Tools & Dies in Stamping of Steel Sheets*, 2004.

[48] R. A. Mesquita, *Tool Steels: Properties and Performance*, 1st editio. Boca Raton, USA: CRC Press, 2016.

[49] E. Billur, “Die materials and wear in stamping AHSS - Part I: Die wear and die coatings,” *Stamping Journal*, no. Jan/Feb, pp. 8–9, 2010.

[50] T. Altan and S. Subramonian, “Punch wear in blanking - Part I: Punch geometry and failure,” *Stamping Journal*, no. Jul/Aug, pp. 14–15, 2012.

[51] ASTM International, “G40-17, Standard Terminology Relating to Wear and Erosion.” West Conshohocken, PA, USA, 2017.

[52] M. Eriksen, “The influence of die geometry on tool wear in deep drawing,” *Wear*, vol. 207, no. 1–2, pp. 10–15, 1997.

[53] X. Z. Wang and S. H. Masood, “Optimisation of die radius geometry in sheet metal stamping,” *Adv. Mater. Res.*, vol. 337, pp. 350–353, 2011.

[54] C. Wang, J. Chen, Z. C. Xia, and F. Ren, “Die wear prediction by defining three-

stage coefficient K for AHSS sheet metal forming process," *Int. J. Adv. Manuf. Technol.*, vol. 69, no. 1–4, pp. 797–803, 2013.

[55] K. Ersoy-Nürnberg, G. Nürnberg, M. Golle, and H. Hoffmann, "Simulation of wear on sheet metal forming tools—An energy approach," *Wear*, vol. 265, no. 11–12, pp. 1801–1807, Nov. 2008.

[56] X. Z. Wang and S. H. Masood, "Investigation of die radius arc profile on wear behaviour in sheet metal processing of advanced high strength steels," *Mater. Des.*, vol. 32, no. 3, pp. 1118–1128, 2011.

[57] S. Y. Luo, "Effect of the geometry and the surface treatment of punching tools on the tool life and wear conditions in the piercing of thick steel plate," *J. Mater. Process. Tech*, vol. 88, no. 1, pp. 122–133, 1999.

[58] P. Sartkulvanich and T. Altan, "Examining edge cracking in hole flanging of AHSS Part III: The effects of punch speed, material, and tool wear," *Stamping Journal*, no. October, pp. 16–17, 2008.

[59] S. Subramonian, "Improvement of Punch and Die Life and Part Quality in Blanking of Miniature Parts," The Ohio State University, 2013.

[60] J. J. Hernández, P. Franco, M. Estrems, and F. Faura, "Modelling and experimental analysis of the effects of tool wear on form errors in stainless steel blanking," *J. Mater. Process. Tech*, vol. 180, no. 1, pp. 143–150, 2006.

[61] N. Perez, *Fracture Mechanics*, 2nd ed. Switzerland: Springer Nature, 2017.

[62] L. Pook, *Metal Fatigue; What It Is, Why It Matters*, 1st Editio. Dordrecht, Netherlands: Springer Dordrecht, 2016.

[63] H. E. Boyer, *Atlas of Fatigue Curves*. Materials Park, OH. USA: ASM International, 1986.

[64] M. Li, "An experimental investigation on cut surface and burr in trimming aluminum autobody sheet," *Int. J. Mech. Sci.*, vol. 42, no. 5, pp. 889–906, 2000.

[65] W. Johnson and R. Slater, "A Survey of the Slow and Fast Blanking of Metals at Ambient and High Temperatures," in *Proceedings of the International Conference of Manufacturing Technology, CIRP-ASTME*, 1967, pp. 825–851.

[66] S. Jana and N. S. Ong, "Effect of punch clearance in the high-speed blanking of thick metals using an accelerator designed for a mechanical press," *J. Mech. Work. Technol.*, vol. 19, no. 1, pp. 55–72, 1989.

[67] A. M. Ilinich, S. F. Golovashchenko, and L. M. Smith, "Material anisotropy and

trimming method effects on total elongation in DP500 sheet steel," *J. Mater. Process. Tech*, vol. 211, no. 3, pp. 441–449, 2011.

[68] J. Chintamani and S. Sriram, "Sheared Edge Characterization of Steel Products used for Closure Panel Applications," in *SAE World Congress*, 2006.

[69] T. Wiedenmann, R., Sartkulvanich, P. and Altan, "Finite Element Analysis on the Effect of Sheared Edge Quality in Blanking Upon Hole Expansion of Advanced High Strength Steel," in *International Deep Drawing Research Group Conference, IDDRG*, 2009, no. June, pp. 559–570.

[70] K. Mori, T. Maeno, and S. Fuzisaka, "Punching of ultra-high strength steel sheets using local resistance heating of shearing zone," *J. Mater. Process. Technol.*, vol. 212, no. 2, pp. 534–540, Feb. 2012.

[71] S. F. Golovashchenko, "A study on trimming of aluminum autobody sheet and development of a new robust process eliminating burrs and slivers," *Int. J. Mech. Sci.*, vol. 48, no. 12, pp. 1384–1400, 2006.

[72] S. F. Golovashchenko, "Robust Trimming of Automotive Panels," *Mater. Sci. Forum*, vol. 539–543, pp. 423–428, 2007.

[73] S. F. Golovashchenko, "Quality of trimming and its effect on stretch flanging of automotive panels," *J. Mater. Eng. Perform.*, vol. 17, no. 3, pp. 316–325, Jun. 2008.

[74] S. P. Keeler and W. A. Backofen, "plastic instability and fracture in sheet stretched over rigid punches," *ASM Trans Q*, vol. 56, no. 1, pp. 25–48, 1963.

[75] R. D. Adamczyk and G. M. Michal, "Sheared Edge Extension of High-Strength Cold-Rolled Steels," *J. Appl. Metalwork.*, vol. 4, no. 2, pp. 157–163, 1986.

[76] K. ichiro Mori, Y. Abe, and Y. Suzui, "Improvement of stretch flangeability of ultra high strength steel sheet by smoothing of sheared edge," *J. Mater. Process. Technol.*, vol. 210, no. 4, pp. 653–659, 2010.

[77] K. Hasegawa, K. Kawamura, T. Urabe, and Y. Hosoya, "Effects of Microstructure on Stretch-flange-formability of 980 MPa Grade Cold-rolled Ultra High Strength Steel Sheets," *ISIJ Int.*, vol. 44, no. 3, pp. 603–609, 2004.

[78] R. J. Comstock, D. K. Scherrer, and P. D. Adamczyk, "Hole expansion in a variety of sheet steels," *J. Mater. Eng. Perform.*, vol. 15, no. 6, pp. 675–683, 2006.

[79] M. Stanton, R. Bhattacharya, I. Dargue, R. Aylmore, and G. Williams, "Hole expansion of aluminum alloys for the automotive industry," *AIP Conf. Proc.*, vol. 1353, no. April 2011, pp. 1488–1493, 2011.

[80] C. Mcewan, R. Underhill, N. Langerak, G. Botman, and M. De Bruine, “A New Approach To Predicting Edge Splits the Combined FlC/ HEC Diagram,” in *IDDRG2009 International Conference*, 2009, no. June, pp. 65–72.

[81] C. Chiriac and M. F. Shi, “Experimental Study of Edge Stretching Limits of DP980IBF Steel in Multistage Forming Process,” *SAE Int. J. Mater. Manuf.*, vol. 8, no. 2, pp. 415–418, Jun. 2015.

[82] C. Chiriac, M. F. Shi, and T. M. Link, “The prestrain effect on the sheared edge flangeability of dual phase 780 steels,” *SAE Technical Paper*, 2012.

[83] A. Karelova, C. Krempaszky, E. Werner, P. Tsipouridis, T. Hebesberger, and A. Pichler, “Hole Expansion of Dual-phase and Complex-phase AHS Steels - Effect of Edge Conditions,” *Steel Research International*, vol. 80, no. 1, pp. 71–77, 2009.

[84] B. M. Hance, R. J. Comstock, and D. K. Scherrer, “The influence of edge preparation method on the hole expansion performance of automotive sheet steels,” *SAE Technical Paper*, vol. 2, 2013.

[85] A. G. Atkins, M. Afzal Khan, and J. H. Liu, “Necking and radial cracking around perforations in thin sheets at normal incidence,” *Int. J. Impact Eng.*, vol. 21, no. 7, pp. 521–539, 1998.

[86] C. Chiriac, “A study of the plastic deformation of sheared edges of dual phase 780 steel,” *SAE Technical Paper*, 2010.

[87] J. Wang, T. M. Link, and M. J. Merwin, “AHSS Edge Formability in Sheared-Edge Tension,” in *International Conference on New Developments in Advanced High-Strength Sheet Steels*, 2008, pp. 361–366.

[88] N. Wang and S. F. Golovashchenko, “Mechanism of fracture of aluminum blanks subjected to stretching along the sheared edge,” *J. Mater. Process. Technol.*, vol. 233, pp. 142–160, Jul. 2016.

[89] S. F. Golovashchenko, N. Wang, and Q. Le, “Trimming and sheared edge stretchability of automotive 6xxx aluminum alloys,” *J. Mater. Process. Technol.*, vol. 264, no. September 2018, pp. 64–75, 2019.

[90] S. Nasheralahkami, S. Golovashchenko, K. Pan, L. Brown, and B. Gugnani, “Characterization of Trimmed Edge of Advanced High Strength Steel,” in *SAE World Congress*, 2016, no. April.

[91] S. Golovashchenko, W. Zhou, S. Nasheralahkami, and N. Wang, “Trimming and Sheared Edge Stretchability of Light Weight Sheet Metal Blanks,” *Procedia Eng.*, vol. 207, pp. 1552–1557, 2017.

[92] S. Nasheralahkami, S. Golovashchenko, S. Dawson, and R. Sohmshetty, "Analysis of Tool Wear for Trimming of DP980 Sheet Metal Blanks," *SAE Int. J. Engines*, vol. 10, no. 2, pp. 233–238, 2017.

[93] P. B. Popat, A. Ghosh, and N. N. Kishore, "Theoretical investigation of optimum clearance in blanking," *J. Mech. Work. Technol.*, vol. 19, no. 2, pp. 251–259, 1989.

[94] U. P. Singh, W. Klingenberg, and W. Urquhart, "Effect of tool geometry on punching performance," *J. Manuf. Sci. Eng. Trans. ASME*, vol. 116, no. 4, pp. 508–513, 1994.

[95] A. M. Goijaerts, L. E. Govaert, and F. P. T. Baaijens, "Evaluation of ductile fracture models for different metals in blanking," *J. Mater. Process. Technol.*, vol. 110, no. 3, pp. 312–323, 2001.

[96] A. M. Goijaerts, L. E. Govaert, and F. P. T. Baaijens, "Prediction of ductile fracture in metal blanking," *J. Manuf. Sci. Eng. Trans. ASME*, vol. 122, no. 3, pp. 476–483, 2000.

[97] X. H. Hu, K. S. Choi, X. Sun, and S. F. Golovashchenko, "Edge Fracture Prediction of Traditional and Advanced Trimming Processes for AA6111-T4 Sheets," *J. Manuf. Sci. Eng.*, vol. 136, no. 2, p. 21016, Feb. 2014.

[98] X. H. Hu, X. Sun, and S. F. Golovashchenko, "Predicting tensile stretchability of trimmed AA6111-T4 sheets," *Comput. Mater. Sci.*, vol. 85, pp. 409–419, 2014.

[99] J. F. Archard, "Contact and rubbing of flat surfaces," *J. Appl. Phys.*, vol. 24, no. 8, pp. 981–988, 1953.

[100] J. F. Archard and W. Hirst, "The wear of metals under unlubricated conditions," *Proc. R. Soc. London. Ser. A. Math. Phys. Sci.*, vol. 236, no. 1206, pp. 397–410, 1956.

[101] S. C. Lim and M. F. Ashby, "Overview no. 55 Wear-Mechanism maps," *Acta Metall.*, vol. 35, no. 1, pp. 1–24, 1987.

[102] M. F. Ashby and S. C. Lim, "Wear-mechanism maps," *Scr. Metall. Mater.*, vol. 24, no. 5, pp. 805–810, 1990.

[103] H. Hoffmann, C. Hwang, and K. Ersoy, "Advanced wear simulation in sheet metal forming," *CIRP Ann. - Manuf. Technol.*, vol. 54, no. 1, pp. 217–220, 2005.

[104] M. P. Pereira, W. Yan, and B. F. Rolfe, "Contact pressure evolution and its relation to wear in sheet metal forming," *Wear*, vol. 265, no. 11–12, pp. 1687–1699, 2008.

[105] M. P. Pereira, W. Yan, and B. F. Rolfe, “Wear at the die radius in sheet metal stamping,” *Wear*, vol. 274–275, pp. 355–367, 2012.

[106] P. Palanisamy, I. Rajendran, and S. Shanmugasundaram, “Prediction of tool wear using regression and ANN models in end-milling operation,” *Int. J. Adv. Manuf. Technol.*, vol. 37, no. 1–2, pp. 29–41, 2008.

[107] D. C. Ko and B. M. Kim, “Development of an analytical scheme to predict the need for tool regrinding in shearing processes,” *Int. J. Mach. Tools Manuf.*, vol. 40, no. 9, pp. 1329–1349, 2000.

[108] D. C. Ko, D. H. Kim, and B. M. Kim, “Finite element analysis for the wear of Ti-N coated punch in the piercing process,” *Wear*, vol. 252, no. 11–12, pp. 859–869, 2002.

[109] R. Hambli, “Blanking tool wear modeling using the finite element method,” *Int. J. Mach. Tools Manuf.*, vol. 41, no. 12, pp. 1815–1829, 2001.

[110] C. Husson, J. P. M. M. Correia, L. Daridon, and S. Ahzi, “Finite elements simulations of thin copper sheets blanking: Study of blanking parameters on sheared edge quality,” *J. Mater. Process. Tech*, vol. 199, no. 1, pp. 74–83, 2008.

[111] H. Makich, L. Carpentier, G. Monteil, X. Roizard, J. Chambert, and P. Picart, “Metrology of the burr amount - correlation with blanking operation parameters (blanked material – wear of the punch),” *Int. J. Mater. Form.*, vol. 1, pp. 1243–1246, 2008.

[112] S. Y. Luo, “Studies on the wear conditions and the sheared edges in punching,” *Wear*, vol. 208, no. 1, pp. 81–90, Jul. 1997.

[113] Ö. N. Cora and M. Koç, “Experimental investigations on wear resistance characteristics of alternative die materials for stamping of advanced high-strength steels (AHSS),” *Int. J. Mach. Tools Manuf.*, vol. 49, no. 12–13, pp. 897–905, 2009.

[114] B. Krause and T. Bell, “Increasing the Efficiency of Metalform Tooling for Advanced High Strength Steels,” *Great Design in Steel, Livonia, MI*, 2005.

[115] A. Zeidi, F. Ben Saada, K. Elleuch, and H. Atapek, “AISI D2 punch head damage: Fatigue and wear mechanism,” *Eng. Fail. Anal.*, vol. 129, p. 105676, 2021.

[116] H. S. Choi, B. M. Kim, and D. C. Ko, “Effect of clearance and inclined angle on sheared edge and tool failure in trimming of DP980 sheet,” *J. Mech. Sci. Technol.*, vol. 28, no. 6, pp. 2319–2328, Jun. 2014.

[117] C. C. Chu, “Comparison of Mean Stress Correction Methods for Fatigue Life Prediction,” *SAE Tech. Pap. Ser.*, 2000.

[118] J. O. Smith, “The Effect of Range of Stress on the Fatigue Strength of Metals,” in *Bulletin No. 334, University of Illinois, Engineering Experiment Station,* Urbana, IL, 1942.

[119] J. D. Morrow, *Fatigue Design Handbook, Section 3.2, SAE Advances in Engineering*, vol. 4. Warrendale, PA: Society of Automotive Engineers (SAE), 1968.

[120] C. R. Soderberg, “Factor of Safety and Working Stress,” *ASME Trans.*, vol. 52, no. APM-52-2, pp. 13–28, 1930.

[121] N. E. Dowling, *Mechanical Behavior of Materials - Engineering Methods for Deformation, Fracture, and Fatigue*, 4th ed. Harlow, England: Pearson Education Limited, 2013.

[122] A. Ince, “A mean stress correction model for tensile and compressive mean stress fatigue loadings,” *Fatigue Fract. Eng. Mater. Struct.*, vol. 40, no. 6, pp. 939–948, 2017.

[123] T. H. Smith, K. N., Watson, P., Topper, “A Stress-Strain Function for the Fatigue of Metals,” *J. Mater.*, vol. 5, pp. 767–778, 1970.

[124] K. Walker, “The Effect of Stress Ratio During Crack Propagation and Fatigue for 2024-T3 and 7075-T6 Aluminum,” in *Effects of Environment and Complex Load History on Fatigue Life, ASTM STP 462*, Philadelphia, PA: American Society for Testing and Materials, 1970, pp. 1–14.

[125] N. Dowling, C. A. Calhoun, and A. Arcari, “Mean stress effects in stress-life fatigue and the Walker equation,” *Fatigue Fract. Eng. Mater. Struct.*, vol. 32, pp. 163–179, 2009.

[126] I. Amarir, H. Mounir, and A. E. L. Marjani, “Modeling the Mean Stress Effect on the Fatigue Life of Welded Profiles Under Damped Loads for Automotive Applications,” in *Distributed Sensing and Intelligent Systems*, 2022, pp. 711–721.

[127] S. Zhu, Q. Lei, H. Huang, Y. Yang, and W. Peng, “Mean stress effect correction in strain energy-based fatigue life prediction of metals,” *Int. J. Damage Mech.*, vol. 26, pp. 1219–1241, 2017.

[128] M. M. Pedersen, “Introduction to Metal Fatigue: Concepts and Engineering Approaches,” Denmark, 2018.

[129] J. Schijve, *Fatigue of Structures and Materials*, 2nd ed. Dordrecht, Netherlands: Springer Dordrecht, 2009.

[130] N. Dowling, “Mean Stress Effects in Stress-Life and Strain-Life Fatigue,” in *2nd*

SAE Brasil International Conference on Fatigue, 2004.

[131] N. M. Meyer, "Effects of mean stress and stress concentration on fatigue behavior of ductile iron," M.Sc. Thesis, The University of Toledo, 2014.

[132] D. G. da Silva, J. T. Lockwood, W. Liang, and T. H. Topper, "Mean stress effect in stress-life for hard steels," *Int. J. Fatigue*, 2021.

[133] J. F. Bonnen, "Multiaxial Fatigue Response of Normalized 1045 Steel Subjected to Periodic Overloads: Experiments and Analysis," Ph.D. thesis, University of Waterloo, Waterloo, Canada, 1998.

[134] K. Kluger and R. Pawliczek, "Assessment of Validity of Selected Criteria of Fatigue Life Prediction," *Materials (Basel).*, vol. 12, no. 14, Jul. 2019.

[135] G. Stanfield, "The Strength of Metals Under Combined Alternating Stresses," in *Proceeding of the Institution of Mechanical Engineers 131, 93*, 1935.

[136] W. N. Findley, "A Theory for the Effect of Mean Stress on Fatigue of Metals Under Combined Torsion and Axial Load or Bending," *J. Eng. Ind.*, vol. 81, pp. 301–305, 1959.

[137] K. Dang Van and B. Griveau, "On a new multiaxial fatigue limit criterion: Theory and application," *Biaxial multiaxial fatigue (A 90-16739 05-39). London, Mech. Eng. Publ. Ltd.*, pp. 479–496, 1989.

[138] A. Fatemi and D. F. Socie, "A Critical Plane Approach to Multiaxial Fatigue Damage Including Out-Of-Phase Loading," *Fatigue Fract. Eng. Mater. Struct.*, vol. 11, no. 3, pp. 149–165, 1988.

[139] M. W. Fu, M. S. Yong, and T. Muramatsu, "Die fatigue life design and assessment via CAE simulation," *Int. J. Adv. Manuf. Technol.*, vol. 35, pp. 843–851, 2008.

[140] K. K. Tong, M. S. Yong, M. W. Fu, T. Muramatsu, C. S. Goh, and S. X. Zhang, "CAE enabled methodology for die fatigue life analysis and improvement," *Int. J. Prod. Res.*, vol. 43, pp. 131–146, 2005.

[141] L. Long, X. Zhang, S. Gu, X. Li, X. Cheng, and G. Chen, "Experimental and Simulation Investigation on Fatigue Performance of H13 Steel Tools in Friction Stir Welding of Aluminum Alloys," *Materials (Basel).*, vol. 17, 2024.

[142] P. Brøndsted and P. Skov-Hansen, "Fatigue Properties of High-Strength Materials used in Cold-forging Tools," *Int. J. Fatigue*, vol. 20, no. 5, pp. 373–381, 1998.

[143] P. Skov-Hansen, N. Bay, Gronbae, J. K, and P. Brøndsted, "Fatigue in Cold-forging Dies: Tool Life Analysis," *J. Mater. Process. Technol.*, vol. 95, pp. 40–48,

1999.

[144] S. Alimov, Artem, Sviridov Alexander, Härtel, “Fatigue life analysis of hot forming dies produced by the L-PBF and WA-DED additive technologies,” *Mater. Res. Proc.*, vol. 41, pp. 2154–2163, 2024.

[145] A. R. Ab-Kadir, A. R. Othman, A. B. Abdullah, M. R. Ibrahim, and M. H. Osman, “Prediction of Fatigue Life in Cold Forging Punch Design for Fastener Using Integrated FEA and Stress Life Approach,” *Procedia Eng.*, vol. 50, pp. 505–515, 2012.

[146] S. Salunkhe, S. Kumar, and H. M. A. Hussein, “Prediction of Life of Compound Die Using Artificial Neural Network,” in *AI Applications in Sheet Metal Forming*, S. Kumar and H. M. A. Hussein, Eds. Singapore: Springer Singapore, 2017, pp. 217–243.

[147] I. Picas, “Mechanical behaviour of tools for shearing Ultra High-Strength Steels: influence of the microstructure on fracture and fatigue micro-mechanisms of tool steels and evaluation of micro-mechanical damage in tools,” Ph.D. thesis, Universitat Politècnica de Catalunya, Barcelona, Spain, 2012.

[148] J. R. Davis, *ASM Specialty Handbook: Tool Materials*. Materials Park, OH. USA: ASM International, 1995.

[149] The Mathworks Inc., *Matlab User’s Guide*, vol. 9.3. Natick, MA. USA, 2017.

[150] ASTM International, “ASTM E140-12B: Standard Hardness Conversion Tables for Metals Relationship Among Brinell Hardness, Vickers Hardness, Rockwell Hardness, Superficial Hardness, Knoop Hardness, Scleroscope Hardness, and Leeb Hardness.” West Conshohocken, PA, USA, 2019.

[151] S. S. Hecker, “Simple technique for determining forming limit curves,” *Sheet Metal Industries*, vol. 11, pp. 671–673, 1975.

[152] Z. Marciniak, J. L. Duncan, and S. J. Hu, *Mechanics of Sheet Metal Forming*, 2nd ed. Oxford, UK: Butterworth-Heinemann, 2002.

[153] D. L. Steinbrunner, D. K. Matlock, and G. Krauss, “Void formation during tensile testing of dual phase steels,” *Metall. Trans. A*, vol. 19, pp. 579–589, 1988.

[154] J. Kadkhodapour, A. Butz, S. Ziaei-Rad, and S. Schmauder, “A micro mechanical study on failure initiation of dual phase steels under tension using single crystal plasticity model,” *Int. J. Plast.*, vol. 27, pp. 1103–1125, 2011.

[155] N. Pathak, C. Butcher, M. J. Worswick, E. Bellhouse, and J. Gao, “Damage Evolution in Complex-Phase and Dual-Phase Steels during Edge Stretching,”

Materials (Basel)., vol. 10, no. 4, 2017.

[156] X. Wu and H. Bahmanpour, *Characterization of Mechanically Sheared Edges of Dual Phase Steels*. Southfield, MI. USA: Auto/Steel Partnership, 2010.

[157] T. Ferreira and W. Rasband, *ImageJ User Guide, Ver. 1.46r*. http://imagej.nih.gov/, 2012.

[158] Dassault Systèmes Simulia Corp., *ABAQUS Analysis User's Guide*, vol. 6.14. http://www.3ds.com/, 2014.

[159] MSC Software Company, *SIMUFACT User Manual*. http://www.simufact.com/, 2016.

[160] QForm Group LLC, *QFORM User manual*. http://www.qform3d.com/, 2019.

[161] W. Daodon and V. Saetang, "Improvement of Frictional Property of AISI D2 Tool Steel Surface against JIS SPFC 980Y Advanced High-Strength Steel by Using Laser Texturing Process," *Lubricants*, vol. 11, no. 2, 2023.

[162] G. Cheng, X. Hu, K. Choi, and X. Sun, "Predicting grid-size-dependent fracture strains of DP980 with a microstructure-based post-necking model," *Int. J. Fract.*, vol. 207, no. 2, pp. 211–227, Oct. 2017.

[163] D. T. Hecker, S. S., Stout, M. G., Eash, "Experiments on plastic deformation at finite strains," in *Plasticity of metals at finite strain: theory, experiment and computation*, 1981.

[164] J. Gil Sevillano, P. van Houtte, and E. Aernoudt, "Large strain work hardening and textures," *Prog. Mater. Sci.*, vol. 25, no. 2–4, pp. 69–412, 1981.

[165] H. Ford, "Researches into the Deformation of Metals by Cold Rolling," *Proc. Inst. Mech. Eng.*, vol. 159, no. 1, pp. 115–143, Jun. 1948.

[166] ASTM International, "ASTM E8/E8M-09: Standard Test Methods for Tension Testing of Metallic Materials." West Conshohocken, PA, USA, 2011.

[167] W. D. Callister and D. G. Rethwisch, *Materials Science and Engineering: An Introduction, 10th Edition*. New York, USA: Wiley, 2018.

[168] T. L. Anderson, *Fracture Mechanics: Fundamentals and Applications*, 4th Ed. Taylor & Francis, 2017.

[169] Y. Bai and T. Wierzbicki, "A new model of metal plasticity and fracture with pressure and Lode dependence," *Int. J. Plast.*, vol. 24, no. 6, pp. 1071–1096, 2008.

[170] G. R. Johnson, "Materials Characterization for computations involving severe dynamic loading," in *Proc. Army Symp. Of Solid Mechanics*, 1980, pp. 62–67.

[171] S. E. Clift, P. Hartley, C. E. N. Sturgess, and G. W. Rowe, "Fracture prediction in plastic deformation processes," *Int. J. Mech. Sci.*, vol. 32, no. 1, pp. 1–17, 1990.

[172] M. G. Cockcroft and D. J. Latham, "Ductility and the Workability of Metals," *Journal of the Institute of Metals*, vol. 96, no. 1. pp. 33–39, 1968.

[173] J. R. Rice and D. M. Tracey, "On the ductile enlargement of voids in triaxial stress fields," *J. Mech. Phys. Solids*, vol. 17, no. 3, pp. 201–217, 1969.

[174] G. R. Johnson and W. H. Cook, "A Computational Constitutive Model and Data for Metals Subjected to Large Strain, High Strain Rates and High Pressures," *Seventh Int. Symp. Ballist.*, pp. 541–547, 1983.

[175] M. Krinninger, D. Opritescu, R. Golle, and W. Volk, "On the opportunities of problem- and process-adapted shear cutting simulations for effective process design," *Procedia Engineering*, vol. 207. pp. 1570–1575, 2017.

[176] M. Oyane, "Criteria of Ductile Fracture Strain," *Bull. Japan Soc. Mech. Eng.*, vol. 15, no. 90, pp. 1507–1513, 1972.

[177] Y. Lou, H. Huh, S. Lim, and K. Pack, "New ductile fracture criterion for prediction of fracture forming limit diagrams of sheet metals," *Int. J. Solids Struct.*, vol. 49, no. 25, pp. 3605–3615, 2012.

[178] Y. Bao and T. Wierzbicki, "On the cut-off value of negative triaxiality for fracture," *Eng. Fract. Mech.*, vol. 72, no. 7, pp. 1049–1069, 2005.

[179] K. Takada, K. Sato, and N. Ma, "Fracture Prediction for Automotive Bodies Using a Ductile Fracture Criterion and a Strain-Dependent Anisotropy Model," *SAE Int. J. Mater. Manuf.*, vol. 8, no. 3, 2015.

[180] G. R. Johnson and W. H. Cook, "Fracture characteristics of three metals subjected to various strains, strain rates, temperatures and pressures," *Eng. Fract. Mech.*, vol. 21, no. 1, pp. 31–48, 1985.

[181] H. Wang, Y. Yan, F. Jia, and F. Han, "Investigations of fracture on DP980 steel sheet in roll forming process," *J. Manuf. Process.*, vol. 22, pp. 177–184, 2016.

[182] N. Park and H. Huh, "Prediction of fracture strains for DP980 steel sheets using a modified lou-huh ductile fracture criterion," *Key Eng. Mater.*, vol. 626, pp. 347–352, 2015.

[183] F. Gutknecht, F. Steinbach, T. Hammer, T. Clausmeyer, W. Volk, and A. E. Tekkaya, "Analysis of shear cutting of dual phase steel by application of an advanced damage model," *Procedia Struct. Integr.*, vol. 2, pp. 1700–1707, 2016.

[184] Y. H. Guu and H. Hocheng, “Improvement of fatigue life of electrical discharge machined AISI D2 tool steel by TiN coating,” *Mater. Sci. Eng. A*, vol. 318, pp. 155–162, 2001.

[185] Hitachi Metals, “Cold Work Tool Steels, General Catalog of YSS Tool Steels,” Japan, 2015.

[186] “Onlinemetals.com.” [Online]. Available: https://www.onlinemetals.com/en/product-guide/alloy/d2.

[187] K. Fukaura, Y. Yokoyama, D. Yokoi, N. Tsujii, and K. Ono, “Fatigue of cold-work tool steels: Effect of heat treatment and carbide morphology on fatigue crack formation, life, and fracture surface observations,” *Metall. Mater. Trans. A*, vol. 35, pp. 1289–1300, 2004.

[188] Z. Cui, “Wear Mechanisms of Tool Steel and Their Effect on Trimming of High Strength Steel Sheets,” Ph.D. Thesis, University of Windsor, Canada, 2022.

[189] Uddeholm AB, “Uddeholm Cataloge - Sverker 21,” UK, 2019.

[190] M. Knoerr, K. Lange, and T. Altan, “Fatigue failure of cold forging tooling: causes and possible solutions through fatigue analysis,” *J. Mater. Process. Technol.*, vol. 46, pp. 57–71, 1994.

[191] D. W. Tang, C. Y. Wang, Y. N. Hu, and Y. X. Song, “Constitutive equation for hardened SKD11 steel at high temperature and high strain rate using the SHPB technique,” in *International Conference on Experimental Mechanics*, 2009.

[192] K. Masuda, N. Oguma, S. Ishihara, and A. J. Mcevily, “Investigation of subsurface fatigue crack growth behavior of D2 tool steel (JIS SKD11) based on a novel measurement method,” *Int. J. Fatigue*, vol. 133, 2020.

[193] T. Matsuno *et al.*, “Identification of Ductile Fracture Design Curve for Hardened Quasi-Brittle AISI-D2 Tool Steel to Predict Shearing Tool Failure,” *J. Mater. Process. Technol.*, vol. 307, 2022.

[194] D. Gerasimov and A. Gartvig, “Parallel computing of metal forming simulation in QForm software,” *Comput. Methods Mater. Sci.*, vol. 16, no. 3, pp. 139–142, 2016.

[195] O. Sandin *et al.*, “A particle finite element method approach to model shear cutting of high-strength steel sheets,” *Comput. Part. Mech.*, vol. 11, no. 5, pp. 1863–1886, 2024.

[196] M. Söderberg, “Finite Element Simulation of Punching,” M.Sc. Thesis, Luleå University of Technology, 2006.

[197] J. Rizk, M. Rachik, and A. Maillard, "Finite element simulation of the complete sheet metal blanking cycle: Effect of blanking clearance on force curve and cut edge quality," *Heliyon*, vol. 10, no. 9, p. e30334, May 2024.

[198] W. Cha, T. Hammer, F. Gutknecht, R. Golle, A. E. Tekkaya, and W. Volk, "Adaptive Wear Model for Shear-Cutting Simulation with Open Cutting Line," *Wear*, vol. 386–387, pp. 17–28, 2017.

[199] I. Suchy, *Handbook of Die Design*, 2nd ed. New York, USA: McGraw-Hill, 2006.

[200] O. H. Basquin, "The Exponential Law of Endurance Tests," in *Proceedings of American Society for Testing and Materials , Vol. 10*, 1910, pp. 625–630.

[201] S. S. Manson, "Behavior of Materials Under Conditions of Thermal Stress," *NACA TN 2933*, 1953.

[202] L. F. Coffin, "A Study of the Effects of Cyclic Thermal Stresses on a Ductile Metal," *Trans. ASME*, vol. 76, pp. 931–950, 1954.

[203] R. I. Stephens, A. Fatemi, R. R. Stephens, and H. O. Fuchs, *Metal Fatigue in Engineering*, 2nd Ed. New York, USA: John Wiley & Sons, 2000.

[204] M. L. Roessle and A. Fatemi, "Strain-controlled fatigue properties of steels and some simple approximations," *Int. J. Fatigue*, vol. 22, pp. 495–511, 2000.

[205] B. Boardman, "Fatigue Resistance of Steels," in *ASM Handbook, Volume 1 - Properties and Selection: Irons, Steels, and High-Performance Alloys*, ASM International, 1990.

[206] W. Liang, F. A. Conle, and T. H. Topper, "Cyclic Behaviour of Carburized 16MnCr5 Steel: Effects of Retained Austenite Transformation and Residual Stress," *SSRN*, 2024.

[207] W. Liang, "Fatigue Design and Behaviour of Carburized Steel," University of Waterloo, Waterloo, Ontario, CA, 2022.

[208] A. Winkler, S. Holt, and L. Vallance, "Concerning the Synergy of Stress and Strain-based Methods in Modern Metal Fatigue Analysis," in *AVL Advanced Simulation Technologies User Conference*, 2012.

[209] F. Concli, L. Maccioni, L. Fraccaroli, and L. Bonaiti, "Early Crack Propagation in Single Tooth Bending Fatigue: Combination of Finite Element Analysis and Critical-Planes Fatigue Criteria," *Metals (Basel).*, vol. 11, no. 1871, 2021.

[210] M. W. Brown and K. J. Miller, "A Theory for Fatigue Failure under Multiaxial Stress-Strain Conditions," *Proc. Inst. Mech. Eng.*, vol. 187, no. 1, pp. 745–755,

1973.

[211] B. Crossland, “Effect of large hydrostatic pressure on the torsional fatigue strength of an alloy steel,” in *Proceedings of the International Conference on Fatigue of Metals (Institution of Mechanical Engineers)*, 1956, pp. 138–149.

[212] S. Suresh, *Fatigue of Materials (Cambridge Solid State Science Series)*, 2nd Ed. Cambridge, UK: Cambridge University Press, 1998.

[213] T. Dahlberg and A. Ekberg, *Failure Fracture Fatigue: An Introduction*. Professional Pub Service, 2002.

[214] N. Johansson, “Estimation of fatigue life by using a cyclic plasticity model and multiaxial notch correction,” Master thesis, Linköping University, Linköping, Sweden, 2019.

[215] ASTM International, “ASTM E23-24: Standard Test Methods for Notched Bar Impact Testing of Metallic Materials.” West Conshohocken, PA, USA, 2025.

[216] G. W. Stachowiak and A. W. Batchelor, *Engineering Tribology*, 4th ed. Waltham, MA, USA: Elsevier Butterworth-Heinemann, 2013.

[217] T. Y. (Jean) Hsu and Z. Wang, “Fatigue crack initiation at notch root under compressive cyclic loading,” *Procedia Eng.*, vol. 2, no. 1, pp. 91–100, 2010.

[218] N. A. Fleck, C. S. Shin, and R. A. Smith, “Fatigue crack growth under compressive loading,” *Eng. Fract. Mech.*, vol. 21, no. 1, pp. 173–185, 1985.